Pilot study on the detection efficiency of single-photon detectors – Si-SPAD

CCPR WG-SP TG 11 – EURAMET Project 1468

Final report

Stefan Kück[1], Helmuth Hofer[1], Marco López[1], Hayong Gan[2], Geiland Porrovecchio[3], Marek Smid[3], Ingmar Müller[1], Salvatore Virzì[4], Alice Meda[4], Giorgio Brida[4], Tetsuya Tsuruta[5] Daiji Fukuda[5], Dong-Hoon Lee[6], Kee-Suk Hong[6], In-Ho Bae[6], Damian Twerenbold[7], Peter Blattner[7], Christopher Chunnilall[8], Robert Starkwood[8], Joseph Steven Borbely[9], Jeongwan Jin[10], Shivam Chanana[10], Ka-Ming Liu[10], Thomas Gerrits[11]

[1]Physikalisch-Technische Bundesanstalt, Germany, [2]National Institute of Metrology, China, [3]Český metrologický institut, Czech Republic, [4]Istituto Nazionale di Ricerca Metrologica, Italy, [5]National Institute of Advanced Industrial Science and Technology, Tsukuba, Japan, [6]Korea Research Institute of Standards and Science, Korea, [7]Eidgenössisches Institut für Metrologie, Switzerland, [8]National Physical Laboratory, Teddington, U.K., [9]Measurement Standards Laboratory, Wellington, New Zealand, [10]National Research Council Canada, Ottawa, ON, Canada, National Institute of Standards and Technology, USA

Corresponding e-mail address: stefan.kueck@ptb.de

1. Introduction

1.1. To provide a snapshot of measurement capabilities of National Measurement Institutes in the area of photon counting detection, this pilot study will implement a combined round-robin and star-type calibration of test detectors. The results of this effort will provide several benefits to the measurement community. While ultimately it will enable NMIs to improve methodologies and measurement uncertainties, at this initial point it will allow the participants and the community as a whole to better understand the technical and logistical challenges and resources required to move from measurement efforts that are largely research projects to measurements that are practical and robust enough to be considered as a more routine measurement service. In addition, this initial test should provide guidance on what measurement and operational parameters are better suited for those calibrating photon counting detectors and those who wish to make use of high accuracy calibrated detectors.

1.2. This pilot study on detection efficiency measurements will be made on two Si-SPAD single-photon detectors at a wavelength of 850 nm in a free-space beam following a technical protocol agreed upon by all participants of this pilot study.

1.3. The organization of the whole pilot study was described in the technical protocol. PTB is acting as the pilot laboratory in this pilot study. All participants should document traceability to an independent realization of the measurement quantity or should make clear the route of traceability to the quantity via another named laboratory. By their declared intention to participate in this pilot study, the laboratories accepted the general instructions written down in the technical protocol and committed themselves to follow the procedures. The participants' details are given in Table 1.

1.4. According to the Technical protocol, after receipt of all measurement reports from the participating laboratories, the pilot laboratory will analyze the results and prepare a first pre-draft "A" report on the pilot study following the draft guidelines of the CCPR, i.e. CCPR-G7 and CCPR-G2. This Pre-Draft-A report will include measurement reports of the participants and submitted uncertainty tables, but no results. This will be circulated to the participants for comments, additions and corrections.

Laboratory contacts

Table 1: Laboratory contacts

Participant	Laboratory contact person	Institute	Address	Phone	e-mail
Germany (Div. 4 - Pilot)	Stefan Kück	Physikalisch-Technische Bundesanstalt FB 4.1 Photometrie und angewandte Radiometrie	Bundesallee 100 38116 Braunschweig Germany	+49 531 592 4100	stefan.kueck@ptb.de
Canada*	Jeongwan Jin	National Research Council Canada	1200 Montreal Road Building M-58 Ottawa Ontario K1A 0R6	+1 613-993-9101	Jeongwan.Jin@nrc-cnrc.gc.ca
China	Haiyong Gan	National Institute of Metrology Optics Division	Bei San Huan Donglu Road 18 Chaoyang District, Beijing 100029 China	+86 10 64524829	ganhaiyong@nim.ac.cn
Czech Republic	Marek Šmíd	Laboratory of Fundamental Metrology Czech Metrology Institute	V Botanice 4 150 72 Praha 5 Czech Republic	+420 257 288 328	msmid@cmi.cz
Germany (Div. 7)	Ingmar Müller	Physikalisch-Technische Bundesanstalt Arbeitsgruppe 7.33 Detektorradiometrie	Abbestr. 2-12 10587 Berlin Germany	+49 30 3481 7406	ingmar.mueller@ptb.de
Italy	Giorgio Brida	Istituto Nazionale di Ricerca Metrologica (INRiM) Photometry & Radiometry	Strada delle Cacce 91 10135 Torino Italy	+39 011 3919 222	g.brida@inrim.it
Japan	Daiji Fukuda Ken-ichi Watabe	National Metrology Institute of Japan, AIST Research Institute for Physical Measurement Laser Radiometry Research Group	AIST Tsukuba Central 3 Tsukuba 305-856 Japan	+81 29 861 6834 +81 29 861 4270	d.fukuda@aist.go.jp k.watabe@aist.go.jp
Korea	Dong-Hoon Lee Kee Suk Hong	Korea Research Institute of Standards and Science (KRISS) Center for Photometry and Radiometry	267 Gejeong-Ro, Yuseong-Gu 34113 Daejeon Rep. Korea	+82 42 868 5706	dh.lee@kriss.re.kr hongi2011@kriss.re.kr
New Zealand*	Joseph Borbely	Measurement Standards Laboratory of New Zealand	69 Gracefield Rd. Lower Hutt 5010 New Zealand	+64 4 931 3000	Joseph.Borbely@measurement.govt.nz
Switzerland	Peter Blattner	Federal Institute of Metrology (METAS)	Lindenweg 50 3003 Bern-Wabern	+41 58 387 01 11	peter.blattner@metas.ch

			Switzerland		
UK	Christopher Chunnilall	National Physical Laboratory Group: Quantum Detection	Hampton Road Teddington TW11 0LW UK	+44 20 8943 6872	christopher.chunnilall@npl.co.uk
USA	Thomas Gerrits	National Institute of Standards and Technology Applied Physics Division	325 Broadway Boulder, CO 80305 USA	+1 303 497 4661	thomas.gerrits@nist.gov
Russia**	Sergey Moskalyuk Aleksey Mikryukov	NMI - Federal State-Owned Unitary Enterprise “All-Russian Research Institute for Optical and_Physical Measurements” Department: Laser Metrology and Radiometry	119361, Moscow Ozernaia str. 46 Russia,	+7 495 437-34 47	mrsergik@mail.ru anzio64@gmail.com

* Canada and New Zealand joined during the pilot study period.

** Russia was suspended according to EURAMET regulations.

Total schedule of the pilot study

Table 2: Total schedule of the pilot study

Activity	Date – Original	Updated Schedule	Remark
Start of pilot study	May 2016	May 2016	Completed
Measurements at PTB	May - Jun 2016	May - June 2016	Completed
Measurements at NIST	Aug - Sep 2016	Aug - Sep 2016	Completed
Measurement at CMI	Jan - Feb 2017	Feb - Apr 2017	Completed
Intermediate Measurements at PTB	Mar - Apr 2017	May - Jul 2017	Completed
Measurements at NPL	Nov - Dec 2016	Jul - Aug 2017	Completed
Measurement at KRISS	Jul - Aug 2017	Sep - Dec 2017	Completed
Measurements at PTB, Div. 7	Sep - Oct 2017	Jan - Feb 2018	Completed
Measurement at INRIM	May - Jun 2017	Mar - April 2018	Shifted
Intermediate Measurements at PTB	Nov - Dec 2017	Jul - Aug 2018	Completed
Measurements at METAS	Jan - Feb 2018	Oct - Apr 2019	Completed
Measurements at AIST	May - Jun 2018	Aug - Oct 2019	Completed
Measurements at VNIIOFI	Mar - Apr 2018	Jan - May 2021	Completed
Intermediate Measurements at PTB		Jun - Aug 2021	Completed
Measurements at NIM	Jul - Aug 2018	May - Aug 2022	Completed
Re-Measurements at INRIM		Oct - Apr 2023	Completed
Re-Measurements at KRISS		Jun - Aug 2023	Completed
Measurements at MSL		Oct - Dec 2023	Completed
Re-Measurement at AIST		Jan - Jun 2024	Completed
Intermediate Measurements at PTB		Jun - Aug 2024	Completed
Measurements at NRC		Sep – Dec 2024	Completed
Final measurements at PTB	Sep - Oct 2018	Jan - Mar 2025	Completed
Pre-draft A report	Dec 2018	Jan 2026	Completed
Draft A completed	Apr 2019	Jun 2026	Completed
Final report completed	Oct 2019	14.07.2026	Completed

Timeline of the pilot study

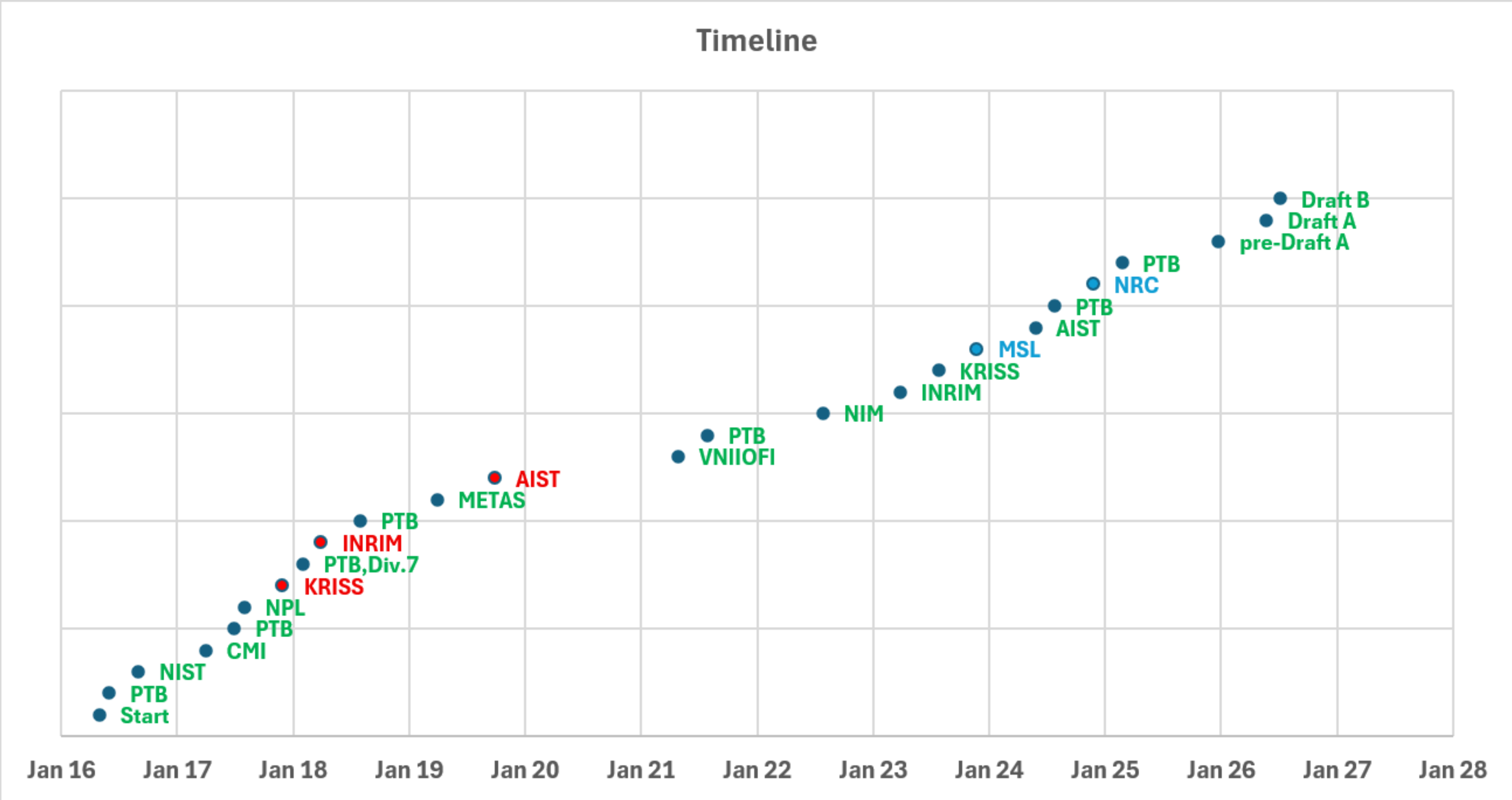

Figure 1: Timeline of the pilot study. Red: first measurements, removed; blue: joined later.

2. Results and Uncertainty budgets

In Table 3 and Table 4 the detection efficiencies (*DE*), the standard uncertainties (*u*(*DE*)) and the expanded uncertainties (*U*(*DE*)) for the detection efficiency of the detectors as reported by the participants based on their reports and uncertainty budgets are listed. The detailed measurement reports including uncertainty analysis submitted by the participants are given in the appendix.

Table 3: Detection efficiencies (DE), standard uncertainties (u(DE)) and expanded uncertainties (U(DE)) for the detection efficiency of detector SN 19743.

	DE	*u(DE)*	*U*(*DE*)	*DE*	*u*(*DE*)	*U*(*DE*)
	Absolute values			Normalized to 1		
PTB	0,544	0,004	0,009	1,003	0,008	0,016
NIST	0,558	0,003	0,005	1,030	0,005	0,009
CMI	0,581	0,012	0,024	1,073	0,022	0,044
NPL	0,521	0,003	0,005	0,961	0,005	0,009
PTB, Div. 7	0,538	0,003	0,005	0,992	0,005	0,010
METAS	0,462	0,035	0,069	0,852	0,064	0,127
NIM	0,501	0,002	0,003	0,924	0,003	0,006
INRIM	0,551	0,003	0,006	1,017	0,005	0,011
KRISS	0,598	0,012	0,024	1,103	0,022	0,044
MSL	0,533	0,019	0,038	0,983	0,035	0,070
AIST	0,580	0,004	0,008	1,069	0,008	0,015
NRC	0,538	0,011	0,022	0,993	0,020	0,041
Mean	**0,542**	**0,011**	**0,021**	1,000	**0,020**	**0,039**

Table 4: Detection efficiencies (*DE*), standard uncertainties (*u*(*DE*)) and expanded uncertainties (*U*(*DE*)) for the detection efficiency of detector SN 18752

	DE	*u(DE)*	*U*(*DE*)	*DE*	*u*(*DE*)	*U*(*DE*)
	Absolute values			Normalized to 1		
PTB	0,497	0,004	0,008	1,009	0,009	0,017
NIST	0,509	0,002	0,005	1,034	0,005	0,010
CMI	0,518	0,015	0,030	1,052	0,030	0,061
NPL	0,465	0,006	0,012	0,944	0,012	0,024
PTB, Div. 7	0,486	0,003	0,005	0,988	0,005	0,010
METAS	0,448	0,034	0,067	0,910	0,068	0,136
NIM	0,457	0,002	0,003	0,928	0,003	0,006
INRIM*	0,508	0,003	0,006	1,032	0,006	0,011
KRISS	0,548	0,009	0,018	1,113	0,018	0,037
MSL	0,505	0,037	0,074	1,026	0,075	0,150
AIST	0,465	0,003	0,007	0,944	0,007	0,013
NRC	0,503	0,010	0,020	1,021	0,020	0,041
Mean	**0,492**	**0,008**	**0,017**	1,000	**0,017**	**0,034**

The measured detection efficiencies for the two transfer detectors are shown in Figure 2 and Figure 4, normalized to the mean value in Figure 3 and Figure 5.

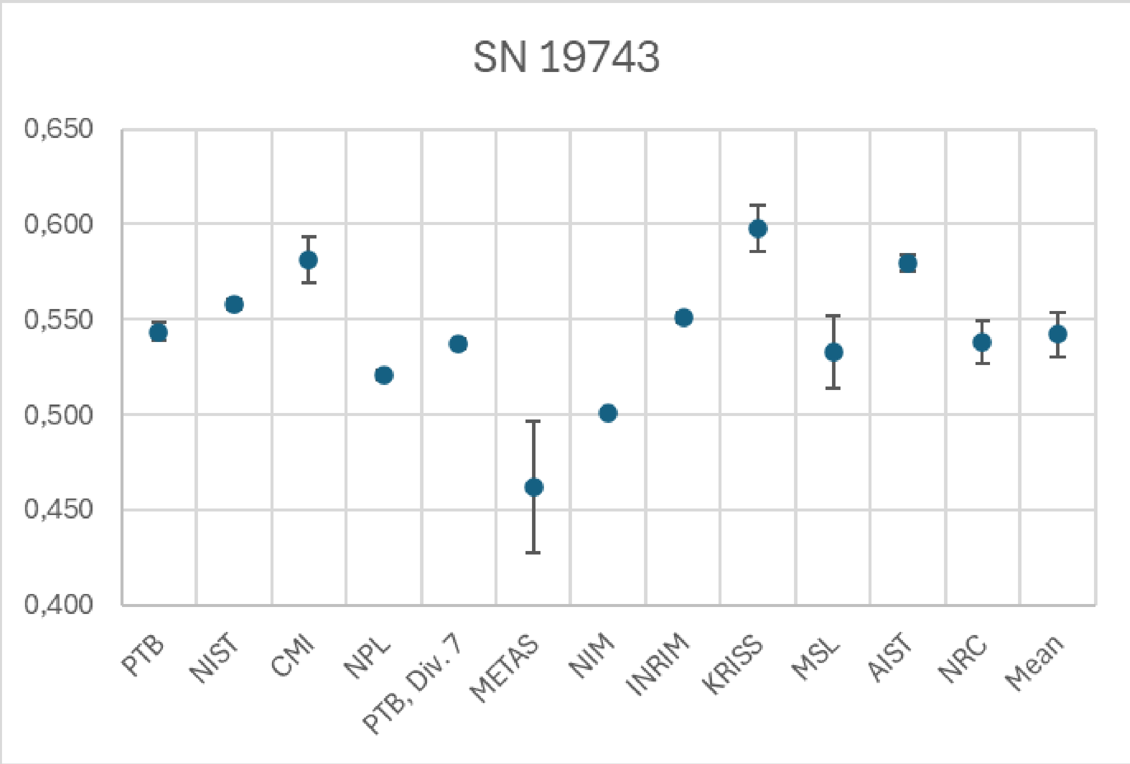

Figure 2: Detection efficiencies (*DE*) with standard uncertainties (*u*(*DE*)) and mean value for detector SN 19743.

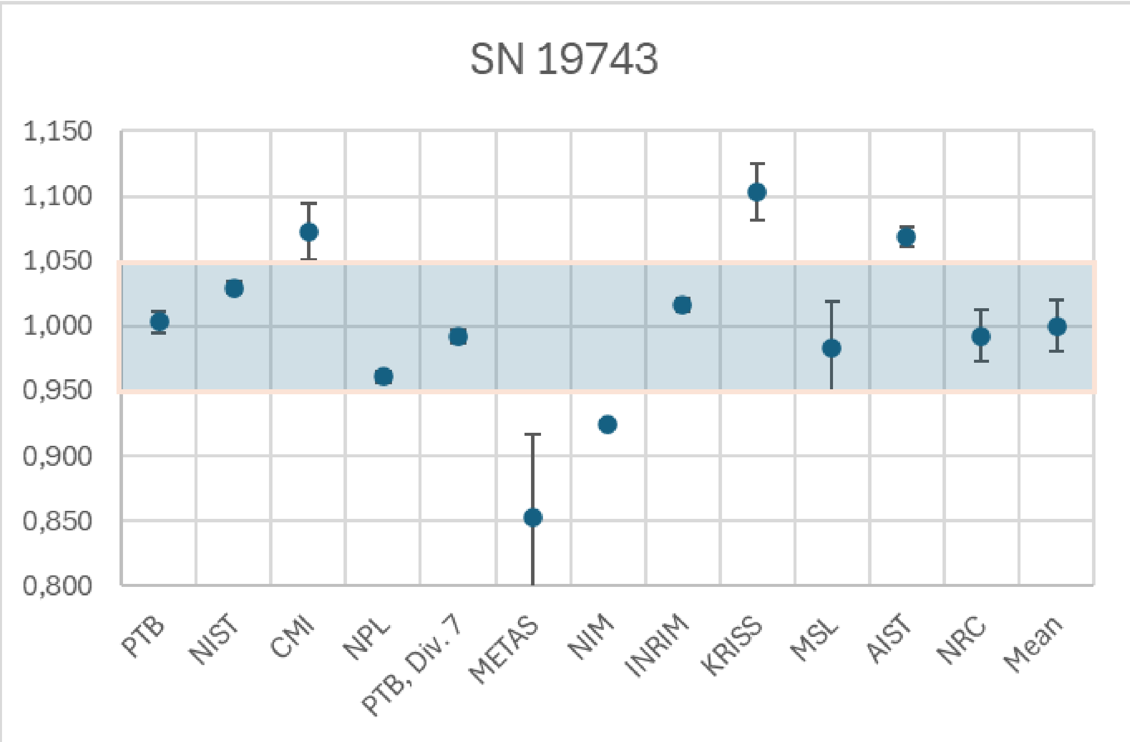

Figure 3: Detection efficiencies (*DE*) with standard uncertainties (*u*(*DE*)) and mean value for detector SN 19743, normalized to the mean value. The blue bar indicates ± 5 %.

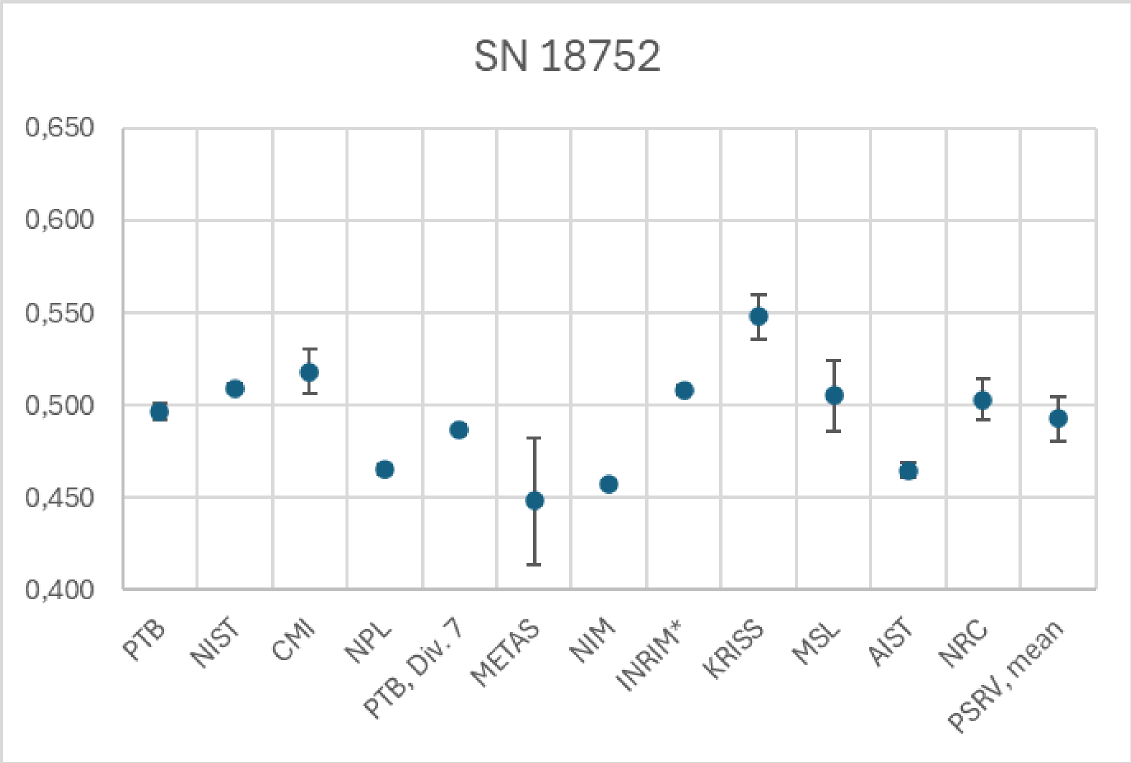

Figure 4: Detection efficiencies (*DE*) with standard uncertainties (*u*(*DE*)) and mean value for detector SN 18752.

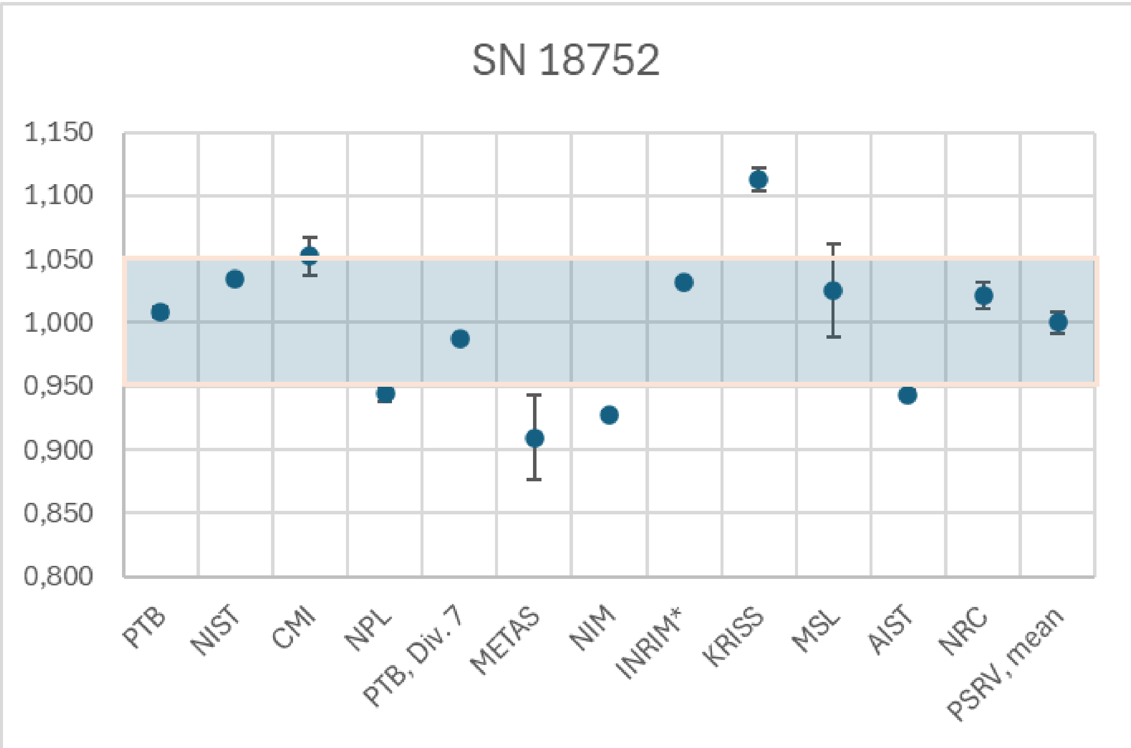

Figure 5: Detection efficiencies (*DE*) with standard uncertainties (*u*(*DE*)) and mean value for detector SN 18752, normalized to the mean value. The blue bar indicates ± 5 %.

3. Performance of the transfer detectors

Although not explicitly stated in the technical protocol, in this Pre-Draft-A report the performance of the transfer detectors is reported. The transfer detectors were measured at the pilot laboratory PTB in total 6 times, covering the years from 2016 to 2025.
The relative detection efficiencies for the two transfer detectors are shown in the following Table 5 and Figure 6 and Figure 7.

Table 5: Performance of the transfer detectors during the 6 measurements at the pilot laboratory PTB.

Year	SPAD 19743 η_0(1 phot./s)	SPAD 19743 $U(k=2)$	SPAD 19743 rel. $U(k=2)$	SPAD 18752 η_0(1 phot./s)	SPAD 18752 $U(k=2)$	SPAD 18752 rel. $U(k=2)$
2016	1,002	0,018	1,8%	1,010	0,019	1,9%
2017	1,002	0,014	1,4%	0,994	0,015	1,5%
2018	1,008	0,016	1,6%	1,002	0,019	1,9%
2021	0,978	0,016	1,6%	0,984	0,014	1,4%
2024	1,000	0,018	1,8%	1,014	0,018	1,8%
2025	1,010	0,016	1,6%	0,996	0,017	1,7%

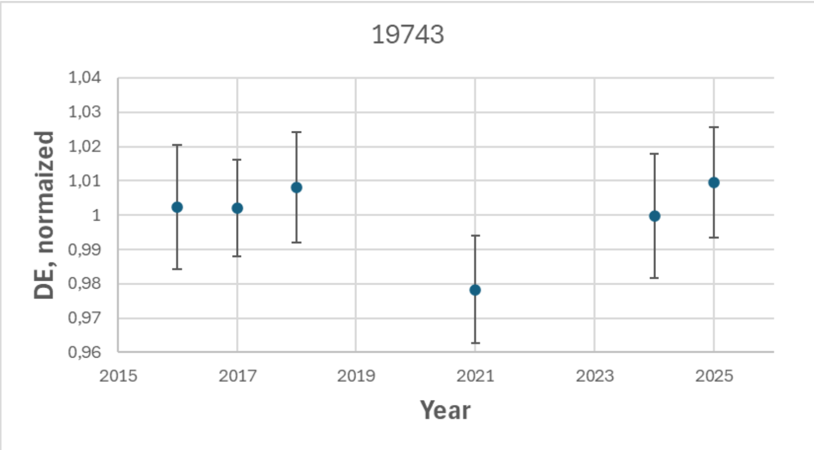

Figure 6: Performance of the SPAD 19743 transfer detectors during the 6 measurements at the pilot laboratory PTB.

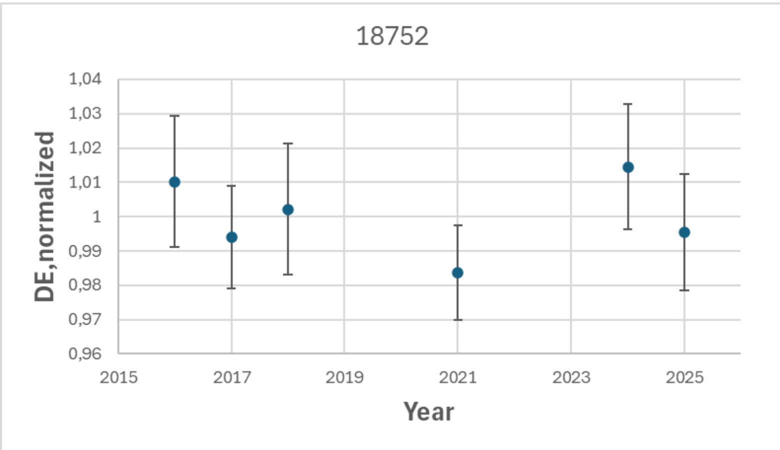

Figure 7: Performance of the SPAD 19743 transfer detectors during the 6 measurements at the pilot laboratory PTB.

In conclusion, the detectors exhibited a very constant detection efficiency within the whole period of the pilot study, which took 9 years in total. The changes in the DE observed at PTB are within the uncertainty of the measurement, with the one exception for the measurement in 2021. Still, all measurements are consistent, so it is concluded that the pilot study is not affected by detector instability or aging.

4. Homogeneity of the transfer detectors

In the following Figure 8 and Figure 9, the homogeneity of the detectors are shown. In Table 6 and Table 7, the results are summarized.

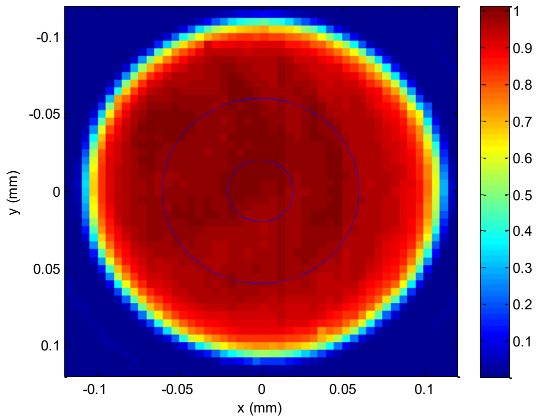

Figure 8: Homogeneity of SPAD 19743

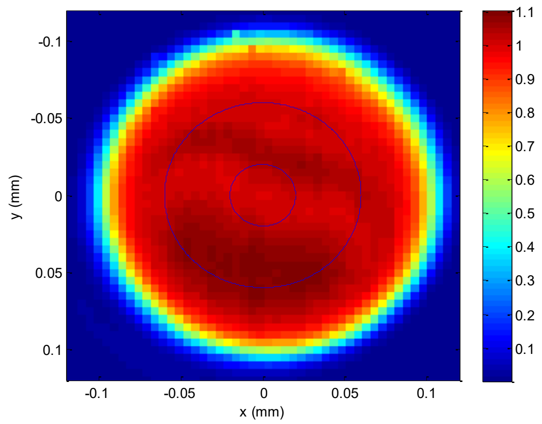

Figure 9: Homogeneity of SPAD 18752

Table 6: Homogeneity of SPAD 19743

Circle	**Mean value**	**Std. dev. (rel.)**
1 (ϕ = 40 μm)	0.9931	1.28 %
2 (ϕ=120 μm)	0.9889	1.23 %

Table 7: Homogeneity of SPAD 18752

Circle	**Mean value**	**Std. dev. (rel.)**
1 (ϕ = 40 μm)	1.0169	1.35 %
2 (ϕ=120 μm)	1.0381	2.83%

Therefore, it can be concluded that the inhomogeneity of the detectors may have a significant influence on the results and uncertainties.

5. Detailed analysis of the comparison

The pilot comparison provides a useful snapshot of the measurement capability of the participating laboratories for the detection efficiency of Si-SPAD single-photon detectors at 850 nm in free-space beam geometry. The two transfer detectors, SN 19743 and SN 18752, show broadly comparable behavior across the participant results, indicating that the observed differences are not dominated by one anomalous detector alone.

For detector SN 19743, the reported detection efficiencies range from 0.462 to 0.598, with a participant mean of approximately 0.542. The normalized results therefore span roughly 0.85 to 1.10 relative to the mean. For detector SN 18752, the reported detection efficiencies range from

0.448 to 0.548, with a participant mean of approximately 0.492. The normalized results span roughly 0.91 to 1.11. The relative dispersion of the laboratory results is approximately 6.8 % for SN 19743 and 5.9 % for SN 18752.

The comparison therefore reveals significant interlaboratory differences. In several cases, the deviations from the mean are larger than the reported standard uncertainties. This indicates that the uncertainty budgets reported by some participants may not fully account for all relevant systematic contributions. Possible contributors include beam alignment on the active detector area, beam diameter and spatial averaging, detector inhomogeneity, photon-flux determination, background subtraction, count-rate linearity, dead-time correction, afterpulsing correction, and differences in the practical realization of the free-space geometry.

The consistency of the relative ranking of several laboratories for the two detectors suggests that laboratory-specific measurement methods or uncertainty evaluations may contribute significantly to the observed spread. Some laboratories report results consistently above the mean, while others report results consistently below the mean. This behavior should be examined in relation to the individual measurement reports and uncertainty budgets.

The long-term measurements at the pilot laboratory show that both transfer detectors were sufficiently stable over the duration of the pilot study. PTB measurements performed between 2016 and 2025 indicate relative changes of about 3 % over the full period, with most results compatible within the expanded uncertainties. The 2021 measurements show a lower value for both detectors and should be discussed, but overall stability remains adequate for the purpose of the comparison.

The homogeneity measurements show that spatial non-uniformity of the detector response is a relevant influence quantity. For SN 19743, the relative standard deviation is about 1.2 % to 1.3 % for the investigated scan regions. For SN 18752, the larger scan region shows a relative standard deviation of 2.83 %, indicating more pronounced spatial dependence. This supports the conclusion that detector inhomogeneity, together with differences in beam size and beam positioning, may have contributed significantly to the spread of participant results.

6. Summary

The pilot study successfully collected detection-efficiency results for two Si-SPAD transfer detectors from a broad group of national metrology institutes. The measurements demonstrate that participating laboratories can realize and report detection-efficiency measurements at 850 nm, but the comparison also shows significant interlaboratory differences.

The mean detection efficiencies are approximately 0.542 for SN 19743 and 0.492 for SN 18752. The relative spread of the laboratory results is about 6 % to 7 %, which is larger than many of the individual reported uncertainties. This indicates that further harmonization of measurement procedures and uncertainty evaluation is needed.

The transfer detectors were sufficiently stable during the comparison period. PTB repeat measurements over approximately nine years show no evidence of large long-term degradation. However, detector homogeneity is a significant factor, particularly for SN 18752, and should be considered carefully when interpreting the comparison results.

Overall, the comparison provides valuable evidence of current measurement capabilities and identifies the main technical issues that should be addressed in future comparisons or key comparison planning.

7. Outlook

Future work should focus on improving the comparability of free-space Si-SPAD detection-efficiency measurements. In particular, future protocols should specify the beam diameter, alignment procedure, detector positioning method, count-rate range, background correction, dead-time correction, and treatment of spatial non-uniformity more explicitly.

A more detailed analysis of the individual uncertainty budgets is recommended to identify which uncertainty components were treated differently by the participants. Special attention should be given to photon-flux calibration, spatial alignment, detector homogeneity, and corrections related to detector counting behavior.

For a possible follow-up pilot comparison, it would be beneficial to include a defined detector mapping procedure before or after the comparison, so that laboratories can relate their beam position and beam size to the spatial response of the detector. Additional repeat measurements at the pilot laboratory before, during, and after circulation would also strengthen the evaluation of transfer-detector stability.

The results of this pilot study can therefore serve as a basis for refining the technical protocol, improving uncertainty models, and preparing a more robust international comparison of single-photon detector detection efficiency.

8. Appendix

8.1. Summary of the calibration procedures

8.1.1. PTB, Division 4 (Pilot Laboratory)

Calibration procedure: PTB employed the double attenuator technique, where two calibrated attenuators were sequentially characterized using a calibrated Si photodiode. The optical power incident on the SPAD was derived from the measured laser power and total attenuation. A third variable attenuator enabled measurements at different photon flux levels. Detection efficiency was measured as a function of count rate and extrapolated to 1 photon/s using an exponential fit.

Traceability route: Cryogenic Radiometer → Si trap detector → Calibrated Si photodiode → Double attenuator calibration → SPAD efficiency. The Si photodiode responsivity at 850 nm was determined via direct comparison with a Si trap detector traceable to PTB's cryogenic radiometer.

Dominant uncertainty contributions: The uncertainty budget showed that the largest contributions originated from: Stray light correction (~ 43 %), Si photodiode nonlinearity (~ 24 %), Filter transmission calibration (~ 14%), Reference photodiode responsivity (~ 11%), Monitor ratio measurements (~ 6%). The dominant systematic effects were therefore associated with attenuation characterization and correction factors rather than counting statistics.

8.1.2. NIST (USA)

Calibration procedure: NIST used an unbalanced beam splitter method with attenuation transfer from conventional optical power measurements into the single-photon regime. A Si-trap detector measured the low-power arm, while monitor detectors tracked source stability. Measurements were performed at multiple count rates between ~ 10^3 and ~ 10^6 counts/s. Afterpulsing and dark counts were corrected, followed by extrapolation to 1 cps using linear regression. A short-coherence-length Ti-Sapphire laser was employed to suppress interference effects caused by the detector windows.

Traceability route: Electrical standards → Laser Optimized Cryogenic Radiometer (LOCR) → Pyroelectric transfer standard → Fiber-coupled Si trap detector calibration → Monitor power meter nonlinearity calibration → SPAD. The Si-trap detector was independently calibrated at both NIST Boulder and NIST Gaithersburg.

Dominant uncertainty contributions: Main contributors were Extrapolation to 1 cps, splitting ratio determination, optical power meter calibration, wavelength correction to exactly 850 nm, afterpulsing corrections. The final expanded uncertainty was among the lowest of the comparison (0.93%).

8.1.3. CMI (Czech Republic)

Calibration procedure: CMI used a substitution method. A calibrated low optical flux detector (LOFD) and the SPAD were sequentially illuminated using an underfilled beam. Additional attenuation was achieved using a 10-element Si tunnel trap detector, which simultaneously acted as monitor detector. Detector alignment was optimized through X-Y scans and focal plane determination.

Traceability route: Cryogenic radiometer → LOFD reference detector → Calibrated switched integrator amplifier → SPAD. The LOFD responsivity provided photon flux determination.

Dominant uncertainty contributions: The dominant source was detector spatial non-uniformity (3.2 % for SPAD 19743, 2.1 % for SPAD 18752. Other contributions included LOFD nonlinearity, LOFD responsivity calibration, Laser stability, Spectral mismatch correction. Detector non-uniformity clearly dominated the uncertainty budget.

8.1.4. NPL (United Kingdom)

Calibration procedure: NPL employed a 10-element transmittance trap detector (10ET) to provide fixed attenuation and monitor optical power. A calibrated 3-element trap detector (3ET) measured the attenuated beam, while the SPAD measured photon counts. The method relied on determining the attenuation factor provided by the 10ET and sequential substitution between the reference detector and DUT.

Traceability route: NPL primary cryogenic radiometer → Working standard 3-element trap detectors → Laboratory transfer standard (3ET) → SPAD. The transfer standard responsivity was interpolated spectrally using calibrated responsivity models.

Dominant uncertainty contributions: Principal contributions arose from high detector spatial non-uniformity, scattered light corrections, reference detector responsivity, wavelength correction, determination of beam overlap. NPL identified pronounced spatial response anomalies in detector 18752.

8.1.5. PTB, Division 7

Calibration procedure: PTB Division 7 employed an independent realization of SPAD efficiency calibration, using free-space substitution radiometry techniques distinct from the pilot laboratory setup.

Traceability route: PTB radiometric primary standards → Calibrated trap detectors → Reference detectors → SPAD.

Dominant uncertainty contributions: Major contributors included: reference detector calibration, beam positioning uncertainty, spatial detector inhomogeneity, count-rate extrapolation. The reported uncertainties were among the smallest of the comparison.

8.1.6. METAS (Switzerland)

Calibration procedure: METAS used a Ti-Sapphire laser system operating between 750–900 nm. Measurements extended beyond the comparison wavelength to characterize spectral dependence. Free-space substitution between SPADs and reference detectors was performed.

Traceability route: METAS radiometric standards → Calibrated Si reference detectors → SPAD.

Dominant uncertainty contributions: The uncertainty budget was dominated by inhomogeneity of illumination across SPAD surface (incl. window) (~ 7 %), attenuation factor of filter combination (~ 2 %), stray light differences (~ 1 %)reflections between attenuation filters (~ 0.5 %), reflections between detector and microscope objective (~ 0.5 %), laser stability (~ 0.5 %), dead-time corrections (~ 1 %). The uncertainty originating from the inhomogeneity of illumination across SPAD surface (incl. window) dominated, leading to the largest uncertainties among participants.

8.1.7. NIM (China)

Calibration procedure: NIM measured SPAD efficiency using calibrated transfer photodetectors and corrections for detector dead time and afterpulsing. Measurements were performed near 844.5 nm and corrected to 850 nm. Spatial scans identified suitable detector alignment positions.

Traceability route: NIM radiometric standards → Transfer photodetector calibration → SPAD.

Dominant uncertainty contributions: Reference photodetector responsivity (0.21 %), wavelength correction (0.24 %), repeatability (~ 0.08 %), detector non-uniformity (~ 0.08 %), afterpulsing correction (~ 0.03 %). The wavelength correction became the largest individual contribution.

8.1.8. INRIM (Italy)

Calibration procedure: INRIM used an attenuation-based method involving characterization of transmission factors and continuous monitoring of source stability. Detection efficiency was extrapolated to low count rates.

Traceability route: INRIM primary radiometric standards → Calibrated reference detectors → Attenuation characterization → SPAD.

Dominant uncertainty contributions: Main uncertainty sources included transmission characterization, trap detector responsivity, source stability, monitor detector nonlinearity, spatial response effects. The uncertainty budget was strongly influenced by attenuation characterization.

8.1.9. KRISS (Korea)

Calibration procedure: KRISS determined efficiency through direct comparison of SPAD counts with a calibrated reference detector. Spatial scans were used to identify the center of the detector plateau region. Dead-time corrections were applied.

Traceability route: Cryogenic radiometer → Reference detector responsivity scale realization → Switched integrating amplifier calibration → SPAD.

Dominant uncertainty contributions: Largest contributors reference detector calibration (1.3 %), repeatability of DUT/reference ratio (0.96 % - 1.45 %), wavelength dependence (0.2 % - 0.35%). Reference detector calibration dominated.

8.1.10. MSL (New Zealand)

Calibration procedure: MSL joined the comparison later and used substitution radiometry with trap detectors similar to NPL methodologies. Sequential measurements of reference detector and SPAD were performed under controlled beam conditions.

Traceability route: PTB spectral responsivity scale → MSL reference detector / transfer standard → SPAD calibration system → DUT SPAD.

Dominant uncertainty contributions: Main contributors were reference detector calibration, amplifier calibration, spatial alignment, repeatability. The relatively large uncertainties suggest detector alignment and transfer standard uncertainties dominated.

8.1.11. AIST (Japan)

Calibration procedure: AIST employed attenuation transfer techniques involving monitor detectors and trap detectors. Measurements were performed over many count-rate points and extrapolated to 1 cps.

Traceability route: AIST primary radiometric standards → Trap detector calibration → Monitor detector calibration → SPAD.

Dominant uncertainty contributions: The dominant uncertainty factor is the spatial uniformity of the DUT. Additional contributors: trap detector responsivity (~ 0.15 %), monitor detector linearity, trap detector amplifier calibration. Spatial non-uniformity clearly dominated the budget.

8.1.12. NRC (Canada)

Calibration procedure: NRC used attenuation-based free-space substitution radiometry with measurements extrapolated to low count rates. The methodology followed established radiometric transfer procedures for photon-counting detectors.

Traceability route: Canadian primary radiometric standards → Calibrated transfer detectors → SPAD.

Dominant uncertainty contributions: The main contributors were reference detector calibration, beam alignment uncertainty, count-rate extrapolation, source stability. The final uncertainties

(~ 2%) indicate a balanced uncertainty budget without a single overwhelmingly dominant component.

8.1.13. General observations

Three dominant themes emerged across participants:

- Detector spatial non-uniformity was identified by CMI, NPL, METAS, AIST, PTB, MSL, and KRISS as a major limitation.
- Reference detector calibration remained one of the largest contributors for laboratories relying on trap detector substitution.
- Attenuation characterization and beam transfer methods introduced significant systematic uncertainties for laboratories using attenuation chains.

These findings strongly support the conclusion that beam positioning, detector homogeneity, and harmonization of calibration protocols are critical for future key comparisons of SPAD detection efficiency.

8.2. Detailed measurement reports and uncertainty tables of the participants.

In the second part of the Appendix, you will find the details reports of all participants:

1. PTB
2. NIST
3. CMI
4. NPL
5. PTB, Div. 7
6. METAS
7. NIM
8. INRIM
9. KRISS
10. MSL
11. AIST
12. NRC

CCPR WG-SP TG 11

Pilot study on the detection efficiency of single-photon detectors – Si-SPAD

Report

Physikalisch-Technische Bundesanstalt

Marco López, Helmuth Hofer, Stefan Kück

Content

1 Introduction 2

2 Setup and measurement procedure 2

3 Transfer standard and measurement conditions 3

4 Traceability chain 4

5 SPAD detector alignment and homogeneity 4

6 Measurement results 6

7 Uncertainty 12

8 References 13

1 Introduction

This document presents the calibration results of the detection efficiency of two Si-SPAD detectors (PerkinElmer, Model: SPCM-AQRH-16, S/N: 19743 and S/N: 18752) determined by the Physikalisch-Technische Bundesanstalt (PTB) during the years 2016-2025. The latter following the technical measurement protocol: CCPR WG-SP TG 11 “Pilot study on the detection efficiency of single-photon detectors – Si-SPAD”.

2 Setup and measurement procedure

The setup and a photograph of the measurement facility used at PTB for the calibration of the detection efficiency of the Si-SPADs are shown in Figure 1. The calibration is performed using the double attenuator technique described in [1, 2]. This technique consists in subsequently calibrating two attenuators using a reference detector. Then, the total attenuation is calculated by multiplying the two attenuations values. From this value and the total photon flux originating from the laser, the photon flux impinging on the Si-SPAD detector under calibration is calculated when both attenuators are moved into the laser beam. Moreover, in order to determine the detection efficiency at different optical fluxes, a third variable attenuator is additionally used in the setup (see Figure 1). That is,

$$\left.\begin{aligned} I_1 &= s_{\mathrm{Si},1} \cdot \Phi_1 \\ I_2 &= s_{\mathrm{Si},2} \cdot \Phi_2 = s_{\mathrm{Si},2} \cdot T_{\mathrm{F2}} \cdot \Phi_1 \\ I_3 &= s_{\mathrm{Si},3} \cdot \Phi_3 = s_{\mathrm{Si},3} \cdot T_{\mathrm{F3}} \cdot \Phi_1 \\ I_4 &= s_{\mathrm{Si},3} \cdot \Phi_4 = s_{\mathrm{Si},4} \cdot T_{\mathrm{F4}} \cdot \Phi_1 \\ CR &= \eta \cdot \frac{\Phi_5}{hc/\lambda} = \eta \cdot \frac{T_{\mathrm{F2}} \cdot T_{\mathrm{F3}} \cdot T_{\mathrm{F4}} \cdot \Phi_1}{hc/\lambda} \end{aligned}\right\}$$

$$\Rightarrow \eta = {hc}/{\lambda} \cdot \frac{CR \cdot I_1^2}{I_2 \cdot I_3 \cdot I_4} \cdot \frac{s_{\mathrm{Si},2} \cdot s_{\mathrm{Si},3} \cdot s_{\mathrm{Si},4}}{s_{\mathrm{Si},1}^2} \tag{2}$$

With: η: detection efficiency, h: Planck constant, c: speed of light and λ: wavelength I_i: photocurrent signals (I_1: signal for the measurement of the laser power, I_2: signal for the measurement of filter 2, I_3: signal for the measurement of filter 3, I_4: signal for the measurement of filter 4 (variable filter), *CR*: count rate of the Si-SPAD, $s_{\mathrm{Si,i}}$: spectral responsivity of the Si photodiode for the different irradiation levels, T_{Fi}: transmissions of the filters used in the measurements 2 – 4, $\Phi_1 - \Phi_5$: optical radiant fluxes in the measurements 1 – 5.

Since the spectral responsivity of the Si-photodiode is practically linear for the applied optical flux levels between approx. 1 nW and 10 µW, its responsivity is considered constant for all measured photocurrent signals I_i. This was proven by measuring the nonlinearity of the Si-diode with the PTB´s in-house facility for the calibration of the nonlinearity. Furthermore, in order to minimize any fluctuation of the laser power, a monitor technique is applied during the measurement. Thus, the Si-SPAD detection efficiency is obtained as:

$$\eta = \frac{hc}{\lambda} \frac{{I_1^2}/{V_{\mathrm{Mon1}}} \; {CR}/{V_{\mathrm{Mon5}}}}{{I_2}/{V_{\mathrm{Mon2}}} \; {I_3}/{V_{\mathrm{Mon3}}} \; {I_4}/{V_{\mathrm{Mon4}}}} s_{Si} F_{\mathrm{filt}} F_{\mathrm{stray}} F_{Si\_\mathrm{NL}} = \frac{hc}{\lambda} \frac{Q_1^2 Q_5}{Q_2 Q_3 Q_4} s_{Si} F_{\mathrm{filt}} F_{\mathrm{stray}} F_{Si\_\mathrm{NL}} \tag{3}$$

With $V_{\mathrm{mon,i}}$: signals from the monitor detector for the measurements 1 – 5, F_{filt} = 0.9998 ± 0.0023, uncertainty component taking into account the uncertainty in the filter transmission measurement, F_{stray} = 1.004 ± 0.004, uncertainty component taking into account the effect of stray light and F_{Si_NL}= 1.00 ± 0.003, uncertainty related to the non-linearity of the reference Si-phododiode.

The detection efficiency η_0 for 1 photon/s is obtained by fitting a model: $\eta = a \cdot e^{-b \cdot P_f}$ to the detection efficiencies values determined with equation 3 for different photon fluxes, where P_f is the photon flux, and a and b are the fitting coefficients.

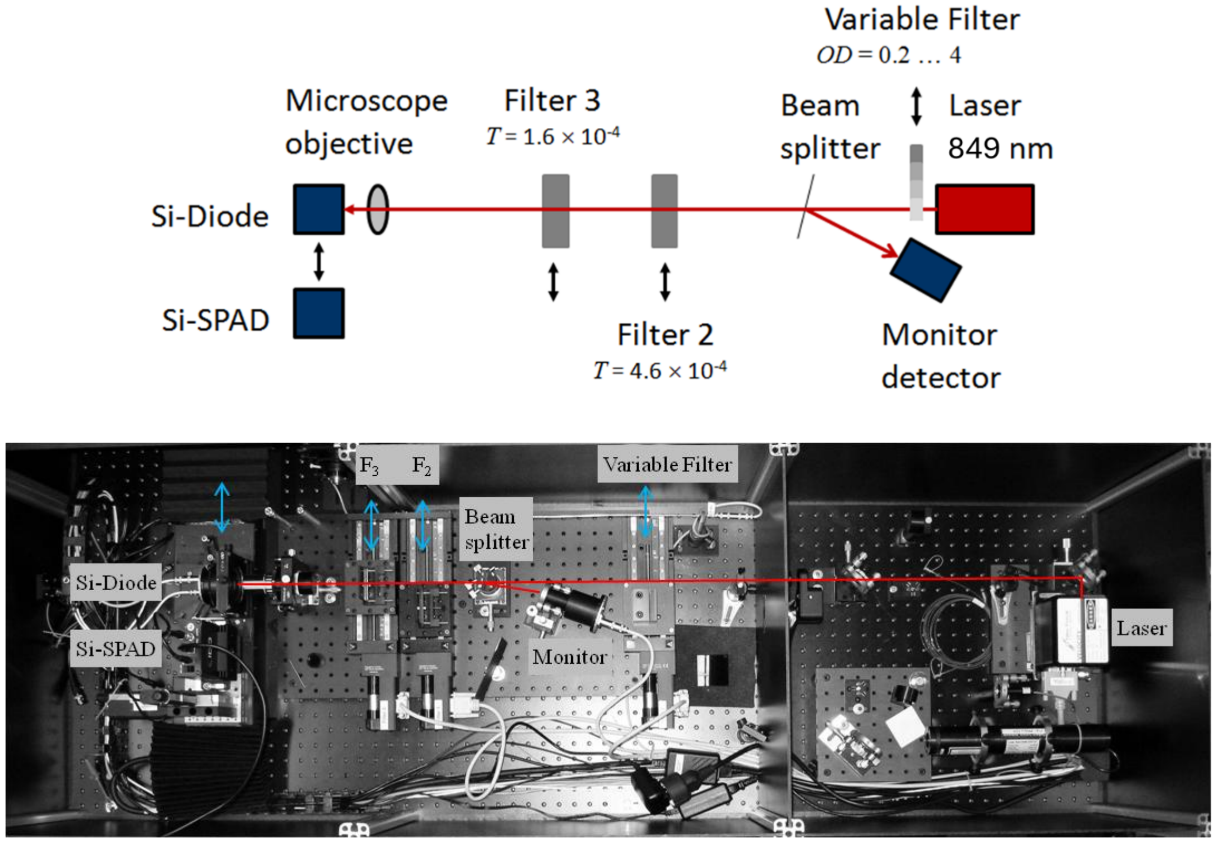

Figure 1: Schematic and photograph of the setup used for the calibration of the Si-SPAD detectors.

3 Transfer standard and measurement conditions

The transfer standard used is a windowless Si photodiode with a photosensitive area of 2.4 mm x 2.4 mm (Hamamatsu, Model: S1227-33). The photocurrent generated by the detector was measured with a Femto/pico amperemeter (Keysight B2981A). Its spectral responsivity was determined by direct comparison with a thermopile whose traceability to the cryogenic radiometer is realized via a Si trap detector (see Figure 2). The spectral responsivity of the Si photodiode at the wavelength of 849 nm is thus obtained:

s_{Si}=0.2937 A/W ± 0.00059 A/W

Measurement conditions:

- Laser peak wavelength: 849 nm ±0.5 nm (Bandwidth, FWHM: 1.23 nm)
- Laser beam diameter: 50 µm ± 5 µm.
- Laboratory temperature: 23.0 °C ± 0.5°C

- Laboratory humidity: 49.0 % ± 0.5 %

4 Traceability chain

The traceability chain for the spectral responsivity s_{Si} of the Si-photodiode used as reference detector is shown in Figure 2, where λ_{i} is the wavelength, Φ is the optical power and u is the standard measurement uncertainty.

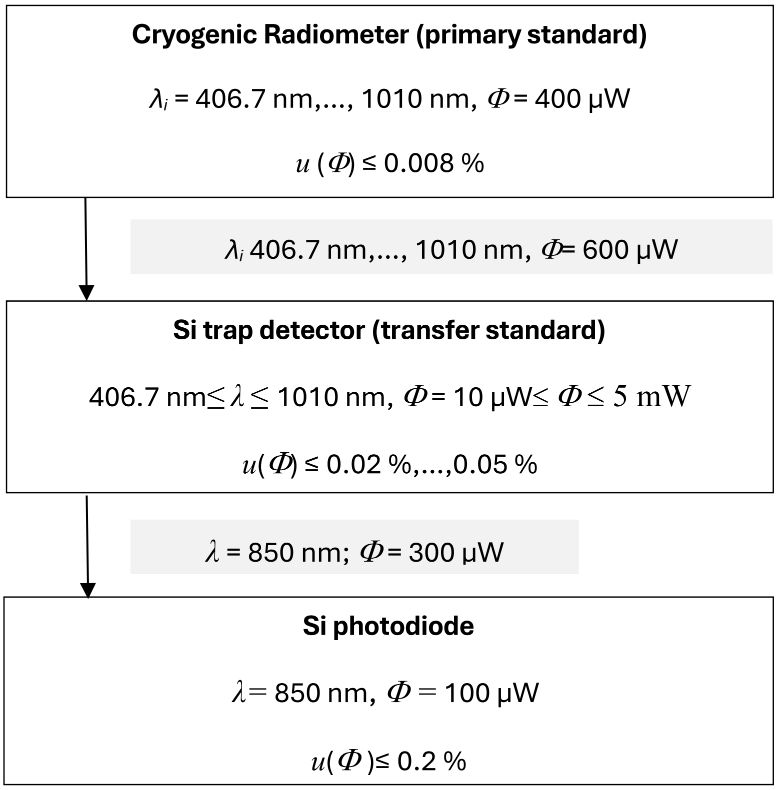

Figure 2. Traceability chain of the Si-Photodiode used as reference detector for the calibration of the detection efficiency of the SPAD detectors under test.

5 SPAD detector alignment and homogeneity

Each SPAD detector is aligned with respect to the laser beam using 3 motorized translation stages in the x, y and z axes. As an example, a scan in the y-axis of the active area of the SPAD detectors under test is shown in Figure 3. From the x and y scans the center position of the active area is determined. By adjusting the z-axis, the diameter of the laser beam irradiating on the detector is defined. The beam diameter can be determined by measuring the distance of the left and right projection slopes of the scan.

The homogeneity of the SPAD detector response is determined by scanning the entire active area with an approx. 10 µm laser beam diameter, as described in [3, 4]. During the scan, a monitor detector is used to correct for possible fluctuation of the laser optical power which may occur during the measurement. The scanning is performed with a step resolution of approx. 5 µm over the complete active area of the sensor. Each signal obtained from the Si-SPAD for each (x, y) scanning position is normalized to the one obtained when the laser beam is impinging at the center of the sensor active area. Changes in detector response as a function of beam position can be clearly seen in Figure 3. The normalized mapping of the detector response for all of its active zones is shown in Figure 4. The homogeneity can be determined as the standard deviation of the relative detection efficiency for a defined region. As an example of the homogeneity analysis, the scanning active areas were divided into two regions (1, 2), each with different diameters (ϕ_1 = 40 µm and ϕ_2 = 120 µm). The results (mean and rel. standard deviation) are shown in Table 1.

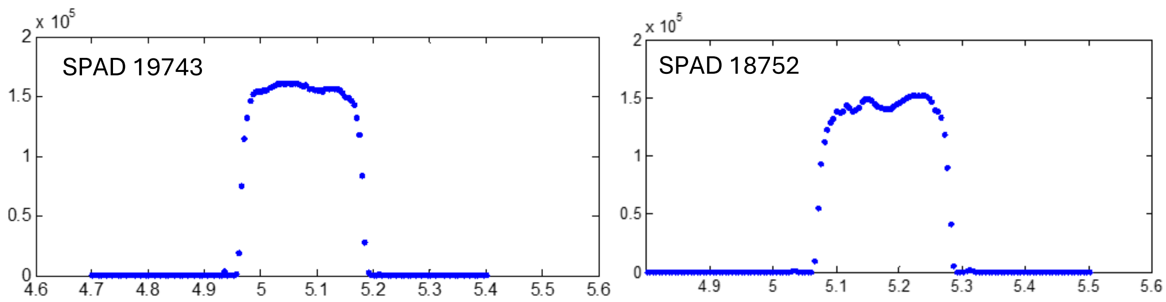

Figure 3. Scanning in the y-axis of the active area of the SPAD detectors under test. The scans were performed with a beam diameter of approximately 10 µm.

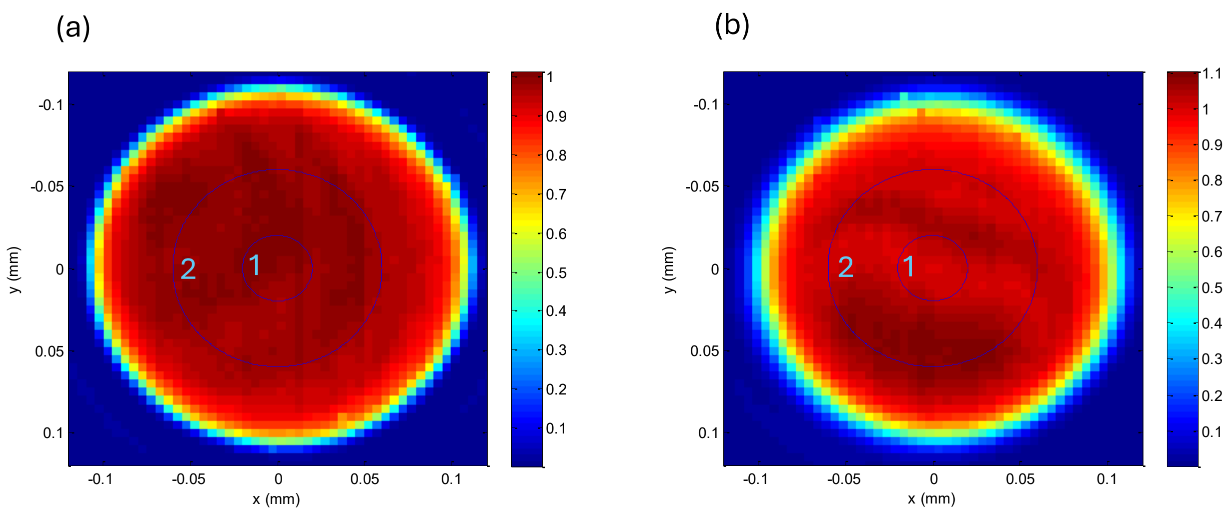

Figure 4. Relative spatial detection efficiency of the Si-SPADs. (a) SPAD 19743 and (b) SPAD 18752. Two regions (1 and 2) were selected to evaluate the homogeneity of the detector response. The regions 1 and 2 are shown with blue circles and have a diameter of 40 µm and 120 µm, respectively. The scans were performed with a beam diameter of approximately 10 µm.

Table 1. Mean value and standard deviation of the relative detection efficiency for the SAPD 19743 and the SPAD 18752.

SAPD 19743:

Circle	Mean value	Std. dev. (rel.)
1 (ϕ = 40 µm)	0.9931	1.28 %
2 (ϕ=120 µm)	0.9889	1.23 %

SAPD 18752:

Circle	Mean value	Std. dev. (rel.)
1 (ϕ = 40 µm)	1.0169	1.35 %
2 (ϕ=120 µm)	1.0381	2.83%

6 Measurement results

The SPAD detection efficiency η_0 for 1 photon/s as well as its associated expanded uncertainty is shown in Table 2. The detection efficiency η for different photon fluxes (and corresponding optical power and count rates) is shown in Table 3.

The measurement uncertainty is estimated by following the guidelines given in the "*Guide to the expression of uncertainty in measurement (GUM)*". As an example, an uncertainty budget for η is shown in table 4 (section 7), where the evaluation model used is the equation (3).

The uncertainty of the detection efficiency η_0 is calculated as

$$U(\eta_0) = 2 \cdot \sqrt{u_m(\eta)^2 + \left(\frac{r_{fit,max} - r_{fit,min}}{2 \cdot \sqrt{3}}\right)^2}$$

where $u_m(\eta)$ is the mean of the standard uncertainties determined for η at different photon fluxes, and $r_{fit,max}$ and $r_{fit,min}$ are the maximum and minimum values of the fitting curve residuals, respectively.

Table 2. Detection efficiency η_0 extrapolated to 1 photon/s using a detection efficiency fitting model for different photon fluxes as shown in Figure 5.

Year	SPAD 19743 η_0(1 phot./s)	SPAD 19743 $U(k=2)$	SPAD 19743 rel. $U(k=2)$	SPAD 18752 η_0(1 phot./s)	SPAD 18752 $U(k=2)$	SPAD 18752 rel. $U(k=2)$
2016	0.5450	0.0098	1.8 %	0.5017	0.0095	1.9 %
2017	0.5449	0.0076	1.4 %	0.4936	0.0075	1.5 %
2018	0.5481	0.0088	1.6 %	0.4977	0.0093	1.9 %
2021	0.5319	0.0084	1.6 %	0.4885	0.0070	1.4 %
2024	0.5436	0.0096	1.8 %	0.5038	0.0092	1.8 %
2025	0.5489	0.0090	1.6 %	0.4944	0.0084	1.7 %

Table 3. Optical power (W), Photon flux (photon/s), count rate (count/s) and detection efficiency η and its uncertainty determined for both SPAD detectors in the years from 2017 to 2025.

Year: 2017

Φ (W)	Photon flux (Photon/s)	Counts SPAD19743	Counts SPAD18752	η_SPAD 19743	$U(k=2)$_SPAD 19743	η_SPAD 18752	$U(k=2)$_SPAD 18752
9.87E-15	42153	22640	20476	0.5394	0.006	0.4881	0.006
2.48E-14	105910	57571	52059	0.5457	0.007	0.4937	0.006
5.79E-14	247608	134187	121641	0.5435	0.006	0.4922	0.006
2.17E-13	927263	496906	452622	0.5384	0.006	0.4900	0.006
5.22E-13	2231022	1162421	1061034	0.5232	0.006	0.4779	0.006
8.14E-13	3478487	1773017	1626246	0.5104	0.006	0.4678	0.006
1.02E-12	4359669	2176307	1990815	0.5027	0.006	0.4606	0.005
1.36E-12	5828714	2841979	2609954	0.4899	0.006	0.4509	0.005
1.69E-12	7215684	3429949	3168807	0.4763	0.006	0.4400	0.005

Year: 2018

Φ (W)	Photon flux (Photon/s)	Counts SPAD19743	Counts SPAD18752	η_SPAD 19743	$U(k=2)$_SPAD 19743	η_SPAD 18752	$U(k=2)$_SPAD 18752
9.87E-15	42153	22640	20476	0.5394	0.006	0.4881	0.006
2.48E-14	105910	57571	52059	0.5457	0.007	0.4937	0.006
5.79E-14	247608	134187	121641	0.5435	0.006	0.4922	0.006
2.17E-13	927263	496906	452622	0.5384	0.006	0.4900	0.006
5.22E-13	2231022	1162421	1061034	0.5232	0.006	0.4779	0.006
8.14E-13	3478487	1773017	1626246	0.5104	0.006	0.4678	0.006
1.02E-12	4359669	2176307	1990815	0.5027	0.006	0.4606	0.005
1.36E-12	5828714	2841979	2609954	0.4899	0.006	0.4509	0.005
1.69E-12	7215684	3429949	3168807	0.4763	0.006	0.4400	0.005

Year: 2021

Φ (W)	Photon flux (Photon/s)	Counts SPAD19743	Counts SPAD18752	η_SPAD 19743	$U(k=2)$_SPAD 19743	η_SPAD 18752	$U(k=2)$_SPAD 18752
5.74E-15	24537	13098	12119	0.5327	0.007	0.4906	0.007
1.09E-14	46434	24885	22801	0.5340	0.007	0.4888	0.007
2.09E-14	89251	47150	43410	0.5286	0.007	0.4855	0.007
3.28E-14	140098	73391	67375	0.5274	0.007	0.4871	0.007
5.34E-14	228225	120783	110285	0.5295	0.007	0.4860	0.006
1.31E-13	559718	291721	270007	0.5221	0.007	0.4825	0.006
2.08E-13	889825	466130	426684	0.5255	0.007	0.4814	0.006
3.37E-13	1439513	747978	687224	0.5217	0.007	0.4800	0.006
7.09E-13	3030812	1515609	1397205	0.5039	0.007	0.4665	0.006
1.16E-12	4976417	2381726	2222924	0.4820	0.006	0.4502	0.006

Year: 2024

Φ (W)	Photon flux (Photon/s)	Counts SPAD19743	Counts SPAD18752	η_SPAD 19743	$U(k=2)$_SPAD 19743	η_SPAD 18752	$U(k=2)$_SPAD 18752
6.39E-15	27302	14922	13897	0.5473	0.007	0.5081	0.007
8.82E-15	37706	20679	19185	0.5474	0.007	0.5079	0.007
1.58E-14	67302	36011	33617	0.5383	0.007	0.4993	0.006
3.60E-14	153892	84056	78288	0.5379	0.007	0.5013	0.007
4.97E-14	212558	113987	106012	0.5418	0.007	0.5047	0.006
9.57E-14	408822	223860	203440	0.5446	0.007	0.4981	0.007
2.34E-13	999049	531395	493259	0.5321	0.008	0.4877	0.007

2.94E-13	1258170	662830	620819	0.5297	0.007	0.4945	0.007
5.27E-13	2252578	1151451	1075152	0.5144	0.007	0.4804	0.006

Year: 2025

Φ (W)	Photon flux (Photon/s)	Counts SPAD19743	Counts SPAD18752	η_SPAD 19743	$U(k=2)$_SPAD 19743	η_SPAD 18752	$U(k=2)$_SPAD 18752
1.64E-14	69986	38440	34724	0.5491	0.007	0.4937	0.006
2.39E-14	102193	56153	50649	0.5501	0.007	0.4944	0.006
3.97E-14	169796	93347	84508	0.5515	0.007	0.4975	0.006
5.66E-14	241929	131991	119231	0.5461	0.007	0.4912	0.006
1.10E-13	469610	253695	228920	0.5415	0.007	0.4869	0.006
1.21E-12	5164297	2547864	2321962	0.4949	0.006	0.4510	0.006
2.70E-13	1154675	619219	560785	0.5376	0.007	0.4866	0.006
3.56E-13	1521551	804532	727147	0.5313	0.007	0.4806	0.006
6.63E-13	2832425	1445875	1310757	0.5122	0.007	0.4641	0.006

Year: 2017

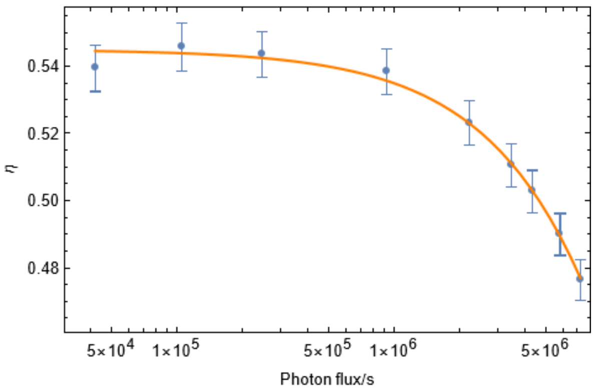

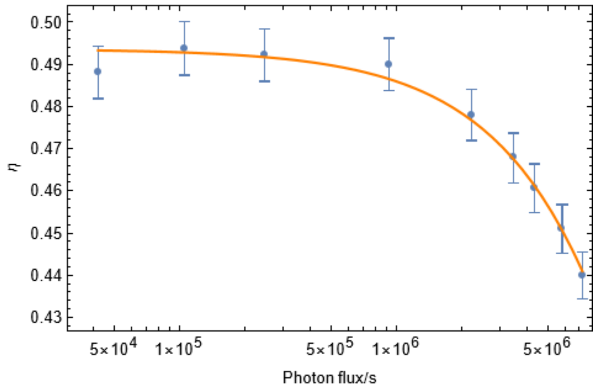

Year: 2018

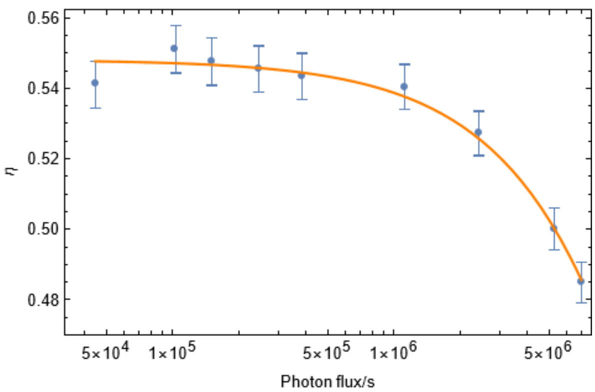

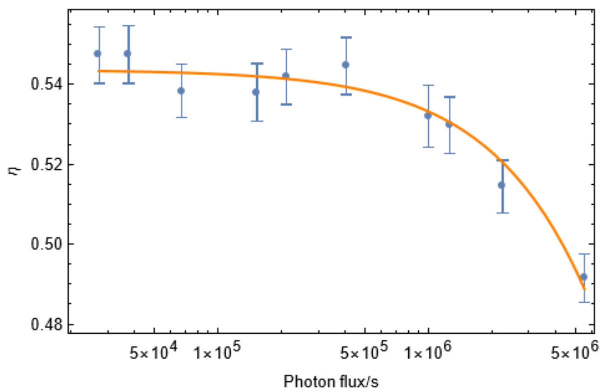

Year: 2021

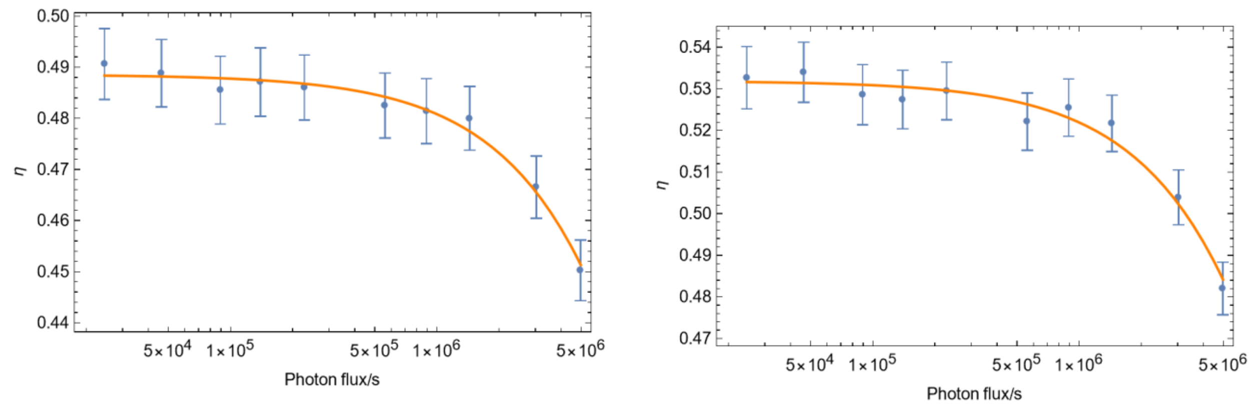

Year: 2024

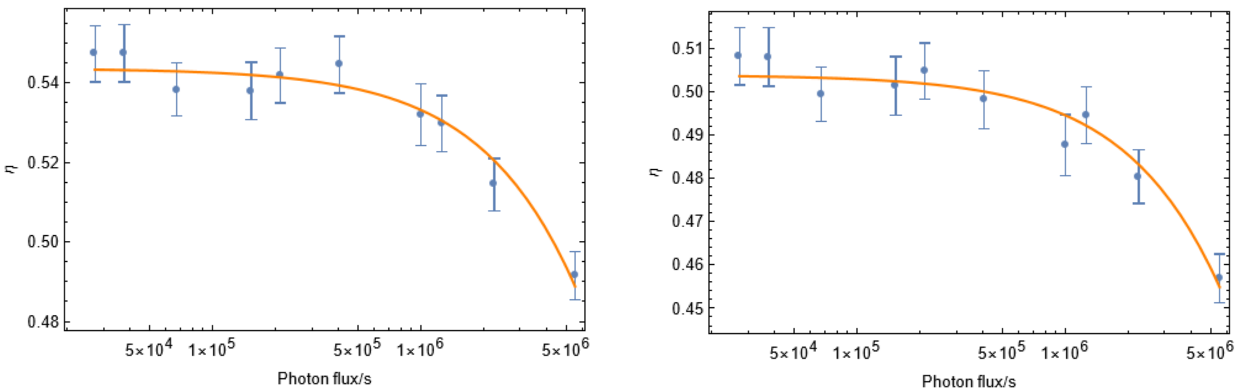

Year: 2025

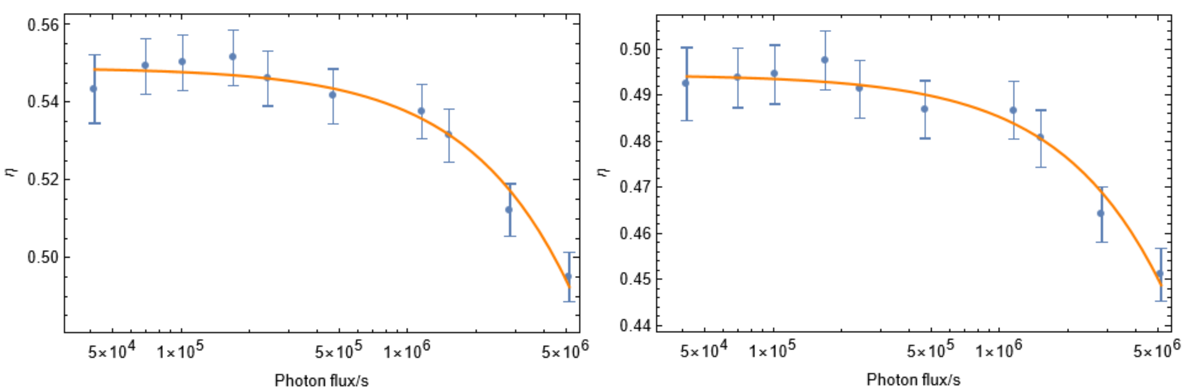

Figure 5. Detection efficiency measurements for different photon fluxes. *Left*: SPAD SN: 19743, *Right:* SPAD SN: 18752. Solid curve (orange): fitted model: $\eta = a \cdot e^{-b \cdot P_f}$, where P_f is the photon flux, a and b are the fit coefficients. Error bars correspond to the expanded uncertainty (k=2) of the measurement.

7 Uncertainty

Table 4. Example of uncertainty budget of the SPAD detection efficiency for a photon flux of approximately 106 kphoton/s.

Measurand	Unit	Description	Value	Standard uncertainty	Distribution	Sensitivity coefficient	Contribution	Contribution
h	Js	Planck constant	$6.626206957 \cdot 10^{-34}$ Js	-	-	-	0	0
c	m/s	Speed of light	$299.792458 \cdot 10^{6}$ m/s	-	-	-	0	0
λ	m	Wavelength	$848.8 \cdot 10^{-9}$ m	$2.887 \cdot 10^{-10}$ m	Rectangular	$-643 \cdot 10^{3}$	$-1.86 \cdot 10^{-4}$	0.31 %
Q_1	A/V	Ratio I_1/V_{Mon1}	$1.35311 \cdot 10^{-4}$ A/V	$6.921 \cdot 10^{-8}$ A/V	Standard	8063.1	$5.58 \cdot 10^{-4}$	2.84 %
Q_2	A/V	Ratio I_2/V_{Mon2}	$2.58086 \cdot 10^{-8}$ A/V	$3.454\ 10^{-12}$ A/V	Standard	$-2.1137 \cdot 10^{7}$	$-7.30 \cdot 10^{-5}$	0.05 %
Q_3	A/V	Ratio I_3/V_{Mon3}	$6.88215 \cdot 10^{-8}$ A/V	$1.055 \cdot 10^{-11}$ A/V	Standard	$-7.9265 \cdot 10^{6}$	$-8.37 \cdot 10^{-5}$	0.06 %
Q_4	A/V	Ratio I_4/V_{Mon4}	$4.7419 \cdot 10^{-7}$ A/V	$8.125 \cdot 10^{-11}$ A/V	Standard	$-1.1504 \cdot 10^{6}$	$-9.35 \cdot 10^{-5}$	0.08 %
Q_5	1/V s	Ratio CR/V_{MonSPAD}	363760 1/V s	408.66 1/V s	Standard	$1.4997 \cdot 10^{-6}$	$6.13 \cdot 10^{-4}$	3.43 %
s_{Si}	A/W	Spectral responsivity of Si-photodiode	0.2937A/W	$5.88 \cdot 10^{-4}$ A/W	Standard	1.86	$1.10 \cdot 10^{-3}$	10.86 %
F_{Filt}	1	Factor for the use of two filters	0.99980 1	$2.31 \cdot 10^{-3}$ 1	Rectangular	0.55	$1.26 \cdot 10^{-3}$	14.49 %
F_{Stray}	1	Factor for stray light	1.004	$4.02 \cdot 10^{-3}$ 1	Rectangular	0.54	$2.18 \cdot 10^{-3}$	43.44 %
F_{NLy}	1	Factor for linearity of Si-photodiode	1.00	$1.00 \cdot 10^{-3}$ 1	Rectangular	0.55	$1.64 \cdot 10^{-3}$	24.44 %
$\boldsymbol{\eta}$	**1**	**Detection efficiency**	0.5455	$3.31 \cdot 10^{-3}$	Standard			

8 References

1. Marco López, Helmuth Hofer and Stefan Kück, "Detection efficiency calibration of single-photon silicon avalanche photodiodes traceable using double attenuator technique", Journal of Modern Optics 62 No. S21-S27 (2015)
2. G. Porrovecchio, M. Šmid, M. López, H. Hofer, B. Rodiek, S. Kück, „Comparision at the sub-100-fW optical power level of calibrating a single-photon detector using a high-sensitive, low-noise silicon photodiode and the double attenuator technique", Metrologia 53, 1115-1122 (2016)
3. K. Dhoska, H. Hofer, B. Rodiek, M. López, T. Kübarsepp, S. Kück, „Improvement of the detection efficiency of Si-SPAD detectors and investigation of the detection efficiency homogeneity", SpringerPlus, 1-14 (2016)
4. Klodian Dhoska, Helmuth Hofer, Marco López, Toomas Kübarsepp, Stefan Kück, "Alignment position method for SPAD detector calibration and homogeneity"; International Journal of Scientific Reports, 1 (7):271-274 (2015)

Pilot study on the detection efficiency of single-photon detectors – Si-SPAD

Thomas Gerrits, John Lehman, Alan Migdall, Sae Woo Nam, Igor Vayshenker, Jack Wang

National Institute of Standards and Technology

August 10, 2017

Table of Contents

Introduction 2
Summary 3
Experimental Setup 4
  Si-trap detector 5
  Pulsed versus CW measurement modes 6
  Polarization dependence 6
  Beam splitting ratio 6
  Allan deviation of laser source 7
Free-space beam geometry 8
  SPAD spatial uniformity 9
Afterpulsing 11
Measurements and extrapolation to 1 cps 12
  Measurement of detection efficiency at a single count rate 12
  Extrapolation to 1 cps 14
  Results 14
Wavelength Correction 15
Final Results 16
Estimation of uncertainties 17
  Uncertainty budget 17
  Estimation of uncertainty at single count rate 17
  Estimation of uncertainty for 1 cps extrapolation 18
  Estimation of uncertainty for wavelength correction 18
Measurement Protocol 19
Disclaimer 19
References 20

Introduction

This document reports the results of the pilot international comparison obtained by the National Institute of Standards and Technology (NIST) on the detection efficiency of two free-space coupled single photon avalanche photodiode detector (SPAD) modules, provided by the Physikalisch Technische Bundesanstalt (PTB) Braunschweig. The two devices are Perkin-Elmer-SPCM-AQR-16* SPADs with serial numbers: 19743 and 18752, labelled PTB19743 and PTB18752, respectively. According to the protocol [1], "*the measurand for the Si-SPAD detector is the detection efficiency of the transfer detector at low signal (close to 1 photon per second) at a wavelength of 850 nm under continuous wave irradiation in free space with a beam diameter (1/e^2-value) of smaller than 40 µm, (or at least 99.9 % beam capture), no matter what conditions are actually used in the measurements. … The detection efficiency is defined as the ratio of the count rate of the transfer detector (minus the dark rate and the after-pulse rate) and the photon rate impinging on the detector. This definition is an extrapolation to low count-rate to provide a standard operating condition for the measurand to minimize effects of dead time. The measurements should be performed in suitable laboratory conditions maintained at a temperature of 23.0 °C $\pm$1°C. The exact temperature of the laboratory during the time of the measurements must be reported.*"

We transferred the calibration of a fiber-coupled optical power meter to the single-photon domain by attenuation of a pulsed laser beam. Our calibration chain is the following:

1) Electrical standard ⇩[2]
2) Primary standard: Laser Optimized Cryogenic Radiometer (LOCR) ⇩ [2]
3) Pryroelectric transfer standard ⇩ [3]
4) Fiber- coupled optical power meter absolute calibration (Si-trap) ⇩ [3, 4]
5) Fiber-coupled optical power meter nonlinearity calibration (monitor power meter) ⇩ [5]
6) Single-photon avalanche photodiode detector module (SPAD)

The calibration of the SPAD modules is tied to our calibration service of optical fiber power meters and nonlinearity measurement [3-5]. We utilized a Si-trap detector and monitor power meter to transfer the calibration of these optical power meters to the single-photon domain. We performed two independent calibrations of the Si-trap detector at NIST Boulder [3] and at NIST Gaithersburg [4]. The calibrations yielded responsivities of 0.6784(3) A/W and 0.6787(2) A/W at 851.2 nm.

Our free-space-coupled optical power meter is an optical Si-trap detector (NIST SIT, S/N 504495) [6] with a high accuracy current-to-voltage amplifier (Gentec SDX-1226-1, S/N 504495)* and high accuracy voltmeter (Agilent 3458A, S/N SG45040625)* for readout. The Si-trap detector has low reflectance (<1%), has low spatial nonuniformity (<10^{-4}), and its amplifier is very linear near 850 nm and has low noise. It was well suited as a transfer standard, and avoids several issues typically encountered when using windowed optical power meters.

Summary

The measurement of the SPAD efficiencies is based on an unbalanced beamsplitter method, where an attenuator is used to attenuate from light levels that allow high accuracy absolute power measurements to levels compatible with photon-counting detectors. First, the splitting ratio of the beamsplitter is measured at optical powers that allow both its input and output powers to be accurately measured with optical power meters, then its input power is reduced such that the output is in the range of the device under test (DUT). So, using this measured splitting ratio and the measured input power, the low level optical power on the DUT can be determined, thus allowing the calibration of the calibrated optical power meter (Si trap) to be transferred to the DUT.

An optical power of ≈7 µW into the beamsplitter, as measured by a monitor optical power meter, yielded a power at the DUT of ≈50 pW, as measured by the Si Trap. The measurement of the ratio of the two powers allowed a high precision determination of the splitting ratio from the input of the unbalanced beam splitter to the DUT. The optical power was then reduced by upstream attenuators so the light at the output of the beamsplitter is compatible with single-photon detection and the DUT is placed into the measurement beam. In addition, the monitor power meter keeps track of the incoming optical power. This measurement scheme assumes a constant beam splitting ratio over the course of the measurements and the range of incoming optical power. Both assumptions were tested.

We found significant spatial variation of response across the active areas of the SPADs due to optical interference originating from the windows when measured with a narrow bandwidth continuous wave (CW) laser (Thorlabs LP852-SF30* serial number: 160628-60). To reduce this etaloning effect, we used a short coherence length, pulsed Ti:Sa oscillator. The coherence length of the transform-limited pulses was 40 µm, short enough to eliminate interference effects from the window itself or the SPAD substrate-window gap.

To determine the DUT efficiency at 1 count per second (cps), a series of measurements from ≈1000 counts per second to ≈1 Million counts per second were performed. The afterpulsing probability was determined and subtracted accordingly from the measured results. Dark counts were also measured and subtracted. From these measurements, the efficiency at each count rate was obtained. These efficiencies versus count rate were fit with a linear regression and extrapolated to yield the DUT efficiency at 1 cps, a value where the effects of detector dead time blocking losses and higher-order Poisson statistics detection events are negligible.

To determine the response at 850 nm, spectral response measurements of the DUTs were taken to correct for any deviation in the input laser wavelength from the desired 850 nm. We used the Ti:Sa oscillator at nominal wavelengths of 845 nm, 850 nm and 855 nm. The efficiencies at each of these wavelengths were extrapolated to 1 cps, and a correction to the measured detection efficiency was applied to estimate the efficiency at 850 nm.

We obtained:

SPAD	Detection efficiency at 1 cps and 850 nm	Relative expanded uncertainty
PTB19743	0.5581(26)	0.93%, k = 2
PTB18752	0.5093(24)	0.93%, k = 2

Experimental Setup

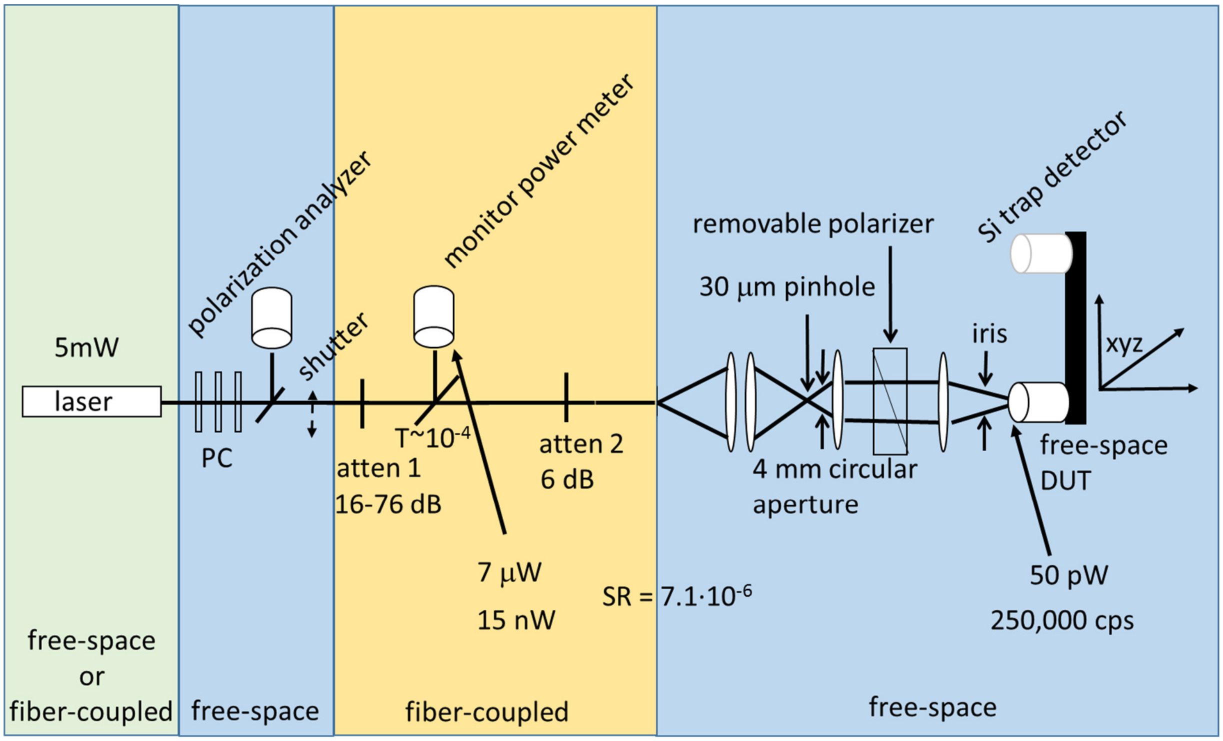

Figure 1: Experimental Setup: Light from a free-space laser is coupled into a fiber. The light in the fiber is then coupled into a free-space polarization control and analysis setup (PC). The light is then coupled into fiber and through a fiber-attenuator (atten 1). The high-power output of the 1:10000 beam splitter is connected to a monitor power meter. The low-power output light is then sent through atten 2 and into free-space collimation and focusing optics. An xyz stage allows switching between the DUT and Si-trap detector. A removable polarizer is used in setting the polarization. The transmittance of the monitor beamsplitter(T) and the overall ratio (SR) of the monitor power to the power incident on the Si trap detector or DUT are indicated.

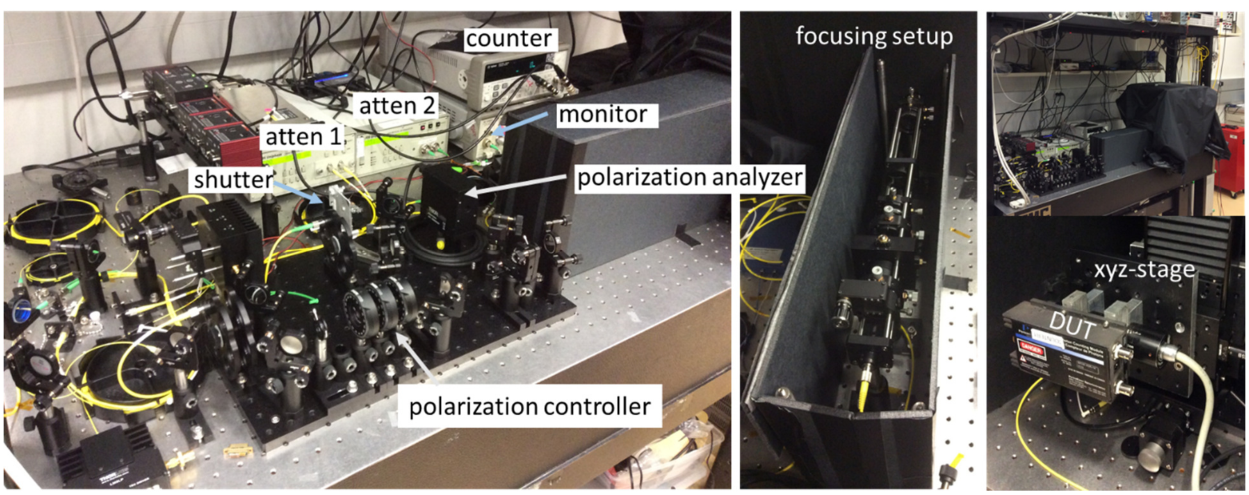

Figure 2: Photos of the experimental setup. The focusing setup and xyz-stage setup are covered with cardboard boxes and black-out cloth.

The experimental setup (Figure 1) begins with a fiber-coupled CW laser or Ti:Sa oscillator coupled into an optical fiber. At the output of the optical fiber, the optical power is ≈5 mW. The light is coupled into a free-space polarization controller consisting of a half-wave/quarter-wave/half-wave plate combination. We use the polarization controller to enable changing the polarization at the DUT and to measure its polarization sensitivity. The input polarization of the laser is measured with a free-space polarization analyzer. The polarization is continuously measured to ensure stable operation. The last component of the free-space setup is a controllable shutter, which serves as a light switch to block or unblock the light entering the setup. After the shutter, the light is coupled into an optical fiber which is multi-mode at 850 nm (Corning SMF28e*). This matches the optical fiber inside the first variable fiber attenuator, atten 1 (JDSU Uniphase HA097+20AFP1 S/N HE104407*). After atten 1, the light is coupled into a single-mode optical fiber (Nufern 780HP*) and directed to a fiber beam splitter. The nominal splitting ratio is 1:10000, where the high-power output port is connected to the monitor optical fiber power meter (Agilent mainframe HP8163A, S/N DE38702803 and Hewlett-Packard detector module: HP81532A, S/N2948G02904)*. The low-power output port of the fiber beam splitter is connected to atten 2, a variable fiber attenuator (JDSU Uniphase HA9W7+20AFA7, S/N KE037092)*, after which the light is coupled to another free-space part of the setup. Atten 2 may be used to adjust the splitting ratio between the DUT and monitor power meter. In free-space, the light out of the fiber is collimated and re-focused onto a 30 μm wide pinhole cleaning up the spatial mode and removing Airy rings originating from the fiber. About 90 % of the light is blocked by the pinhole. The free-space beam is then collimated and a 4 mm circular aperture is placed in front of the collimation lens to block all Airy rings originating from the pinhole. We placed a removable polarizer into the free-space path, which along with the polarization controller at the output of the laser, allow us to set the polarization to be parallel to the longer edge of the front surface of the DUTs. After the polarization is set, we remove the polarizer from the setup. The beam is then focused using an aspheric lens with a 79 mm focal length (Thorlabs ASL10142M-B)*. We chose a long-focal length lens to eliminate the possibility of small back-reflections from the DUT being reflected back onto the DUT. In addition, a variable iris in the optical path after the focusing lens also helped to minimize this back reflection onto the DUT. The beam is focused to a $1/e^2$ beam diameter of ≈20 μm. The Si-trap detector and DUT are co-mounted on an xyz translation stage setup. Thus, the free-space optical beam is stationary, while the DUT and Si-trap detector can in turn be moved into the optical beam.

The splitting ratio between the monitor power meter and the Si trap at the location of the DUT is determined at high power levels, e.g.: monitor power meter: 7μW, Si-trap detector: 50pW. Then, atten 1 is set such that a signal compatible with single photon measurements (e.g.: ≈250,000 counts per second is received at the DUT, with the monitor power meter at 15 nW). Atten 1 can be used to adjust the count rate at the DUT. We also re-measure the splitting ratio about once an hour during a data acquisition to track the splitting ratio over time. Input polarization state, laser power, setup temperature and the input laser wavelength are measured continuously, at a rate of ≈2 measurements per minute.

Si-trap detector

We chose to utilize one of our Si-trap detectors in order to minimize the ultimate uncertainty in determining the detection efficiency at 850nm when using a Ti:Sa oscillator with ≈5 nm bandwidth. The response of the Si-trap detector is extremely linear with respect to wavelength around 850 nm [6], and therefore only the mean energy of the laser's output is required to establish the measurement wavelength. In addition, the reflectivity of the Si trap is less than 1 %, and its spatial response non-uniformity is extremely small, (<10^{-3}) [6]. This allowed us to independently calibrate the Si-trap detector using our calibration service for fiber-coupled optical power meters [3]. The fiber-coupled and free-space calibrations differed by 0.05 %. This is well within the 0.12 % (k = 1) relative standard deviation of the mean of that difference.

Pulsed versus CW measurement modes

Even with the same average optical input power, measurements made using pulsed light may yield different responsivities than measurements made with continuous wave (CW) light due to detector nonlinearities at high peak incident light levels. Because our laser repetition rate is high (≈76 MHz), our average optical input power is low (<10 μW), and the temporal response of our Si-trap detector and monitor power meter is slow (< 1 kHz), we do not expect any discrepancies between CW or pulsed mode measurements [7]. For a single-photon detector at low count rates, the count rate will depend linearly on the average input power, while at high count rates, the dead time of the detector will cause the ratio of count rate to incident light (proportional to the detection efficiency) to drop as the input average power is increased. This is due to missing photon detections within the detector's dead time as the mean photon number per detector dead time is increased. This effect is known as blocking loss. When using a CW laser, the blocking loss is equal to the probability of another photon arriving within the detector's dead time after the first photon was detected. When using a pulsed laser, the blocking loss is equal to the mean number of photons within *n* pulses after a first photon was detected. In our case n = 2, as the dead time was ≈28 ns and the laser repetition time was 13.2 ns. Because we measure the efficiency versus count rate and report the efficiency value extrapolated to 1 cps, both pulsed and CW measurements yield the same value.

Polarization dependence

We measured the DUT's response at two orthogonal linear polarizations to estimate the uncertainty due to polarization fluctuations. We found for both DUTs measured, that the difference in responses is well within the 0.05 % relative standard uncertainty of the measurements themselves.

Beam splitting ratio

To verify that the beam splitting ratio was independent of the optical input power, we measured the beam splitting ratio stability for many different input powers. Figure 3 shows the splitting ratio as a function of attenuator setting (atten 1). Atten 2 was set to 6 dB.

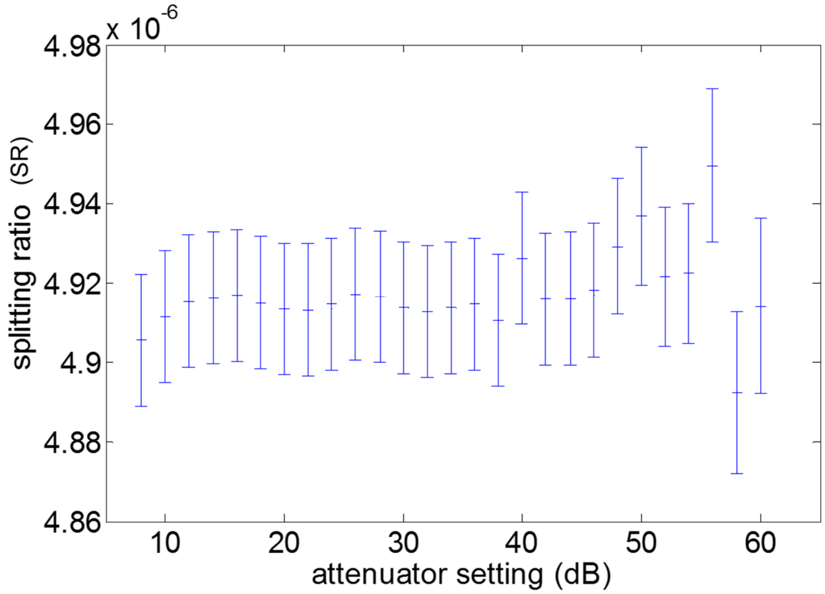

Figure 3: Measured splitting ratio versus attenuator (atten 1) setting.

The splitting ratio (SR) was determined by measuring the ratio between the monitor power meter (Agilent mainframe HP8163A, S/N DE38702803 and Hewlett Packard detector module: 81532A, S/N2948G02904)* and another power meter (Agilent mainframe HP8163A, S/N DE38702803, Hewlett-Packard detector module: HP81533B, S/N 3411G03095 and HP81520A, S/N 2936G00696) at the position of the DUT. Our measurement service for non-linearity for optical fiber power meters [5] was used and applied to the measured power on both power meters. The ratio between both power meters is plotted as a function of atten 1 setting. The splitting ratio is approximately constant, within the combined uncertainty of the non-linearity correction uncertainty and the measurement uncertainty. The errorbars include the combined measurement and non-linearity correction uncertainty.

Allan deviation of laser source

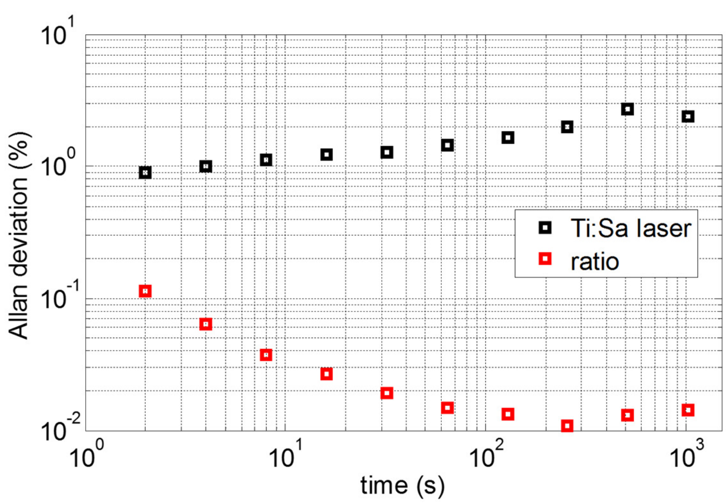

Figure 4: Allan deviation of the laser power at the monitor power meter (black squares) and Allan deviation of the ratio of the power at the DUT location and the monitor power meter (red squares).

To test the stability of the Ti:Sa oscillator, we determined the Allan deviation [8] of the laser power through the setup and the ratio of both powers measured at the monitor power meter and at the DUT location. We measured the power once every second and computed the Allan deviation of the laser power at the monitor power meter as a function of averaging time, as shown in Figure 4. When measuring the detection efficiency of the DUTs, we typically measure the counts and monitor power once every second for 25 s. The average of these 25 measurements is used to calculate the detection efficiency of the SPAD. Thus, we are interested in the laser stability over times of ≈25 s. From the Allan deviation data we can estimate a laser power Allan deviation of about 1.2% at 25 s. All our measurements are based on the ratio of the Si-trap detector and monitor power meter and the ratio of the SPAD count rate and the monitor power meter. Therefore, we calculated the Allan deviation of the ratio of the Si-trap detector and monitor power meter. As seen in Figure 4, the Allan deviation of the ratio is significantly reduced relative to the raw laser power measurements. At an averaging time of 25 s the Allan deviation of the ratio is estimated to be less than 0.02 %. While the observed laser power drift was not ideal, the ratio of the two power meter readings was stable enough for our measurement protocol.

Free-space beam geometry

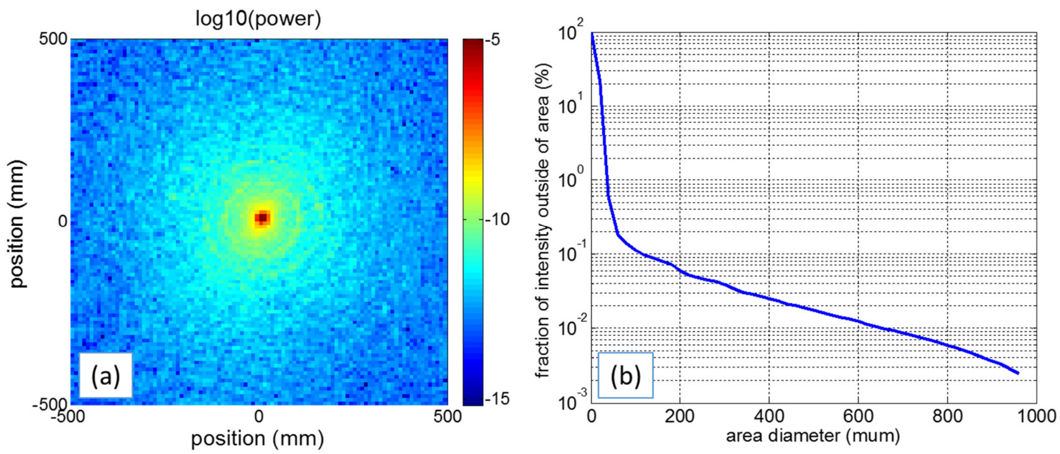

Figure 5: (a) Spatial beam scan at the focal position using a 10 µm pinhole on a logarithmic scale (b) Fraction of light intensity outside of a circular area centered on the peak light intensity.

We measured the spatial distribution of the focused laser beam at the focal plane, the location of the DUT. To quantify the collection efficiency of the total light hitting the 180 µm diameter SPAD, we scanned the laser beam using a 10 µm pinhole mounted on our xyz stage. We moved the pinhole in 10 µm steps and recorded the optical power transmitted through the pinhole. Figure 5 (a) shows the spatial map of the beam. Note the logarithmic intensity scale. Some very weak Airy rings can be seen around the main beam spot. These rings are at least 5 orders of magnitude lower than the central beam intensity, and they result from the 4 mm aperture inserted into the beam path before the collimation lens. Figure 5 (b) shows the fraction of the light intensity outside of a circular area with diameter *D*. At a diameter of ≈150 µm, the fraction of the light intensity outside this area drops below 0.1 %. At 200 µm, this ratio has dropped to ≈ 0.06 %.

SPAD spatial uniformity

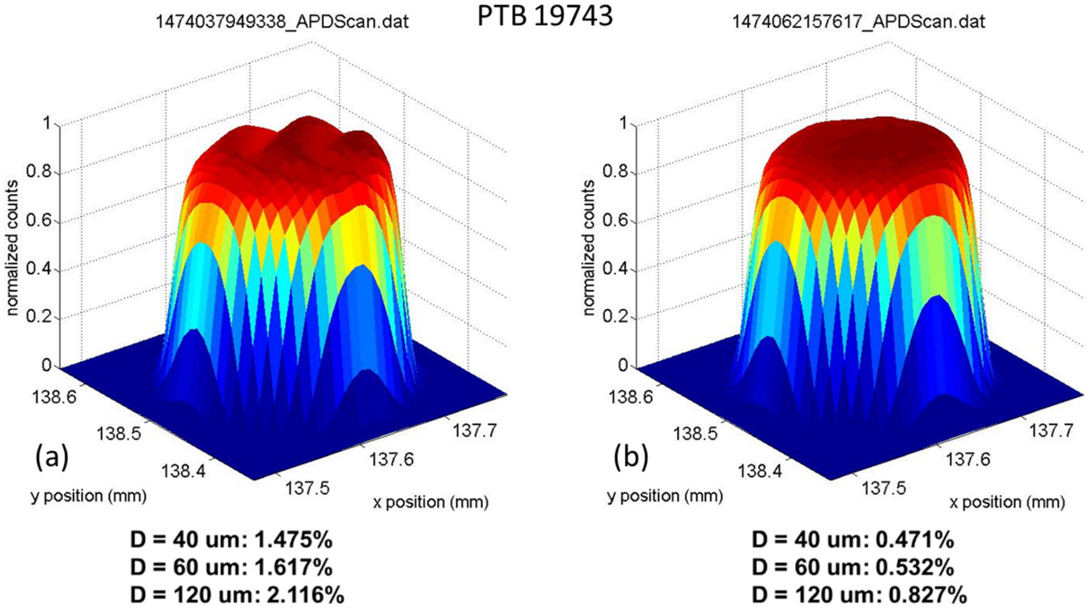

Figure 6: Spatial response scans of PTB 19743 SPAD using (a) a CW laser source and (b) a Ti:Sa oscillator with short coherence length.

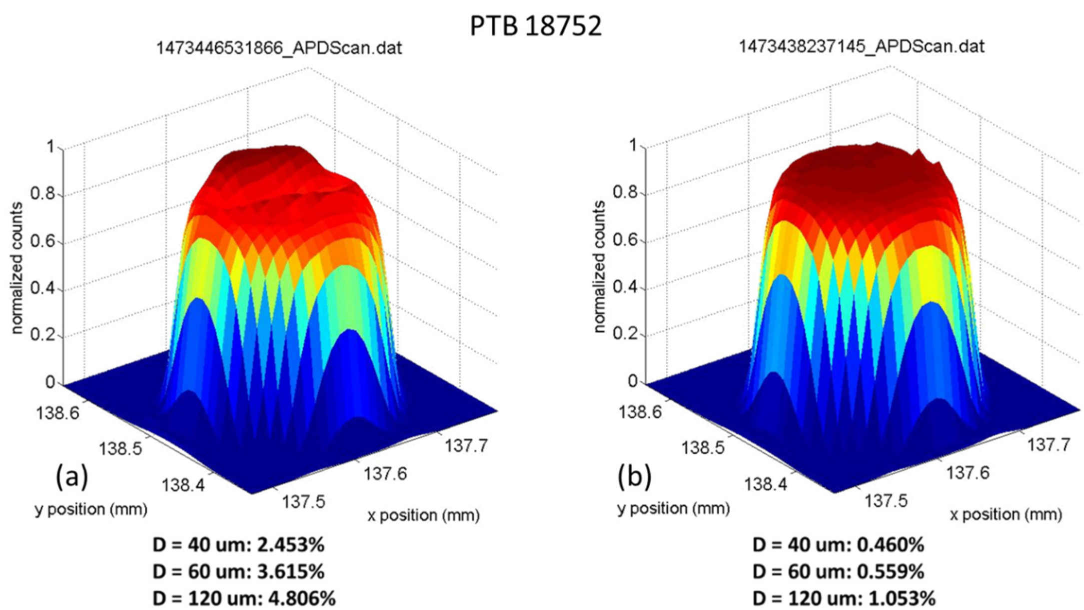

Figure 7: (a) Spatial response scans of PTB 19752 SPAD using (a) a CW laser source and (b) a Ti:Sa oscillator with short coherence length.

Figure 6 and Figure 7 show spatial scans of both SPADs using the CW laser source and the Ti:Sa oscillator. In both figures, (a) shows the spatial response using the CW laser. Strong interference fringes can be observed in these cases. We speculate that these interference fringes originate from the glass window covering the SPAD. We observed fringe contrasts close to 10 % in both cases. When using a short coherence length (≈40 μm) pulsed Ti:Sa oscillator, the interference fringes disappear, as shown in Figure 6(b) and Figure 7(b). One can still observe a slight slope in the detected count rate across both SPADs. The maximum slope for an 80 μm x 80 μm area around the center of the SPADs is $4{\cdot}10^{-4}$ μm^{-1} and $3{\cdot}10^{-4}$ μm^{-1} for PTB 19743 and PTB1872, respectively. We speculate that this is due to the reflection inside the window, which in the CW case caused the interference fringes. Since the coherence length is shorter than the window thickness, we do not observe the interference fringes, but the reflection from the window, only.

Table 1: Calculated standard deviations of counts within a circular area diameter (D) for both SPADs and both laser sources.

PTB 19743				PTB 18752			
CW laser		Ti:Sa laser		CW laser		Ti:Sa laser	
Diameter, *D* (μm)	Standard deviation (%)	Diameter, *D* (μm)	Standard deviation (%)	Diameter, *D* (μm)	Standard deviation (%)	Diameter, *D* (μm)	Standard deviation (%)
40	1.5	40	0.47	40	2.5	40	0.46
60	1.6	60	0.53	60	3.6	60	0.56
120	2.1	120	0.83	120	4.8	120	1.1

Table 1 shows the calculated standard deviation of counts within a circular area with diameter *D*. For both SPADs when using the CW laser, the measurement standard deviations for area diameters ranging from 40 μm to 120 μm are much larger than when using the Ti:Sa oscillator. PTB 18752 shows a prominent interference fringe at the center, which results in larger standard deviations than for PTB 19743. When using the Ti:Sa oscillator the variations are smaller, and below 0.5 % for a 40 μm area. Our setup allows us to find the center of the SPAD with repeatability better than 5 μm. We therefore estimate the uncertainty of the count rate due to detector placement to be less than 0.2 %.

Afterpulsing

We determined the afterpulsing using the CW laser setup. All photon detection events were time-tagged during a full data acquisition, at count rates between 1000 counts per second and 1 Million counts per second. For each count rate we calculated the autocorrelation of the time tags. From the autocorrelation of the time tags we can calculate the probability of subsequent photon detection event (or afterpulsing or darkcount event) at any time after a detection event.

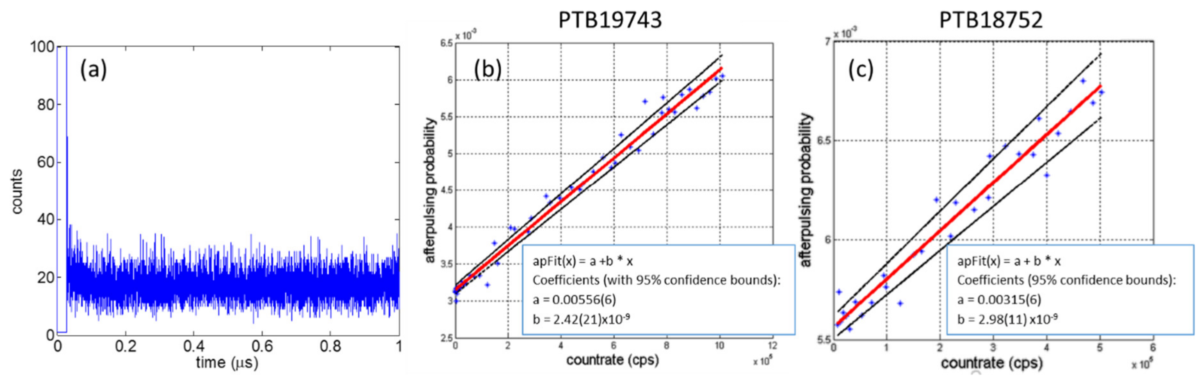

Figure 8: (a) Autocorrelation of raw time tag data for a mean count rate of ≈202000 counts per second for PTB18752 Afterpulsing probability as a function of count rate for (b) PTB19743 and (c) PTB1875. The red line is a linear fit to the data. The black lines represent the 95 % confidence bounds. Fitted parameters are shown along with 95 % confidence bounds

Figure 8(a) shows the time tag autocorrelation at a count rate of ≈202000 counts per second for the detector PTB 18752 (the peak at zero-delay is not shown). First, the autocorrelation is zero for the duration of the dead time of the detector, which was ≈28 ns. When the detector turns on, a peak with exponential decay is seen. We take the average of the number of clicks beyond 500 ns and subtract it from the autocorrelation counts. The sum of the remaining detection events yields the total number of afterpulsing events. Figure 8(b) and (c) show the afterpulsing probability as a function of count rate. The afterpulsing probability increases as the SPAD count rate increases. This effect was previously seen and quantified [9]. It was explained in terms of a “twilight” regime, where a photon absorption occurs while the SPAD voltage bias is returning to its full level, but has not yet reached that full level. In that situation, the detection output pulse is somewhat delayed in time. This probability increases as the average photon flux onto the device increases. The afterpulsing probabilities for both DUTs are less than 1% for all count rates measured, and the 95 %-confidence interval spans a region of less than 10 % of the measured values. Thus, we estimate a relative standard uncertainty of less than 0.05 % due to the afterpulsing correction.

Measurements and extrapolation to 1 cps

The measurements and analysis were done according to the pilot protocol. The detection efficiency results presented here are at 1 cps and corrected for afterpulsing effects and dark counts. A series of measurements between 10^3 counts per second and 10^6 counts per second was taken to determine the slope of the efficiency versus wavelength. The decreasing efficiency with higher count rate is due to the blocking loss related to the SAPD's dead time. The data are fitted to line and extrapolated to determine the detection efficiency of the SPADs DE close to 1 cps.

Measurement of detection efficiency at a given count rate

The detection efficiency (DE) of the SPAD at a given count rate is calculated via:

$$DE = [(C-C_d)/(PM1-PM1_d)] \cdot (h \cdot c/\lambda) / SR, \qquad (1)$$

where C and C_d are the photon counts and dark counts, respectively. $PM1$ and $PM1_d$ are the power measured at the monitor power meter and its dark reading, respectively. h is Planck's constant, c is the speed of light, λ is the mean wavelength and SR is the splitting ratio between the monitor power meter and the Si-trap detector, given by:

$$SR = [(PM2-PM2_d)/(PM1_{SR}-PM1_{SRd})], \qquad (2)$$

where $PM2$ and $PM2_d$ are the power measured at the Si-trap detector and its dark reading, respectively. $PM1_{SR}$ and $PM1_{SRd}$ are the power measured at the monitor power meter and its dark reading, respectively when measuring the splitting ratio. The splitting ratio is measured three times before and three times each hour during the acquisition of one dataset. We close the shutter to perform the dark measurements. Before opening the shutter, we start the power measurements. This allows us to observe and record the start time of the power measurements and to verify that the measurement has settled temporally. Since the integration time of the optical power meters is 1 s, we omit 5 s of data after the shutter opens. Therefore, one measurement consisted of 23 to 25, 1 s measurements of the power at the monitor and trap detector. The averages of these measurements were used to calculate the splitting ratio. Depending on the time it took to acquire the dataset, there are 3 to 21 such measurements for each dataset. The count rate and monitor power is measured in a similar fashion, where the shutter closing is used to indicate the dark counts and dark reading of the monitor power meter. After the shutter opens, we can correlate count rate and optical power measurements in time. Also, 23 to 25, 1 s measurements were used in this case.

Figure 9 depicts the measured efficiencies as a function of count rate for PTB19743 and PTB18752. Figure 9(a) and Figure 9(b) show the results of three datasets and two runs for PTB19473. Between the two runs, the detector was taken out of the setup and remounted about a week later. The figures show the datapoints with associated errorbars. The errorbars were obtained by calculating the type A standard measurement uncertainty for each DE measurement and adding the type B uncertainties obtained from our uncertainty budget estimation. See the Uncertainty budget section for a detailed description of all uncertainty estimates and calculations. Figure 9(c) and Figure 9(d) show the results obtained for detector PTB18752.

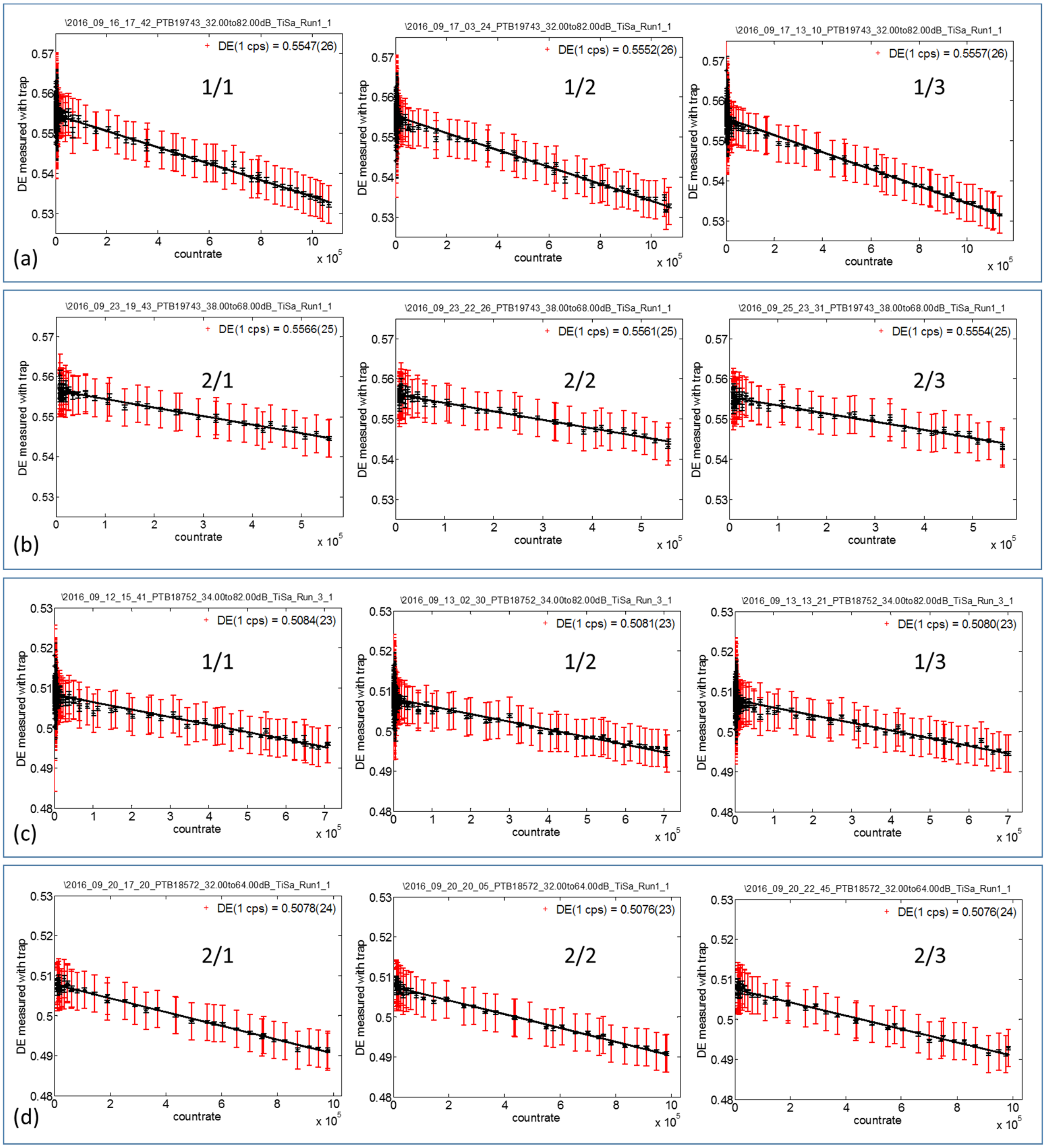

Figure 9: Measured efficiencies versus count rate for 2 runs of 3 datasets each for (a,b) PTB19743 and (c,d) PTB18752. The black datapoints and errorbars represent the measured value and calculated standard type A uncertainty at each count rate. The red errorbar represents the typical combined (type A and B) standard uncertainty of each measurement. The black line is a linear fit to the data. The integration time for each measurement was 23 s to 25 s.

Extrapolation to 1 cps

The extrapolation to 1 cps is performed using a linear regression. The regression fit accounts for the dead time of the SPADs and the Poisson statistics, which accounts for a linear decrease of the measured DE vs. count rate due to detector dead time blocking losses at high count rates. The regression was done using the curve fitting toolbox of Matlab*. At low count rates the spread in the data and the uncertainties are increased. Therefore, we ensured that at each attenuator setting (atten 1), we had $\approx 10^6$ photon detection events. For example, at a count rate of 3000 counts per second, we performed >14 measurements at this attenuator setting. The uncertainty for the DE close to 1 cps was determined using a parametric bootstrapping method, described in the Estimation of uncertainty for 1 cps extrapolation section below.

Results

Table 2 and Table 3 summarize the results at 1 cps for PTB19743 and PTB 18752. The mean measurement wavelength, DE at about 1 cps, the respective splitting ratio (SR) and lab temperature are given along with their standard uncertainties.

Table 2: Extrapolation results for PTB19743 at 1 cps

Run/dataset	λ (nm)	DE (1 cps)	Splitting Ratio (x10^{-5})	Temperature (°C)
1/1	851.06(2)	0.5547(26)	1.613(2)	22.27(17)
1/2	851.08(2)	0.5552(26)	1.614(1)	22.23(9)
1/3	851.07(1)	0.5557(26)	1.615(1)	22.24(9)
2/1	851.02(2)	0.5566(26)	2.088(1)	21.98(11)
2/2	850.99(1)	0.5561(26)	2.089(1)	21.95(13)
2/3	851.07(1)	0.5554(26)	2.084(1)	21.95(7)

Table 3: Extrapolation results for PTB18752 at 1 cps.

Run/dataset	λ (nm)	DE (1 cps)	Splitting Ratio (x10^{-5})	Temperature (°C)
1/1	850.56(1)	0.5084(23)	1.525(1)	22.40(9)
1/2	850.57(1)	0.5081(23)	1.523(1)	22.38(7)
1/3	850.58(1)	0.5080(23)	1.524(1)	22.40(7)
2/1	850.57(2)	0.5078(24)	1.619(1)	22.31(17)
2/2	850.53(1)	0.5076(23)	1.620(1)	22.29(11)
2/3	850.53(1)	0.5076(24)	1.619(1)	22.26(10)

Wavelength Correction

A wavelength correction is necessary to report the DE at a wavelength of 850 nm. We measure the SPADs responses close to 850 nm, typically between 850 nm and 851 nm. To determine the DE wavelength dependence of the SPADs, we tune the output center wavelength of the Ti:Sa oscillator to about ± 5 nm away from 850 nm. The extraction of DE at these wavelengths is performed in a similar way as the extraction of DE at 1 cps. The DE is obtained at 1 cps for each of the measured wavelengths. However, we only measure the SPADs' responses for count rates between 10000 counts per second and 400000 counts per second. Table 4 and Table 5 summarize the results for both SPADs. Figure 10(a) and (b) show the results and the wavelength dependence of the SPADs. To determine the DE at 1 cps and 850 nm, we use a linear interpolation based on the slope of the SPAD wavelength dependence. The uncertainty originating from this wavelength interpolation is estimated by another parametric bootstrap, outlined in the Estimation of uncertainty for wavelength correction section below.

Table 4: wavelength dependence for PTB19743 at 1 cps.

λ (nm)	DE (1 cps)	Splitting Ratio (x10^{-5})	Temperature (°C)
845.67(2)	0.5663(26)	1.624(1)	22.30(18)
850.60(2)	0.5551(26)	1.619(2)	22.22(22)
855.98(2)	0.5417(25)	1.666(2)	22.18(24)

Table 5: wavelength dependence for PTB18752 at 1 cps.

λ (nm)	DE (1 cps)	Splitting Ratio (x10^{-5})	Temperature (°C)
845.43(2)	0.5191(24)	1.624(1)	22.33(18)
850.57(2)	0.5078(24)	1.619(1)	22.31(34)
855.58(1)	0.4935(23)	1.659(1)	22.29(18)

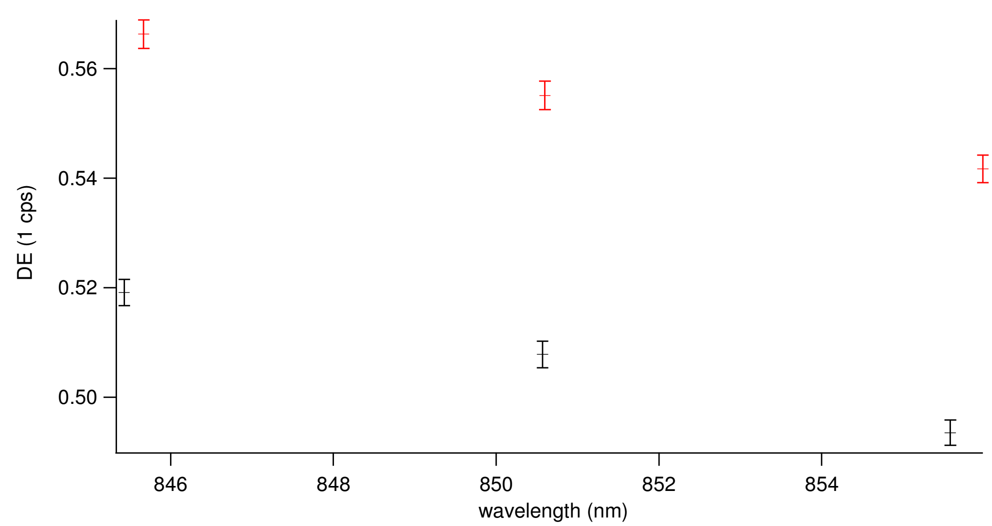

Figure 10: wavelength dependence of DE at 1 cps for PTB19743 (red) and PTB18752 (black). (b) wavelength dependence of DE at 1 cps for PTB18752

Final Results

Table 6 summarizes the results of the detection efficiency after wavelength correction at 1 cps. The final efficiencies are quoted with their standard uncertainties (x)(y), where (x) is the combined standard uncertainty obtained from the 1 cps extrapolation and the standard uncertainty obtained from the parametric bootstrap; (y) is the standard uncertainty obtained from the parametric bootstrap only.

Table 6: Results of six measurements each of the detection efficiency at 1 cps and at 850 nm for PTB19743 and PTB18752 with the combined (bootstrapping and type B)(bootstrapping) uncertainties. Averages of the six measurements is shown.

PTB19743		PTB18752	
Run/Dataset	DE (1 cps)@850 nm	Run/Dataset	DE (1 cps)@850 nm
1/1	0.5572(26)(4)	1/1	0.5098(23)(2)
1/2	0.5578(26)(4)	1/2	0.5095(23)(2)
1/3	0.5583(26)(4)	1/3	0.5095(23)(2)
2/1	0.5590(26)(4)	2/1	0.5092(24)(2)
2/2	0.5585(26)(4)	2/2	0.5089(23)(2)
2/3	0.5580(26)(4)	2/3	0.5089(24)(2)
Average	**0.5581(26)**	**Average**	**0.5093(24)**

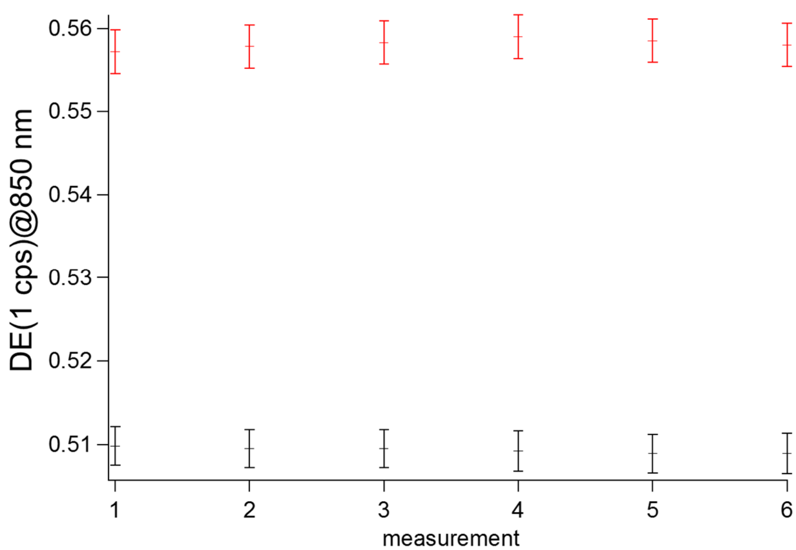

Figure 11: Six measurements of detection efficiencies for PTB19743 (red) and PTB18752 (black).

Figure 11 shows the detection efficiencies for both SPADs for 3 datasets and 2 runs, each. The errorbars represent the combined standard uncertainty of the parametric bootstrap and extrapolation to 1 cps.

Estimation of uncertainties

Uncertainty budget

Type B relative standard uncertainties for DE measurements at a given count rate:

Monitor power meter linearity (x2):	0.23%
Blocking loss correction (nonlinearity):	0.01%
Afterpulsing correction:	0.05%
Si-trap detector calibration:	0.22%
Amplifier calibration:	0.01%
Voltmeter calibration:	0.01%
OSA calibration:	0.05%
Beam collection:	0.10%
Beam alignment:	0.20%
Open beam vs. free-space:	0.05%
Polarization Dependence:	0.05%
Total:	**0.46% (0.92%; *k* =2)**

Estimation of uncertainty at single count rate

We determine the uncertainty of the extracted detection efficiency by combining the above type B uncertainties with the measurement type A uncertainties according to the Guide to the Expression of Uncertainty in Measurement (GUM) [10]. The type B uncertainties are taken from the calibration reports for our power meters and are also estimated based on our characterization of the setup, as described in the preceding sections.

The type A uncertainty for a measurement at a single count rate is the combined uncertainty of the splitting ratio measurement uncertainty and the efficiency measurement uncertainty. Both measurements are based on ratios. To obtain the ratio uncertainty, we take the splitting ratio as an example and derive:

Let X_{ij} and Y_{ij}, $i = 1, 2, \ldots, n$, $j = 1, 2, \ldots, N$, denote the j^{th} measurement of the i^{th} experiment from power meters 1 and 2, respectively. We use:

$$SR_i = \sum_{j=1}^{N} X_{ij} / \sum_{j=1}^{N} Y_{ij} = \overline{X_i}/\overline{Y_i} \qquad \text{(U1)}$$

to estimate the power ratio for the i^{th} experiment, i.e. we take the ratio of the averages of the two powers for one experiment. The uncertainty of SR_i is given by

$$u(SR_i) = \frac{\overline{X_i}}{\overline{Y_i}} \cdot \sqrt{\frac{u^2(X_i)}{X_i^2} + \frac{u^2(Y_i)}{Y_i^2} - \frac{2u(Y_i,X_i)}{X_i Y_i}} \qquad \text{(U2)}$$

where $u(X_i)$, $u(Y_i)$, and $u(X_i, Y_i)$ are the standard uncertainty of $\overline{X_i}$, the standard uncertainty of $\overline{Y_i}$, and the covariance of $\overline{X_i}$ and $\overline{Y_i}$, respectively. Since we cannot measure X and Y perfectly simultaneous, the covariance cannot be adequately estimated. However, we found a positive correlation between X and Y, *e.g.* potentially consistent with laser drift. Therefore, omitting the covariance term from equation U2 does result in an overestimation of the uncertainty of SR_i.

We find $u(X_i)$ by finding the variance and dividing by the number of measurements N:

$$u^2(X_i) = \frac{\sum_{j=1}^{N}\left(X_j - \bar{X}\right)^2}{N(N-1)} \qquad \text{(U3)}$$

The final splitting ratio and its uncertainty are determined by calculating the mean of all SR_i and the standard deviation divided by the number of experiments n:

$$u(SR) = \frac{\sqrt{\sum_{i=1}^{n}(SR_i - \overline{SR})^2}}{\sqrt{n(n-1)}} \qquad \text{(U4)}$$

Estimation of uncertainty for 1 cps extrapolation

Figure 9 shows the detection efficiency versus count rate. To determine the efficiency at 1 cps, we perform a linear regression to the data and extrapolate the result to 1 cps. To estimate the uncertainty associated with this extrapolation we use parametric bootstrapping [11] and resample the data 5000 times with a variation set by the combined uncertainty. The combined uncertainty is comprised of two different types (type A and type B). For our parametric bootstrap we model the type A and type B as distributions with a Gaussian envelope. First, we randomly resample each datapoint with its type A distribution. We then add one random resample from the type B distribution to each datapoint. Performing this resampling 5000 times, fitting the resampled data by linear regression and extrapolating to 1 cps results in a distribution of extrapolating outcomes, where the mean is the quoted detection efficiency at 1 cps and their standard deviation is the quoted standard uncertainty. Because we are adding a constant random resample of the type B uncertainty to each datapoint and the type A uncertainty is small compared to the type B uncertainty, the resulting standard uncertainty at 1 cps is close to the value of the type B uncertainty.

Estimation of uncertainty for wavelength correction

Figure 10 shows the wavelength dependence of the SPADs. To determine the uncertainty associated with the interpolation we also use a parametric bootstrap. We resample the datapoints using a Gaussian envelope distribution with standard deviation equal to the standard uncertainty obtained from the 1 cps extrapolation. Here, we randomly resample each data point from its distribution. Then, we use a linear regression to find the wavelength dependence of the detection efficiency and interpolate to 850 nm. After 5000 resamples we obtain a distribution of detection efficiencies and quote its mean and standard deviation as the detection efficiency at 1 cps and 850 nm.

Measurement Protocol

1) Mount DUT
2) Find the center of the Si-trap detector with respect to the laser beam.
3) Adjust Ti:Sa laser wavelength (if necessary)
4) Insert polarizer (used as a polarization reference) and adjust polarization controller such that polarization is aligned with that polarization reference
5) Remove polarizer from setup
6) Measure laser wavelength
7) Reduce photon flux to ≈250,000 counts per second using atten 1
8) Roughly find center of DUT with xyz stages
9) Fine z-scan (along the optical axis) to find the beam waist on the DUT
10) Fine xy scan to find the center of the DUT
11) Center the DUT on the free-space beam
12) Measure counts versus attenuator (atten 1) setting (to determine the number of measurements needed at each attenuator setting)
13) Measure DE vs. attenuator setting
    a. Measure trap/monitor power meter splitting ratio three times and repeat measurement about once every hour (atten 1 = 0dB)
    b. Set atten 1 to desired value
    c. Move DUT into the beam and measure photon count response
    d. Repeat 10b and 10c for different attenuator settings, unless one hour has passed since the last splitting ratio measurement, then repeat 10a, 10b and 10c

Disclaimer

* Certain commercial equipment, instruments or materials are identified in this report to foster understanding. Such identification does not imply recommendation or endorsement by the National Institute of Standards and Technology, nor does it imply that the materials or equipment are necessarily the best available for the purpose.

References

1. Kück, S., *CCPR WG-SP TG 11, Pilot study on the detection efficiency of single-photon detectors – Si-SPAD.* 2016.
2. Livigni, D., *High-Accuracy Laser Power and Energy Meter Calibration Service.* NIST Special Publication 250–62, 2003.
3. Vayshenker, I., et al., *Optical Fiber Power Meter Calibrations at NIST.* NIST Special Publication 250–54, 2000.
4. Larason, T.C. and J.M. Houston, *Spectroradiometric Detector Measurements: Ultraviolet, Visible, and Near-Infrared Detectors for Spectral Power.* NIST Special Publication 250-41, 2008.
5. Vayshenker, I., et al., *Optical Fiber Power Meter Nonlinearity Calibrations at NIST.* NIST Special Publication 250–56, 2000.
6. Lehman, J.H. and C.L. Cromer, *Optical trap detector for calibration of optical fiber powermeters: coupling efficiency.* Applied Optics, 2002. **41**(31): p. 6531-6536.
7. Gentile, T.R. and C.L. Cromer, *Mode-locked lasers for high-accuracy radiometry.* Metrologia, 1995. **32**(6): p. 585.
8. Allan, D.W., *The statistics of atomic frequency standards.* Proc. IEEE, 1966. **54**(2): p. 221-230.
9. Polyakov, S.V. and A.L. Migdall, *High accuracy verification of a correlated-photon-based method for determining photon-counting detection efficiency.* Optics Express, 2007. **15**(4): p. 1390-1407.
10. BIPM, *Evaluation of measurement data — Guide to the expression of uncertainty in measurement.* 2008.
11. Efron, B. and R.J. Tibshirani, *An Introduction to the Bootstrap.* Chapman & Hall, 1993.

CCPR WG-SP TG 11

Pilot study on the detection efficiency of single-photon detectors – Si-SPAD

CMI Report

Geiland Porrovecchio and Marek Smid

Contents

Measurement Facility 1
Artefacts 2
Source spectrum 2
Spectral mismatch factor 3
Polarization 3
Laser stability 3
Reference detector 3
LOFD Photodiode responsivity 4
LOFD uniformity 4
Measurement model 5
Artefacts uniformity 6
SPCM1 non uniformity uncertainty contribution 7
SPCM2 non uniformity uncertainty contribution 8
Artefact relative spectral dependence 8
Laboratory conditions 9
Uncertainty Budget 10
Dead time model 10
Results 11
Works Cited 12

Measurement Facility

The calibration method used is the substitution method on which the reference detector and the artefact are illuminated sequentially by a normally impinging radiation that is optically setup to underfill both the detectors. The radiation source is composed by a single mode pigtailed temperature-controlled laser diode source with a nominal emitted wavelength of 852 nm that is attenuated up to 60dB by a fibre coupled Agilent 850nm attenuator. The attenuated output radiation coming out from the end of the fibre is then collimated into the input of a ten element Si tunnel trap detector (TET) that, when properly aligned, provides an additional attenuation factor of about 60dB while preserving the input beam shape. The TET is used as both attenuator and monitor detector to measure the source stability. The attenuated beam coming out from the TET is focused with a 75 mm focal length (FL) lens into the detectors' plane. The beam diameter was measured by a CCD camera placed on the beam focal plane with a value of 45 um 90% energy while the shape of the beam was quasi-gaussian. Both the reference detector and the artefact are placed on X Y Z motorized stages and on a raw, pitch, yaw gimble for their fine angular alignment.

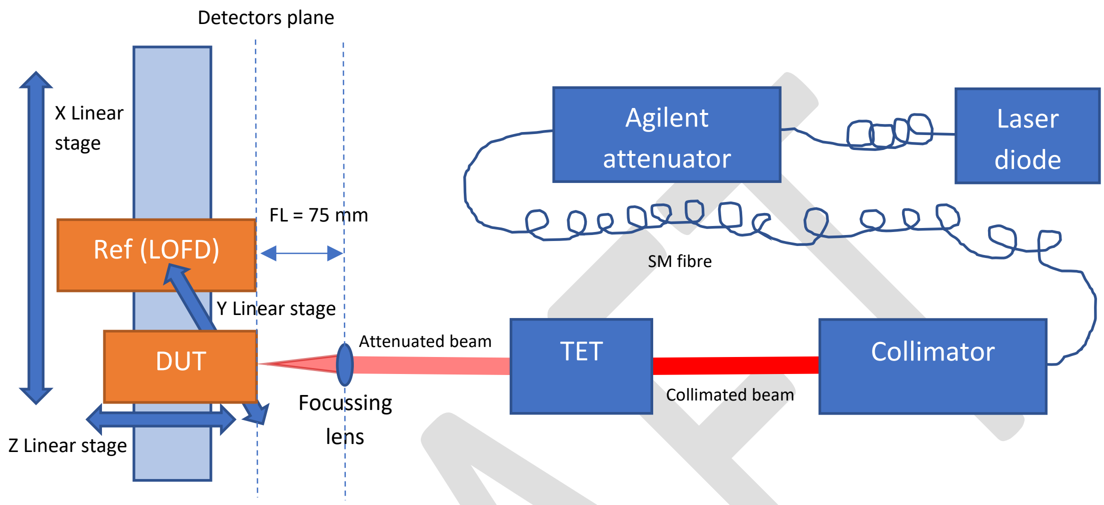

Figure 1 Calibration schema

Thanks to the x, y and motorized stages used to adjust the position of the DUT it was possible to find the optimal distance from the focussing lens by measuring the detector's output signal. The criteria used to determine the focal plane was the steepness of the horizontal (X) and vertical (Y) scans measured as the gradient of the signal measured at half height.

Artefacts

There are two artefacts (DUTs) to be calibrated for this comparison. Throughout this document they will be named as SPCM1 and SPCM2 identified by their serial numbers:

SPCM1 – SN 18752

SPCM2 – SN 19743

Source spectrum

The spectrum of the light source was measured with a Fourier transformer spectrometer. The laser is not a single frequency one (does not work in single longitudinal mode regime). In order to compensate for the non ideality of the source the reference and the DUT detectors responsivity spectral dependence have been measured.

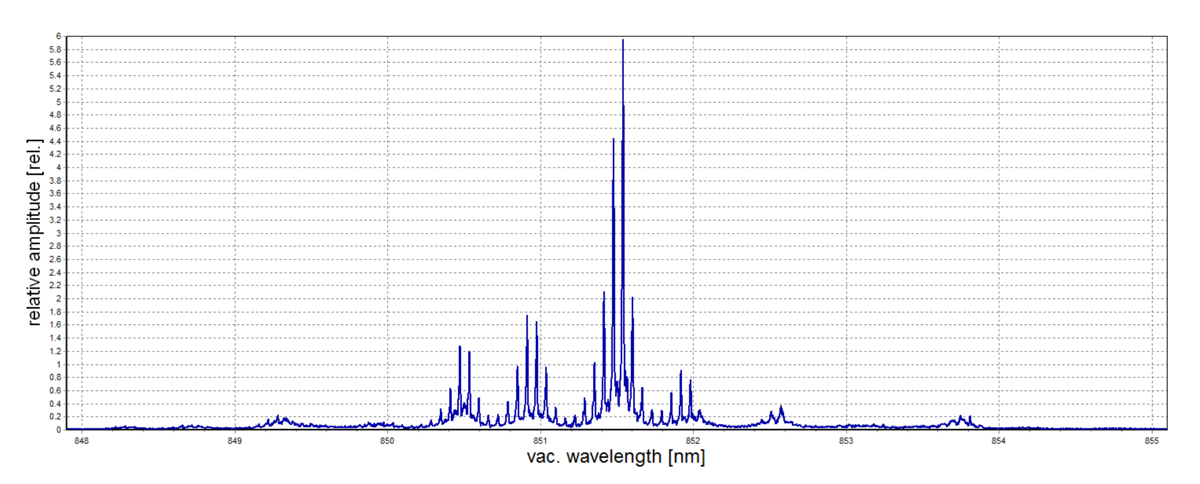

Figure 2 relative spectral irradiance of laser source

The center of mass of the relative spectral irradiance of the laser source is 851.5 nm

Spectral mismatch factor

The spectral mismatch correction factor F_i is calculated by the equation :

$$F_i = \frac{\int_{\lambda_1}^{\lambda_2} r_{LOFD}(\lambda)\cdot s_{LP852}(\lambda)\cdot d\lambda}{r_{LOFD}(850)} \cdot \frac{r_{SPCM}(850)}{\int_{\lambda_1}^{\lambda_2} r_{SPCM}(\lambda)\cdot s_{LP852}(\lambda)\cdot d\lambda}$$

Where r_{LOFD} is the spectral responsivity of the LOFD

r_{SPCM} is the relative spectral quantum efficiency of the SPCM under test

S_{LP852} is the relative spectral irradiance of the laser source

The integrals are calculated in the spectral interval ranging from λ_1 = 841.5 nm to λ_2 = 861.5 nm

Polarization

No polarization control has been used.

Laser stability

The laser intensity fluctuations were continuously monitored by the TET during all measurements performed during this comparison and its relative standard deviation has always been below 0.2%.

Reference detector

The reference detector used is the CMI Low Photons Reference detector (LOFD) (Porrovecchio, et al., 2016) the comprises a 3mmx3mm low noise and temperature cooled (12°C) Si photodiode in conjunction with a switched integrator with 1 pF capacitor. Thanks to its low noise the LOFD can perform traceable measurement of optical radiation of few tents of fW with a statistical spread lower than 1%. In fact, the LOFD measured noise equivalent power (NEP) has been measured at 1fW/Hz at 770 nm. For further details (Porrovecchio, et al., 2016).

LOFD Photodiode responsivity

The LOFD photodiode responsivity has been calibrated against the CMI SI05 transfer standard for visible spectral range. The calibration was performed on a double monochromator facility and it is traceable to the primary standard for optical radiometry: the cryogenic radiometer.

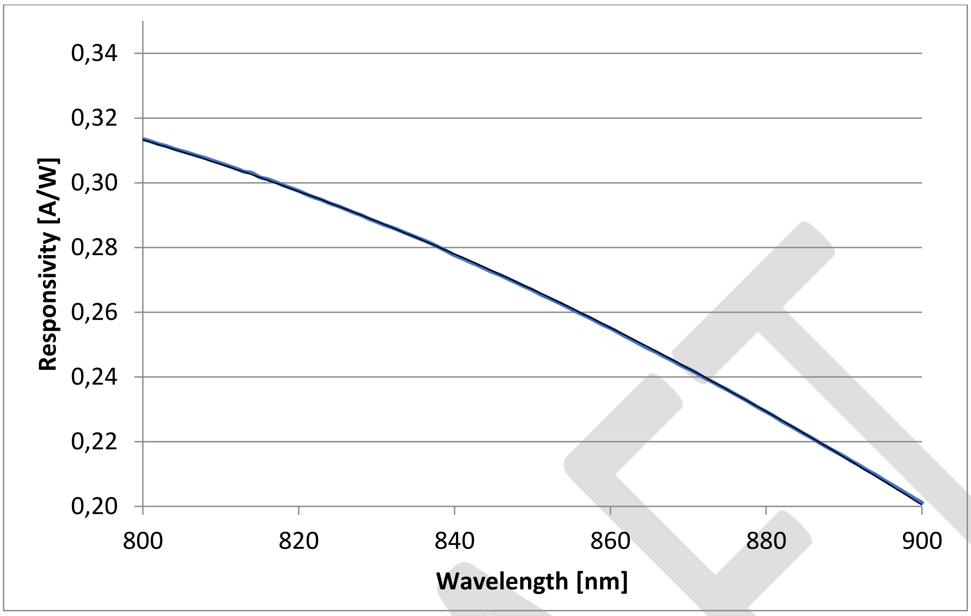

Figure 3 LOFD photodiode responsivity

The uncertainty of this calibration is reported in the uncertainty budget paragraph.

LOFD uniformity

An estimation for the uniformity of response of the reference detector was performed with a horizontal and a vertical scan around the photodiode geometrical middle.

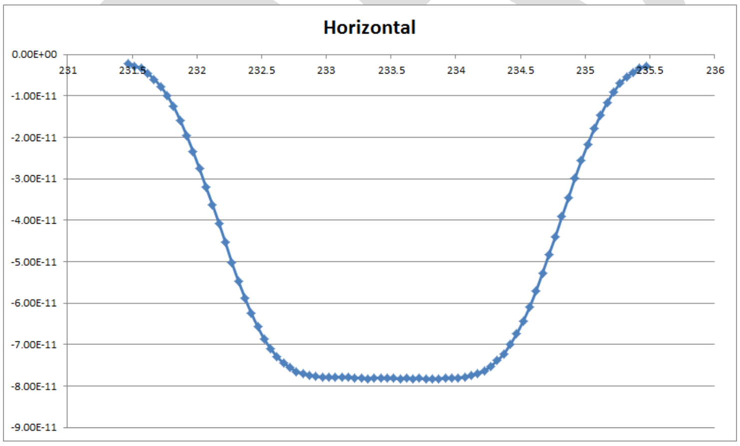

Figure 4 LOFD uniformity of the response in the horizontal direction (X)

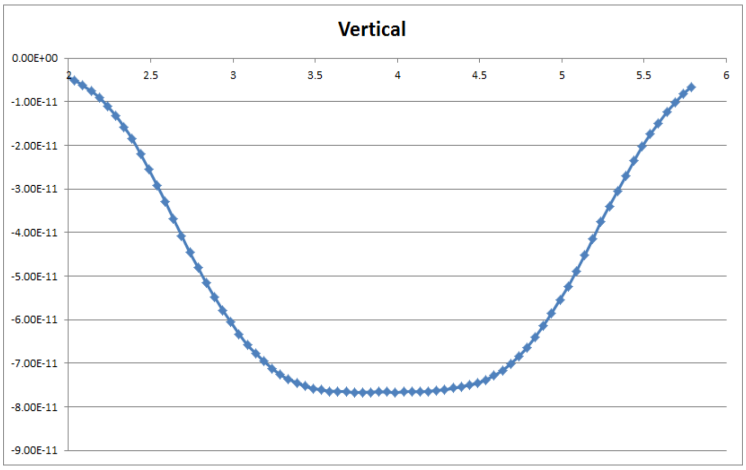

Figure 5 LOFD uniformity of the response in the vertical direction (Y)

The LOFD non uniformity relative uncertainty contribution around the middle considering an absolute position uncertainty of 0.1 mm is calculated to be 0.5%

Measurement model

The measurement model of the SPCM Q.E. calculated at 850 nm is given by the equation:

$$Q.E.(850) = \frac{Counts_{SPCM}}{N_{ph/s} F_i}$$

Where F_i is the spectral mismatch factor, $Counts_{SPCM}$ is the counting rate output of the SPCM and $N_{ph/s}$ is the number of photons per second measured by the reference detector that is given by the equation:

$$N_{ph/s} = \frac{V_{out}}{r_{LOFD}(\lambda_{laser})} \frac{C_{int}}{e_{ph}(\lambda_{laser})}$$

Where V_{out} is the voltage output of the LOFD measured with a calibrated Digital Voltmeter (DVM), C_{int} is the LOFD integration capacitor, $e_{ph}(\lambda)$ is the energy of one photon at the laser wavelength λ_{laser} = 851.5 nm

Artefacts uniformity

As described earlier the comparison artefact is placed on X Y Z stages. In order to evaluate the uncertainty contribution due to the non-uniform sensitivity of the artefact a X Y scan has been performed on the artifact 1.

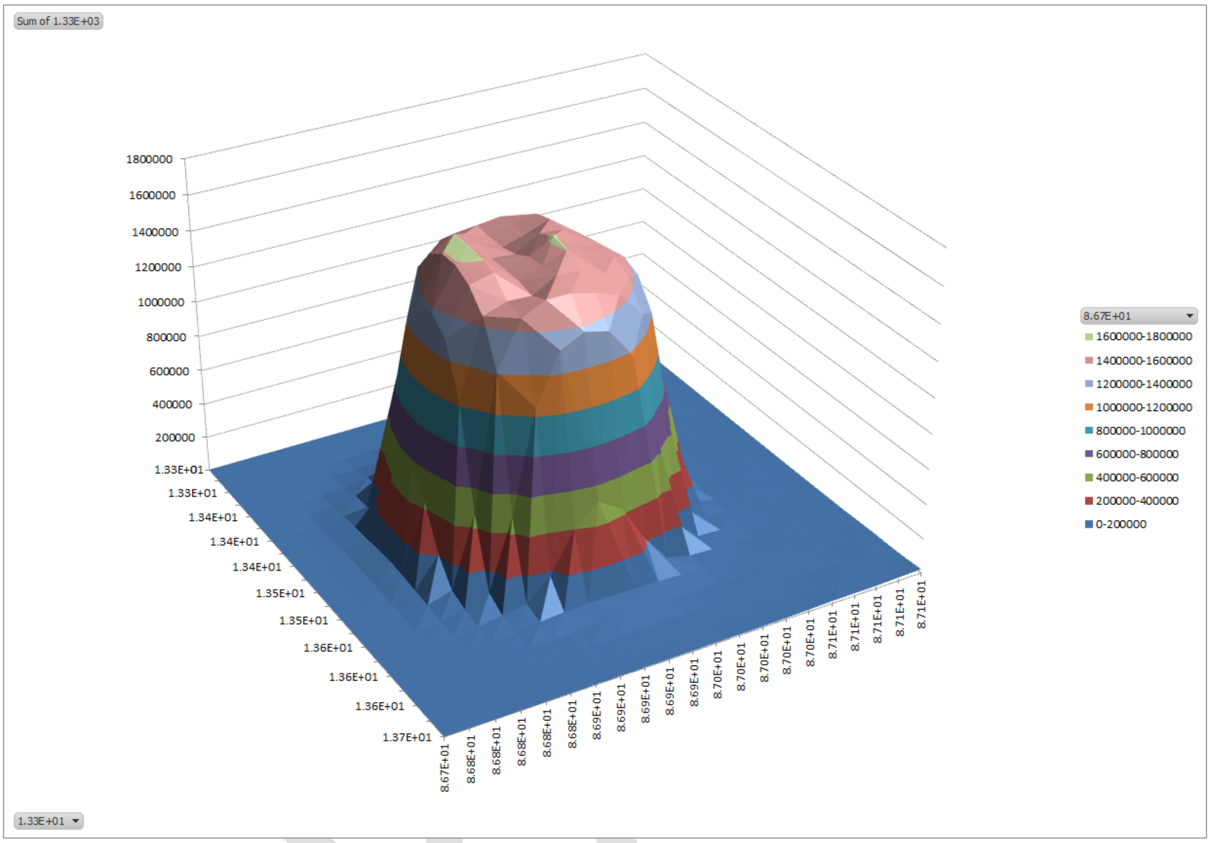

Figure 6 SPCM1 XY complete scan around the middle

The non uniformity of the artefact as shown later is one of the main contribution of the total measurement uncertainty of Q.E. The middle position is calculated performing a X Y scans that include both edges and evalutaing the center of mass of the signals using the equations :

$$P_X = \frac{\sum S_{x,i} P_{x,i}}{\sum S_{x,i}}$$

$$P_Y = \frac{\sum S_{y,i} P_{y,i}}{\sum S_{y,i}}$$

Where $S_{x(y),i}$ are the ith signal values measured and $P_{x(y),i}$ is the correspondant X (Y) position. The center is indicated in the graph by a cross. The detector was placed in the focal plane.

SPCM1 non uniformity uncertainty contribution

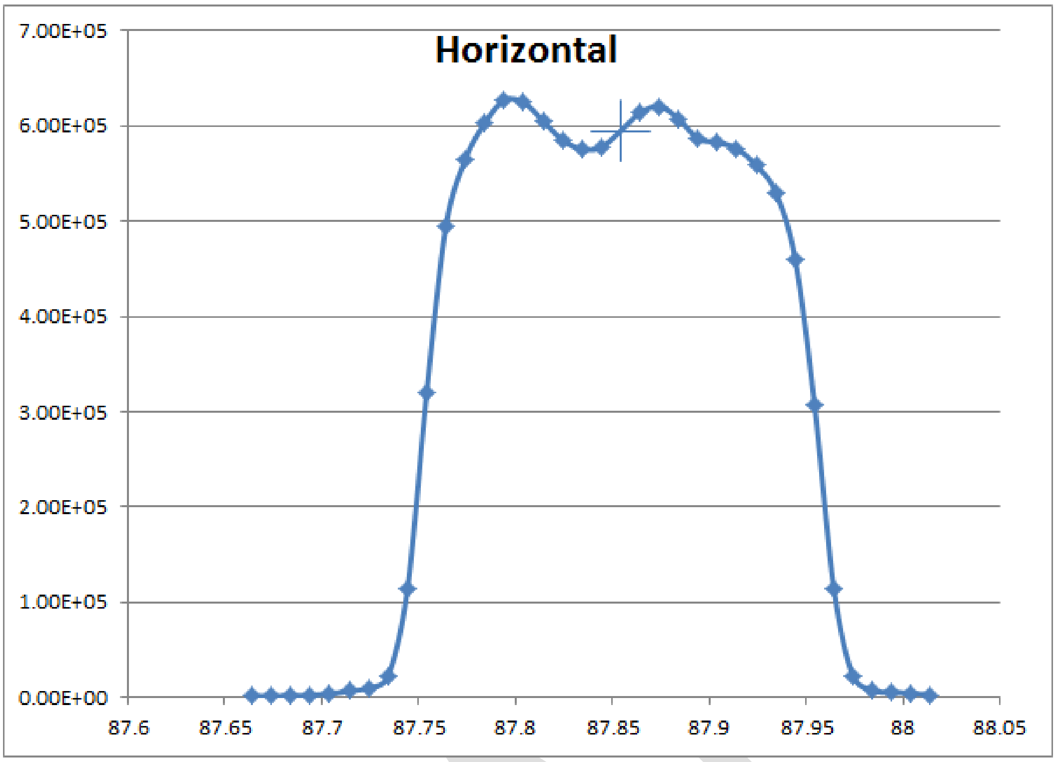

Figure 7 SPCM 1 Horizontal scan around the middle

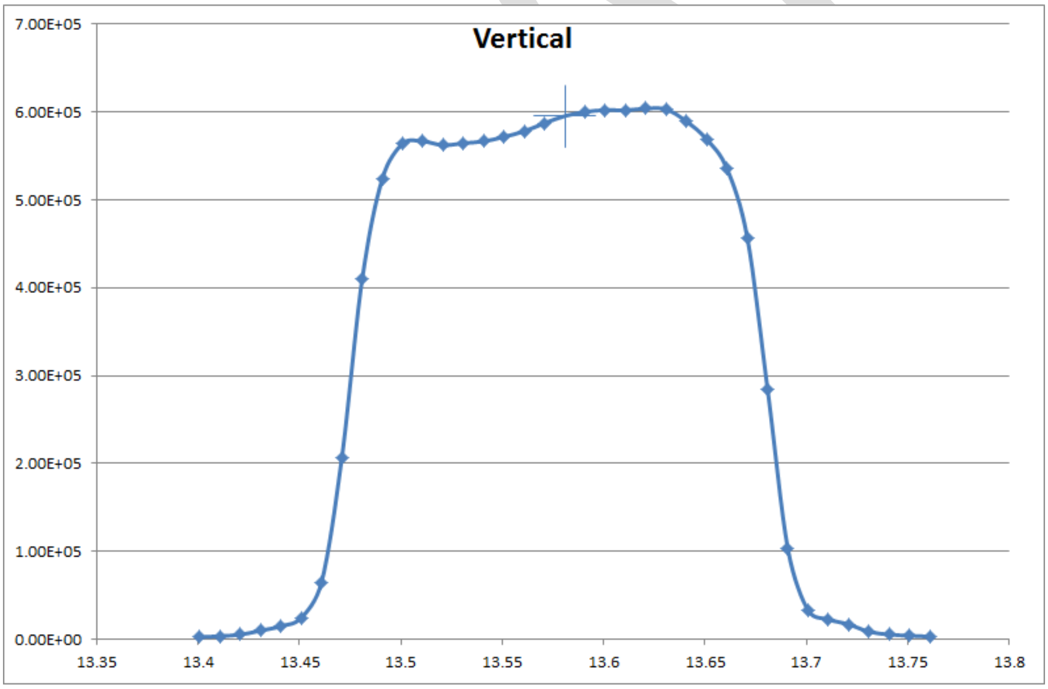

Figure 8 SPCM1 vertical scan around the middle

The SPCM1 non uniformity relative uncertainty contribution around the middle considering an absolute position uncertainty of 0.05 mm is calculated to be 3.2%

SPCM2 non uniformity uncertainty contribution

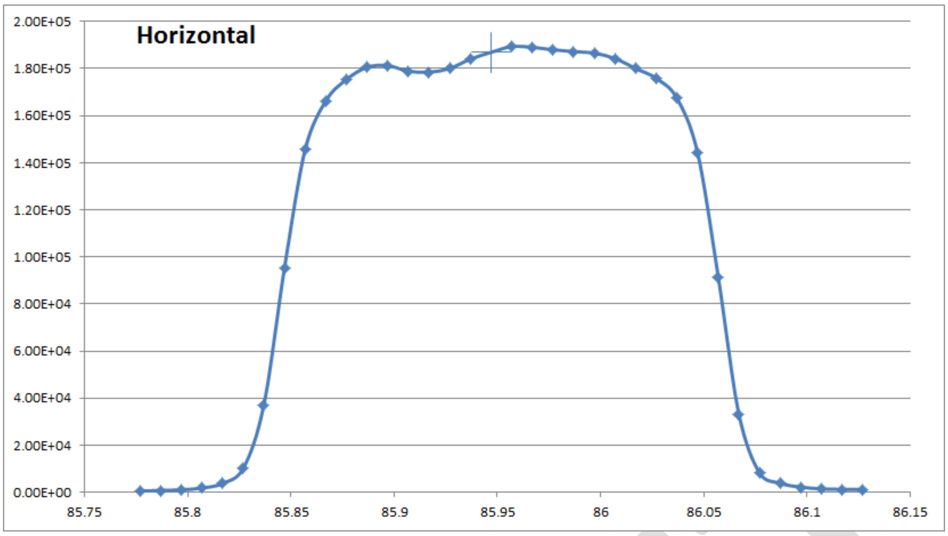

Figure 9 SPCM2 horizontal scan around the middle

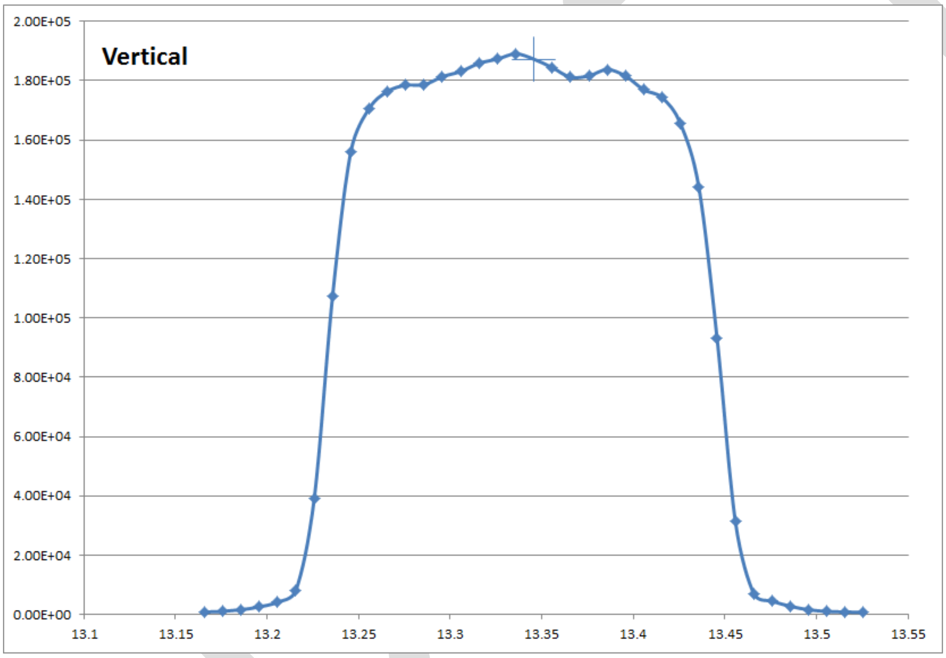

Figure 10 SPCM2 vertical scan around the middle

The SPCM1 non uniformity relative uncertainty contribution around the middle considering an absolute position uncertainty of 0.05 mm is calculated to be 2.1%

Artefact relative spectral dependence

To measure the relative spectral dependence of the artefact Q.E. an halogen lamp is reimaged at the entrance slit of a double monochromator. The spatially spectrally dispersed radiation is selected by the monochromator output slit and coupled to a SM fibre. The output of the fibre illuminates sequentially the detectors. Using the substitution method and knowing the LOFD spectral responsivity is possible to measure the relative Q.E. of the DUT on the range of interest 800nm to 875 nm.

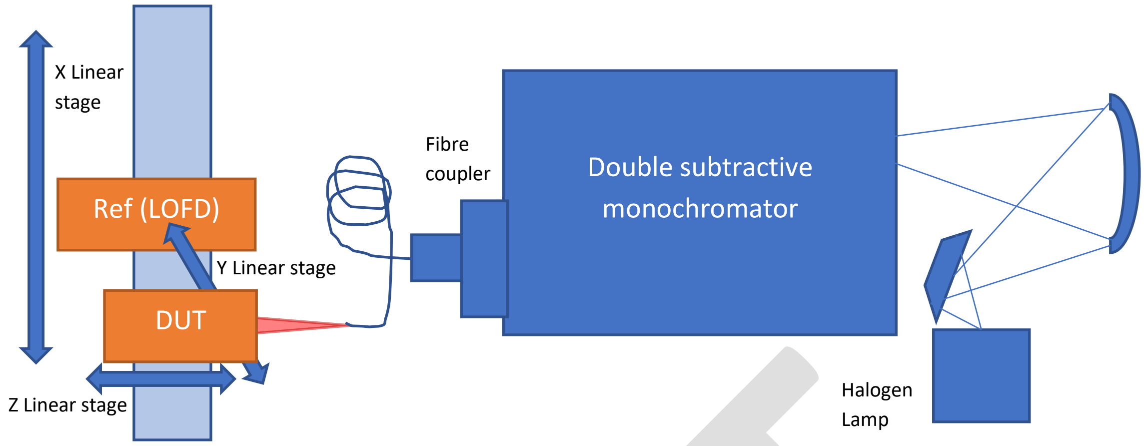

Figure 11 Optical setup for measurement of relative specrtral dependence of DUT's Q.E.

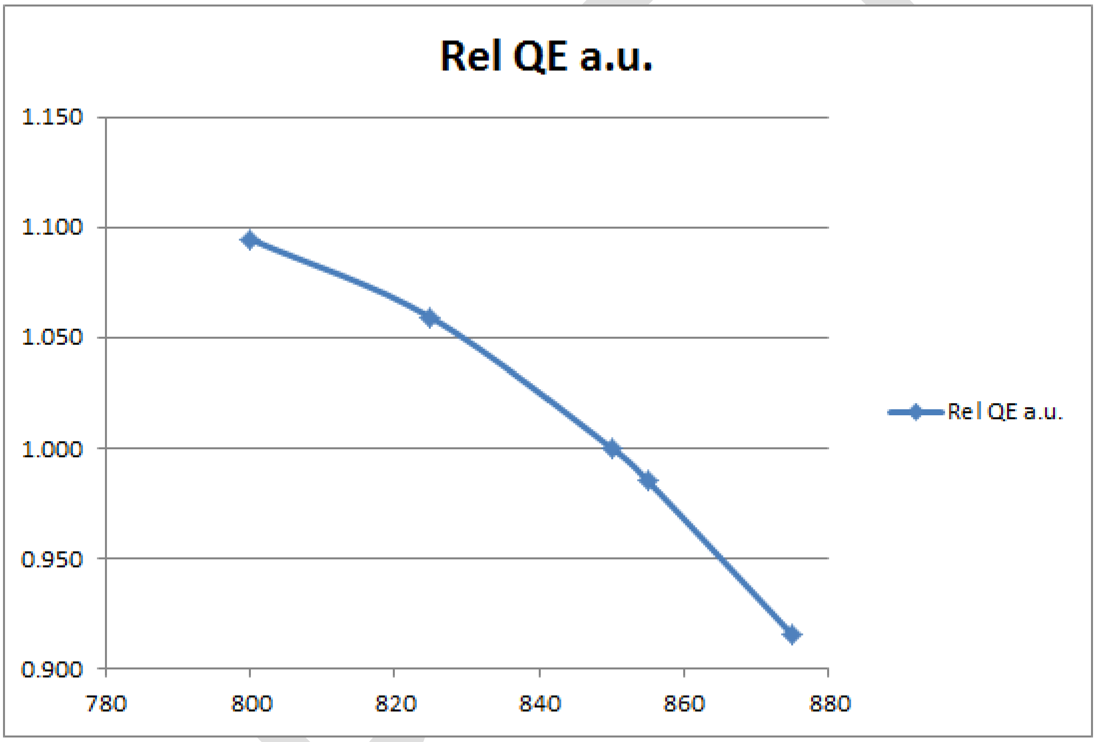

Figure 12 Relative spectral SPCM1 Q.E. normalized at 850nm

Laboratory conditions

The measurements were performed with a laboratory temperature of 23.5 +-0.5 °C and a relative humidity between 35% and 45%

Uncertainty Budget

In the following table the uncertainty budget for SPCM1 is reported. For more details see (Porrovecchio, et al., 2016)

Measurand	Unit	Description	Value	Standard unc	Distribution	Sensitivity coeff	Contribution
R_{std}	Ohms	Standard resistor	1.0000E+08	1.00E+04	Standard	1.0456E-20	1.0456E-16
T_{int}	s	LOFD integration time	2.00E-02	2.00E-07	Standard	5.2283E-11	1.0457E-17
V_{out}	V	LOFD output voltage	1.24	2.48E-05	Standard	8.4327E-13	2.0913E-17
Vs	V	Calibrator voltage output	6.48E-03	5.19E-07	Standard	1.6128E-10	8.3653E-17
G	V/A	Linear fit	1.91E+10	6.36E+06	Standard	5.4670E-23	3.4747E-16
C_{int}	F	LOFD integration capacitor	1.046E-12			**Combined unc**	3.73E-16

Measurand	Unit	Description	Value	Standard unc	Distribution	Sensitivity coeff	Contribution
h	Js	Planck constant	6.62621E-34	1.67E-42	Rectangular	3.521E+14	3.39E-28
c	m/s	speed of light	2.99792E+08	0			
λ	m	Wavelength	8.52E-07	5.77E-11	Rectangular	2.740E-13	9.13E-24
e_{ph}	J	Energy of photon at 851 nm	2.333E-19			**Combined unc**	9.13E-24

Measurand	Unit	Description	Value	Standard unc	Distribution	Sensitivity coeff	Contribution
V_{out}	V	LOFD output voltage	8.764E-03	1.578E-04	Standard	1.684E+07	2.657E+03
C_{int}	F	LOFD integration capacitor	1.045E-12	3.731E-16	Standard	1.412E+17	5.270E+01
r_{LOFD}	A/W	LOFD photodiode responsivity	2.660E-01	5.320E-04	Standard	5.549E+05	2.952E+02
e_{ph}	J	Energy of photon at 851.54 nm	2.333E-19	9.126E-24	Standard	6.327E+23	5.774E+00
LOFD photodiode non uniformity		photodiode resp. variation around the middle	2.629E-05	2.629E-05	Rectangular	1.684E+07	2.556E+02
LOFD Non linearity	V	Maximum residual from linear fit	2.500E-04	2.500E-04	Rectangular	1.684E+07	2.431E+03
$N_{ph/s}$	ph/s	Number of photons per second	1.48E+05			**Combined unc**	3.62.E+03

Measurand	Unit	Description	Value	Standard unc	Distribution	Sensitivity coeff	Contribution
	c/s	Laser stability		2.50E+02	Standard	3.56E-06	8.90E-04
		SPCM uniformity		4.00E+03	Rectangular	6.76E-06	1.56E-02
F_i		Spectral mismatch	0.9981	6.25E+02	Rectangular	6.76E-06	2.44E-03
$Counts_{SPCM}$	c/s	SPCM counts	6.59E+04	80	Standard	8.00E-06	6.40E-04
$N_{ph/s}$	ph/s	Number of photons per second	1.25E+05	3.62.E+03	Standard	4.22E-06	1.53E-02
Q.E.			**0.5182**			**Combined unc**	0.022

Table 1 Uncertainty budget Q.E. SPCM1

For SPCM2 the contribution due to its non-uniformity is smaller and the final absolute combined uncertainty of Q.E. is 0.018 (k = 1).

Dead time model

The Q.E. values of the artefacts have been measured using photon flux values that range from 10^5 to 10^7 Photons/s. In this way is possible to fit the dead time model of the detector to the measurement data (Lopez, Hofer, & Kueck, 2015) and verify that the measurement at lowest photon flux is inside the SPCM Q.E. expected plateau region. In the figure below the error bars represent the standard deviation of the measurement.

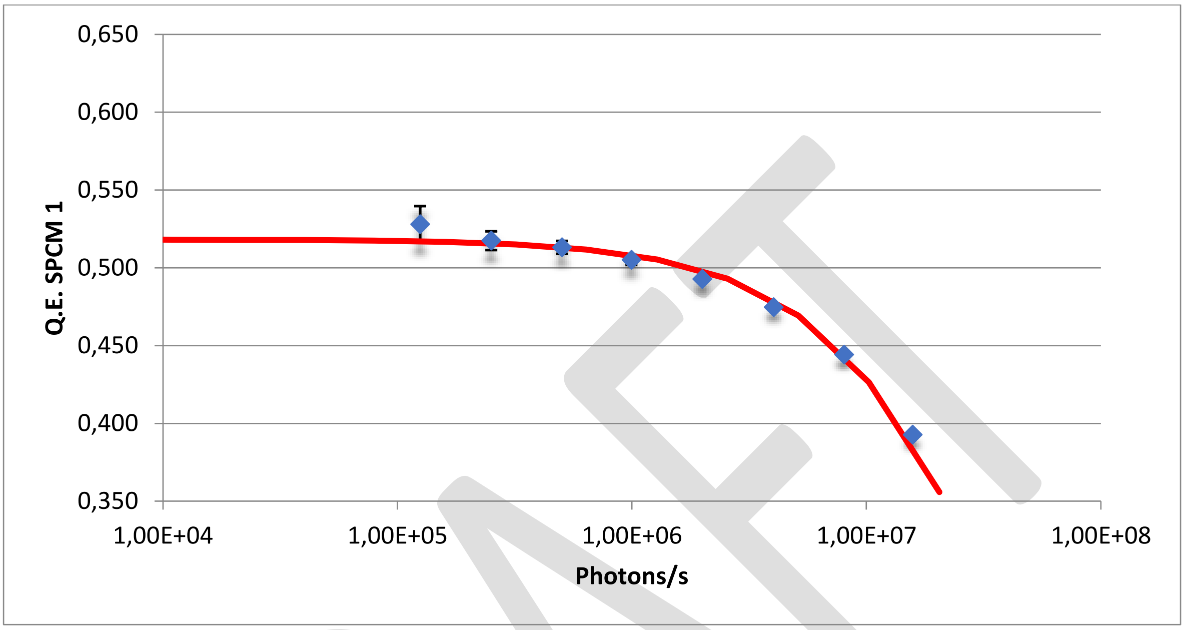

Figure 13 SPCM1 Q.E. calibration data and dead time model

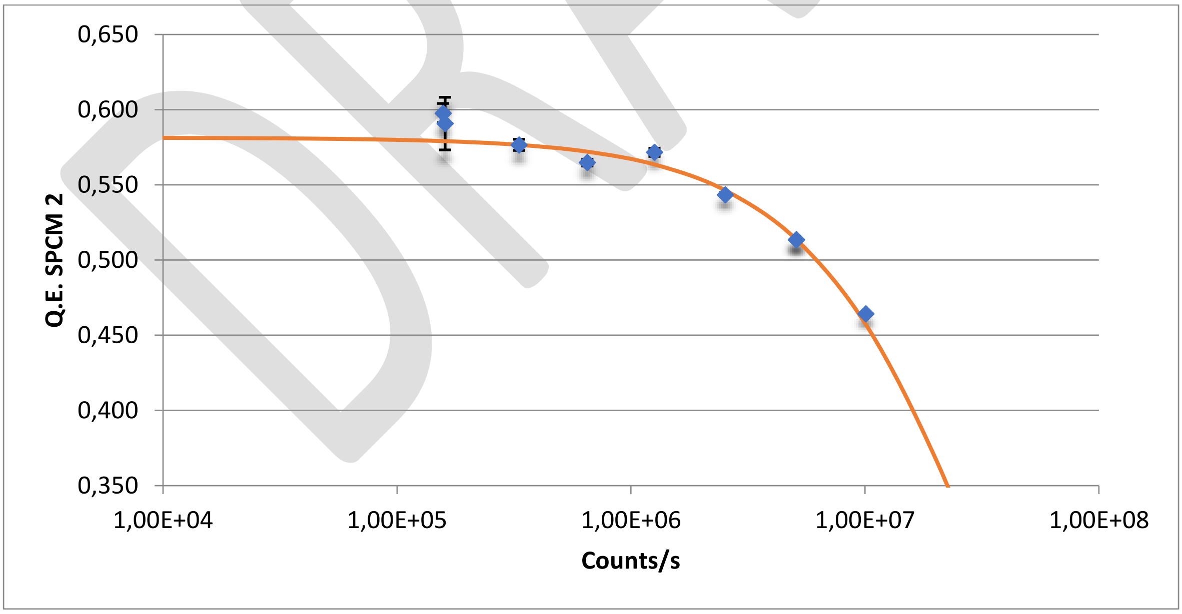

Figure 14 SPCM2 Q.E. calibration data and dead time model

Results

SPCM1 (SN 18752) Q.E. **0.5182** ± 0.022 (k = 1)
SPCM2 (SN 19743) Q.E. **0.5814** ± 0.018 (k = 1)

Works Cited

Lopez, M., Hofer, H., & Kueck, S. (2015). Detection efficiency calibration of single-photon silicon avalanche photodiodes traceable using. *Journal of Modern Optics, 62*, 21-27.

Porrovecchio, G., Smid, M., Lopez, M., Rodiek, B., Koeck, S., & Hofer, H. (2016). Comparison at the sub-100 fW optical power level of calibrating a single-photon detector using a high-sensitive, low-noise silicon photodiode and the double attenuator technique. *Metrologia*(53), 1115-1122.

CCPR WG-SP TG 11

Pilot study on the detection efficiency of single-photon detectors – Si-SPAD

NPL measurements: 16-19 September 2017

Table of Contents

1. Measurement facility 3
 1.1 Method 3
 1.2 Determination of detection efficiency 5
 1.3 Degrees of freedom 6
 1.4 Experimental layout 7
2. Make and type of primary standard 10
3. Laboratory transfer standard used 11
4. Traceability to primary scale 11
5. Measurement dates 11
6. Environmental conditions 11
7. Spectrum of light 12
8. Scattered light 13
9. Extreme spatial non-uniformity of detector response in plateau region 13
10. Beam diameter at detector 13
11. Measurement of DUT1 (PTB43) 14
 11.1 Spatial dependency of count rate 14

11.2 Dead-time ... 14
11.3 Calibration of $\alpha = I^{3ET}/I^{10ET}$ ... 15
11.4 Incident photon flux ... 17
11.5 Detection efficiency ... 18
12. Measurement of DUT2 (PTB52) ... 20
12.1 Spatial dependency of count rate ... 20
12.2 Dead-time ... 20
12.3 Calibration of $\alpha = I^{3ET}/I^{10ET}$ ... 21
12.4 Incident photon flux ... 23
12.5 Detection efficiency ... 24
13. Summary ... 26
References ... 26
Appendix 1. Calibrations ... 27
A1.1 ... 27
A1.2 ... 28
A1.3 ... 28
Appendix 2. 3ET reference detector ... 29
Appendix 3. Derivation of equation (11). ... 30

1. Measurement facility

1.1 Method

The NPL method for detection efficiency measurement utilises a ten-element silicon photodiode transmittance trap [1] (10ET) which provides both a fixed attenuation and a measure of the optical power incident at its entrance. The power transmitted by the 10ET is measured by a three-element silicon photodiode trap detector (3ET) that carries the SI reference.

The transmittance and the responsivity of the 10ET is assumed to be independent of the incident optical power (< 0.1 mW), once the alignment and polarisation of the beam through the 10ET remains constant. The voltage signal due to the power incident on each trap detector is obtained by amplifying the summed photocurrents from the component photodiodes with a current-to-voltage amplifier.

At relatively high incident power on the 10ET (< 0.1 mW) the power transmitted by the 10ET is measured absolutely by the 3ET. The voltage signal from the 10ET is also recorded. This enables the photocurrent ratios of the traps to be measured. Note that the measurements by the 10ET are not absolute – the 10ET is used as a linear, not an absolute, attenuator.

The power incident on the 10ET can then be reduced, and the previously-measured photocurrent ratio can be used to infer the optical power / photon flux incident at the 3ET. The device under test (DUT) can then be positioned where the 3ET was located, and its detection efficiency measured.

P_{IN10} = power incident on 10ET (W)

P_{IN3} = power incident on 3ET (W)

I_{10ET} = photo-induced current in 10ET generated by P_{IN10} (A)

I_{3ET} = photo-induced current in 3ET generated by P_{IN10} (A)

R_{10ET} = responsivity of 10ET (A W^{-1}, uncalibrated, assumed constant for all input powers < 0.1 mW)

R_{3ET} = responsivity of 3ET (A W^{-1}, calibrated, assumed constant for all input powers < 0.1 mW)

V_{10ET} = voltage output of 10ET amplifier (V, measured with a calibrated digital multimeter)

V_{3ET} = voltage output of 3ET amplifier (V, measured with a calibrated digital multimeter)

G_{10ET} = current-to-voltage gain of the 10ET amplifier (V A^{-1}, calibrated over the range of gain settings used)

G_{3ET} = current-to-voltage gain of 3ET amplifier (V A^{-1}, calibrated over range of gain settings used)

N_{IN3} = calculated incident photon flux at 3ET (s^{-1})

N_{IN} = calculated photon flux at DUT (s^{-1}; calculated as for N_{IN3})

N_{DUT} = recorded counts from DUT (s^{-1}, dark-corrected)

τ_d = dead-time of DUT (s)

μ_d = mean incident number of photons within a DUT dead-time interval

h = Planck's constant (J s)

c = speed of light (m s^{-1})

λ = mean wavelength of the incident photons (m)

The measured incident powers, P^{10ET}, P^{3ET} to the 10ET and 3ET are given by:

$$P_{IN10} = \frac{I_{10ET}}{R_{10ET}} = \frac{V_{10ET}}{R_{10ET}\,G_{10ET}} \tag{1}$$

$$P_{IN3} = \frac{I_{3ET}}{R_{3ET}} = \frac{V_{3ET}}{R_{3ET}\,G_{3ET}} \tag{2}$$

where

$$V_{3ET} = I_{3ET}\,G_{3ET} \tag{3}$$

$$V_{10ET} = I_{10ET}\,G_{10ET} \tag{4}$$

The transmittance t_{10ET} of the 10ET is assumed to be constant for all values of P_{IN10} < 0.1 mW.

The combined transmittance t_{OPTICS} of any optical elements between the 10ET and 3ET is also assumed to be constant.

Hence the ratio

$$r = \frac{P_{IN3}}{P_{IN10}} = \frac{I_{3ET}R_{10ET}}{I_{10ET}R_{3ET}} = t_{10ET}t_{OPTICS} \tag{5}$$

is therefore a constant.

Since R_{10ET} and R_{3ET} are also assumed constant, then

$$\alpha = \frac{I_{3ET}}{I_{10ET}} = r\frac{R_{3ET}}{R_{10ET}} \tag{6}$$

is also a constant.

α is measured at relatively high P_{IN10} (< 0.1 mW), from measurements of V_{3ET} and V_{10ET}. This value of α is then used to calculate the value of I_{3ET}, and hence P_{IN3}, corresponding to any other value of I_{10ET}

$$P_{IN3} = \frac{\alpha\ V_{10ET}\ \xi}{R_{3ET}\ G_{10ET}} \tag{7}$$

where the term ξ covers any geometrical instability in the measurement set-up.

The corresponding incident photon flux is given by

$$N_{IN3} = \frac{\alpha\ \ V_{10ET}\ \xi\ \lambda}{R_{3ET}\ G_{10ET}\ h\ c} \tag{8}$$

The input power to the 10ET can therefore be reduced until the calculated photon flux at the 3ET is at the level which can be measured with the DUTs.

1.2 Determination of detection efficiency

Equations (3) and (4) give the following expressions that are required to measure α:

$$I_{3ET} = \frac{V_{3ET}}{G_{3ET}} \tag{9}$$

$$I_{10ET} = \frac{V_{10ET}}{G_{10ET}} \tag{10}$$

The quantities that need to be measured are V_{3ET} and V_{10ET}; firstly to obtain the current ratio α between the 3ET and 10ET [equations (9,10)]; subsequently V_{10ET} is measured to derive the photon flux at the 3ET/DUT as the input power to the 10ET is reduced [equation (8)]. Calibrated values of R_{3ET}, G_{3ET}, G_{10ET} and λ are also required.

The detection efficiency is calculated using equation (11) which takes account of the dead-time of the DUTs (See Appendix 3 for derivation).

$$\eta = -\frac{1}{N_{IN}\tau_d}\ln(1 - N_{DUT}\tau_d) \tag{11}$$

Each measurement comprised measurements with the shutter open (light) and closed (dark), and hence $V_{10ET} = V_{light10} – V_{dark10}$, $V_{3ET} = V_{light3} – V_{dark3}$, $N_{DUT} = N_{lightDUT} - N_{darkDUT}$.

1.3 Degrees of freedom

In all numerical calculations involving degrees of freedom, a value of $\nu = 1000$ was used as an approximation to $\nu = \infty$.

1.4 Experimental layout

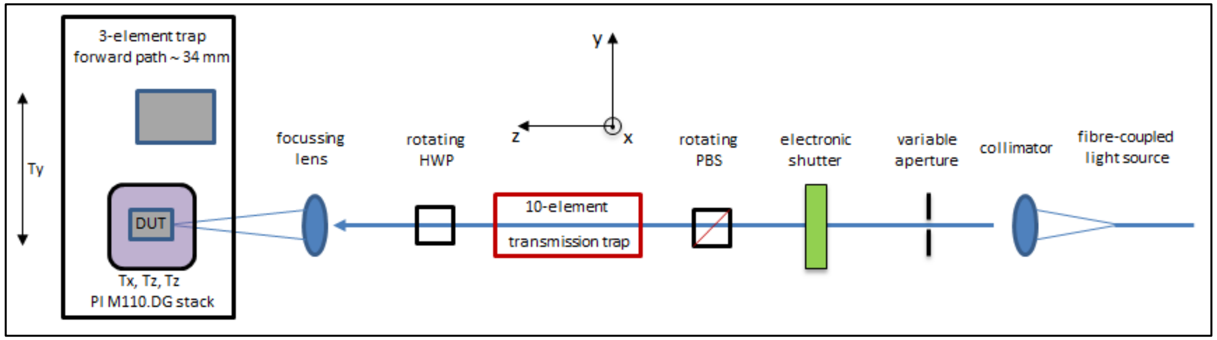

Figure 1. Facility lay-out

A fibre-pigtailed diode laser (Thorlabs LP852-SF30) provided the source of light, which was fibre-coupled into an adjustable in-fibre attenuator. The output from the attenuator is collimated into free-space. These components are enclosed in a light-tight box to limit stray light from the fibre reaching the detectors. A variable aperture is used to limit stray light from this box.

An electronic shutter is used to block the beam path immediately after it exits the light-tight enclosure. A polarising beam splitter (PBS) is used to control the polarisation state of photons incident at the entrance of the 10ET. This was set either vertical or horizontal in the laboratory frame of reference. The input/output polarisation axis of the 10ET was fixed to be vertical with respect to the laboratory frame of reference. An additional half-wave plate (HWP) is placed between the 10ET and the focussing lens to adjust the polarisation of photons incident on the DUT/3ET.

The focussing lens was used to focus light onto the DUT/3ET. A CCD beam profiler was placed at the beam waist to measure the spot size.

A mechanical translation stage is used to bring the DUT, 3ET, and beam profiler (not shown) into the beam focus.

Each DUTs was mounted in turn on an xyz stage comprising 3 PI M110.DG stages, as well as a manual 5-axis tilt/translation stage, enabling them to be centred on the beam and positioned at its focus. The base of the DUT was parallel to the vertical plane.

A light-tight enclosure encloses the entire facility to minimise the background count rate on the detectors. Electrical feed-throughs were used to convey electrical signals from inside the enclosure to the control and measurement electronics.

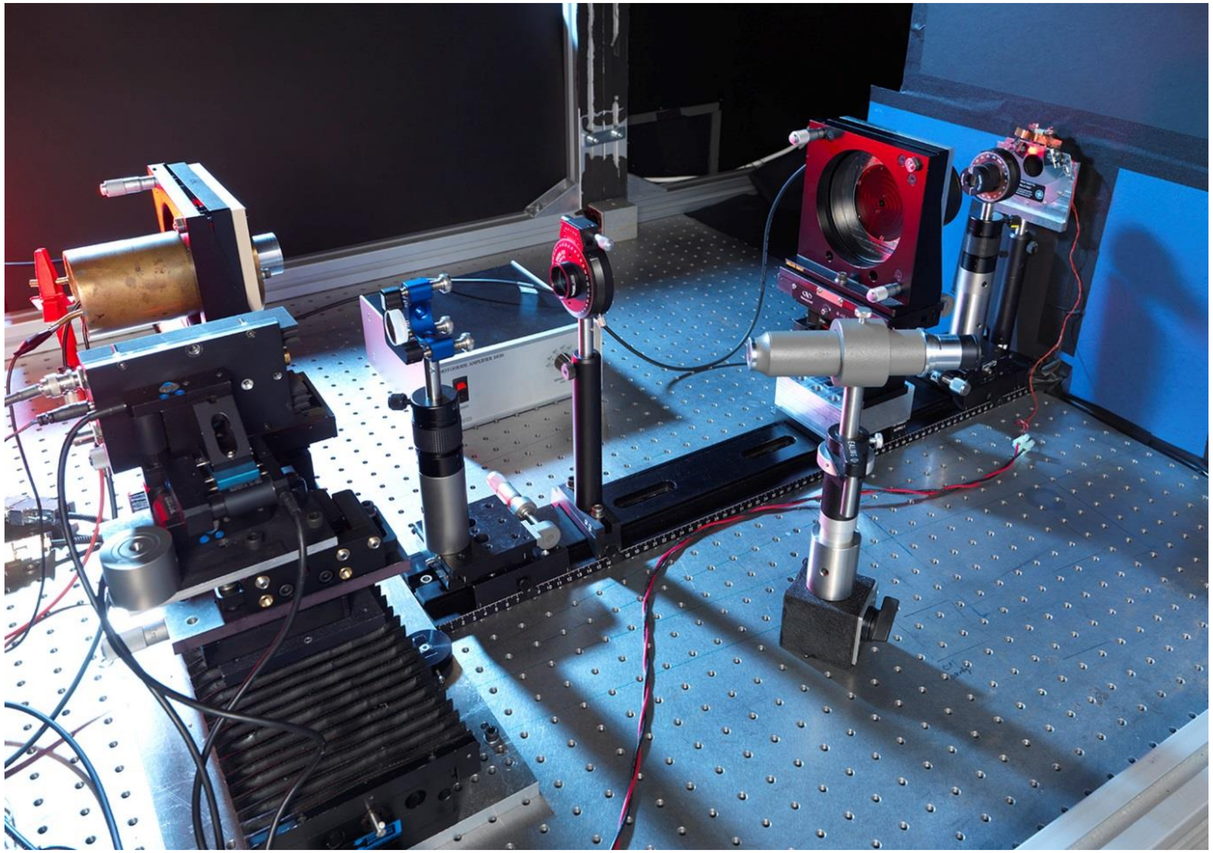

Figure 2. Measurement facility. The 3ET is in a brass water jacket at left background (no water-cooling of the3ET was used for these measurements). An NPL Perkin-Elmer SPCM is at the left centre; both are mounted on the same computer-controlled translation stage. The 3ET is additionally mounted on a manual elevating stage and a manual kinematic mirror mount. The SPCM is additionally mounted on a computer-controlled 3-axis xyz stage comprising PI M110.DG translation stages as well as a manual 5-axis tilt/translation stage. The 10ET (behind the travelling microscope) is mounted on manual translation stages and a manual kinematic mirror mount, as well as on an optical rail for translation along the optical path. On the right it can be seen that all optical elements before the shutter are enclosed in an additional light tight enclosure. The travelling microscope (right centre) is used to initially locate the centre of the DUT active area and the 3ET aperture at the approximate focus of visible wavelength (633 nm) radiation. The MSL amplifier can be seen behind the optical rail.

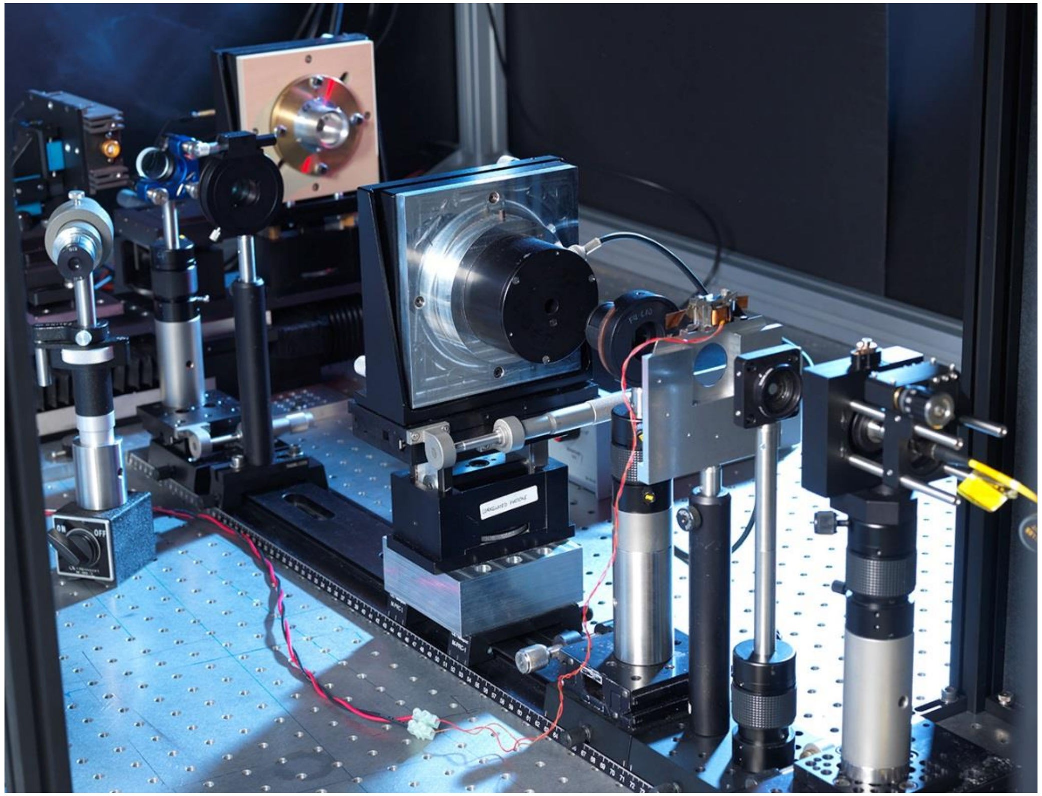

Figure 3. Measurement facility with additional light tight enclosure containing the optical fibre, fibre collimator, and aperture (front right) removed.

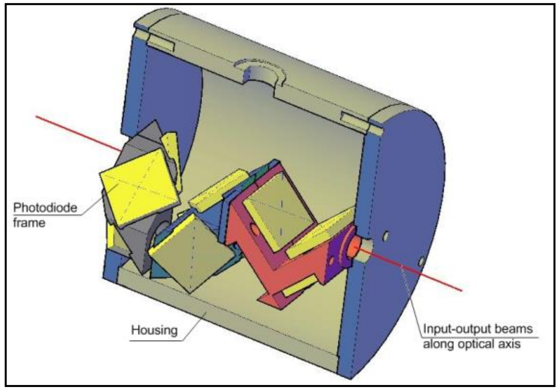

Figure 4. Diagram of 10-element trap. Note that beam propagation is from left to right in this diagram.

The 10ET and 3ET comprise windowless silicon photodiodes (Hamamatsu S1337). The 3ET signal was amplified and converted into a voltage using a CMI switched-integrator amplifier, and the 10ET signal was amplified and converted into a voltage using an MSL trans-impedance amplifier. The output voltage signals from the amplifiers were read by Keithley 2000 Digital Multimeters (DMMs). Light and dark measurements corrected for any offset in the DMM readings. The fractional error in the DMM measurements, ignoring offset errors, was less than 100 ppm. This level of uncertainty is insignificant in comparison to other sources of uncertainty, and is therefore ignored.

The devices under test (DUTs) were Si-SPADs with active areas approximately 180 μm in diameter. The DUTs produce a TTL pulse for each detector event – true count, dark count or after-pulse. The pulses from the DUT were read with an Agilent 53131A digital counter, with no uncertainty in counted pulses.

c (the speed of light) is a constant, and the uncertainty in h (Planck's constant) is negligible, and hence ignored.

2. Make and type of primary standard

The NPL primary scale cryogenic radiometer

3. Laboratory transfer standard used

A three-element silicon photodiode trap detector (3ET), s/n NPL11033T, comprising windowless Hamamatsu 1337 silicon photodiodes.

4. Traceability to primary scale

Two NPL working standard three-element trap detectors, comprising windowless Hamamatsu 1337 silicon photodiodes, were calibrated against the primary cryogenic radiometer using laser lines from a Kr^+-ion laser in the 350 nm – 800 nm spectral region. The laser light was $\sim$0.1 mW in intensity, polarised, and at normal incidence.

A model was used to fit a functional relationship between responsivity and wavelength over the 350 nm – 920 nm region for each working standard.

The laboratory transfer standard, s/n NPL11033T, was then calibrated against the two working standards using a grating spectrometer. The incident light was $\sim$ 0.5 μW in intensity, partially-polarised, and at normal incidence.

5. Measurement dates

16 September 2017 – 19 September 2017

6. Environmental conditions

Laboratory temperature: 22.5 °C $\pm$ 0.5 °C

Laboratory humidity: 35% - 45%

7. Spectrum of light

Measurements were performed with a Yokogawa AQ6370D spectrum analyser. Wavelength uncertainty = 0.1 nm (1 std. unc).

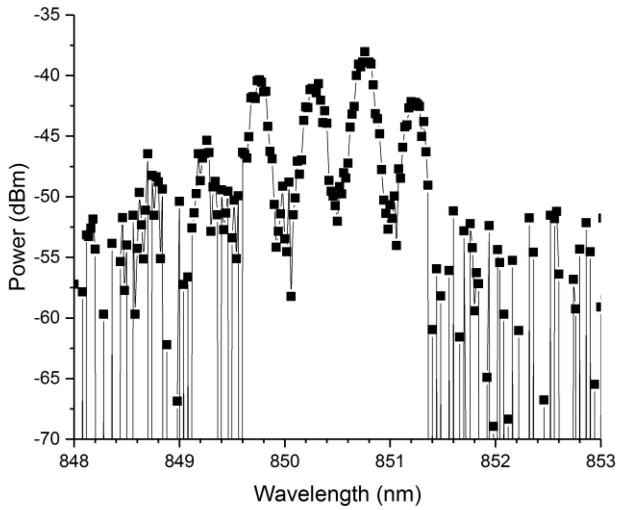

Figure 5. Optical spectrum of the diode laser source after the in-fibre attenuator recorded with a Yokogawa AQ6370D optical spectrum analyser.

Mean wavelength = 850.36 nm $\pm$ 0.12 nm (1 std. unc., ν=200)

Mean responsivity of 3ET at 850.357 nm = 0.6844 $\pm$ 0.00032 (1 std. unc., ν=1000) [See Appendix 2]

The change in responsivity of DUT with wavelength (inferred from EXCELITAS SPCM online datasheet downloaded 13 July 2018) is given by

$$\frac{\eta_{850}}{\eta_{850.3573}} = 1.0016 \pm 0.0005 \text{ (1 std. unc., } \nu\text{=4)}$$

Measurement data will result in a measured value for η at 850.357 $\pm$ 0.12 nm; this measured value has to be multiplied by the correction factor C1 = $\eta_{850}/\eta_{850.357}$ = 1.0016 $\pm$ 0.0005 (1 std. unc.) to obtain the value for η at 850 nm.

8. Scattered light

An estimate was made of the scattered light incident from the 10ET trap on the 3ET trap which lies outside the sensitive area of the DUT, and is therefore not incident on the DUT.

It was estimated that $C2 = P_{DUT}/P_{3ET} = 0.99 \pm 0.0035$ (1 std. unc.), where P_{DUT} is the total light incident on the DUT, and P_{3ET} is the total light incident on the 3ET.

The measured value of η has to be divided by the correction factor C2 to obtain the ‘true’ value for η.

9. Extreme spatial non-uniformity of detector response in plateau region

It was observed, see figure 10, that there appeared to be a high responsivity peak within the plateau of the responsivity region for PTB52.

Therefore a correction factor C3 was introduced to account for the additional effect this has on the measurement of η, as a consequence of instability in the positioning of the probe beam on the DUT.

It was estimated that $C3_{PTB52} = 1.00 \pm 0.0108$ (1 std. unc.). The range of the measured values of η for PTB52 was taken to define a rectangular distribution, leading to the std. unc. being evaluated as $0.0373/\sqrt{12}$.

For uniformity of calculations, a value for $C3_{PTB43}$ was assigned for PTB43. This was set to be $C3_{PTB43} = 1.00 \pm 0.0$ (1 std. unc.).

10. Beam diameter at detector

The full-width at half-height was estimated to be 18 μm, while the full width at the $1/e^2$ intensity level was estimated to be 59 μm. No corrections have been made to account for the beam profile.

11. Measurement of DUT1 (PTB43)

11.1 Spatial dependency of count rate

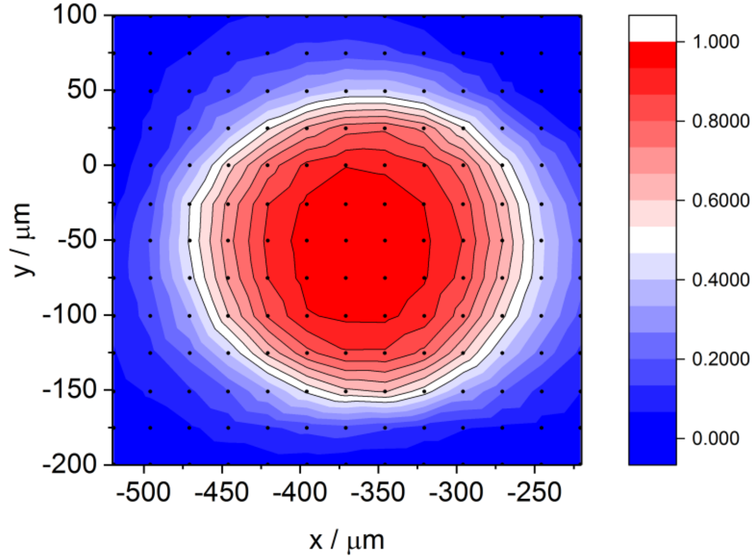

Figure 6. Spatial dependency of count rate for DUT1. Data normalised.

11.2 Dead-time

The dead-time of the detector was measured by using time-tagging to measure the intervals between counts from the non-illuminated detector. This was found to be 28.6 ns $\pm$ 0.1 ns. The time/counter was uncalibrated, and therefore an overall conservative uncertainty of 0.5 ns was ascribed to the measurements.

11.3 Calibration of $\alpha = I^{3ET}/I^{10ET}$

Equation (6) is expanded thus

$$\alpha = \frac{I_{3ET}}{I_{10ET}} = \frac{V_{3ET}}{V_{10ET}}\frac{G_{10ET}}{G_{3ET}} \tag{12}$$

Table 1 presents the measured voltages and amplifier gains from the 3ET and 10ET traps for a range of input light powers to the 10ET.

3ET mean V	Std. Unc	ν	10ET mean V	Std. Unc	ν	G (SIA)	Std. Unc.	ν	G (MSL)	Std. Unc.	ν	i(3et)	i(10ET)	α	Std. Unc.	ν(eff)
9.763E-03	1.588E-05	48	7.384E-01	3.359E-04	26	1.001E+09	1.007E+06	1000	9.996E+05	2.358E+01	1000	9.754E-12	7.387E-07	1.320E-05	2.60E-08	100
5.220E-02	2.634E-05	28	3.939E+00	5.699E-05	26	1.001E+09	1.007E+06	1000	9.996E+05	2.358E+01	1000	5.215E-11	3.941E-06	1.323E-05	1.49E-08	487
1.349E-01	4.596E-05	18	1.017E+01	2.930E-04	17	1.001E+09	1.007E+06	1000	9.996E+05	2.358E+01	1000	1.348E-10	1.018E-05	1.324E-05	1.41E-08	725
1.349E-01	2.450E-05	38	1.017E+00	2.566E-05	29	1.001E+09	1.007E+06	1000	9.997E+04	4.518E-01	1000	1.348E-10	1.018E-05	1.324E-05	1.35E-08	1039
4.657E-01	2.757E-05	23	3.513E+00	8.586E-06	21	1.001E+09	1.007E+06	1000	9.997E+04	4.518E-01	1000	4.652E-10	3.514E-05	1.324E-05	1.33E-08	1006
1.395E+00	1.713E-03	14	1.056E+01	4.489E-03	14	1.001E+09	1.007E+06	1000	9.997E+04	4.518E-01	1000	1.394E-09	1.056E-04	1.320E-05	2.17E-08	44
1.399E+00	9.914E-04	16	1.056E+00	3.541E-04	16	1.001E+09	1.007E+06	1000	9.999E+03	5.422E-02	1000	1.398E-09	1.056E-04	1.323E-05	1.69E-08	151
3.706E+00	3.275E-03	15	2.805E+00	9.637E-04	15	1.001E+09	1.007E+06	1000	9.999E+03	5.422E-02	1000	3.702E-09	2.805E-04	1.320E-05	1.82E-08	86
1.437E+00	1.376E-04	28	1.084E+01	5.833E-05	25	1.001E+10	3.103E+07	1000	9.996E+05	2.358E+01	1000	1.436E-10	1.084E-05	1.324E-05	4.11E-08	1002
2.648E-01	1.985E-04	24	2.003E+00	3.431E-05	23	1.001E+10	3.103E+07	1000	9.996E+05	2.358E+01	1000	2.646E-11	2.004E-06	1.320E-05	4.21E-08	983
5.284E-02	4.832E-05	112	3.988E-01	3.654E-06	71	1.001E+10	3.103E+07	1000	9.996E+05	2.358E+01	1000	5.280E-12	3.990E-07	1.323E-05	4.28E-08	1107
1.268E-02	4.847E-05	93	9.571E-02	1.207E-06	121	1.001E+10	3.103E+07	1000	9.996E+05	2.358E+01	1000	1.267E-12	9.575E-08	1.323E-05	6.51E-08	245
1.573E-01	4.319E-05	192	1.190E+00	1.098E-05	76	1.001E+10	3.103E+07	1000	9.996E+05	2.358E+01	1000	1.572E-11	1.191E-06	1.321E-05	4.11E-08	1016

Table 1. Measured values and uncertainty budget for estimating α.

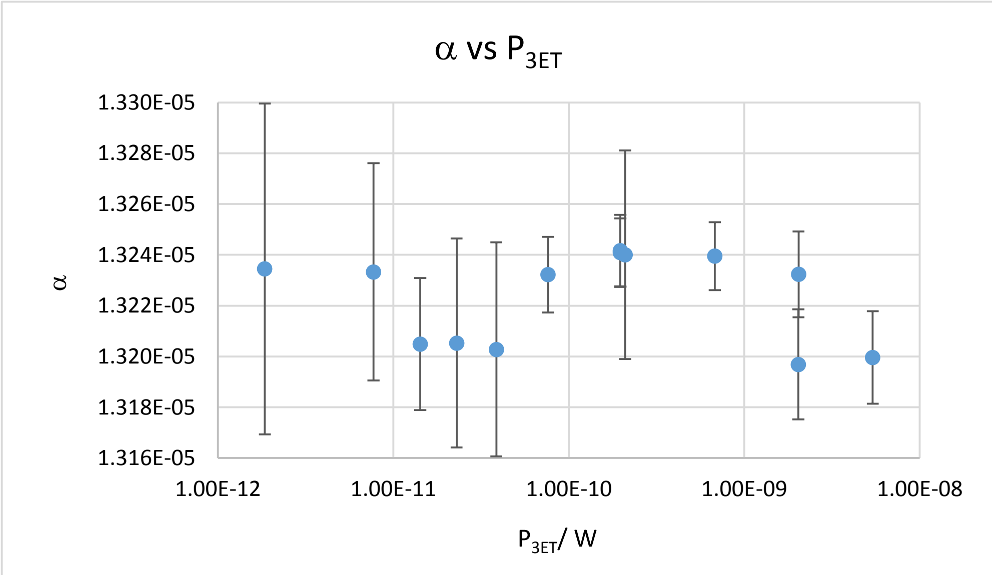

Figure 7. Calculated values of α versus incident power measured at 3ET. Uncertainties are standard uncertainties.

Figure 7 shows the calculated values of $\alpha = i_{3ET}/i_{10ET}$ as a function of incident power P_{3ET} measured at 3ET, calculated from equation (13). Uncertainties in P_{3ET} are not shown, since they are not relevant. The value of α appears to be fairly constant over almost 4 orders of optical power.

The weighted mean of the 13 values of α in table 1 was calculated.

The weighted mean value was found to be $(1.3229 \pm 0.00055) \times 10^{-5}$ (std. unc., ν=1000). ν was calculated to be 2460, but a value of ν=1000 was then used in subsequent calculations, since ν=1000 was generally used as an approximation to $\nu=\infty$.

11.4 Incident photon flux

Table 2 shows the calculated incident photon flux on PTB43. The counts from PTB43 were also recorded.

V_10ET			R_3ET			G_10ET			α			λ			ξ					
mean	Std. Unc.	ν	mean	Std. Unc.	ν	mean	Std. Unc.	ν	mean	Std. Unc.	ν	mean	Std. Unc.	ν	mean	Std. Unc.	ν	N_IN	Std. unc.	ν
4.917E-03	3.69E-07	109	0.6844	0.00032	1000	9.996E+05	2.36E+01	1000	1.3229E-05	5.48E-09	1000	8.5036E-07	6.5E-11	200	1	3.90E-03	7	4.070E+05	1.61E+03	7
2.406E-03	5.84E-07	107	0.6844	0.00032	1000	9.996E+05	2.36E+01	1000	1.3229E-05	5.48E-09	1000	8.5036E-07	6.5E-11	200	1	3.90E-03	7	1.992E+05	7.89E+02	7
1.221E-03	1.59E-07	128	0.6844	0.00032	1000	9.996E+05	2.36E+01	1000	1.3229E-05	5.48E-09	1000	8.5036E-07	6.5E-11	200	1	3.90E-03	7	1.011E+05	4.00E+02	7
1.935E-04	6.80E-08	219	0.6844	0.00032	1000	9.996E+05	2.36E+01	1000	1.3229E-05	5.48E-09	1000	8.5036E-07	6.5E-11	200	1	3.90E-03	7	1.602E+04	6.36E+01	7
2.238E-05	8.47E-08	303	0.6844	0.00032	1000	9.996E+05	2.36E+01	1000	1.3229E-05	5.48E-09	1000	8.5036E-07	6.5E-11	200	1	3.90E-03	7	1.853E+03	1.01E+01	27

Table 2. Incident photon flux on PTB43 count rate (dark-corrected) calculated from equation (8).

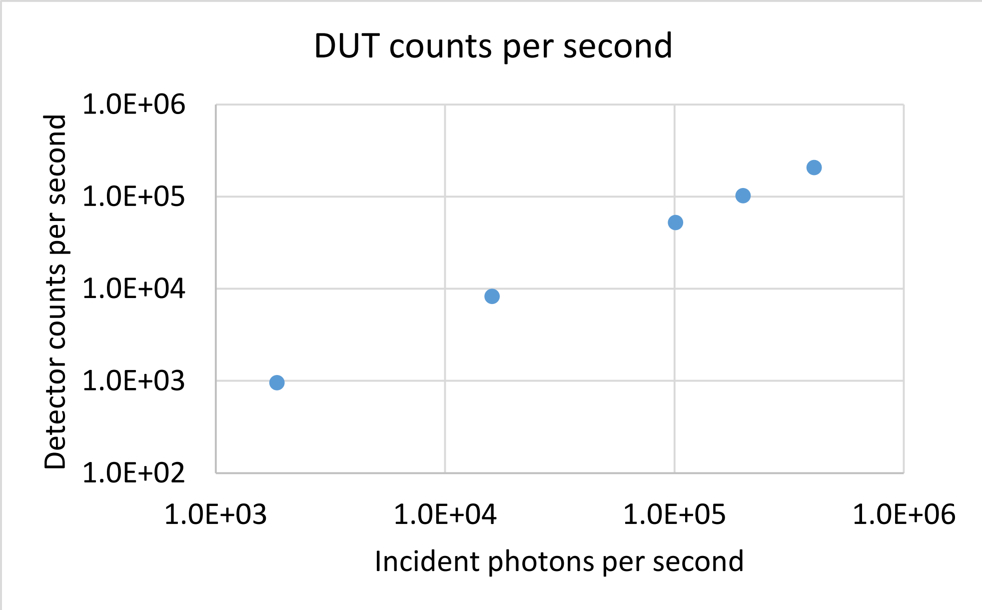

Figure 8. The count rate of PTB43 as a function of incident photon flux.

11.5 Detection efficiency

Table 3 presents the measured counts from DUT43 and the other parameters required to estimate the detection efficiency using equation (11).

N_IN	Std. unc.	ν	τ_d	Std. Unc.	ν	N_DUT	Std. Unc.	ν	η	Std. Unc.	ν(eff)
4.070E+05	1.61E+03	7	2.86E-08	5.0E-11	1000	2.07E+05	4.9E+01	49	0.5107	0.0020	7
1.992E+05	7.89E+02	7	2.86E-08	5.0E-11	1000	1.03E+05	1.8E+02	81	0.5163	0.0022	11
1.011E+05	4.00E+02	7	2.86E-08	5.0E-11	1000	5.23E+04	7.1E+01	99	0.5175	0.0022	9
1.602E+04	6.36E+01	7	2.86E-08	5.0E-11	1000	8.26E+03	1.3E+01	159	0.5157	0.0022	10
1.853E+03	1.01E+01	27	2.86E-08	5.0E-11	1000	9.58E+02	2.1E+00	319	0.5172	0.0031	36

Table 3. Measured values and uncertainty budget for estimating η using equation (11).

The count rate (shutter closed, detector uncapped) was typically around 105 counts per second.

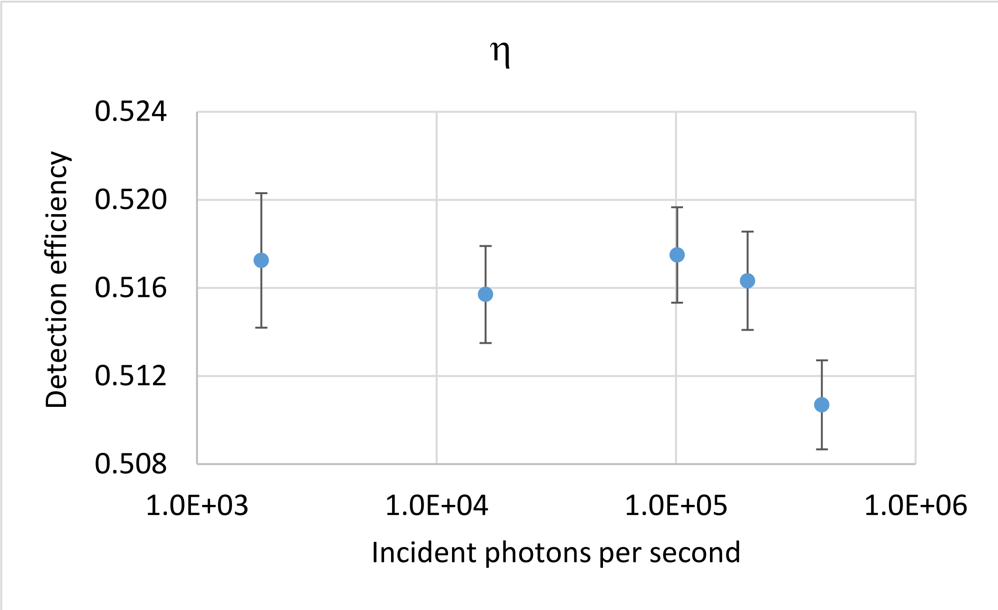

Figure 9. The measured detection efficiency of PTB43 as a function of incident photon flux. Uncertainties are standard uncertainties.

The weighted mean of the 5 values of η in table 3 was calculated. This was found to be 0.5151 ± 0.0010 (1 std. unc., ν=44). This is the measured detection efficiency, η_meas, measured at 850.357 nm, the mean wavelength of the light used in the measurement.

Applying correction factors C1 [Section 7], C2 [Section 8] and C3 [Section 9] results in a final estimate of η = 0.521 ± 0.005 (95% coverage interval) at 850 nm.

η_meas	Std. Unc.	ν	C1	Std. Unc.	ν	C2	Std. Unc.	ν	C3	Std. Unc.	ν	η	Std. Unc.	ν	*k*	95%
0.5151	0.0010	44	1.0016	0.00053	4	0.99	0.0035	5	1	0	1000	0.521	0.0021	9	2.31	0.005

Table 4. Input values and uncertainty calculation for estimating η at 850 nm.

12. Measurement of DUT2 (PTB52)

12.1 Spatial dependency of count rate

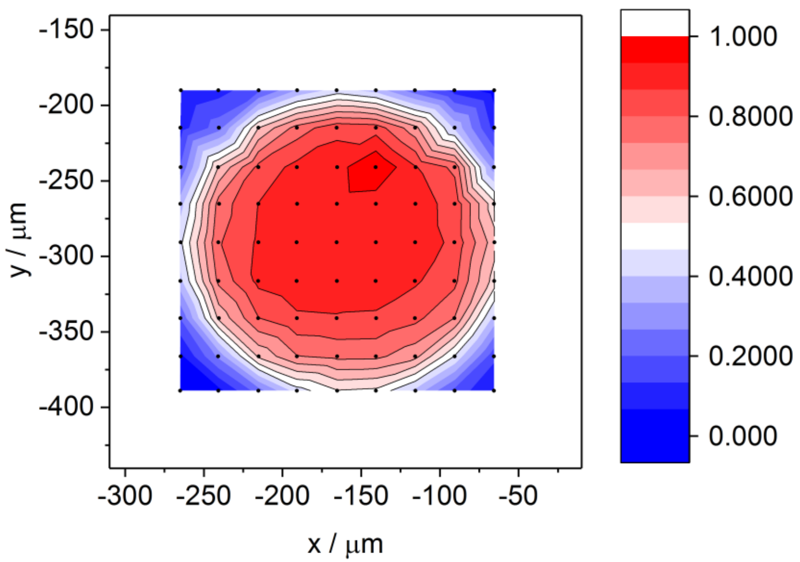

Figure 10. Spatial dependency of count rate for DUT2. Data normalised. Note the high responsivity peak at approximately x= -137 μm, y = -237 μm.

12.2 Dead-time

The dead-time of the detector was measured by using time-tagging to measure the intervals between counts from the non-illuminated detector. This was found to be 28.1 ns ± 0.1 ns. The time/counter was uncalibrated, and therefore an overall conservative uncertainty of 0.5 ns was ascribed to the measurements.

12.3 Calibration of $\alpha = I^{3ET}/I^{10ET}$

Equation (12) is restated below.

$$\alpha = \frac{I_{3ET}}{I_{10ET}} = \frac{V_{3ET}}{V_{10ET}} \frac{G_{10ET}}{G_{3ET}} \tag{12}$$

Table 5 presents the measured voltages and amplifier gains from the 3ET and 10ET traps for a range of input light powers to the 10ET.

V_3ET	Std. Unc.	ν	V_10ET	Std. Unc.	ν	G (SIA)	Std. Unc.	ν	G (MSL)	Std. Unc.	ν	i(3et)	i(10ET)	α	Std. Unc.	ν(eff)
1.573E-01	4.28E-05	195	1.190E+00	3.38E-04	76	1.001E+10	3.10E+07	1000	9.996E+05	2.36E+01	1000	1.572E-11	1.191E-06	1.320E-05	4.13E-08	1031
1.725E-01	7.02E-05	158	1.305E+00	4.36E-04	119	1.001E+10	3.10E+07	1000	9.996E+05	2.36E+01	1000	1.724E-11	1.306E-06	1.320E-05	4.15E-08	1055
2.092E-01	8.56E-05	34	1.578E+00	1.16E-04	9	1.001E+10	3.10E+07	1000	9.996E+05	2.36E+01	1000	2.090E-11	1.579E-06	1.324E-05	4.14E-08	1027
2.924E-01	8.03E-05	54	2.205E+00	3.94E-04	14	1.001E+10	3.10E+07	1000	9.996E+05	2.36E+01	1000	2.922E-11	2.206E-06	1.325E-05	4.13E-08	1021
4.917E-01	8.22E-05	56	3.710E+00	2.55E-04	16	1.001E+10	3.10E+07	1000	9.996E+05	2.36E+01	1000	4.914E-11	3.712E-06	1.324E-05	4.11E-08	1007
1.115E-01	1.12E-04	20	8.407E-01	1.97E-04	10	1.001E+10	3.10E+07	1000	9.996E+05	2.36E+01	1000	1.114E-11	8.411E-07	1.324E-05	4.33E-08	795
6.657E-02	1.43E-04	10	5.031E-01	2.01E-04	7	1.001E+10	3.10E+07	1000	9.996E+05	2.36E+01	1000	6.653E-12	5.033E-07	1.322E-05	5.01E-08	98
3.585E-02	1.21E-04	14	2.718E-01	1.65E-03	8	1.001E+10	3.10E+07	1000	9.996E+05	2.36E+01	1000	3.583E-12	2.720E-07	1.317E-05	1.00E-07	19
2.336E-02	7.08E-05	88	1.762E-01	4.27E-05	45	1.001E+10	3.10E+07	1000	9.996E+05	2.36E+01	1000	2.335E-12	1.762E-07	1.325E-05	5.75E-08	338

Table 5. Measured values and uncertainty budget for estimating α from equation (11).

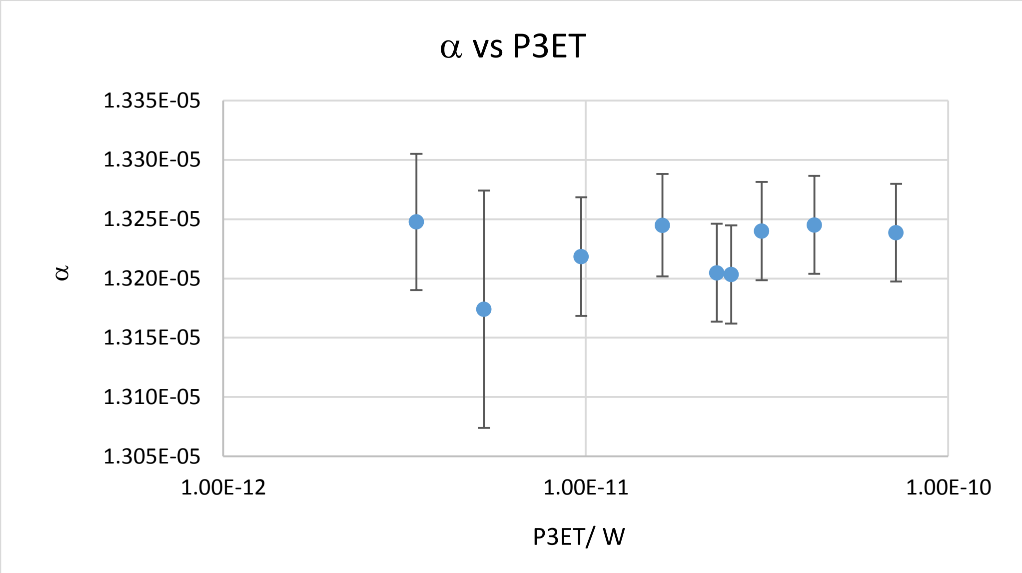

Figure 11. Calculated values of α versus incident power measured at 3ET. Uncertainties are standard uncertainties.

Figure 11 shows the calculated values of $\alpha = i_{3ET}/i_{10ET}$ as a function of incident power P_{3ET} measured at 3ET, calculated from equation (11). Uncertainties in P_{3ET} are not shown, since they are not relevant. The value of α appears to be fairly constant over 1½ orders of optical power.

The weighted mean of the 9 values of α in table 1 was calculated.

The weighted mean value was found to be $(1.3228 \pm 0.0015) \times 10^{-5}$ (std. unc., ν=1000). ν was calculated to be 4080, but a value of ν=1000 was then used in subsequent calculations, since ν=1000 was generally used as an approximation to $\nu=\infty$.

12.4 Incident photon flux

The power incident on the 10ET is reduced; the incident photon flux on the DUT was calculated from equation (6), using α and the measured voltage on the 10ET. The counts on PTB52 were recorded.

V_10ET			R_3ET			G_10ET			α			λ			ξ			N_IN		
mean V	Std. Unc.	ν	mean	Std.Unc.	ν	mean	Std.Unc.	ν	mean	Std.Unc.	ν	mean	Std.Unc.	ν	mean	Std.Unc.	ν	N_IN	Std. Unc.	ν(eff)
1.144E-05	3.27E-07	18	0.6844	0.00032	1000	9.996E+05	2.36E+01	1000	1.3228E-05	1.53E-08	8	8.5036E-07	1.20E-10	200	1.00E+00	3.90E-03	7	9.469E+02	2.73E+01	19
3.868E-05	5.21E-07	18	0.6844	0.00032	1000	9.996E+05	2.36E+01	1000	1.3228E-05	1.53E-08	8	8.5036E-07	1.20E-10	200	1.00E+00	3.90E-03	7	3.202E+03	4.51E+01	21
1.176E-04	3.38E-07	18	0.6844	0.00032	1000	9.996E+05	2.36E+01	1000	1.3228E-05	1.53E-08	8	8.5036E-07	1.20E-10	200	1.00E+00	3.90E-03	7	9.734E+03	4.87E+01	17
2.487E-04	4.00E-07	18	0.6844	0.00032	1000	9.996E+05	2.36E+01	1000	1.3228E-05	1.53E-08	8	8.5036E-07	1.20E-10	200	1.00E+00	3.90E-03	7	2.059E+04	9.07E+01	11
1.565E-03	4.89E-07	24	0.6844	0.00032	1000	9.996E+05	2.36E+01	1000	1.3228E-05	1.53E-08	8	8.5036E-07	1.20E-10	200	1.00E+00	3.90E-03	7	1.295E+05	5.33E+02	9
3.135E-03	6.09E-07	13	0.6844	0.00032	1000	9.996E+05	2.36E+01	1000	1.3228E-05	1.53E-08	8	8.5036E-07	1.20E-10	200	1.00E+00	3.90E-03	7	2.595E+05	1.07E+03	9
1.293E-02	5.92E-07	10	0.6844	0.00032	1000	9.996E+05	2.36E+01	1000	1.3228E-05	1.53E-08	8	8.5036E-07	1.20E-10	200	1.00E+00	3.90E-03	7	1.070E+06	4.39E+03	8
1.761E-03	3.23E-07	37	0.6844	0.00032	1000	9.996E+05	2.36E+01	1000	1.3228E-05	1.53E-08	8	8.5036E-07	1.20E-10	200	1.00E+00	3.90E-03	7	1.458E+05	5.98E+02	9
3.050E-03	1.23E-06	20	0.6844	0.00032	1000	9.996E+05	2.36E+01	1000	1.3228E-05	1.53E-08	8	8.5036E-07	1.20E-10	200	1.00E+00	3.90E-03	7	2.525E+05	1.04E+03	9
1.814E-03	2.66E-07	38	0.6844	0.00032	1000	9.996E+05	2.36E+01	1000	1.3228E-05	1.53E-08	8	8.5036E-07	1.20E-10	200	1.00E+00	3.90E-03	7	1.502E+05	6.16E+02	8
1.839E-03	1.29E-07	131	0.6844	0.00032	1000	9.996E+05	2.36E+01	1000	1.3228E-05	1.53E-08	8	8.5036E-07	1.20E-10	200	1.00E+00	3.90E-03	7	1.522E+05	6.24E+02	8

Table 6. Incident photon flux on PTB52 count rate (dark-corrected) calculated from equation (8).

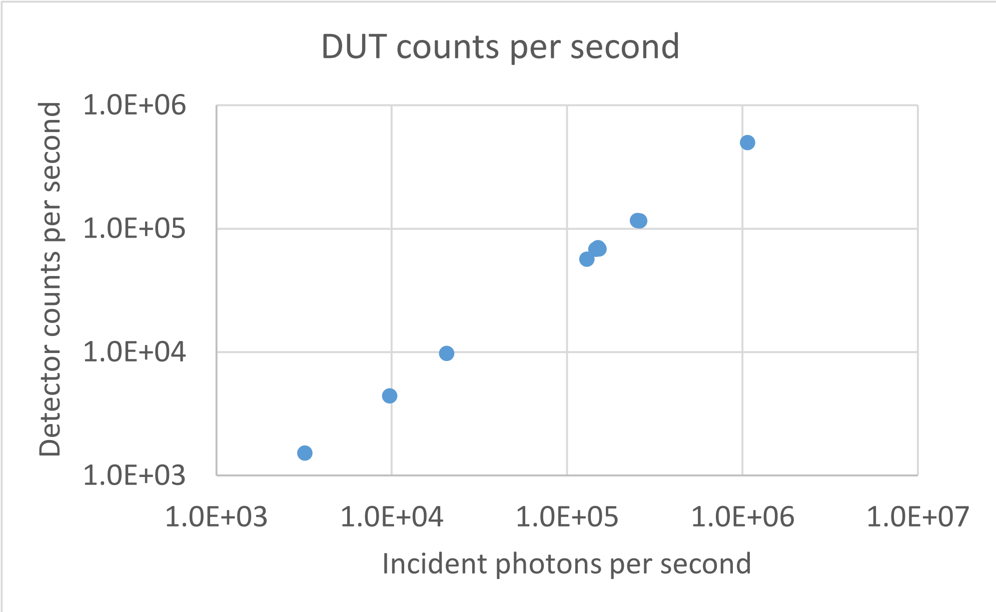

Figure 12. The count rate of PTB52 as a function of incident photon flux.

12.5 Detection efficiency

Table 7 presents the measured counts from DUT43 and the other parameters required to estimate the detection efficiency using equation (11).

N_IN	Std. Unc.	ν	t_d	Std. Unc.	ν	N_DUT	Std.Unc.	ν	η	Std. Unc.	ν(eff)
9.469E+02	2.73E+01	19	2.810E-08	5.00E-11	1000	4.446E+02	4.68E+00	17	0.4696	0.0144	24
3.202E+03	4.51E+01	21	2.810E-08	5.00E-11	1000	1.520E+03	4.17E+00	9	0.4746	0.0068	22
9.734E+03	4.87E+01	17	2.810E-08	5.00E-11	1000	4.413E+03	1.77E+01	8	0.4534	0.0029	24
2.059E+04	9.07E+01	11	2.810E-08	5.00E-11	1000	9.742E+03	9.73E+00	9	0.4732	0.0021	12
1.295E+05	5.33E+02	9	2.810E-08	5.00E-11	1000	5.666E+04	3.16E+01	9	0.4377	0.0018	9
2.595E+05	1.07E+03	9	2.810E-08	5.00E-11	1000	1.160E+05	1.29E+03	7	0.4479	0.0053	9
1.070E+06	4.39E+03	8	2.810E-08	5.00E-11	1000	4.998E+05	1.11E+02	7	0.4704	0.0019	9
1.458E+05	5.98E+02	9	2.810E-08	5.00E-11	1000	6.800E+04	2.43E+01	16	0.4669	0.0019	9
2.525E+05	1.04E+03	9	2.810E-08	5.00E-11	1000	1.164E+05	1.73E+02	19	0.4619	0.0020	11
1.502E+05	6.16E+02	8	2.810E-08	5.00E-11	1000	7.021E+04	2.27E+01	11	0.4680	0.0019	9
1.522E+05	6.24E+02	8	2.810E-08	5.00E-11	1000	6.844E+04	1.14E+02	99	0.4500	0.0020	11

Table 7. Measured values and uncertainty budget for estimating η.

The count rate (shutter closed) was typically around 90 counts per second.

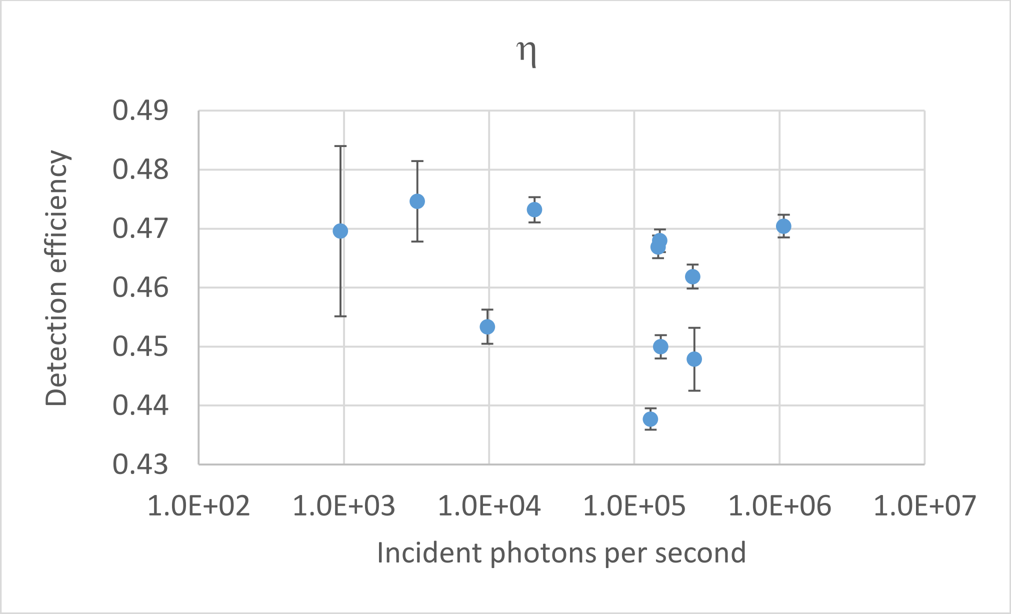

Figure 13. The measured detection efficiency of PTB52 as a function of incident photon flux. Uncertainties are standard uncertainties.

We observe that the spread of data in figure 13 is incompatible with the estimated uncertainties. We believe that this is due to the combined effect of alignment instability and the spike in the spatial profile of the detector efficiency, as discussed in section 9, and which is accounted for by correction factor C3.

The weighted mean of the 11 values of η in table 5 was calculated. This was found to be 0.4600 ± 0.0007 (1 std. unc., ν=78). This is the measured detection efficiency, η_meas, measured at 850.357 nm, the mean wavelength of the light used in the measurement.

Applying correction factors C1 [Section 7], C2 [Section 8] and C3 [Section 9] results in a final estimate of $\eta = 0.465 \pm 0.012$ (95% coverage interval) at 850 nm. *However, we note again that the spike in the spatial profile of the detector efficiency can lead to significant variation in measurement results.*

η_meas	Std. Unc.	ν	C1	Std. Unc.	ν	C2	Std. Unc.	ν	C3	Std. Unc.	ν	η	Std. Unc.	ν	*k*	95%
0.4600	0.0007	78	1.0016	0.00053	4	0.99	0.0035	5	1	0.0108	10	0.465	0.0053	12	2.18	0.012

Table 8. Input values and uncertainty calculation for estimating η at 850 nm.

13. Summary

PTB43: $\eta = 0.521 \pm 0.005$ at a 95% coverage interval.

PTB52: $\eta = 0.465 \pm 0.012$ at a 95% coverage interval.

We observed that there is a spike in the spatial profile of the detector efficiency of PTB52, which can lead to significant variation in measurement results.

References

[1] T. Kübarsepp, and M. G. White, "Ten-element photodetector for optical power and attenuation measurements," Appl. Opt. **49**, 3774-3779 (2010).

[2] M. López, H. Hofer, and S. Kück, "Detection efficiency calibration of single-photon silicon avalanche photodiodes traceable using double attenuator technique," J. Mod. Optics **62**, 1732-1738 (2015).

[3] H. B. Coldenstrodt-Ronge, and C. Silberhorn, "Avalanche Photo-Detection for High Data Rate Applications," J. Phys. B: At. Mol. Phys. **40**, 3909 (2007).

Appendix 1. Calibrations

A1.1

<u>3ET trap detector (s/n NPL11033T); calibrated 5-6 January 2017</u>
Calibrated with MSL Industrial Research Ltd amplifier (model: Photodiode Amplifier 1039; s/n PA1039-06) set to 10^6 V A^{-1} gain setting.

Wavelength (nm)	Responsivity (A W^{-1})	% fractional uncertainty	Coverage interval	$v(eff)$
600	0.4820	0.10	95%	∞
633	0.5088	0.10	95%	∞
650	0.5225	0.10	95%	∞
700	0.5628	0.10	95%	∞
750	0.6032	0.10	95%	∞
800	0.6435	0.09	95%	∞
840	0.6757	0.09	95%	∞
850	0.6838	0.09	95%	∞
860	0.6918	0.09	95%	∞
900	0.7240	0.10	95%	∞

Table A.1.

A1.2

MSL amplifier (s/n PA1039-06); calibrated 1 December 2016

Set gain	Actual/set gain	% uncertainty	Coverage interval	$v(eff)$
10^3	0.99986031	0.00013	95%	∞
10^4	0.99985897	0.00108	95%	∞
10^5	0.99967058	0.00090	95%	∞
10^6	0.99956296	0.00472	95%	∞
10^7	0.99962180	0.00377	95%	∞
10^8	0.99977621	0.00441	95%	∞
10^9	0.99955444	0.02213	95%	∞

Table A.2.

A1.3

CMI SIA amplifier (s/n 8018); calibrated 13 December 2016

Set gain	Actual/set gain	% uncertainty	Coverage interval	$v(eff)$
10^7	1.00118574	0.00323	95%	∞
10^8	1.00146064	0.26624	95%	∞
10^9	1.00093792	0.20124	95%	∞
10^{10}	1.00062796	0.62029	95%	∞

Table A.3.

Appendix 2. 3ET reference detector

The NPL 3ET reference trap detector, used in combination with the MSL trans-impedance amplifier, was calibrated traceably to the NPL primary scale.

In that calibration, [section A1.1], the nominal value of the amplifier 10^6 V A^{-1} gain setting was used in calculating the 3ET responsivity.

Table A2.1 below gives the responsivity values for the 3ET, corrected for the true values of the MSL amplifier gain at the 10^6 V A^{-1} gain setting, including at the experimental mean wavelength of 850.357 nm ± 0.119 nm.

Wavelength (nm)	Responsivity (A W^{-1})	std. unc.	ν_eff
600	0.4822	0.00024	1000
633	0.5090	0.00025	1000
650	0.5227	0.00026	1000
700	0.5630	0.00028	1000
750	0.6035	0.00030	1000
800	0.6438	0.00029	1000
840	0.6760	0.00030	1000
850	0.6841	0.00031	1000
860	0.6921	0.00031	1000
900	0.7243	0.00036	1000
850.357	0.6844	0.00032	1000

Table A2.1. Spectral responsivity of 3ET - NPL reference detector

Appendix 3. Derivation of equation (11).

Accounting for dead-time effects follows a similar argument to that described in [2]. From the calculated incident photon flux (N_{IN}), the mean number of photons (μ_d) incident within the DUT deadtime (τ_d) is calculated:

$$\mu_d = N_{IN}\tau_d \tag{A3.1}$$

If two of more photons are incident within a dead-time interval, there can be at most one detection event. Therefore the probability of a detection event within a dead-time interval is given by

$$P_{click} = 1 - e^{-\eta\mu_d} \tag{A3.2}$$

using the relation derived in [3] to account for the fact that if two or more photons are incident on a non-photon-number resolving detector within the same pulse there can be at most one detection event.

Hence the observed DUT count rate (s^{-1}) is given by

$$N_{DUT} = \frac{P_{click}}{\tau_d} = \frac{1-e^{-\eta\mu_d}}{\tau_d} = \frac{1-e^{-\eta\, N_{IN}\,\tau_d}}{\tau_d} \tag{A3.3}$$

Re-arranging (A3.3) leads to

$$\eta = -\frac{1}{N_{IN}\tau_d}\ln(1 - N_{DUT}\tau_d) \tag{A3.4}$$

i.e. equation (11).

Physikalisch-Technische Bundesanstalt
Braunschweig und Berlin
Nationales Metrologieinstitut

Bericht

Report

Report on the results obtained for the CCPR WG-SP TG 11 "Pilot study on the detection efficiency of single-photon detectors – Si-SPAD"

Anzahl der Seiten: 8
Number of pages:

Geschäftszeichen: 7.3-2.66
Reference No.:

393 00A o

Im Auftrag
On behalf of PTB

Berlin, 2019-06-28

Siegel
Seal

Im Auftrag
On behalf of PTB

Dr. I. Müller

Dr. L. Werner

1. Introduction

The measurements described here were performed within the framework of the **CCPR WG-SP TG 11 Pilot study on the detection efficiency of single-photon detectors – Si-SPAD**. The measurements were conducted from 23. January to 24. January 2018 at the Metrology Light Source in Berlin-Adlershof. The pilot study is a combined round-robin and star like type of comparison. Two Silicon avalanche photodiodes made by Perkin-Elmer with the model number SPCM-AQR-16 were used as transfer detectors. The nominal wavelength is 850 nm and the detectors are operated in free-space.

2. Description of the Calibration Facility

The measurements were conducted at the Metrology Light Source (MLS), the dedicated electron storage ring for radiometry of the Physikalisch-Technische Bundesanstalt (PTB). At the MLS several beamlines are available for different metrological purposes. For the radiometric calibration of single photon detectors, two different beamlines were used thus far. For free-space detectors the white light beamline using bending magnet radiation was used while for fibre-coupled detectors undulator radiation was used. A description of the setups for calibration schemes as well as results can be found in [1-3]. The calibration schemes are both based on the unique properties of synchrotron radiation and the special equipment operated at the MLS to render possible the metrological use of the synchrotron radiation.

Synchrotron radiation emitted by a single electron moving in a magnetic field is described by means of the so-called Schwinger theory [4]. The total emitted spectral radiant power is then calculated by multiplying the radiant power of a single electron with the number of stored electrons in the MLS. At the MLS, all the necessary equipment is installed to vary the electron beam current from 200 mA down to 1 pA, which equals a single stored, in a controlled way. Thus, the emitted spectral radiant power can be varied over 11 orders of magnitude without any changes to the emitted spectrum creating a valuable tool to bridge the radiometric gap between classical radiometry and the detection of single photons.

However, for the calibration of single photons detectors several optical elements (e.g. lenses, interference filters ...) have to be installed in the beam path render a mathematical treatment of the problem impossible. Hence, for these measurements the MLS was not used as a primary radiation source. Here, the MLS was used as calibrated radiation source with a huge dynamic range. The calibration of the MLS was done by means of a three-element silicon photodiode trap detector calibrated traceable to the laser-based cryogenic radiometer of PTB [5]. The photon statistics of the MLS was calculated and experimentally validated in [6]. It was shown that the photon statistics of the MLS can be well approximated with a Poissonian radiation source.

3. Description of the Artefact and Measurement Conditions

For the pilot study two single photon counting modules of type SPCM-AQR-16 produced by Perkin-Elmer were used. The general specifications are given below:

Arrangement of the detectors:	horizontally
State of polarization:	linearly polarized
Reference detector:	T13-4m, silicon-photodiodes, three-element-element trap design, calibrated traceable to the cryogenic radiometer of PTB

Aperture of the reference detector:	11.5 mm
Transfer detector a:	SPCM-AQR-16, SN: 19743
Transfer detector b:	SPCM-AQR-16, SN: 18752
Electrometer:	Keithley 617, SN: 367202 ID-number: 7.1-E02
Focal point of the radiation:	in the plane of the Si-SPAD, centred 3 mm behind the plane of the third photodiode of T13-4m, centred
Laboratory temperature:	(23 ± 0.5) °C
Temperature of the setup:	Measured with a LUFFT 80 thermometer, calibrated by a direct comparison with a calibrated thermometer in Department 7.4 at 23 °C
Interference filter:	BK-850, calibrated at the spectral-comparator facility of PTB resembling the beam properties of the MLS
Wavelength:	848.488 nm
Photon counter	SR 400, Stanford Research Systems, SN: 2431, calibrated against the normal frequency provided on the PTB campus in Braunschweig

4. Results

The measurement equation and the necessary correction factors are described in detail in [1].
As described in [1], the uncorrected detection efficiency QE^*_{SPAD} of a Si-SPAD detector is given by:

$$DE^*_{\mathrm{SPAD}} = \frac{CR_{\mathrm{SPAD}}}{N_{\mathrm{I_{low}}}} \cdot \frac{s_{\mathrm{trap}} \cdot E_{\mathrm{phot}} \cdot I_{\mathrm{high}} \cdot \tau}{e^- \cdot i_{\mathrm{trap}}} \quad (1)$$

with CR_{SPAD} the measured count rate of the SPAD, s_{trap} the spectral responsivity of the trap detector, E_{phot} the energy of a photon, I_{high} the measured ring current in the high current range,
τ the revolution time of a stored electron of 160 ns, e^- the elementary charge, $N_{\mathrm{I_{low}}}$ the number of stored electrons and i_{trap} the measured photocurrent of the calibrated trap detector.

4.1 Correction and Uncertainties

To obtain the true detection efficiency of the SPAD detectors several corrections are necessary [1].

The corrected detection efficiency $DE_{\mathrm{a,b}}$ for transfer detector a and b, respectively, is given by

$$DE_{\mathrm{SPAD}} = c_{\mathrm{s}} \cdot c_{\mathrm{bw}} \cdot c_{\mathrm{ap}} \cdot c_{\mathrm{dt}} \cdot DE^{*}_{\mathrm{SPAD}} \quad (2)$$

With c_s the correction for the different detector sizes, c_{bw} the correction for the influence of the bandwidth of the synchrotron radiation, c_{ap} the correction for afterpulsing of the detector, c_{dt} the deadtime correction for the Si-SPADs.

4.1.1 Correction for Different Detectors Sizes of Si-SPAD and Reference Detector

The nominal effective area of the Si-SPADs is 180 µm and the entrance aperture of the reference detector is approximately 11.5 mm. Hence, the Si-SPAD is very likely detecting a significant smaller fraction of the radiation field as compared to the reference detector. To estimate the necessary correction the active areas of the Si-SPAD, the reference detector and several pinholes with different apertures were scanned with focused synchrotron radiation at the position of the Si-SPAD detectors by an x-y-z-translation stage.

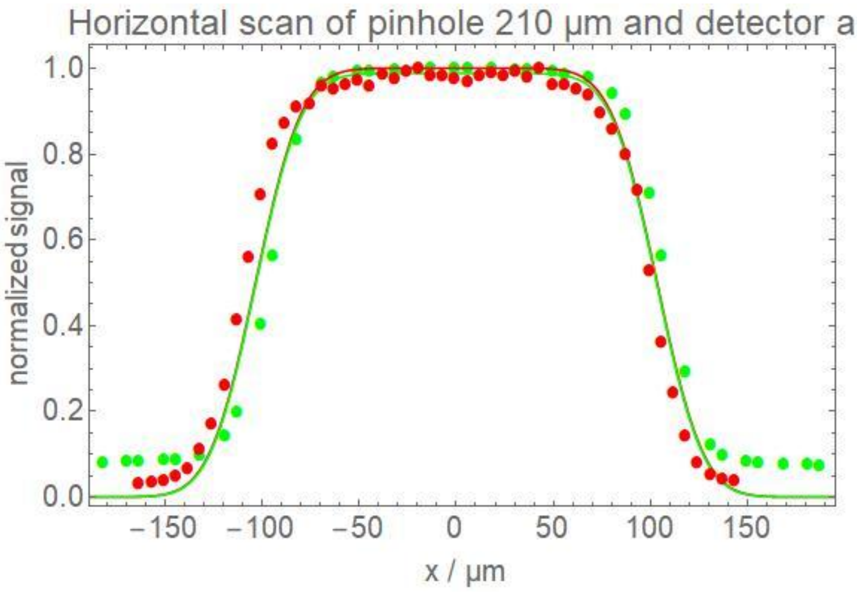

Figure 1: Normalized photocurrent of a detector measuring the radiation transmitted through a 210 µm pin hole (red points) plotted over the translation in x-direction. Normalized signal of transfer detector a plotted over the translation in x-direction (green points). Calculated result of the pinhole measurement for an assumed pinhole diameter of 210 µm and FWHM of the focal spot of 44 µm (solid line).

From the measured signals, the spot size was calculated to 44 µm. In addition, the fraction of radiation vignetted by the transfer detectors was measured. The results are given in Figure 2.

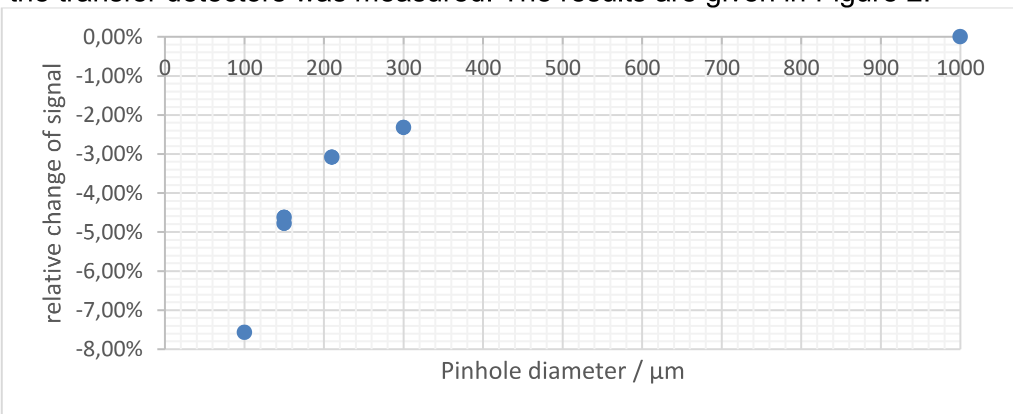

Figure 2: Measured relative change of the transmitted radiation plotted over the pinhole diameter.

The measured correction factor for the different detector sizes is c_s=1.0319±0.0016. This correction factor was used for transfer detector a and b.

4.1.2 Bandwidth correction

To correct for the spectral dependence of the calculated emitted photon flux of the MLS $\Phi_{MLS}(\lambda)$, of the transmittance of the interference filter used $F(\lambda)$ and the different spectral shapes of the responsivity of the trap detector $s_{trap}(\lambda)$ and the quantum efficiency $QE_{SPAD}(\lambda)$ of the Si-SPADs a correction factor was determined. The correction factor is described in [1]. $F(\lambda)$ was measured at the spectral comparator facility of PTB for a beam configuration approximating the conditions during the calibration at the MLS. The correction factor is $c_{bw} = \frac{c_{SPAD}}{c_{trap}} = 0.9952 \pm 0.0008$ for detector a and b respectively.

4.1.3 Afterpulsing corrrection

An afterpulse of a SPAD is characterized to be not initiated by an incoming photon but to appear statistically directly after the dead time after a photon absorption. To measure the afterpulsing probability, an oscilloscope was used to sample approximately 3000 count events. To determine the afterpulsing probability the number of events that showed an additional pulse directly after the initial pulse were divided by the total number of sampled events. Since the afterpulsing probability is photon flux dependent the measurements were made at an electron beam current very similar to the electron beam current used during the calibration. The resulting afterpulsing probability is p_{ap1}=(0.267 ± 0.011) % for detector a and p_{ap2}=(0.433 ± 0.009) % for detector b at a count rate of about 2000 Hz. The afterpulsing correction factor is obtained by calculating $c_{ap1,2}=1-p_{ap1,2}$.

4.1.4 Deadtime correction

The deadtime *dt* has been determined to be 29.3 ns for detector a and 28.3 ns for detector b by means of an oscilloscope LECROY Waverunner 640Zi. At a count rate of about 2000 Hz only a minor correction of $c_{dt,a,b}$=1.00005 for detector a and b calculated from $c_{dt}=(1-dt\cdot\mathrm{CR})^{-1}$.

4.1.5 Revolution frequency

The uncertainty associated with the revolution time of a single stored electron τ is of the order of 10^{-7} and is negligible for the evaluation of *DE**.

4.1.6 Uncertainty budget

The uncertainty budgets for the two calibrations performed on January 23 and January 24 are given in Table 1. The combined relative expanded (k=2) uncertainties are stated.

Table 1: Uncertainty budget for the calibration of Si-SPAD by means of synchrotron radiation at a wavelength of 848.488 nm. If not stated else, relative standard uncertainties are given.

	Value	*Measurement 1* *23.01.2018*		*Measurement 2* *24.01.2018*	
		Det. a	Det. b	Det. a	Det. b
CR_{SPAD}	≈ 2000 / s	0.09%	0.10%	0.09%	0.09%
$N_{I_{low}}$	≈ 700 e^-	0.00001%	0.00001%	0.00001%	0.00001%
s_{trap}	0.68234 A/W	0.091%	0.091%	0.091%	0.091%
E_{phot}	2.3404E-19 J	0.006%	0.006%	0.006%	0.006%
I_{high}		0.18%	0.18%	0.09%	0.09%
i_{trap}		0.014%	0.014%	0.008%	0.008%
I_{high}/i_{trap}		0.012%	0.012%	0.004%	0.004%
c_s		0.09%	0.09%	0.09%	0.09%
Positioning uncertainty		0.02%	0.02%	0.02%	0.02%
$c_{bw,a,b}$		0.080%	0.080%	0.080%	0.080%
Repeatability day 1 / day 2		0.3%	0.3%	0.3%	0.3%
Combined expanded relative standard uncertainty *(k=2)*		**0.78%**	**0.79%**	**0.72%**	**0.72%**

4.2 Results

The measured detection efficiencies for detector a (SN:19743) and detector b (SN:18752) at a wavelength of 844.488 nm are given in Table 2.

Table 2: Measured detection efficiencies for Det. a and Det. b at a wavelength of 844.488 nm and the expanded uncertainties (*k* = 2).

Detector	2018-01-23 *DE*(844.488 nm)	2018-01-24 *DE*(844.488 nm)
a (SN: 19743)	0.5421 ± 0.0042	0.5396 ± 0.0039
b (SN: 18752)	0.4883 ± 0.0038	0.4910 ± 0.0035

The resulting detection efficiency of Det a. and Det. b. at the nominal wavelength of 850 nm is given in Table 3. The resulting expanded uncertainty contains an additional extrapolation uncertainty for the calculation of *DE*(850 nm) from *DE*(844.488 nm) obtained by multiplying the correction by 1/Sqrt(3).

Table 3: Corrected detection efficiency of Det a. and Det. b. at the nominal wavelength of 850 nm and the expanded uncertainties (*k* = 2).

Detector	2018-01-23 *DE*(850 nm)	2018-01-24 *DE*(850 nm)
a (SN: 19743)	0.5388 ± 0.0055	0.5363 ± 0.0054
b (SN: 18752)	0.4850 ± 0.0052	0.4877 ± 0.0051

5. References

[1] *Müller I et al 2012 Metrologia **49** S152*
[2] *Mueller* I et al *2014 Metrologia **51** S329*
[3] *Mueller I et al 2017 Optics Express **25** 18 21483-21495*
[4] *Schwinger J 1949 Phys Rev **75***
[5] *Lutz CR-paper*

Die Physikalisch-Technische Bundesanstalt (PTB) in Braunschweig und Berlin ist das nationale Metrologieinstitut und die technische Oberbehörde der Bundesrepublik Deutschland für das Messwesen. Die PTB gehört zum Geschäftsbereich des Bundesministeriums für Wirtschaft und Energie. Sie erfüllt die Anforderungen an Kalibrier- und Prüflaboratorien auf der Grundlage der DIN EN ISO/IEC 17025.

Zentrale Aufgabe der PTB ist es, die gesetzlichen Einheiten in Übereinstimmung mit dem Internationalen Einheitensystem (SI) darzustellen, zu bewahren und weiterzugeben. Die PTB steht damit an oberster Stelle der metrologischen Hierarchie in Deutschland. Die Kalibrierscheine der PTB dokumentieren eine auf nationale Normale rückgeführte Kalibrierung.

Zur Sicherstellung der weltweiten Einheitlichkeit der Maßeinheiten arbeitet die PTB mit anderen nationalen metrologischen Instituten auf regionaler europäischer Ebene in EURAMET und auf internationaler Ebene im Rahmen der Meterkonvention zusammen. Dieses Ziel wird durch einen intensiven Austausch von Forschungsergebnissen und durch umfangreiche internationale Vergleichsmessungen erreicht.

The Physikalisch-Technische Bundesanstalt *(PTB) in Braunschweig and Berlin is the National Metrology Institute and the supreme technical authority of the Federal Republic of Germany for metrology. The PTB comes under the auspices of the Federal Ministry of Economics and Energy. It meets the requirements for calibration and testing laboratories as defined in DIN EN ISO/IEC 17025.*

The central task of PTB is to realize, to maintain and to disseminate the legal units in compliance with the International System of Units (SI). PTB thus is at the top of the metrological hierarchy in Germany. The calibration certificates issued by PTB document a calibration traceable to national measurement standards.

PTB cooperates with other national metrology institutes - at the regional European level within EURAMET and at the international level within the framework of the Metre Convention - with the aim of ensuring the worldwide coherence of the measurement units. This aim is achieved by an intensive exchange of the results of research work and by comprehensive international comparison measurements.

CCPR WG-SP TG 11

Pilot study on the detection efficiency of single-photon detectors – Si-SPAD

Preliminary Report: METAS measurements March-April 2019

METAS / Damian Twerenbold and Peter Blattner / 14-October-2019

1. Introduction

Metas has decided to participate at a pilot study of the CCPR WG-SP TG 11, which wants to investigate the measurement capabilities of National Measurement Institutes in the area of photon counting detection. This pilot study implements a round-robin calibration of test detectors. In the first phase of this pilot study, the detection efficiency measurements will be made on several Si-SPAD single-photon detectors at a wavelength of 850 nm in free-space beam.

In this preliminary report from Metas, we present our results for the detection efficiency measurements of the two Perkin-Elmer Si-SPAD single-photon detectors provided by the pilot laboratory PTB and our own Excelitas Si-SPAD (identical model).

In addition to the protocol wavelength of 850 nm, we have extended the wavelength region from 750 nm to 900 nm using our tunable MIRA Optima 900-D Ti:sapphire laser (MMDB 6227) pumped by a diode-pumped solid-state laser Verdi V10 532 nm (MMDB 6163).

The detectors were mounted on a 3D-scanning support (positional precision of all three coordinates < 5 μm) and the laser beam was focused with a microscope lens to a spot size of <15 μm onto the active area of the detectors. This allowed us to scan the 2D detection efficiency profile of the two detectors of the pilot study

2. SPAD detectors of the pilot study

The following two Photon Counting Module (Si-SPAD) were provided by the pilot laboratory PTB: PerkinElmer SPCM AQR 16 S/N 19743 and S/N 18752, respectively. For convenience, the two SPAD detectors were numbered Metas internally according to the following figure:

EXC1

EXC2

Figure 1: The two Perkin Elmer SI-SPAD of the pilotestudy

In addition, we included our own Excelitas SPCM-AQRH-16 S/N E2701 SPAD detector (designated as EXCM) which is identical to the Perkin Elmer models.

The active area of the SPAD is circular with a diameter of approximately 180 μm.

3. Metas Si reference detector

As reference detector for providing the SI-traceable spectral irradiance (W/m2/nm) we used a Hamamatsu S1336-8BQ (5.8 mm x 5.8 mm) Si detector

Figure 2: Our Hamamatsu Si-reference detector

This detector was calibrated at METAS on 04.02.2019 using the monochromatic light source Jobin-Yvan (MMDB 2203) and the three reference Metas Si-trap detectors (EAM4 MMDB 4772, EAM5 MMDB 4774 and EAM6 MMDB 4775). The calibration results are stored in the Excel file Metas_S1336-8BQ_M1_5p8mm.xls:

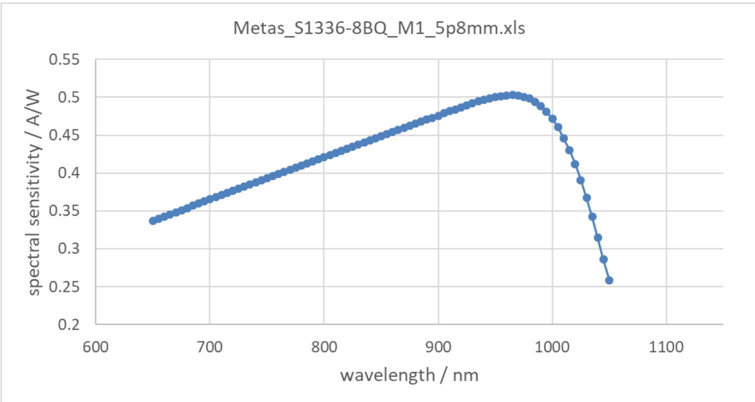

Figure 3: The spectral sensitivity of our Hamamatsu Si-reference detector

The following table shows the values in the wavelength range used in this report.

Metas_S1336-8BQ_M1_5p8mm.xls
measured on 04.02.2019

nm	A/W	nm	A/W	nm	A/W
740	3.878E-01	795	4.184E-01	850	4.487E-01
745	3.906E-01	800	4.212E-01	855	4.514E-01
750	3.933E-01	805	4.240E-01	860	4.543E-01
755	3.961E-01	810	4.267E-01	865	4.569E-01
760	3.990E-01	815	4.294E-01	870	4.597E-01
765	4.017E-01	820	4.323E-01	875	4.625E-01
770	4.045E-01	825	4.349E-01	880	4.651E-01
775	4.073E-01	830	4.377E-01	885	4.680E-01
780	4.101E-01	835	4.406E-01	890	4.705E-01
785	4.128E-01	840	4.433E-01	895	4.732E-01
790	4.156E-01	845	4.460E-01	900	4.759E-01

Figure 4: The values of the spectral sensitivity of our Si-reference detector at selected wavelength

4. Experimental setup

The following diagram shows our experimental setup:

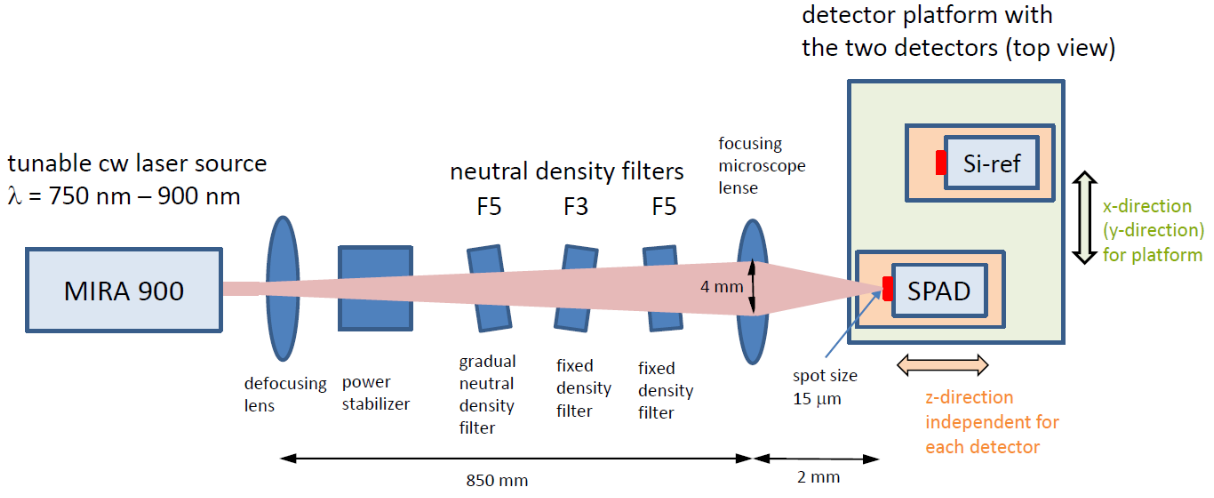

Figure 5: Our experimental setup for determining the external quantum efficiency of the Si-SPAD

The laser beam was defocused so to optimally fill (4 mm) the microscope lens at a distance of 850 nm. At a focal distance of about 2 mm, the beam could be focused to a spot size of about 15 µm. The filters were tilted slightly in order to minimize reflection effects.

We measured the spot size with a CMOS camera, which was placed at the position of the sensitive area of the SPAD. By varying the z-distance of the position of the CMOS camera we could measuring the varying beam waist (spot size) of the laser, as is shown in the following figure for a wavelength of 850 nm:

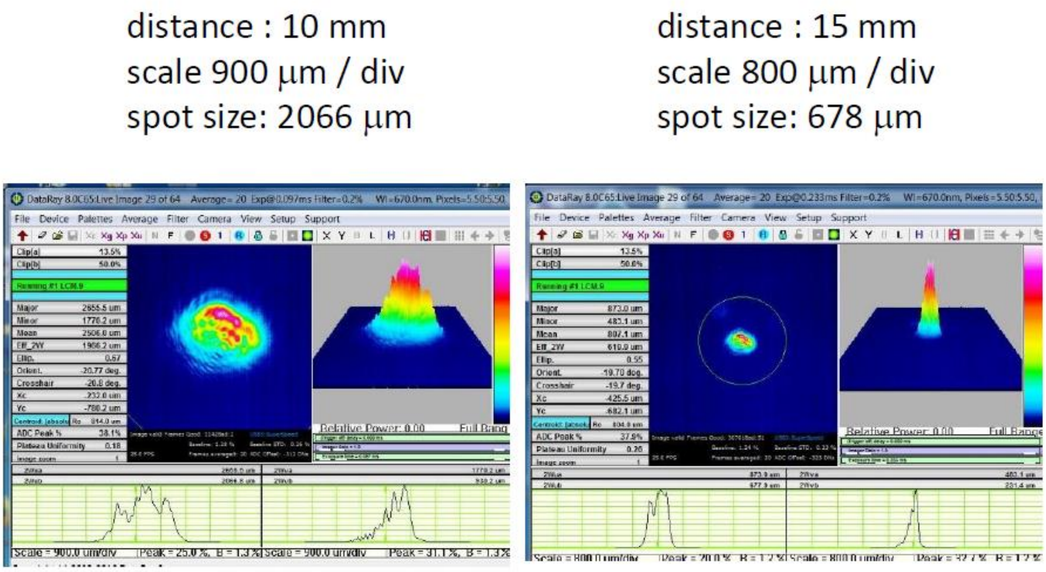

Figure 6: CMOS camera 2D images of the beam profile at the position of the detectors

distance : 17.4 mm
scale 200 µm / div
spot size: 23.7 µm

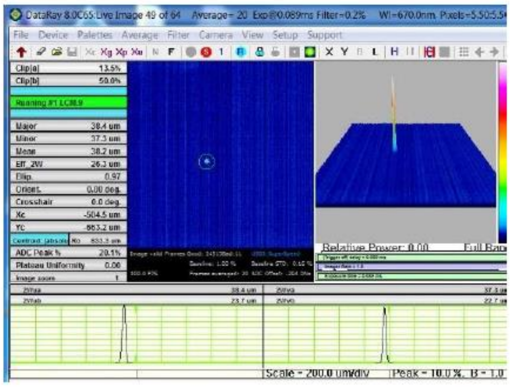

Figure 7: CMOS camera 2D image of the beam at the optimal focusing position of the microscope lens

The strong focusing effect of the microscope lens can also been seen by varying the distance between the active area SPAD and the microscope (z-distance) as can be seen by the following figure:

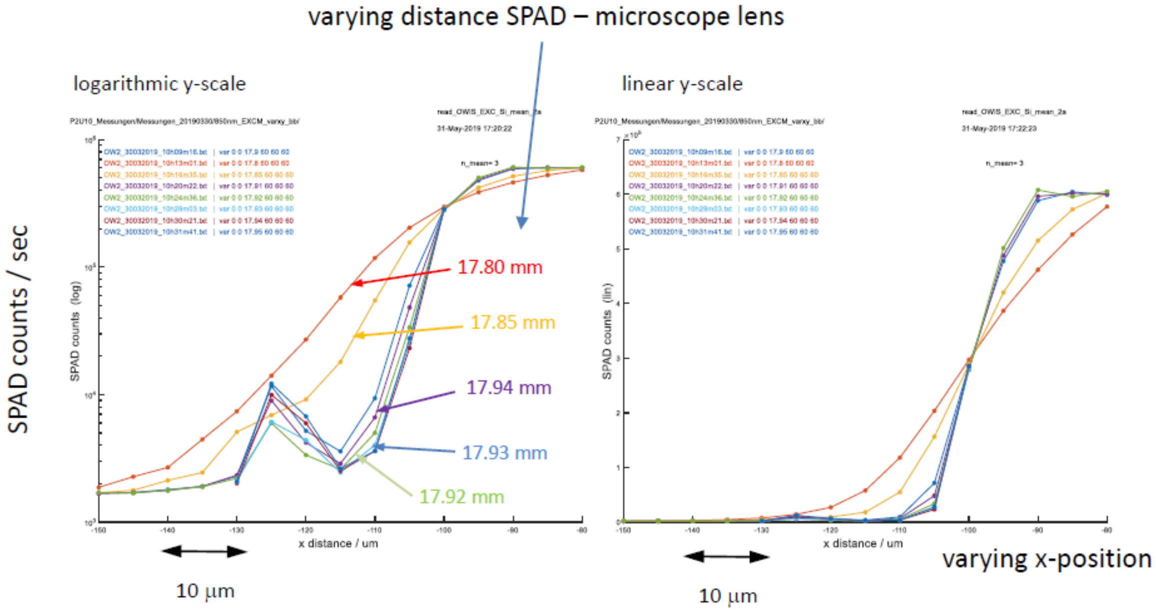

Figure 8: SPAD count rates for various microscope lens positions at the edge of the active SPAD region.

At the position of minimal beam waist (here about 17.92 mm beam relative to the home position of the SPAD) varying the z-distance by 0.01 mm (10 µm) an effect in the slope of the SPAD count rate can be seen. The optimal SPAD – microscope distance is where the slope is the steepest, i.e. the spot size is minimal.

As the diameter of the Perkin Elmer / Excelitas SPAD detectors is 180 µm, our setup satisfies sufficiently the requirement of under filling the detector.

5. 2D scans of Perkin Elmer / Excelitas SPAD detector count rate

As the spatial resolution of about 10 µm is sufficiently smaller than the active area of the SPAD, we have used our setup to measure the 2D x-y dependence of the SPAD count rate.

EXC1 (PE S/N 18752) λ = 850nm   EXC2 (PE S/N 19743) λ = 850nm

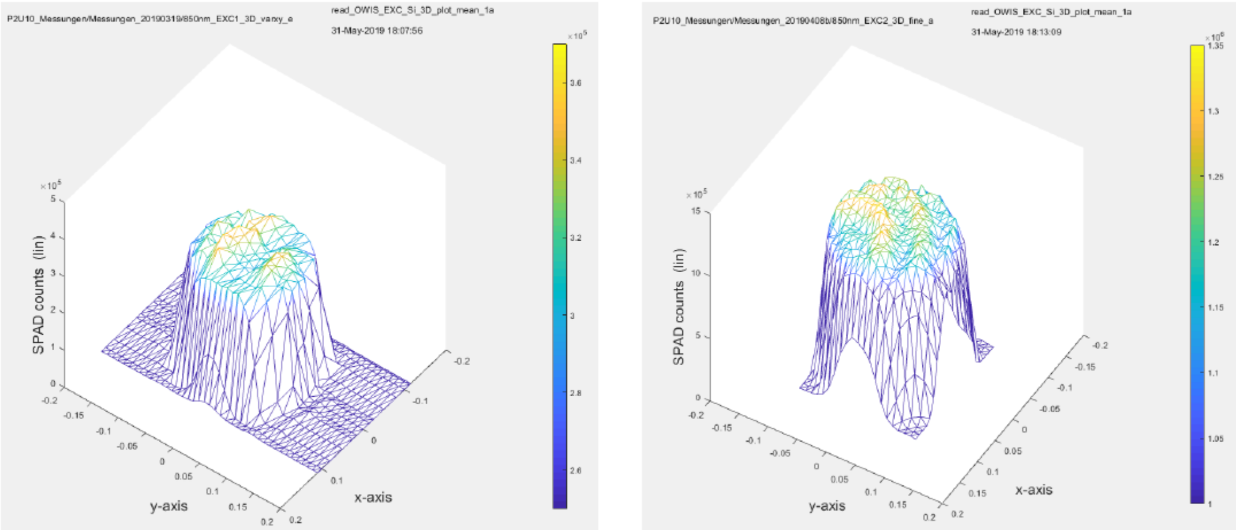

Note: absolute count rates not comparable because of different neutral density filters in beam line

Figure 9: 2D distribution of SPAD count rates across the area of the active area of the SPAD for the Perkin Elmer Si-SPADs used for the pilot study at a wavelength of 850 nm.

There are variations of at least 10% across the surface of the SPAD. From the pattern structure of these variations, we assume that this may be owing to caustic effects of the window of the SPAD (which is required to prevent ice formation on the surface because the SPAD is cooled by a Peltier to below -20°C).

EXCM (Excelitas SPCM-AQRH-16 S/N E2701) λ = 850nm

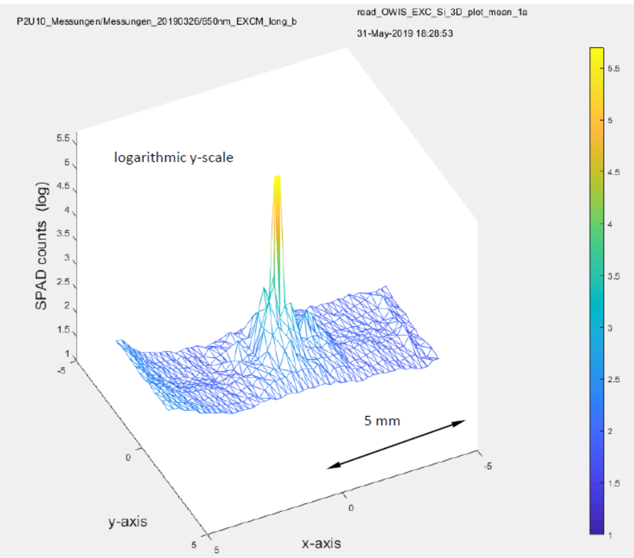

Interesting is also to scan over larger distances: there the SPAD detects "out of focus" photons from the beam (stray light), which will probably be an important contribution to the uncertainty budget of determining the SPAD detection efficiency with the method described in this report.

Figure 10: 2D distribution of SPAD count rates outside of the focal point of the microscope lens showing stray light contribution of the microscope lens setup (note logarithmic scale of count rate)

6. Determination of the filter attenuation factors

The detection efficiency of a given SPAD detector is determined by attenuating the beam with a suitable combination of neutral density filters (before the focusing microscope lens) in order to get count rates between 10^5 and 10^6 counts per seconds. After the SPAD count rate measurements, the platform (on which both detectors are fixed) is moved by about 40 mm in
x-direction such that the beam spot illuminates the calibrated Si-reference detector and the attenuating filters are removed and the radiative power before the filters is measured.

For the comparison, it is necessary to determine the attenuation factors of the three filters F3, F4 and F5 experimentally (we used the Si-reference detector). As we wanted to determine the detection efficiency of the SPAD for wavelengths between 750 nm and 900 nm, we also had to determine the wavelength dependent attenuation factors of the filters. The following diagram shows the measured attenuation of the filter F5 (at fixed position 60 degrees) and the corresponding linear fit function:

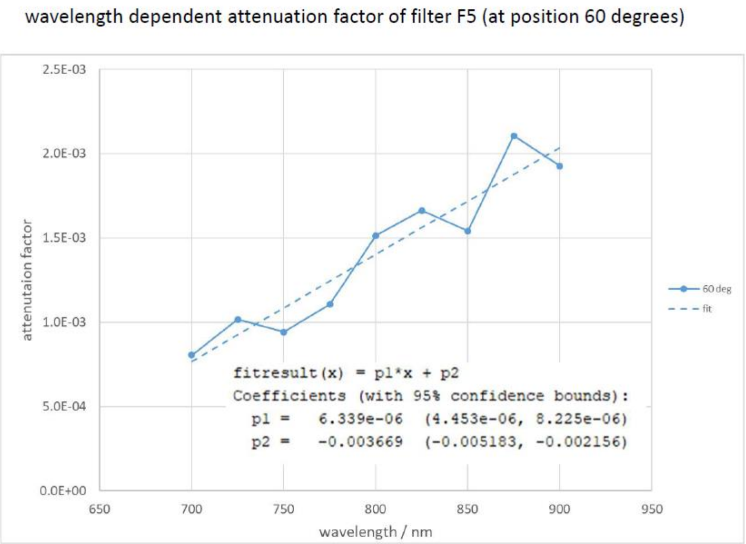

Figure 11: Attenuation factor of filter 5 for wavelengths between 700 nm and 900 nm at 60°

This filter F5 was used for setting the beam intensities such that both SPAD and Si-reference detectors would operate in reasonable ranges (one could also change the power of the laser, however for stability reasons we preferred to keep the laser settings untouched).

When comparing SPAD count rates with currents from a Si-reference detector, a strong attenuation of the order of 10^{-6} to 10^{-7} is required. This we achieve by putting two strong attenuating neutral density filters in series. The following diagram shows the wavelength dependent attenuation factors of each of the filters F3 and F4 which should nominally have a optical density of 6:

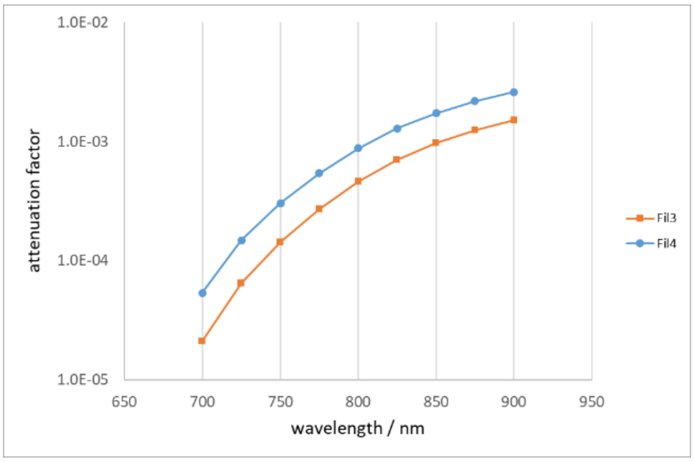

Figure 12: Attenuation factor of filters 3 and 4 for wavelengths between 700 nm and 900 nm

However, for the detection efficiency measurements both filters were placed in series, so the relevant diagram is the following, which contains also the 5.order polynomial fit:

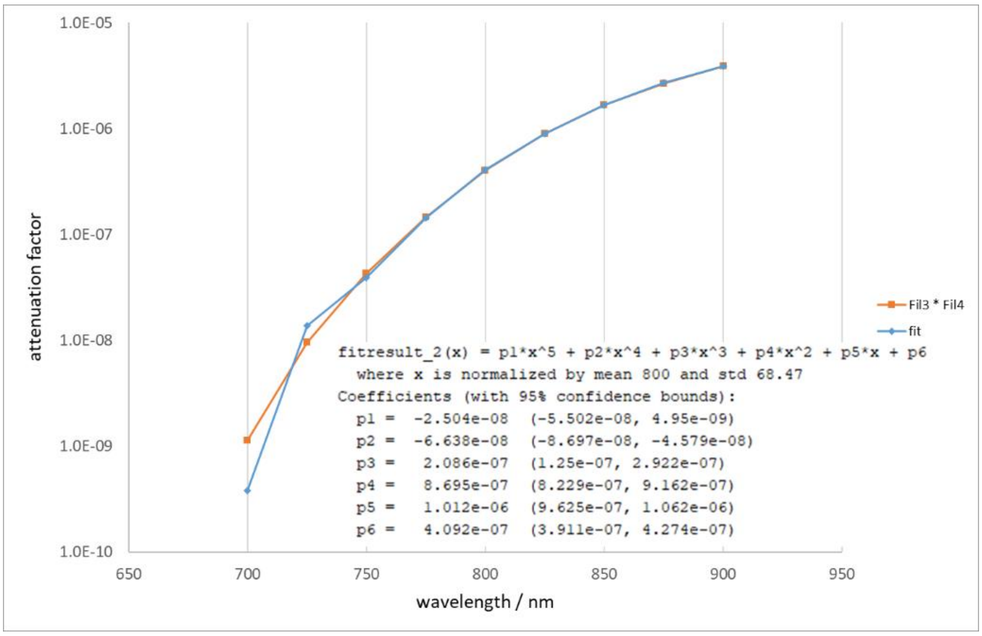

Figure 12: Attenuation factor of combined filters 3 and 4 for wavelengths between 700 nm and 900 nm

The filters were AR coated Neutral Density Filters from Thorlabs and varied from NE02B-A (optical density 0.2) to NE60B-A (optical density 6.0) and were fabricated for wavelengths between 350 and 700 nm. Which means that we selected the wrong filters for our application.

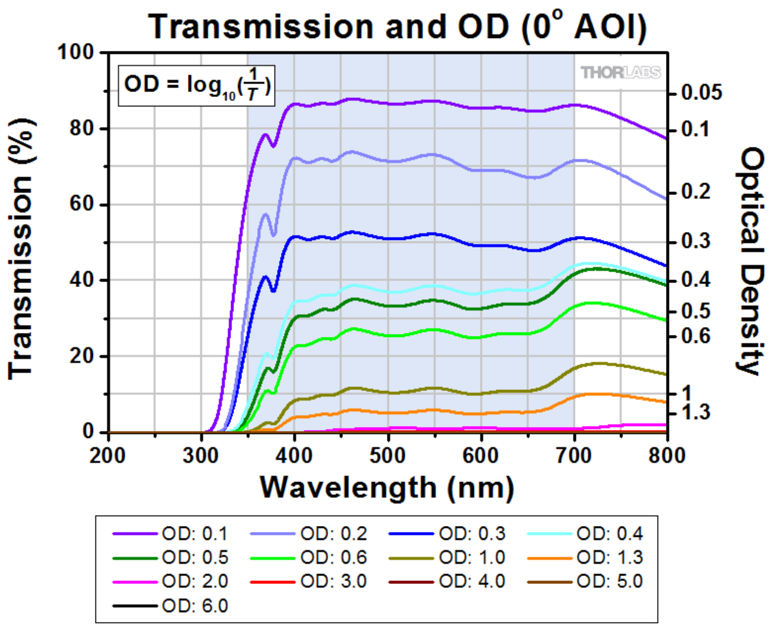

Figure 13: Specifications of selected filters of the NEXXB-A series of Thorlabs

The following diagram shows the results of transmission (optical density = log10 (1/T)) measurements using our variable wavelength EKSPLA laser for the five filters we used.

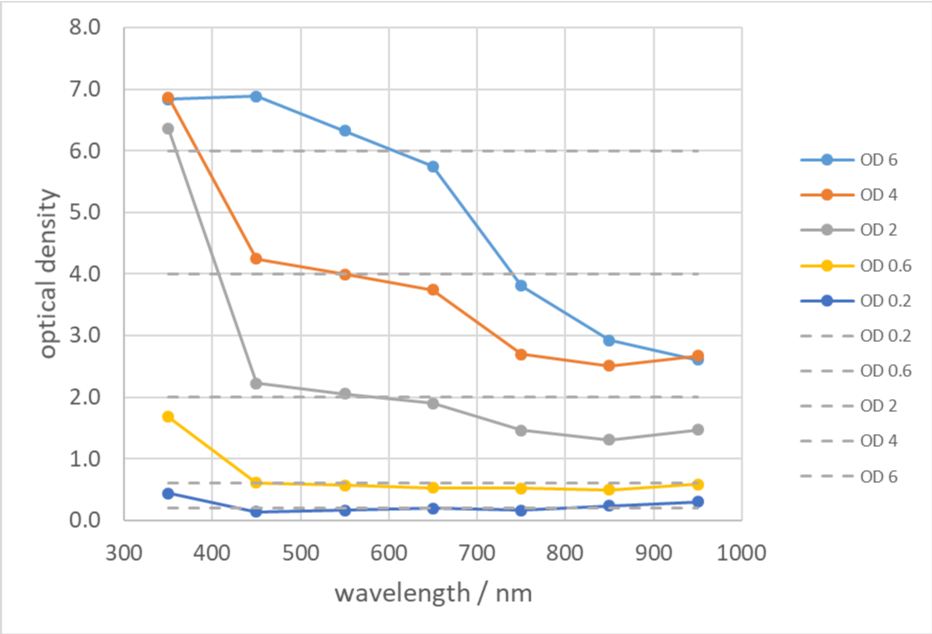

Figure 14: Optical density of the 5 filters of the NEXXB-A series of Thorlabs between 350 nm and 950 nm

This confirms the strong wavelength dependence of the attenuation of our OD 6 filter between 700 nm and 900 nm as shown in the figure 12 above.

7. Radiative power on Si-reference detector and raw SPAD count rates

For completeness, and in order to interpret the results accordingly, we show in the following figure the radiative power on the Si-reference detector, which changed with wavelength:

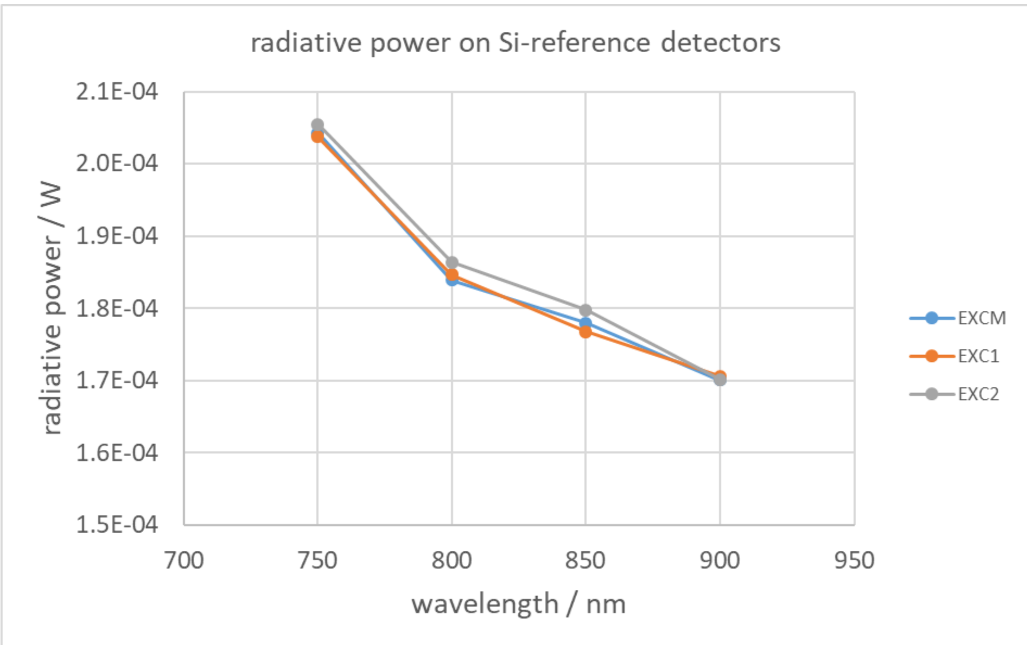

Figure 15: The radiative power on the Si-reference detector between 750 nm and 900 nm.

In the following figure, the corresponding count rates are shown for the corresponding radiative powers when the filter combination F3 and F4 where put accordingly into the beam line:

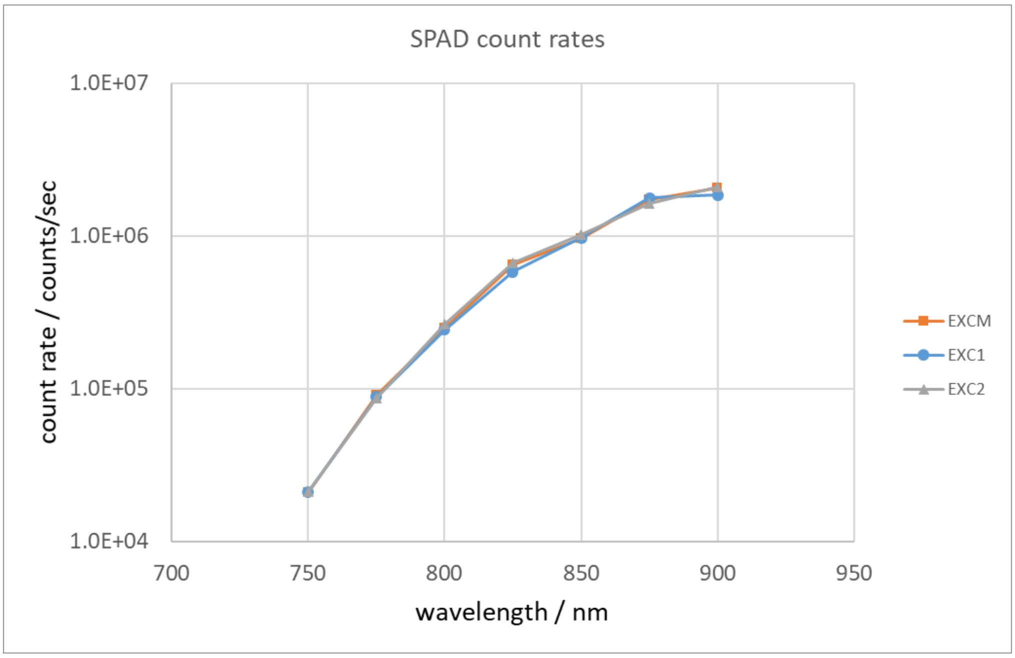

Figure 16: The raw SPAD count rates between 750 nm and 900 nm.

8. Results: detection efficiency of Perkin Elmer / Excelitas SPAD detectors

The measurements were performed in the laser laboratory of METAS (P2U10) with the following ambient conditions: temperature T = 23 °C +/- 1 °C and humidity 42% rh +/-5 % rh.

The following diagram shows the results of our wavelength dependent corrected detection efficiencies of the three Perkin Elmer / Excelitas SPAD detectors:

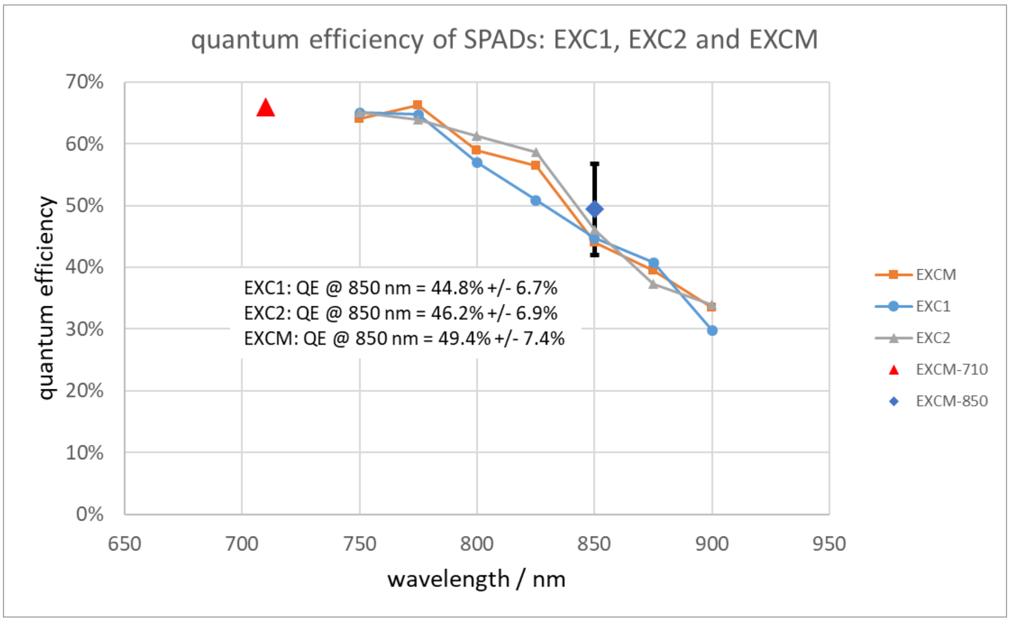

Figure 17: Corrected detection efficiency of the three Perkin Elmer Si-SPAD between 350 nm and 950 nm

By varying the count rate of the SPAD from several 10^4 to 10^7 counts, we could see the effect of dark counts and dead time. By using the appropriate correction formula, we obtained a consistent quantum efficiency for both wavelengths 850 nm and 719 nm, as is shown in the following figure 18:

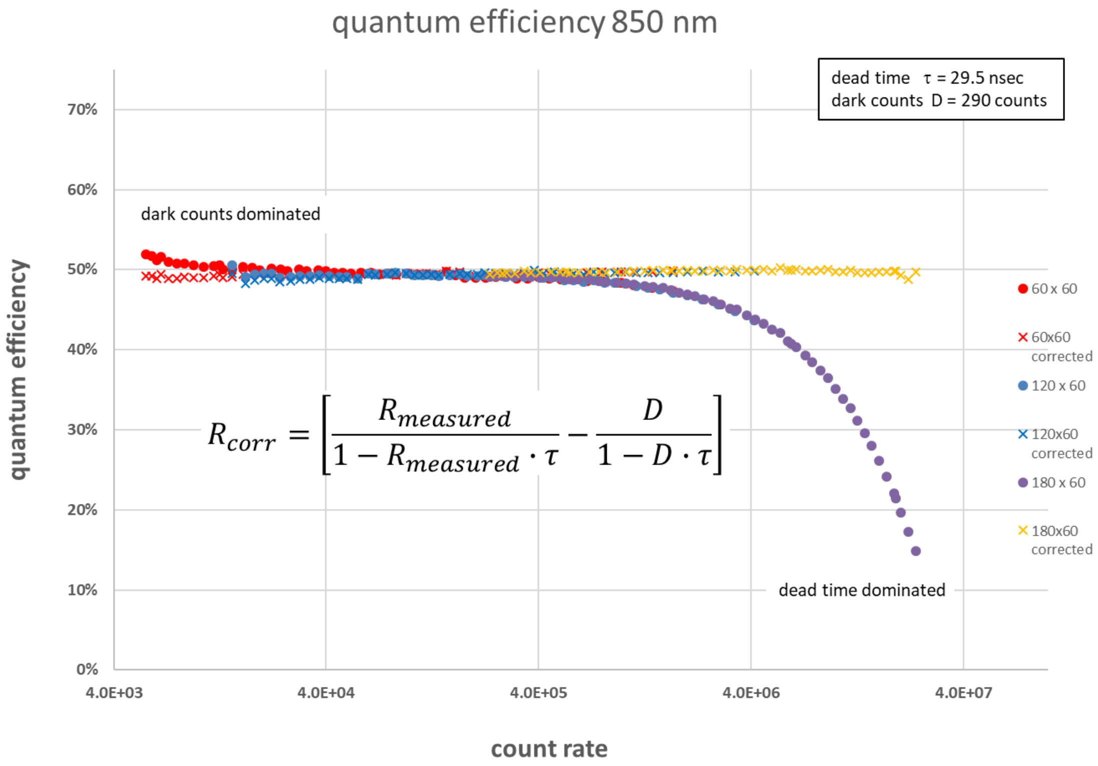

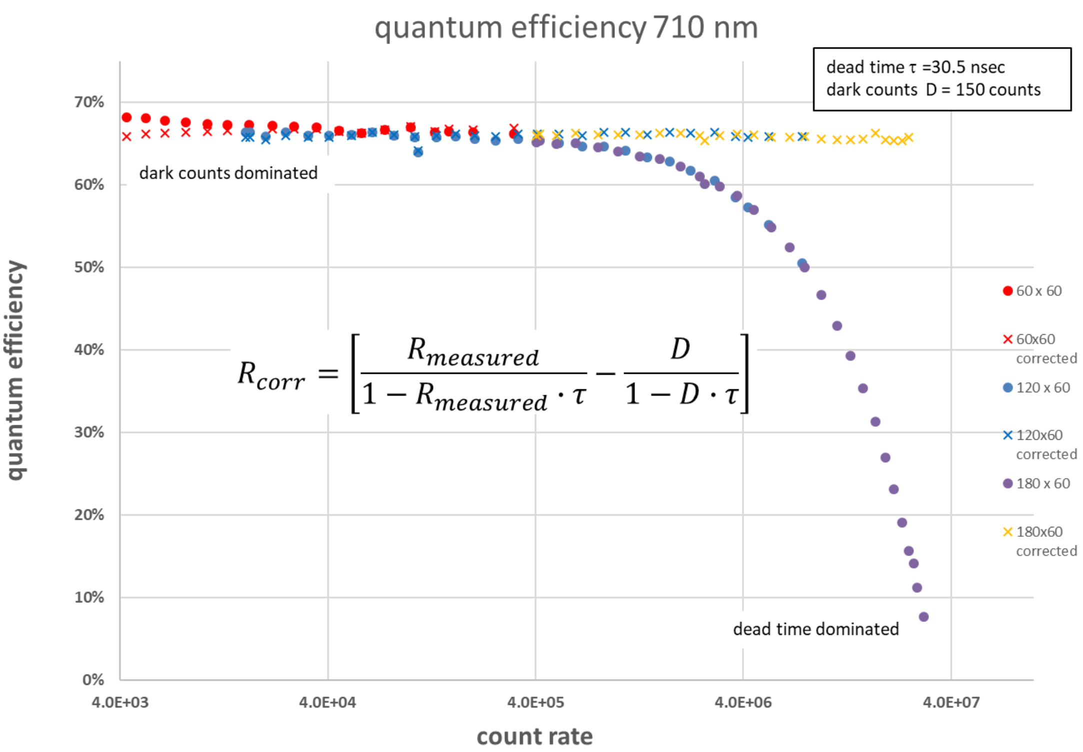

Figure 18: Correcting for dark counts and dead time at 850 nm and 710 nm.

The dead time was about 30 nsec in both cases (determined basically by the SPAD electronics) and the dark counts differed slightly, 290m counts for 850 nm and 150 counts at 710 nm which could be caused by the different off beam scattering of the two wavelengths.

9. Uncertainty Budget

The following table summarizes our various uncertainty budget contributions (uncertainty k=1) when determining the external quantum efficiency of Si-SPAD detectors at the wavelength of 850 nm

Spectral sensitivity calibration of reference Si-detector	0.3 %
Attenuation factor of filter combination	2 %
Stray light differences	1 %
Inhomogeneity of illumination across SPAD surface (incl. window)	7 %
Uncertainty of determination of nominal wavelength	0.05 %
Reflections between attenuation filters	0.5 %
Reflections between detector surface and focusing microscope	0.5 %
Stability of laser source	0.5 %
Dead time and count rate correction	1 %
uncertainty (k=1)	7.5%
Total expanded uncertainty (k=2)	15 %

10. Discussion

We have measured the quantum efficiency of three PerkinElmer SPCM type SPADs:

Two SPADs from the pilot study:

EXC1: PerkinElmer SPCM AQR 16 S/N 18752
EXC2: PerkinElmer SPCM AQR 16 S/N 19743

And our own METAS PerkinElmer SPCM type SPAD

EXCM: Excelitas SPCM-AQRH-16 S/N E2701

As a light source we used tunable MIRA Optima 900-D Ti:sapphire laser (MMDB 6227) pumped by a diode-pumped solid-state laser Verdi V10 532 nm (MMDB 6163).

The quantum efficiencies at the pilot study wavelength of 850 nm of those three SPADs are:

EXC1: 44.8% +/- 6.7%
EXC2: 46.2% +/- 6.9%
EXCM:49.4% +/- 7.4%

National Institute of Metrology (NIM), China

Transmission of International Comparison Results

The title of international comparison:

Pilot study on the detection efficiency of single-photon detectors (Si-SPAD)

Serial number for international comparison:

CCPR WG-SP TG 11 CCPR.PR-Pxxx

Comparison experiment period:

2022.04.02 ~ 2022.08.11

Experiment reporter:

Haiyong Gan & Xiangliang Liu

Phone number of experiment reporter: +86 10 64526331
E-mail: ganhaiyong@nim.ac.cn & liuxl@nim.ac.cn
Address: No.18, Bei San Huan Donglu Rd., Beijing 100029, China

Transmission date: 2025.07.21

CONTENTS

1. Measurement traceability 1

2. Measurement conditions 2

2.1 Measurement facility 2

2.2 Measurement temperature 3

2.3 Voltages of the power supply for the DUT single-photon detectors 3

2.4 Measurement wavelength 3

3. Beam size for measurement 3

4. Non-uniformities and measurement positions of DUT single-photon detectors 4

5. Measurement results and uncertainty analyses 6

5.1 The spectral responsivity of the transfer photodetector 6

5.2 Repeatability of calibration 6

5.3 Non-uniformity of the DUT single-photon detector 7

5.4 Dead-time impact correction 7

5.5 After-pulsing probability correction 7

5.6 Combined uncertainty at 844.5 nm 8

5.7 Wavelength correction 8

5.8 Combined uncertainty after wavelength correction 9

1. Measurement traceability

The detection efficiencies of single-photon detectors are ultimately traceable to the absolute cryogenic radiometer at NIM via the scheme as shown in Figure 1. The spectral responsivities of a reference photodetector (Hamamatsu S2592) are calibrated at the wavelengths near 850 nm. The linearity of the reference photodetector from ~0.1 mW to ~10 pW is measured and the spectral responsivities at ~10 pW are derived. Then the spectral responsivities of a transfer photodetector are calibrated using the reference photodetector at ~10 pW and the spectral responsivities at ~0.1 pW are derived after the linearity measurement from ~10 pW to ~0.1 pW. The detection efficiencies of the DUT single-photon detectors are calibrated at 0.1pW ~1 pW against the reference photodetector and the quantum efficiencies at 1 photon are deduced after dead-time and after-pulsing corrections.

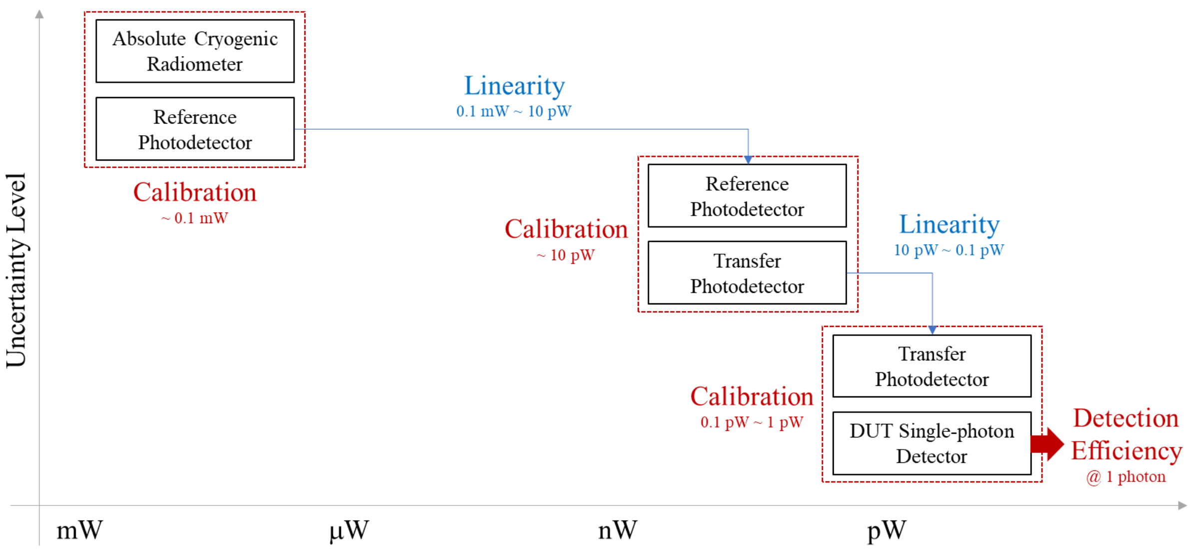

Fig. 1. Traceability of the detection efficiencies measurements of single-photon detectors.

2. Measurement conditions

2.1 Measurement facility

The measurement facility for the detection efficiencies of single-photon detectors is shown in Figure 2. An LED light source is coupled into a monochromator for wavelength tuning and spectral bandwidth control, and then focused into a fiber-optical attenuator for spatial filtration and power adjustment. The light is collimated and directed through a polarization-insensitive beamsplitter, with one output beam going into a monitor photodetector as the feedback for power stabilization, and the other going into a long-working-distance objective lens with a beam diameter of 32 μm (>99.9% beam power coverage) at the focal point. The transfer photodetector and DUT single-photon detector are mounted on a 3D translation stage with sub-1-micron precision.

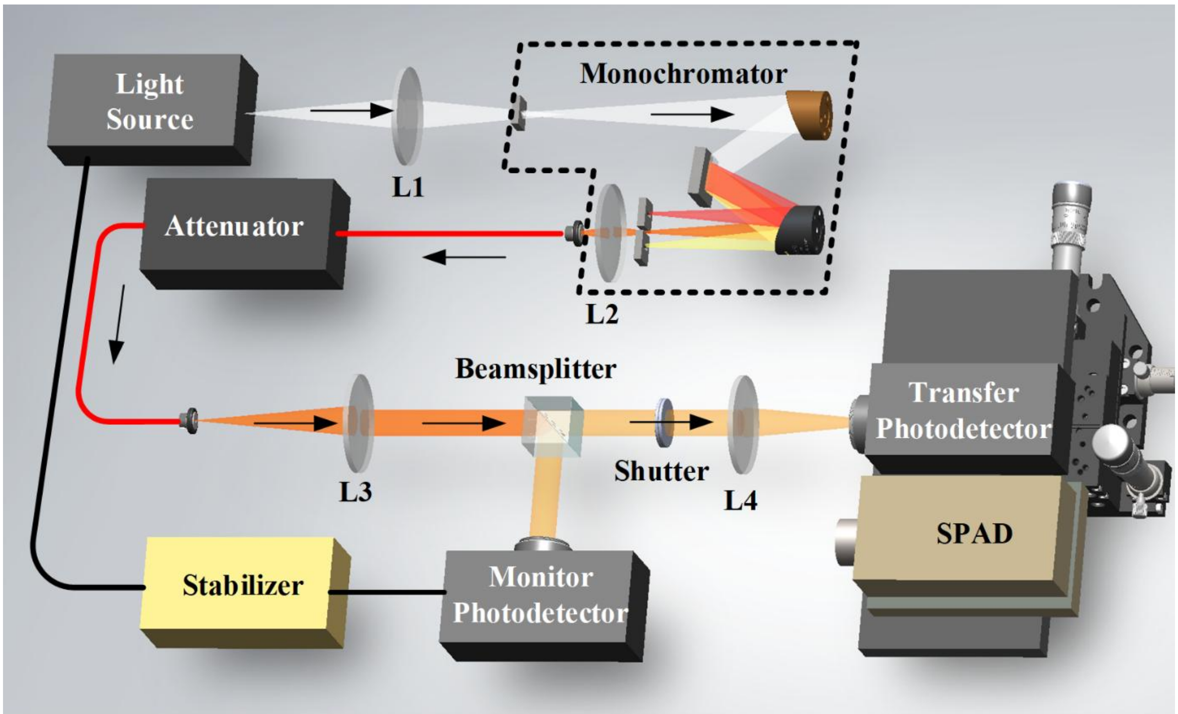

Fig. 2. The detection efficiency measurement facility for single-photon detectors at NIM.

The transfer photodetector is based on a Si photodiode (Hamamatsu S2386) with an active area of 1.1×1.1 mm^2, a transimpedance gain of 1×10^{12} V/A, and an NEP of $0.7\ \mathrm{fW}/\sqrt{\mathrm{Hz}}$. The spectral responsivities of the transfer photodetector are calibrated against the reference photodetector at ~10 pW using the same facility.

2.2 Measurement temperature

23.0 °C ± 0.5 °C.

2.3 Voltages of the power supply for the DUT single-photon detectors

5.00 V ± 0.01 V using a Keithley 2400 source meter.

2.4 Measurement wavelength

Central wavelength = 844.5 nm.

Spectral bandwidth (FWHM) = 4.6 nm.

2.5 Polarization of incident light

Non-polarized.

3. Beam size for measurement

The beam profile at the focal point of the objective lens for the measurement is recorded and shown in Figure 3. The size of each pixel is 8 μm × 8 μm and the beam diameter is estimated to be 32 μm (with >99.9% beam power coverage).

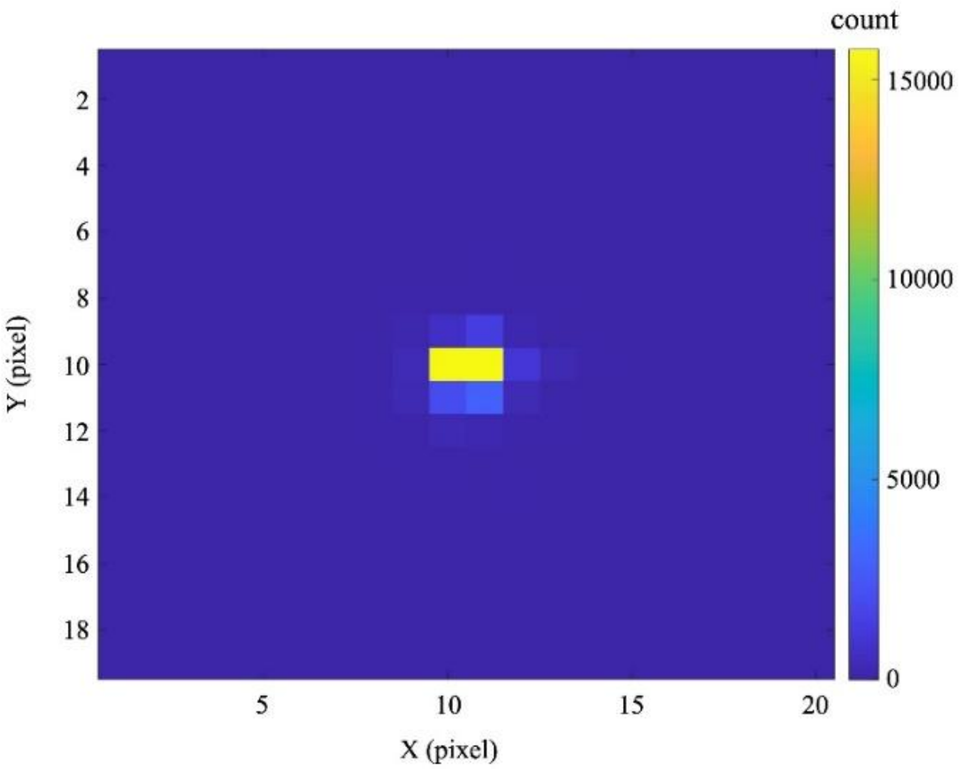

Fig. 3. Beam profile at the focal point of the objective lens.

4. Non-uniformities and measurement positions of DUT single-photon detectors

Fig. 4. The coordinates for non-uniformity scanning

The non-uniformities of the DUT single-photon detectors are scanned using the measurement facility shown in Figure 2. The coordinates relative to each DUT single-photon detector is illustrated in Figure 4 and the scanning results of the two DUT single-photon detectors are shown in Figure 5 and Figure 6, respectively.

The measurement positions for the DUT single-photon detectors Det-18752 and Det-19743 are (–40 µm, 0) and (+25µm, +10µm), respectively, relative to the center of the sensor of the DUT single-photon detectors (0, 0).

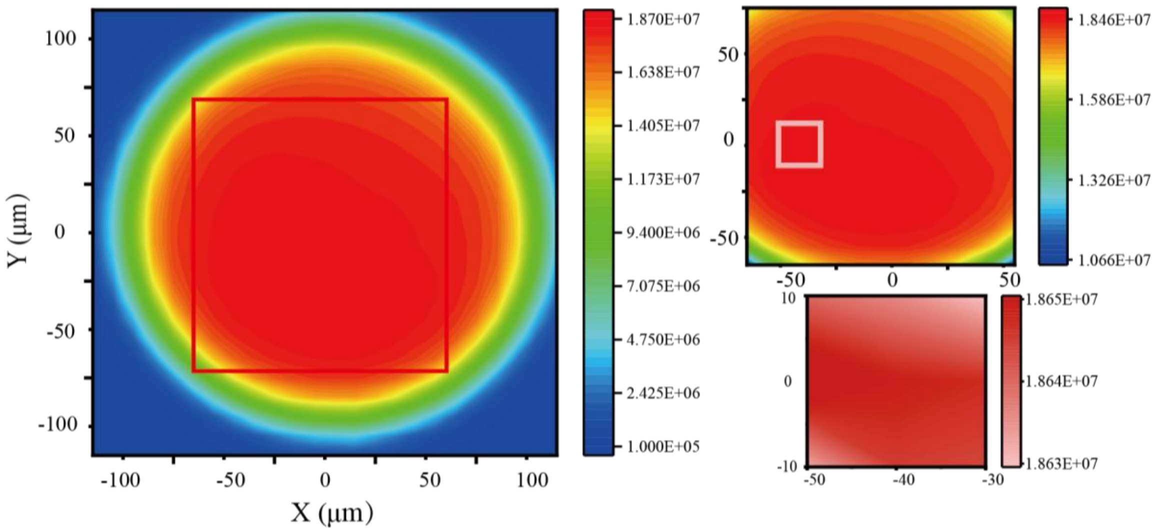

Fig. 5. Non-uniformity of DUT single-photon detector Det-18752.

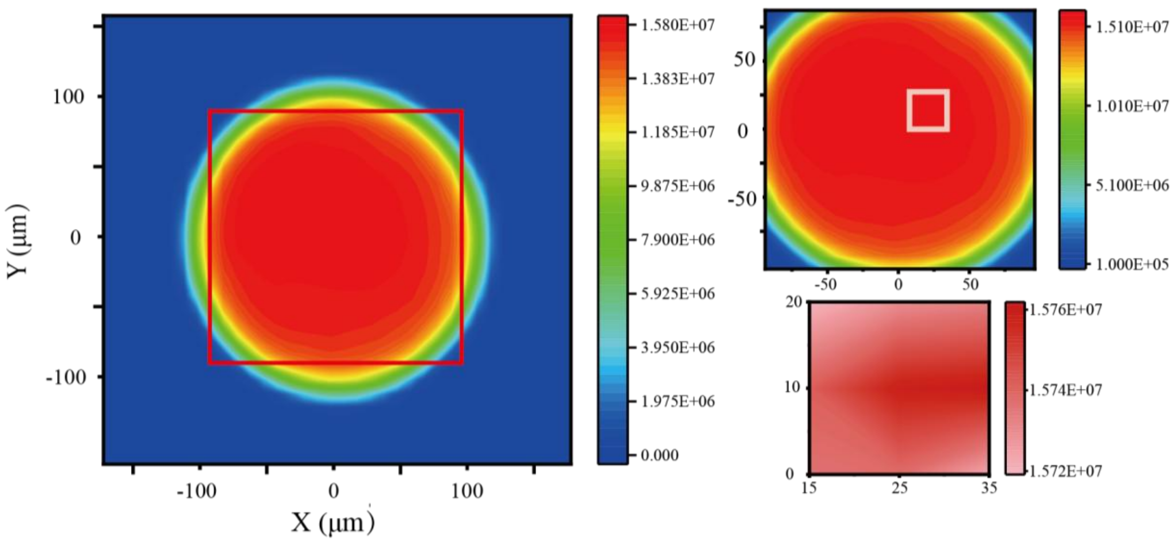

Fig. 6. Non-uniformity of DUT single-photon detector Det-19743.

Table 1. The measurement positions of the DUT single-photon detectors

DUT single-photon detectors	The measurement positions relative to the center of the DUT single-photon detectors (0, 0)
Det-18752	(–40 μm, 0)
Det-19743	(+25 μm, +10 μm)

5. Measurement results and uncertainty analyses

The equation to calculate the detection efficiency of the single-photon detectors, $E_{SPAD}(\lambda)$, is:

$$E_{SPAD}(\lambda) = \frac{N_{SPAD}\cdot(h\cdot c)/\lambda}{P},$$

where N_{SPAD} is the number of photons detected by the single-photon detector within unit amount of time, *h* Planck Constant, *c* the velocity of light in vacuum, λ wavelength, and *P* the optical power.

5.1 The spectral responsivity of the transfer photodetector

The spectral responsivity of the transfer photodetector is traceable to absolute cryogenic radiometer via the reference photodetector. Through calibration and wavelength interpolation, the spectral responsivity of the transfer photodetector is determined to be 0.5247×10^{11} V/W at 844.5 nm @~10 pW. The linearity of the transfer photodetector is measured from 10 pW to 0.1 pW. The spectral responsivity @~0.1 pW is 0.5238×10^{11} V/W with a combined uncertainty of 0.21%.

5.2 Repeatability of calibration

The transfer photodetector is used to calibrate the DUT single-photon detectors. 10 rounds of measurements have been conducted. In each round, the transfer photodetector collects 600 readings with 0.1 s integration time for each reading and the average of the 600 readings is used for detection efficiency calculation; the DUT single-photon detector collects the photon counts within exactly 60.00 s and the photon counts per second is used for detection efficiency calculation; the background photon count rate is <1000 /s and the standard deviation is <5 /s. The repeatabilities of the detection efficiency measurements are 0.078% (Det-18752) and 0.083% (Det-19743), respectively.

5.3 Non-uniformity of the DUT single-photon detector

Within ±10 μm to the measurement positions (as listed in Table 1.), the non-uniformity is measured to be 0.043% (Det-18752) and 0.079% (Det-19743), respectively.

5.4 Dead-time impact correction

The detection efficiencies of the DUT single-photon detectors are calibrated from 0.1 pW to 0.5 pW. High-resolution temporal profiles of the analog voltage outputs of the DUT single-photon detectors are recorded and show the dead-time and after-pulsing effects. A Monte Carlo simulation validates that for the DUT single-photon detectors measured at the power level of 0.1 pW to 0.5 pW, the detection efficiencies at 1 photon can be linearly extrapolated with uncertainties of 0.020%.

5.5 After-pulsing probability correction

The high-resolution temporal profiles of the analog voltage outputs of the DUT single-photon detectors are analyzed to find out the universal component of the afterpulsing probabilities are 0.31% (Det-18752) and 0.27% (Det-19743), respectively. The measurement uncertainties are 0.030% (Det-18752) and 0.023% (Det-19743), respectively. The detection efficiencies of the DUT single-photon detectors at 844.5 nm are measured and corrected to be 46.8% (Det-18752) and 51.3% (Det-19743), respectively.

5.6 Combined uncertainty at 844.5 nm

The uncertainty components are combined to evaluate the relative standard combined uncertainty, as listed in Table 2.

Table 2. Measurement results and standard relative uncertainties

Uncertainty sources	Type	Det-18752	Det-19743
Spectral responsivity of the transfer photodetector	B	0.21%	0.21%
Repeatability of calibration	A	0.078%	0.083%
Non-uniformity of the DUT single-photon detector	B	0.043%	0.079%
Dead-time impact correction	B	0.020%	0.020%
After-pulsing probability correction	B	0.030%	0.023%
Combined relative standard uncertainty (k=1)		0.23%	0.24%

The detection efficiencies of the DUT single-photon detectors at **844.5 nm** are **46.8%** for **Det-18752** with a relative standard uncertainty of **0.23%**, and **51.3%** for **Det-19743** with a relative standard uncertainty of **0.24%**, respectively.

5.7 Wavelength correction from 844.5 nm to 850 nm

Based on the relative spectral responsivity curve, the detection efficiencies of the DUT single-photon detectors at 850 nm are evaluated to be 45.7% (Det-18752) and 50.1% (Det-19743), respectively. The uncertainties for the wavelength corrections are 0.24%.

5.8 Combined uncertainty at 850 nm

The uncertainty components are combined to evaluate the relative standard combined uncertainty, as listed in Table 3.

Table 3. Measurement results and standard relative uncertainties

Uncertainty sources	Type	Det-18752	Det-19743
Spectral responsivity of the transfer photodetector	B	0.21%	0.21%
Repeatability of calibration	A	0.078%	0.083%
Non-uniformity of the DUT single-photon detector	B	0.043%	0.079%
Dead-time impact correction	B	0.020%	0.020%
After-pulsing probability correction	B	0.030%	0.023%
Wavelength correction (from 844.5 nm to 850 nm)	B	0.24%	0.24%
Combined relative standard uncertainty (k=1)		0.33%	0.34%

The detection efficiencies of the DUT single-photon detectors at **850 nm** are **45.7%** for **Det-18752** with a relative standard uncertainty of **0.33%**, and **50.1%** for **Det-19743** with a relative standard uncertainty of **0.34%**, respectively.

CCPR WG-SP TG 11

Pilot study on the detection efficiency of single-photon detectors – Si-SPAD

INRIM - Technical Report

Alice Meda, Salvatore Virzì, Ivo Pietro Degiovanni and Giorgio Brida

Table of Contents

1.1 Definition of the measurand 2
1.2 Description of the measurement facility 3
1.3 Experimental model and traceability 4
1.3.1 Transmissivity characterization 4
1.3.2 Source stability 5
1.3.3 Estimation of efficiency 5
1.4 Results 5
1.5 Uncertainty budget 8
1.6 DUTs active area characterization 9
1.7 Wavelength dependence 10
1.8 References 11
1.9 Summary of results 12
Detection efficiency of Si-SPAD 1 - Measurement results 12
Detection efficiency of Si-SPAD 2 - Measurement results 13

1.1 Definition of the measurand

The measurand is the **detection efficiency** [1] of the transfer detector (here and after DUT).

More precisely, as reported in the CCPR WG-SP TG 11 “Pilot study on the detection efficiency of single-photon detectors – Si-SPAD” technical report: “..the measurand for the Si-SPAD detector is the detection efficiency of the transfer detector at low signal (close to 1 photon per second) at a wavelength of 850 nm under continuous wave irradiation in free space with a beam diameter (1/e2-value) smaller than 40 µm, (or at least 99.9 % beam capture)”.

The INRiM adopted method for measuring the detection efficiency is the substitution method [2, 3], based on the direct comparison of the DUT with respect to a classical reference detector. Such a comparison is possible only after a strong attenuation of the source when measured by the DUT, allowing to switch from the macroscopic (> nW) to the photon-counting regime.

The classical detector provides a SI-traceable measurement of the optical power *P* of the source (a stable laser source); its output is compared to the output of the SPAD, that is the corresponding single-photon rate *R* after the attenuation. The attenuation measurement traceability is ensured by measuring it with the classical standard detector too.

Following the substitution method, for a wavelength λ, the detection efficiency of the SPAD η(λ) can be estimated comparing the macroscopic optical power P of the laser source, measured with a SI-traceable calibrated detector, and the counts *N* measured by the DUT after attenuating the same signal down to the single-photon level:

$$\eta(\lambda) = \frac{hc}{\lambda t}\frac{\mathrm{N}}{\tau P} \quad (1)$$

where *h* is the Planck constant, *c* is the speed of light in vacuum, *t* is the acquisition time, and τ the transmissivity due to the introduced attenuation.

1.2 Description of the measurement facility

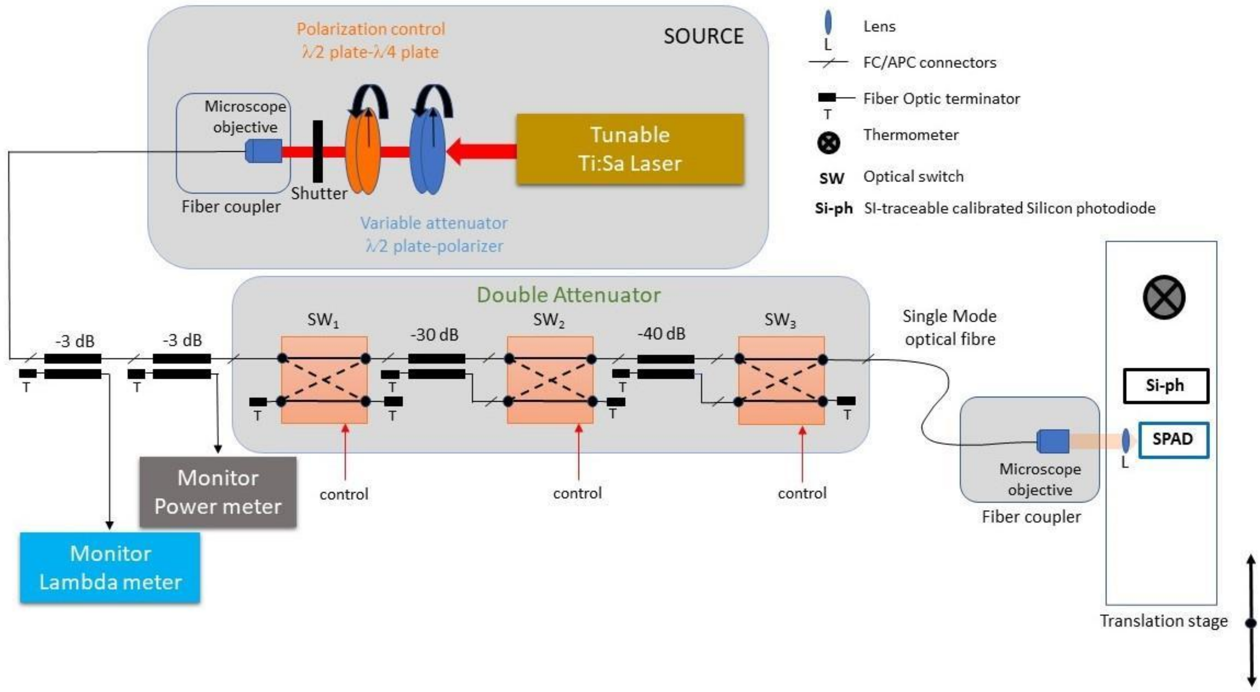

Figure 1 The INRiM measurement facility for the detection efficiency

The measurement facility allows measuring η at a wavelength of 850 nm when the photons are sent in free space with a spatial-distribution diameter smaller than 40 μm.

The calibration setup is depicted in Figure 1. The source is a Ti:Sa laser tunable in wavelength, set to at the wavelength of $\lambda = (850.711 \pm 0.006)\ nm$. The optical power is controlled by a polarization-based variable attenuator, composed by a half waveplate and a polarizer, to select the required single-photon rate *R=N/t.*

Thereafter, the source polarization is properly rotated by a system of half waveplate and quarter waveplate, to result horizontal on the DUT, as required by the measurement protocol CCPR WG-SP TG 11.

Then, the photons pass through a mechanical shutter, and are fiber-coupled, by a 20X microscope Objective, in a single-mode fiber. Exploiting two 50:50 beamsplitters, both the optical power and the emission wavelength stability of the source are monitored. The photons are then addressed to a second fully-pigtailed attenuator stage to obtain the strong attenuation needed to pass from the classical to the photon counting regime. It consists of two unbalanced beam splitters: the former 999:1 and the latter 9999:1, respectively allowing introducing a 30dB and a 40dB attenuation. The light path is selected thanks to three pc-controlled optical switches. Selecting the path corresponding to the maximum attenuation (nominal 70dB), the double-attenuator stage reproduces the transmissivity τ required in Eq. 1.

Finally, the photons will be out-coupled and collimated in free space with a Gaussian spatial mode to be sent into a shielding box for minimizing environmental photons.

The temperature is maintained within the range of (23±1) ◦C, as requested by the protocol.
A motorized translation stage allows selecting the measuring detector depending on the introduced attenuation: a SI traceable Silicon photodiode (Si-ph, Hamamatsu S1337-1010BQ) for the traceable measurements of *P*, and the Si-SPAD device under test (DUT) for the measurement of *N*, when the attenuation reproduces τ and the photon flux goes down to the single-photon level.

Since the usual diameter of a free-space Si-SPAD active area is about hundreds of micrometers, a lens focuses the photons spatial distribution on it in a diameter of 40μm.

The DUT position is optimized exploiting three actuators in the x,y and z directions. All the devices of the depicted set-up are connected to a computer via LabVIEW interface, and the measurement routines are automatized.

1.3 Experimental model and traceability

The detection efficiency is estimated adapting Eq. 1 to the measurements realized with the experimental apparatus described in the previous section, i.e. comparing the DUT measurements and the output photocurrent of the silicon photodiode.
The SPAD produces a macroscopic pulse for each revealed photon and sends it to the electronics that collects *N* counts in a time interval *t*, whereas the output photocurrent from the photodiode is the incident optical power times the spectral responsivity $s(\lambda)$; the photocurrent is measured by a picoammeter with calibration factor *C*. The transmissivity τ is pc-controlled, and it has been independently measured (see below). Furthermore, one has to consider also the transmissivity *T* of the lens in front of the DUT (see Fig. 1) and the (intrinsic and environmental) noise level for both the DUT and the photocurrent measurements (N^{env} and A^{env}), that account for dark counts and background photons as well as for the dark current. For the *i*-th measurement run Eq. 1 becomes:

$$\eta_i(\lambda) = \frac{hc}{\lambda t} \frac{s(\lambda)\left(N_i - N_i^{env}\right)}{\tau\, C\left(A_i - A_i^{env}\right)T} \quad (2)$$

The calibration of the picoammeter for the photocurrent measurement (factor *C*) is traceable to INRIM while the photodiode absolute spectral responsivity s at the wavelength of 850 nm is traceable to PTB.

1.3.1 Transmissivity characterization

The transmissivity τ is characterized exploiting the Si-ph detector. Our dual-attenuator approach enables us to divide the introduced attenuation, which is crucial for maintaining the linear response of the detector. Introducing the entire attenuation at once would compromise this linearity, increasing the related uncertainty and the accuracy and reliability of the experimental data. Therefore, τ is evaluated as $\tau = \tau_{30dB}\tau_{40dB}$, where:

$$\tau_{x\,dB} = \frac{A_{x\,dB} - A^{env}}{A_{0\,dB} - A^{env}} \quad (3)$$

with the subscript *x* indicating the selected attenuation by the optical switches.

We characterize τ (Eq. 3) averaging over a sequence of 100 measurements. Then, we repeat ten times the τ characterization in different days, i.e. evaluating the repeatability behaviour of our double-attenuator system, obtaining $\tau = (2.160 \pm 0.007) \cdot 10^{-7}$ highlighting a reasonable repeatability of our system day by day.
We underline that our double-attenuator approach allows good repeatability since it does not require to disconnect the optical fibers.

1.3.2 Source stability

To monitor the source stability, we exploit the power meter measurements at the source monitor stage. This allows us to correct the measured N_i and A_i in Eq.s 2 and 3 with respect to the source fluctuations according to:

$$N_i \rightarrow N_i' = N_i \rho_i^{DUT} \quad (4)$$

$$A_i \rightarrow A_i' = \varepsilon A_i \rho_i^{Si-ph} \quad (5)$$

where: $\rho_i^{DUT} = \langle P_i^{DUT} \rangle / P_i^{DUT}$ represents the correction with respect to the monitor power meter measurement P occurred during the *i*-th run of the DUT measurement N_i; the same argument holds for ρ_i^{Si-ph}. Furthermore, since an unbalancement may happen between the average source optical power emission during the DUT and the Si-ph measurements, we have introduced the parameter $\varepsilon = \langle P_i^{DUT} \rangle / \langle P_i^{Si-ph} \rangle$.

1.3.3 Estimation of efficiency

To remove the arbitrary dependence on the count rate, we estimate the zero-flux efficiency η_0, i.e. the detection efficiency extrapolated to the zero-flux level, whose value is not affected by the presence of the SPD dead time.

The behavior of the detection efficiency can be described as:

$$\eta_i(\langle N_i' \rangle) = \eta_0 (1 - D \frac{\langle N_i' - N^{env} \rangle}{t}) \quad (6)$$

where D is the dead time and N_i' is defined in Eq. 4. Hence, estimating the efficiency for different photon fluxes, η_0 comes out from a linear regression.

1.4 Results

We measured the detection efficiency of two Si-SPADs:

DUT1 - Perkin-Elmer-SPCM-AQR-16 – SN: 19743

DUT2 - Perkin-Elmer-SPCM-AQR-16 – SN: 18752

We measured the DUTs detection efficiency (accordingly to Eq. 2) at different photon fluxes acting on the variable attenuator depicted in Figure 1, obtaining various count-rate regimes, from 5000 counts/s to $2 \cdot 10^6$ counts/s. After collecting ten data points, we perform the linear regression as described in Eq. 6 to estimate η_0.

We obtained:

DUT1: $\boldsymbol{\eta_0} = \mathbf{0.553} \pm \mathbf{0.003}$ (coverage factor K = 1).

DUT2: $\boldsymbol{\eta_0} = \mathbf{0.533} \pm \mathbf{0.003}$ (coverage factor K = 1).

Figure 2,3 report DUT1 and DUT2 detection efficiency measurements, respectively, for different count rates R = $\frac{\langle N_i' - N^{env} \rangle}{t}$.

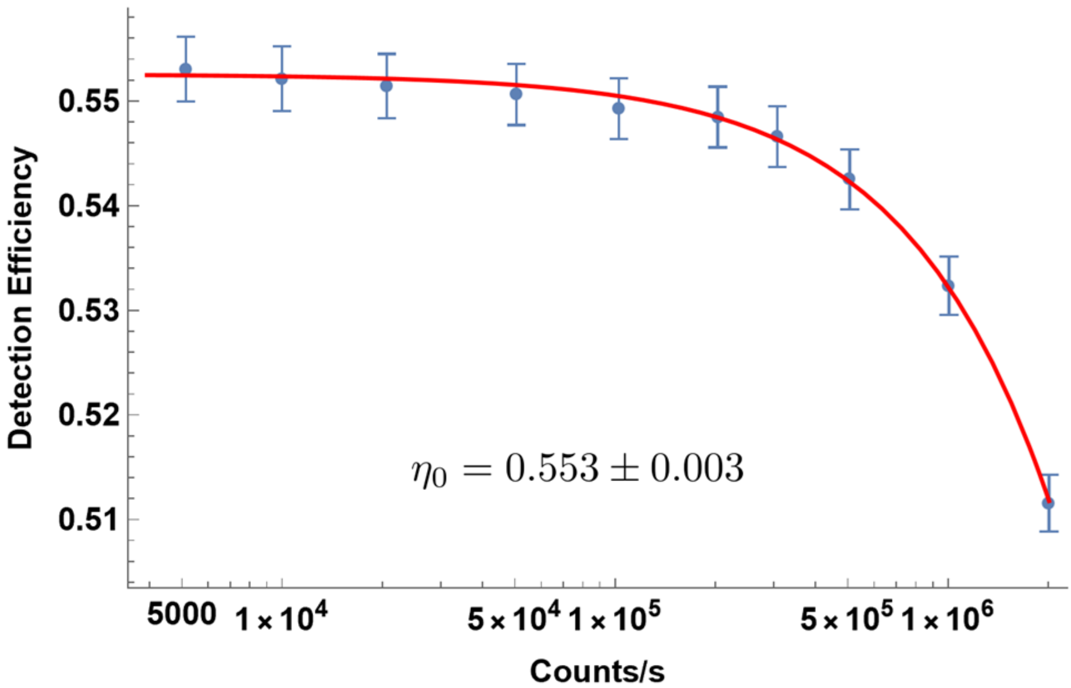

Figure 2 DUT1 detection efficiency estimation for different count rates R. The blue dots represent the calculated detection efficiencies with their related uncertainties, as determined by Eq. (2), while the red line is the result of the linear regression according to Eq. (6). η_0 is obtained as the intercept of the fit with the y-axis. All the shown uncertainties consider the standard measurement uncertainty

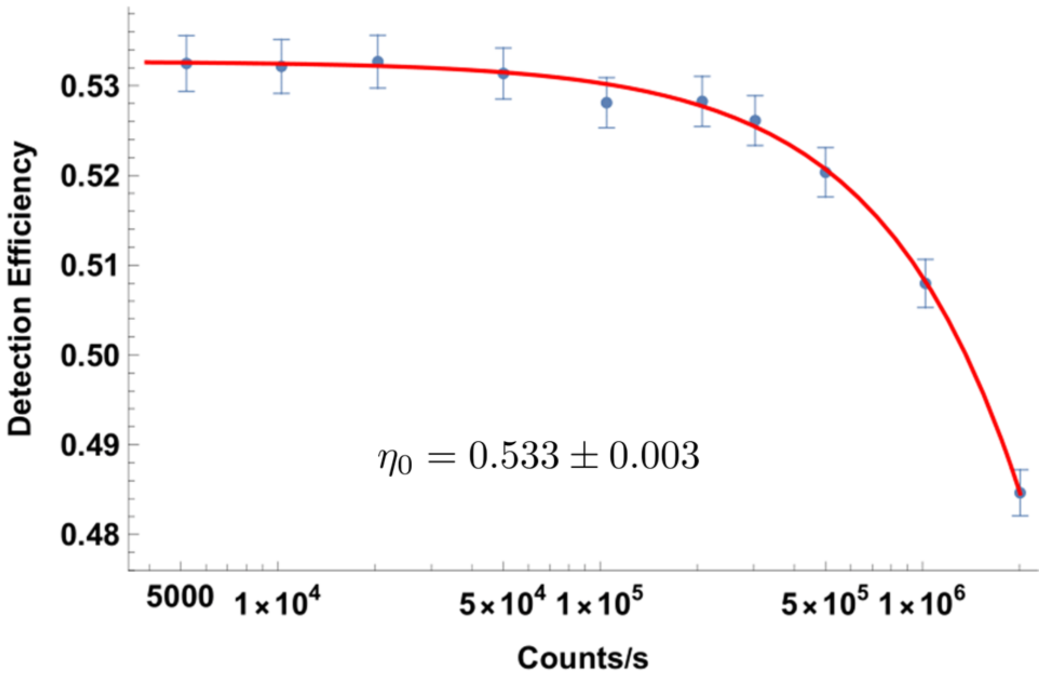

Figure 3 DUT2 detection efficiency estimation for different count rates R. The blue dots represent the calculated detection efficiencies with their related uncertainties, as determined by Eq. (2), while the red line is the result of the linear regression according to Eq. (6). η_0 is obtained as the intercept of the fit with the y-axis. All the shown uncertainties consider the standard measurement uncertainty

To assess the robustness of the technique, we repeat the entire estimation process for both DUT1 and DUT2 ten times.

The results are illustrated in Figure 4,5, respectively. For DUT1, the resulting estimations of η_0 exhibit strong agreement. The average value obtained for the detection efficiency at zero-photon flux is: $\langle \boldsymbol{\eta_0} \rangle = \mathbf{0.551 \pm 0.003.}$

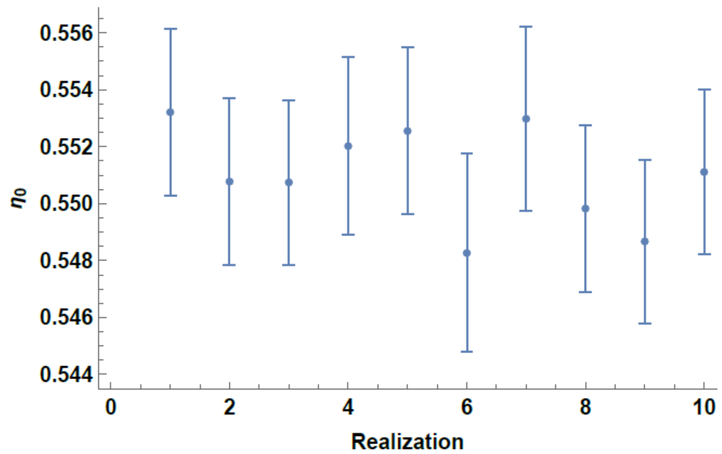

Figure 4 Repetition of the estimation process for DUT1

On the other hand, measurements on DUT2 show an unexpected behaviour of the SPAD, with unstable results that suggests that the efficiency jumps between two different levels: $\langle \boldsymbol{\eta_{0A}} \rangle = \mathbf{0.508 \pm 0.003}$, and $\langle \boldsymbol{\eta_{0B}} \rangle = \mathbf{0.531 \pm 0.003.}$

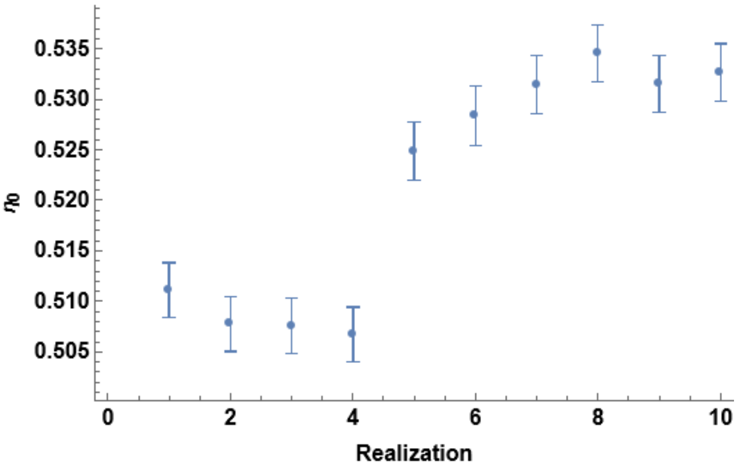

Figure 5 Repetition of the estimation process for DUT2

We demonstrate it with a Welch's *t*-test, in order to recognize the two data populations.
In particular, if one implements such a test only on the estimated efficiencies the probability that the two populations are the same is $1.2 \cdot 10^{-6}$, while adding the maximum likelihood estimation such probability becomes $1.3 \cdot 10^{-5}$.

Since the behaviour of DUT2 is unstable, in the following sections we report details on the measurement and uncertainty budget only for the measurements of η_0 relative to DUT1.

1.5 Uncertainty budget

Uncertainties are propagated from Eq. 2, considering both statistical and non-statistical contributions. Figure 6 reports an example of uncertainty budget for a fixed count rate with $N' = 20655 \pm 27$.

Coefficient	Value	Uncertainty	% Contribution
N'	20655	27	5.47
N^{env}	28	1	0.012
A'	$1.92807 \times 10^{-8}\,\mathrm{A}$	$4.9 \times 10^{-12}\,\mathrm{A}$	0.06
A^{env}	$4.88 \times 10^{-14}\,\mathrm{A}$	$1.3 \times 10^{-15}\,\mathrm{A}$	1.5×10^{-8}
τ	2.1601×10^{-7}	7.0×10^{-10}	33.83
ε	1.0148	1.4×10^{-3}	5.70
s	$0.4766\,\mathrm{W/A}$	$1.9 \times 10^{-3}\,\mathrm{W/A}$	51.55
C	1.000023	1.0×10^{-5}	3.2×10^{-4}
T	0.985000	3.0×10^{-5}	3.0×10^{-3}
λ	$8.50711 \times 10^{-7}\,\mathrm{m}$	$6 \times 10^{-12}\,\mathrm{m}$	1.6×10^{-4}
t	$1.0000\,\mathrm{s}$	$1.0 \times 10^{-3}\,\mathrm{s}$	3.22
$\langle \eta(N', \lambda) \rangle$	0.5514	0.0031	

Figure 6 Uncertainty budget related to the detection efficiency

The data analysis is performed from experimental data via Wolfram Mathematica software. Both the data and the Mathematica files are saved into a dedicated PC.

1.6 DUTs active area characterization

We characterize the spatial response of the DUT, that presents a circular active area of 200 μm in diameter. We illuminate the surface with the light source and exploited two actuators in the x and y directions. The z direction was previously fixed, by using a third actuator, where the beam was focused with waist around 40 μm. Results of the characterization of the surfaces of DUT1 and DUT2 are reported in Figure 7 a) and b), respectively.

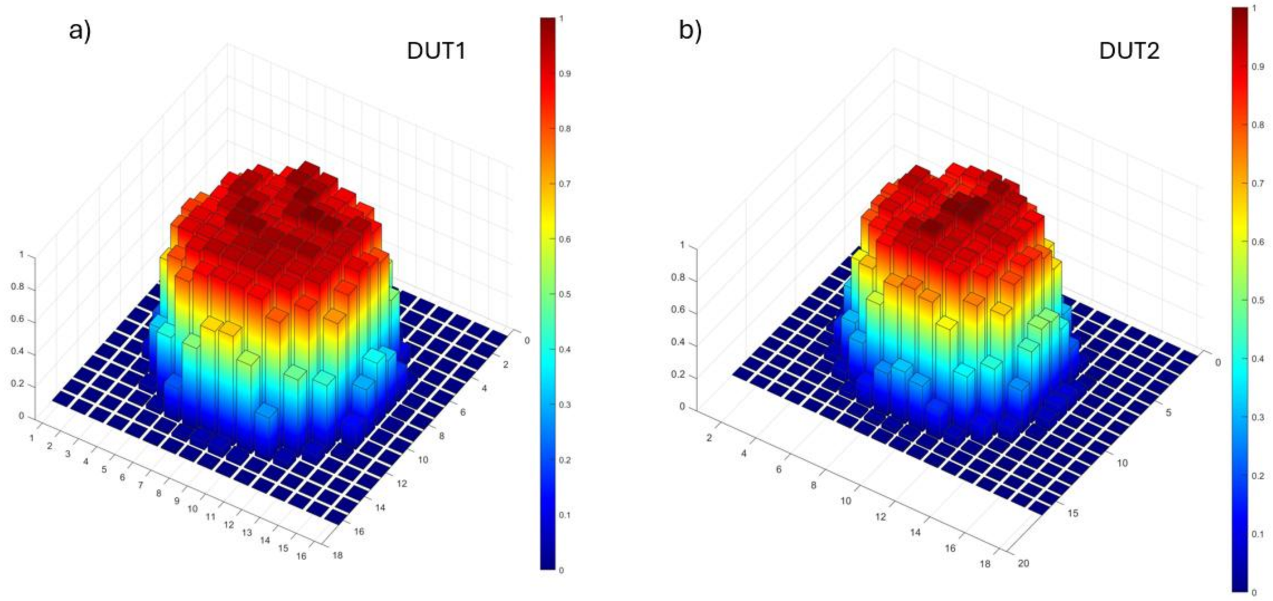

Figure 7 Scan of the Si-SPAD's active area obtained by setting a step size of 20 μm in both the directions transversal to the photons propagation.

The surface of the active area of DUTs is measured with steps of 20 μm; results are summarized in Figure 7 that shows the normalized counts registered for different positions of the beam on the active surface of the SPAD. Counts are corrected for the fluctuations of the beam by using the monitor power meter. In DUT1 spatial response is relatively uniform while the surface of DUT2 presents more irregularities; for this reason, we decided to perform a measurement on DUT 2 with steps of 10 μm, reported in Figure 8. The surface presents dips located on the left side of the scan.

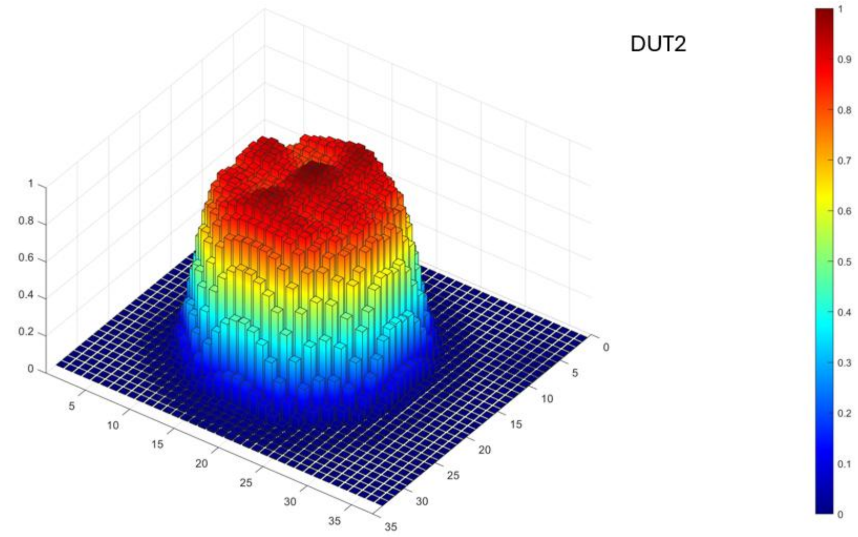

Figure 8 Scan of the DUT2 active area obtained by setting a step size of 10 µm in both the directions transversal to the photons propagation

During the procedures for the measurements of the efficiency, the DUT2 position is fixed far from the dips.

1.7 Wavelength dependence

Measuring detection efficiency of DUT1, at a fixed count rate, slightly tuning the emission of the laser in wavelength, we observed a dependence of the efficiency on the wavelength of the laser source. The experimental data exhibit a distinctive sinusoidal pattern (see Figure 9), which we attribute to an etaloning effect caused by the two surfaces of the optical window in the SPAD packaging (note that the reference detector used in this study is windowless). Specifically, for a window with thickness *L* and refractive index *n*, the transmissivity varies with the wavelength through the parameter Γ, as expressed in Ref. [4]

$$\Gamma(\lambda, n, L) = \frac{\gamma(1-\exp\left[-2i\frac{2\pi}{\lambda}n\,L\right])}{1-\gamma^2\exp\left[-2i\frac{2\pi}{\lambda}n\,L\right]} \qquad (7)$$

where $\gamma = (n - n_a)/(n + n_a)$, with n_a the air refractive index.
The overall detection efficiency in Eq. 2 can be generalized as:

$$\eta_i(\lambda, n, L) = \eta_i(\lambda)(1 - |\Gamma(\lambda, n, L)|^2) \qquad (8)$$

Our proposed model shows good agreement with the experimental data, as shown in Figure 9, where we adopted the refractive index of quartz (*n* = 1.4525) and the nominal thickness (*L* = 100 µm) as specified by the SPAD manufacturer.

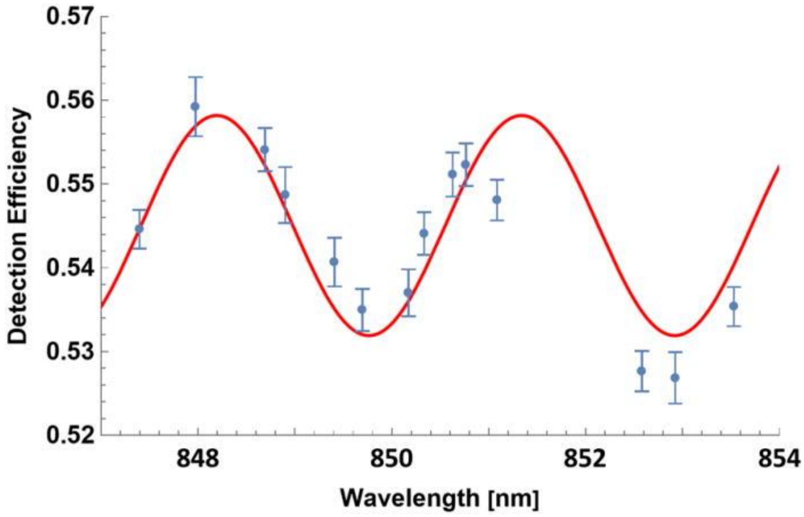

Figure 9 Detection efficiency as a function of wavelength. The number of detected photons, for each acquisition, is approximately $N' \simeq 10^5$ counts/s. The blue dots represent the experimental results while the red line corresponds to the fitted model described by Equation 8

These results emphasize the significant influence (about 5% of detection efficiency variation for 3 nm of wavelength range) of transmittance effects caused by the optical window. This result suggests to account for these effects for a complete metrological characterization of the detection efficiency of free-space SPADs, rather than limiting the analysis to a single wavelength.

1.8 References

[1] J. C. Bienfang, J. Bienfang, T. Gerrits, P. Kuo, A. Migdall, S. Polyakov, and O. T. Slattery, "Single-Photon Sources and Detectors Dictionary", US Department of Commerce, National Institute of Standards and Technology (2023).
[2] M. Lopez, H. Hofer, and S. Kück, "Detection efficiency calibration of singlephoton silicon avalanche photodiodes traceable using double attenuator technique," J. Mod. Opt. 62, 1732–1738 (2015).
[3] M. Lopez, A. Meda, G. Porrovecchio, R. Starkwood, M. Genovese, G. Brida, M. Smid, C. Chunnilall, I. Degiovanni, and S. Kück, "A study to develop a robust method for measuring the detection efficiency of free-running InGaAs/InP single-photon detectors," EPJ Quantum Technol. 7, 14 (2020).
[4] H. A. Macleod and H. A. Macleod, Thin-Film Optical Filters (CRC Press, 2010).

1.9 Summary of results

Detection efficiency of Si-SPAD 1 - Measurement results

Device Under Test (DUT) Silicon Single Photon Avalanche Diode, type Perkin-Elmer-SPCM-AQR-16 – SN: 19743

Table 1 Measurement results at 850 nm of DUT

Incident signal (photons/s)	Detection Efficiency	Combined uncertainty K=1
1	0.551	0.003

Ambient temperature: (23 ± 1) °C

Wavelength: (850.711 ± 0.006) nm

Polarization with respect the detector module: horizontal

Source used: CW Ti:Sa laser

Beam diameter at detector: 40 μm

Detection efficiency of Si-SPAD 2 - Measurement results

Device Under Test (DUT) Silicon Single Photon Avalanche Diode, type Perkin-Elmer-SPCM-AQR-16 – SN: 18752

Table 1 Measurement results at 850 nm of DUT2

Incident signal (photons/s)	Detection Efficiency	Combined uncertainty K=1
1	0.508	0.003
1	0.531	0.003

Ambient temperature: (23 ± 1) °C

Wavelength: (850.711 ± 0.006) nm

Polarization with respect the detector module: horizontal

Source used: CW Ti:Sa laser

Beam diameter at detector: 40 μm

Result Report for CCPR WG-SP TG 11
Pilot study on the detection efficiency of single-photon detectors – Si-SPAD

KRISS, Korea

Dong-Hoon Lee, Kee Suk Hong, In-Ho Bae

dh.lee@kriss.re.kr

1. Calibration Results

SPAD	*DE* at 850 nm	U(*DE*) (k = 2)	Measurement Date
#18752	0.548	0.018	2023.07.27
#19743	0.598	0.024	2023.07.27

2. Measurement Setup and Instruments

The measurement is performed by using the responsivity comparison setup as shown in the following figure. A tunable monochromatic light is provided in a wavelength range from 250 nm to 1000 nm from a laser-driven light source (LDLS) and a double-grating monochromator. As the reference detector, a photodiode with a switched integrating amplifier is used, whose spectral responsivity is calibrated at a photo-current level of pico-Ampere. A fibre-based spatial filter is used to form a beam focus that is focused to a diameter of less than 100 μm at the detector under test (DUT). The DUT is mounted on a motorized 3-axis stage for a precision alignment. The technical details of the setup is described in the following publication:

[BAE2019] In-Ho Bae *et al.*, *Detection efficiency measurement of single photon avalanche photodiodes by using a focused monochromatic beam tunable from 250 nm to 1000 nm*, Metrologia 56 (2019) 035003.

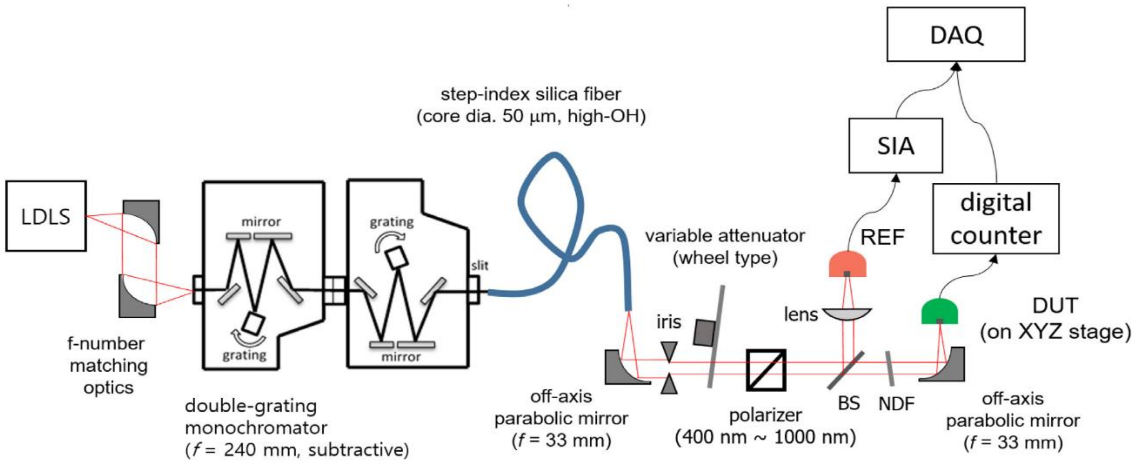

Fig. 1 Responsivity comparison setup of KRISS used for DE calibration of SPAD detectors

3. Measurement Conditions and Parameters

- spectral bandwidth: less than 4.5 nm in full-width at half maximum (FWHM)
- polarization: random
- beam diameter: 100 μm in full-width at 13.5%
- photon flux level for calibration: : 20 kcps ~ 30 kcps
- dead time (measured): 23.4 ns (#18752), 23.9 ns (#19743)
- after-pulsing probability (measured): 0.14% (#18752), 0.13% (#19743)
- laboratory conditions: temperature (23 ± 2) °C, relative humidity < 45 %

The following figures show the results of spatial scan of the DUT responsivity performed at a wavelength of 550 nm. The position of the beam incidence was aligned at the middle of the observed response plateaus.

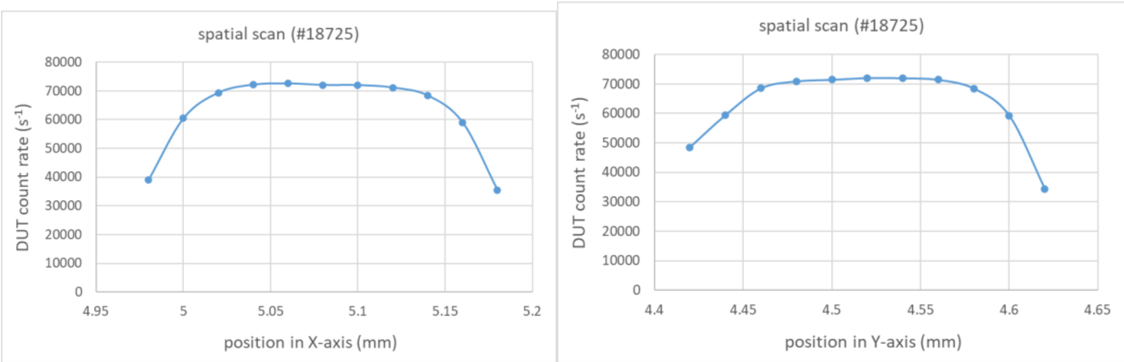

Fig. 2 Spatial scan results of responsivity for DUT #18725.

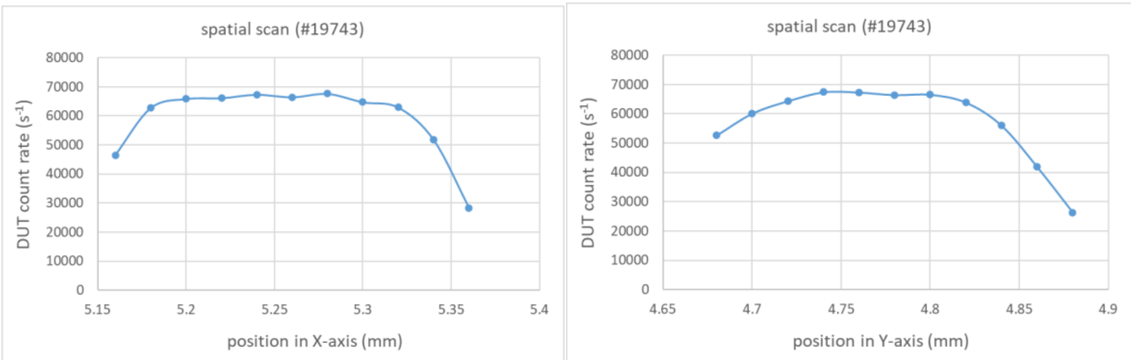

Fig. 3 Spatial scan results of responsivity for DUT #19743.

4. TRACEABILITY OF MEASUREMENT

The reference detector used for the spectral responsivity measurement is calibrated traceable to the scale realisation at KRISS based on the absolute cryogenic radiometer at two laser wavelengths and the spectral reflectance of a pyroelectric detector at other wavelengths. The electrical measurements by using a switched integrating amplifier was calibrated traceable to the up-to-date realisation of the measurement standards at KRISS. The following publications can be referenced for the traceability of the DE measurement at KRISS:

[PARK2022] Seongchong Park *et al.*, *Measurement-based extrapolation of spectral responsivity by using a low-NEP pyroelectric detector*, Meas. Sci. Technol. 33 (2022) 01513.

[PARK2016] Seongchong Park *et al.*, *Switched integration amplifier-based photocurrent meter for accurate spectral responsivity measurement of photometers*, Appl. Opt. 55 (2016) 2285.

5. MEASUREMENT UNCERTAINTY

The equations and detailed analysis of measurement uncertainty for DE are described [BAE2019]. The uncertainty budgets are summarized in the following tables.

Table 1. Uncertainty budget of DE at 850 nm for the DUT #18752.

Uncertainty Component	**Standard uncertainty (%)**	**Type**	**Probability distribution**	**Sensitivity coefficient**	**Contribution (%)**	**Deg. of freedom**
REF calibration	1.3	B	normal	1	1.3	∞
Read repeatability of the ratio (DUT counts/REF current)	0.96	B	student-t	1	0.96	30
Wavelength error of the ratio (DUT counts/REF current)	0.35	B	rectangular	1	0.35	∞
Spatial beam mismatch of the ratio (DUT counts/REF current)	0.09	B	rectangular	1	0.09	∞
Beam position instability of the ratio (DUT counts/REF current)	0.13	B	rectangular	1	0.13	∞
Uncertainty of dead time measurement	0.1	A	student-t	0.0005	<0.01	4
Combined standard uncertainty (%)	**--**	**--**	**normal**	**--**	**1.66**	**>1000**

Table 2. Uncertainty budget of DE at 850 nm for the DUT #19743

Uncertainty Component	**Standard uncertainty (%)**	**Type**	**Probability distribution**	**Sensitivity coefficient**	**Contribution (%)**	**Deg. of freedom**
REF calibration	1.3	B	normal	1	1.3	∞
Read repeatability of the ratio (DUT counts/REF current)	1.45	B	student-t	1	1.45	30
Wavelength error of the ratio (DUT counts/REF current)	0.21	B	rectangular	1	0.21	∞
Spatial beam mismatch of the ratio (DUT counts/REF current)	0.09	B	rectangular	1	0.09	∞
Beam position instability of the ratio (DUT counts/REF current)	0.13	B	rectangular	1	0.13	∞
Uncertainty of dead time measurement	0.1	A	student-t	0.0005	<0.01	4
Combined standard uncertainty (%)	**--**	**--**	**normal**	**--**	**1.97**	**>1000**

Measurement Standards Laboratory of New Zealand

CCPR WG-SP TG 11

Pilot study on the detection efficiency of single-photon detectors – Si-SPAD

January 31, 2025

Prepared by: Joseph Borbely

Contents

1 Overview ... 1

2 Apparatus ... 3

3 Uncertainty Contributions ... 6
- 3.1 Fundamental Constants ... 6
- 3.2 Light Source ... 6
  - 3.2.1 Wavelength ... 6
  - 3.2.2 Polarization ... 8
  - 3.2.3 Bandwidth/Linewidth ... 8
  - 3.2.4 Power Stability ... 8
- 3.3 Transmission Coefficient ... 9
- 3.4 Standard Photodiode ... 9
  - 3.4.1 Spectral Responsivity ... 10
  - 3.4.2 Transimpedance Amplifier Gain ... 10
  - 3.4.3 Photodiode Voltage ... 10
- 3.5 SPAD ... 11
  - 3.5.1 Count Rate ... 11
  - 3.5.2 Spatial Non-Uniformity ... 12

4 Results ... 15
- 4.1 Software ... 15
- 4.2 Si-SPAD (Sn: 18752) ... 15
  - 4.2.1 DFB Laser and Aspheric lens ... 15
  - 4.2.2 LDLS and 10x Objective ... 23
- 4.3 Si-SPAD (Sn: 19743) ... 30
  - 4.3.1 DFB Laser and Aspheric lens ... 30
  - 4.3.2 LDLS and 10x Objective ... 37
- 4.4 Detection Efficiency ... 44

A Measurement Procedures ... 46
- A.1 SPAD Alignment ... 46
- A.2 Detection-Efficiency Acquisition ... 47

B References ... 49

1 Overview

The measurement apparatus incorporates a 850-nm light source and utilizes the double-attenuation technique [1]. Detection efficiency calibration of a silicon single-photon avalanche diode (SPAD) at incident photon rates in the range of 10^3 photon counts per second (0.23 fW) to 10^6 photon counts per second (230 fW) are SI-traceable through a silicon transfer standard photodiode.

The detection efficiency, η, of a SPAD is defined as

$$\eta = \frac{E_{sp} \times CR}{\Phi_{incident}} \tag{1}$$

where, E_{sp} is the energy of a single photon, CR is the count rate (dark-count subtracted) of the SPAD, and $\Phi_{incident}$ is the incident power to the SPAD.

To attenuate the optical power from the SI-traceable regime to the photon-counting regime, multiple neutral-density filters are inserted into the beam path. The transmission coefficient of a neutral-density filter is measured using the standard photodiode when all other neutral-density filters are removed from the beam path. The combined transmission coefficient when all neutral-density filters are in the beam path is taken as the product of the transmission coefficient for each neutral-density filter.

To compensate for instabilities in the source power during the measurement, the voltage from a monitor photodiode is measured simultaneously with the count rate of the SPAD as well as the voltage from the standard photodiode and the corresponding signals are normalized against the monitor signal.

Equation 1 can therefore be expressed as

$$\eta = \frac{\left(\frac{hc}{\lambda}\right) \times \frac{CR}{V_{SPAD}^{Mon}}}{\frac{\Phi_{STD}}{V_{STD}^{Mon}} \times T} \tag{2}$$

where, h is the Planck constant, c is the speed of light in vacuum, λ is the vacuum wavelength of the light source, V_{SPAD}^{Mon} is the monitor photodiode voltage (dark-voltage subtracted) measured simultaneously with CR, Φ_{STD} is the traceable power measurement from the standard photodiode, V_{STD}^{Mon} is the monitor photodiode voltage (dark-voltage subtracted) measured simultaneously with Φ_{STD}, and, T is the combined transmission coefficient of the neutral-density filters that are inserted into the beam path.

To extrapolate to low count rates (approximately 1 count per second), data are fit to the following equation (see Equation 4 in Reference [1]),

$$\eta = \frac{1 - \exp(-\eta_0 \mu)}{\mu} \quad (3)$$

where, η_0 is the ideal detection efficiency of the SPAD without any detection artefacts (such as afterpulsing and dead time) and μ is the mean photon number defined as $\mu = \frac{CR}{\eta} t_{off}$, where t_{off} is the sum of the dead time and recovery time of the SPAD. Equation 3 is valid for a light source that follows a Poissonian distribution, such as a laser.

2 Apparatus

The free-space optical path of the setup is shown in Figure 1. Light from a 850-nm source passes through a shutter, not shown in Figure 1, before entering a light-tight enclosure that contains various connector feedthroughs for signals, power and computer control of equipment. The light is split using a 50:50 non-polarizing beam-splitting cube to create the monitor beam path (transmitted) and the device-under-test beam path (reflected). The monitor photodiode (Thorlabs, SM1PD1A) is connected to a transimpedance amplifier (MSL, Sn: PH1048-03) which is connected to a digital multimeter (Keysight 3458A, Sn: MY45053748). The device-under-test beam path passes through a 12-position neutral-density filter wheel with neutral-density filters ranging from optical density 0 (i.e., no filter) to 3 and two neutral-density filters mounted on motorized flip mounts before entering a separate enclosure. Within the second enclosure, the height of the beam above the optical table is adjustable by two periscope mirrors and the beam is focused to a diameter of approximately 25 μm.

The SPAD is mounted on XYZ translation stages and aligned to the focal spot of the beam (see Section A.1). The X stage is mounted on the optical table and provides up to 150 mm of travel to position either the standard photodiode or the SPAD in the beam path. The Z stage has 25 mm of travel, is mounted on the X stage and changes the distance between the SPAD and the focusing optic. The Y stage has 13 mm of travel, is mounted on the Z stage and adjusts the height of the SPAD relative to the optical table. The count rate of the SPAD is measured with either a DAQ (NI USB-6361, Sn: 1D4FB0F) or a Time Controller (IDQ ID900, Sn: 1813050T010).

The standard photodiode (MSL, Sn: S1337-B02) is mounted on the X stage and is not positioned at the focal plane, but slightly further away from the focusing optic to allow the beam to expand to a diameter of approximately 3 mm. The standard photodiode is connected to a transimpedance amplifier (MSL, Sn: PA1039-03) which is connected to a digital multimeter (Hewlett Packard 3458A, Sn: 2823A07124).

The spatial non-uniformity of the SPAD (see Section 3.5.2) contributes the largest systematic uncertainty to the measured detection efficiency. To understand the effect of the non-uniformity of the SPAD on the detection efficiency, data are acquired using two different sources to generate 850-nm photons

- A laser-driven light source, LDLS, (Energetiq, EQ-99X) shines white light into a monochromator (Princeton Instruments, HRS-500) and the monochromatic light is coupled into a 50-μm, multimode fibre (Thorlabs, FG050LGA)
- A fibre coupled, distributed feedback laser, DFB, (Nanoplus) is controlled by a laser-diode controller (Arroyo Instruments, 6305) which regulates the temperature and operating current of the laser to 30.0 $^\circ$C and 39.2 mA, respectively,

and two different lenses are used to focus the light

- 10x plan achromat objective (Thorlabs, RMS10X)
- Aspheric lens, f=50 mm (Thorlabs, AL2550-B).

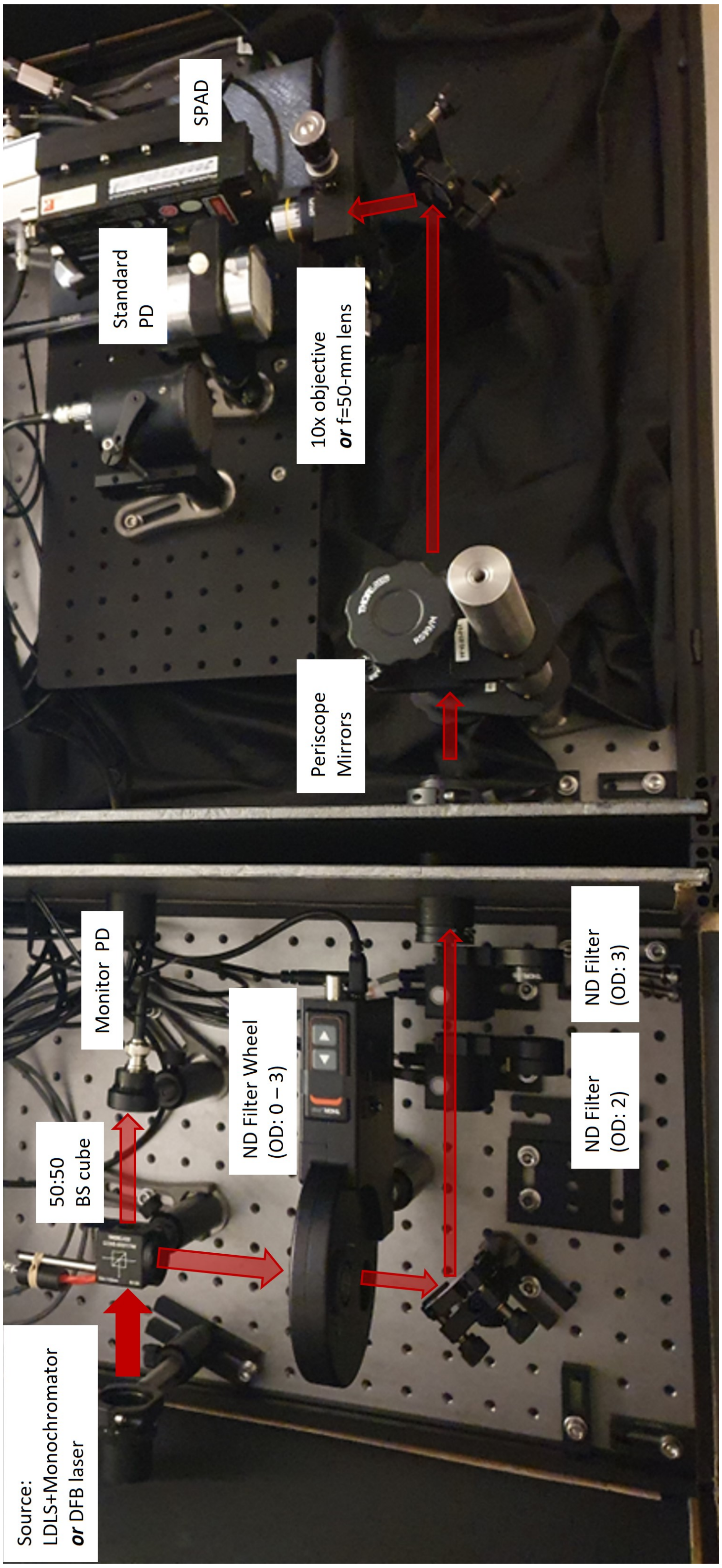

Figure 1: *Free-space setup to measure the detection efficiency of a SPAD. An additional neutral-density (ND) filter (Thorlabs NE80A), not shown, is attached to the entrance side of the beam-splitting (BS) cube when the laser is used as the light source and is kept permanently in the beam path.*

Two different optical systems are used to acquire detection-efficiency data. A comparison between the components in each optical system is shown in Table 1. Components that are the same in each optical system span the entire row.

<table>
<tr><th colspan="2">Optical Systems</th></tr>
<tr><th>Optical System 1</th><th>Optical System 2</th></tr>
<tr><td>Laser-driven light source
(Energetiq, EQ-99X)</td><td rowspan="3">Distributed feedback laser, fibre-coupled package (NanoPlus, Sn: 2439/23-18)</td></tr>
<tr><td>Monochromator
grating: 600 g/mm, blazed: 1 μm
(Princeton Instruments, HRS-500)</td></tr>
<tr><td>Fibre (Thorlabs, FG050LGA)</td></tr>
<tr><td>Collimator (Thorlabs, MPD01M9-F01)</td><td>Collimator (Thorlabs, TC18APC-850)</td></tr>
<tr><td colspan="2">Shutter (Thorlabs, SH1)</td></tr>
<tr><td></td><td>Neutral-density filter (Thorlabs, NE80A)</td></tr>
<tr><td colspan="2">Beam-splitting cube (Thorlabs, CCM5-BS017/M)</td></tr>
<tr><td colspan="2">12-position, neutral-density filter wheel (Thorlabs, FW212CNEB)</td></tr>
<tr><td colspan="2">Mirror (Thorlabs, PF10-03-F01)</td></tr>
<tr><td colspan="2">Flip mount with neutral-density filter (Thorlabs, NE30A)</td></tr>
<tr><td colspan="2">Flip mount with neutral-density filter (Thorlabs, NE40A-B)</td></tr>
<tr><td colspan="2">Periscope mirrors (Thorlabs, PF10-03-F01)</td></tr>
<tr><td colspan="2">Mirror (Thorlabs, PF10-03-P01)</td></tr>
<tr><td>10x objective (Thorlabs, RMS10X)</td><td>Aspheric lens, f=50 mm
(Thorlabs, AL2550-B)</td></tr>
</table>

Table 1: Comparison of the components in the two optical systems that are used.

3 Uncertainty Contributions

This section discusses the uncertainty contributions relevant to Equation 2.

3.1 Fundamental Constants

The fundamental constants, h and c, are defined in the International System of Units [2] and have no uncertainty

$$h = 6.626\,070\,15 \times 10^{-34}\ \mathrm{Js}$$
$$c = 299\,792\,458\ \mathrm{m/s}$$

3.2 Light Source

This section summarizes the properties of the light source producing the 850-nm photons.

3.2.1 Wavelength

A wavemeter (HighFinesse WS5, Sn: 709) is used to measure the wavelength of the laser and a spectrum analyser (HighFinesse LSA, Sn: 2095) is used to measure the wavelength of the monochromatic light from the monochromator.

The wavelength of the source is defined as

$$\lambda = \lambda_{display} + \lambda_{offset} + E_{offset} + E_{resolution} + E_{stability} \tag{4}$$

where, $\lambda_{display}$ is the wavelength displayed on the measuring device, λ_{offset} is the difference between standard wavelengths and the displayed wavelength, $E_{resolution}$ is the error due to the resolution of the measuring device, and $E_{stability}$ is the error associated with the long-term wavelength stability of the source.

Three standard wavelengths are used to characterise the offset of the wavemeter and the spectrum analyser at 850 nm *(the uncertainties in the standard wavelengths are much less than the resolution of the measuring device and are ignored)*

- 532.2456 nm, Nd:YAG laser locked to the *a1* component of the R(56) 32-0 transition [4]
- 632.9912 nm, HeNe laser locked to the R(127) 11-5 transition [5]
- 1064.4912 nm, Nd:YAG laser locked to the *a1* component of the R(56) 32-0 transition [4].

The standard lasers are maintained by the Length team at MSL.

Since the value of the speed of light is defined in vacuum and the standard wavelengths [3] for the realization of the metre are defined in vacuum, the wavemeter and spectrum analyser are configured to measure the vacuum wavelength.

The wavemeter and the spectrum analyser are first calibrated using the 532-nm line and then the 532-, 633-, and 1064-nm lines are measured. Next, the 633-nm line is used to calibrate the device and again the 532-, 633-, and 1064-nm lines are measured. The maximum wavelength that can be used to calibrate the spectrum analyser is 800 nm, and 900 nm for the wavemeter, so the 1064-nm line cannot be used to calibrate either device. A linear fit of the differences between the standard wavelength and the displayed wavelength versus the standard wavelength is used to estimate the offset contribution at 850 nm. For the spectrum analyser λ_{offset}=-0.0003(56) nm and for the wavemeter λ_{offset}=-0.00094(73) nm, where the value in brackets corresponds to a standard uncertainty, k=1.

Each measuring device has a resolution of 0.001 nm, which corresponds to a standard uncertainty for the device resolution of 0.00029 nm.

To determine the stability for the wavelength of the source, the value from the measuring device is continually logged for several days. The error associated with the wavelength stability is taken as a uniform distribution with a half width equal to $(\lambda_{maximum} - \lambda_{minimum})/2$ of the logged data. For the monochromatic light from the monochromator the half width is 0.108 nm and for the laser the half width is 0.001 nm, which correspond to a standard uncertainty of 0.062 nm and 0.00058 nm respectively (k=1).

The displayed wavelength when using the LDLS and monochromator is $\lambda_{display}$=850.231 nm. The displayed wavelength when using the laser is $\lambda_{display}$=850.230 nm. Therefore, using the spectrum analyser to measure the wavelength of the monochromatic light from the monochromator is (k=1)

$$\lambda_{LDLS,Mono} = 850.231 - 0.0003(56) + 0.00000(29) + 0.000(62)\ \mathrm{nm}$$
$$\lambda_{LDLS,Mono} = 850.231(62)\ \mathrm{nm}$$

and using the wavemeter to measure the wavelength of the laser is (k=1)

$$\lambda_{Laser} = 850.230 - 0.00094(73) + 0.00000(29) + 0.00000(58)\ \mathrm{nm}$$
$$\lambda_{Laser} = 850.22906(97)\ \mathrm{nm}$$

The index of refraction of air is calculated using the modified Edlén equation [6]. For an air temperature of 23(2) °C, air pressure of 101(3) kPa and relative humidity of 50(30) % in the laboratory, the refractive index of air is $n_{air} = 1.000266(9)$ (k=1). Therefore, the in-air wavelength for the monochromatic light from the monochromator is 850.005(63) nm (k=1) and for the laser is 850.0030(77) nm (k=1).

3.2.2 Polarization

The monochromatic light from the LDLS and monochromator is unpolarized.

The light from the laser is polarized parallel to the long edge of the SPAD, as shown by the blue arrow in Figure 2, to a polarization extinction ratio of approximately 100:1.

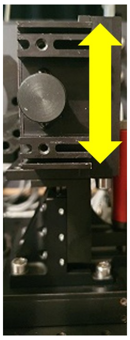

Figure 2: *Polarization of the laser relative to the SPAD.*

3.2.3 Bandwidth/Linewidth

The grating used in the monochromator is composed of 600 g/mm, is blazed at 1 μm and has a manufacturer's specification for a dispersion of 3.2 nm/mm. The exit slit of the monochromator is set to 0.05 mm and the monochromatic light is coupled into a fibre with a core diameter of 0.05 mm. The bandwidth of the monochromatic light is too small to measure with the spectrum analyser and with other spectrometers available at MSL and therefore the dispersion times the slit width calculation is used as an indication of the bandwidth, which corresponds to a bandwidth of $\approx$ 0.16 nm.

The linewidth of the laser is not measured at MSL. According to the manufacturer (Nanoplus), the linewidth is below 3 MHz (< 0.000007 nm) for a typical distributed feedback laser that has a wavelength between 830 nm and 920 nm.

3.2.4 Power Stability

Since the light from the source cannot be incident on the standard photodiode and the SPAD simultaneously, a monitor photodiode is used to normalize instabilities in the optical power of the 850-nm source. Using this normalization method is only valid if the ratio between the power in the monitor beam path and the power in the device-under-test beam path (see Figure 1) remains stable. The standard photodiode signal and the monitor photodiode signal are simultaneously measured for several hours. For the LDLS and monochromator combination the standard deviation of the ratio is 0.005 % and for the laser the standard deviation of the ratio is 0.032 %. These small ratios illustrate that normalizing the SPAD count rate and the standard photodiode voltage against the monitor photodiode voltage is a reliable way to remove power instabilities in the source.

3.3 Transmission Coefficient

The optical power is attenuated to the photon-counting regime of approximately 200 fW (10^6 photon counts per second) by using two neutral-density filters that are each attached to a motorized flip mount and may be inserted into or out of the beam path. Additionally, a motorized, 12-position filter wheel with 11 neutral-density filters installed (one position does not contain a neutral-density filter) which have optical densities ranging from 0.1 to 3 further reduce the optical power to determine how the detection efficiency varies with count rate.

The amplified voltage from the standard photodiode is used to determine the transmission coefficient of each neutral-density filter separately and in-situ. To measure the transmission coefficient, T_1, of the neutral-density filter in the filter wheel the neutral-density filters in the flip mounts are removed from the beam path. To measure the transmission coefficient of the neutral-density filter on the first flip mount, T_2, the neutral-density filter in the second flip mount is removed from beam path and the filter wheel is set to the position that does not have a filter installed. To measure the transmission coefficient of the neutral-density filter on the second flip mount, T_3, the neutral-density filter in the first flip mount is removed from beam path and the filter wheel is set to the position that does not have a filter installed.

The transmission coefficient, T_i $(i = 1..3)$, is measured by moving a neutral-density filter into and out of the beam path and measuring the dark-voltage subtracted standard photodiode voltage and normalizing against the dark-voltage subtracted monitor photodiode voltage

$$T_i = \frac{\frac{V_{in}^i - V_{dark}^i}{V_{in}^{Mon} - V_{dark}^{Mon}}}{\frac{V_{out}^i - V_{dark}^i}{V_{out}^{Mon} - V_{dark}^{Mon}}} \tag{5}$$

where, V_{in}^i (V_{out}^i) is the voltage of the standard photodiode when the neutral-density filter is in (out of) the beam path respectively, V_{in}^{Mon} (V_{out}^{Mon}) is the voltage of the monitor photodiode when the neutral-density filter is in (out of) the beam path respectively, and, V_{dark}^i, V_{dark}^{Mon} are the dark-voltage measurements of the standard photodiode and monitor photodiode respectively.

The combined transmission coefficient is therefore,

$$T = T_1 \times T_2 \times T_3 \tag{6}$$

3.4 Standard Photodiode

The traceable power measurement is performed with the filter wheel set to a position that does not have a neutral-density filter installed and with the neutral-density filters on the flip mounts out of the beam path.

The optical power, Φ_{STD}, is measured with the standard photodiode and is defined as

$$\Phi_{STD} = \frac{V}{GS(\lambda)} \tag{7}$$

where, V is the dark-voltage subtracted standard photodiode voltage, G is the gain of the transimpedance amplifier, and $S(\lambda)$ is the spectral responsivity of the standard photodiode.

3.4.1 Spectral Responsivity

MSL's spectral responsivity scale is currently linked to PTB's scale. Trap detectors (owned by MSL) were calibrated at PTB and the scale was transferred from the traps to a single-element silicon photodiode (MSL, Sn: S1337-B02) using MSL's Detector Responsivity Laboratory. The spectral responsivity of the standard photodiode, at 850 nm, is $S = 0.47570(39)$ A/W, where the uncertainty corresponds to a standard distribution (k=1, DoF=133).

3.4.2 Transimpedance Amplifier Gain

The photocurrent is amplified using a transimpedance amplifier (MSL, Sn: PA1039-03), which is calibrated by the Electrical team at MSL. The gain of the amplifier is calibrated at different output voltages of +0.1 V, +1 V and +10 V

$$\begin{aligned} G_{0.1V} &= 1.00012(44) \times 10^{9}\ \mathrm{V/A} \\ G_{1V} &= 9.99970(71) \times 10^{8}\ \mathrm{V/A} \\ G_{10V} &= 9.99975(42) \times 10^{8}\ \mathrm{V/A} \end{aligned}$$

where the uncertainty corresponds to a standard distribution (k=1). The gain that is used in Equation 7 for the measured photodiode voltage is a linear interpolation of the calibrated gains that depends on the output voltage, for example, if the output voltage, V, is between +1 V and +10 V, the gain is

$$G = \frac{V-1}{10-1} \times (G_{10V} - G_{1V}) + G_{1V} \tag{8}$$

When the LDLS and monochromator is used, the output voltage is $V \approx$ +7.3 V, which corresponds to a typical gain of $G = 9.99974(37) \times 10^{8}$ V/A (k=1). When the laser is used, the output voltage is $V \approx$ +9.4 V, which corresponds to a typical gain of $G = 9.99975(40) \times 10^{8}$ V/A (k=1).

3.4.3 Photodiode Voltage

The output voltage of the transimpedance amplifier is measured with a digital multimeter (Hewlett Packard 3458A, Sn: 2823A07124), which is calibrated by the Electrical team at MSL. The amplified voltage from the standard photodiode has a value of approximately +7.3 V when the LDLS and monochromator is used and approximately +9.4 V when the laser is used.

The digital multimeter was calibrated at +5 V and +10 V, which showed that the following corrections must be applied

$$V_{corr}^{5V} = -5.1(1.5) \times 10^{-6}\ \mathrm{V}$$
$$V_{corr}^{10V} = -1.00(25) \times 10^{-5}\ \mathrm{V}$$

where the uncertainties correspond to a standard distribution (k=1). A linear interpolation of the correction to apply to the amplified voltage, $V^{'}$, (dark-voltage subtracted) of the standard photodiode is

$$V = V^{'} + (\frac{V^{'} - 5}{10 - 5} \times (V_{corr}^{10V} - V_{corr}^{5V}) + V_{corr}^{5V}). \tag{9}$$

As a sample calculation, if $V^{'} = 9.4256(69)$ V (where the value is the average and the uncertainty is the standard deviation of the mean for 10 samples acquired by the digital multimeter), then $V = 9.4256(69)$ V, indicating that the voltage corrections to apply are smaller than the noise in the voltage signal.

3.5 SPAD

This section describes the uncertainty contributions that relate to the single-photon avalanche diode.

3.5.1 Count Rate

The count rate is corrected for dark counts and scaled for inaccuracies in the timebase of the counter

$$CR = (CR_{light} - CR_{dark}) \times F_{counter} \tag{10}$$

where, CR_{light} is the measured count rate in the presence of incident light, CR_{dark} is the measured count rate in the absence of incident light, and $F_{counter}$ is a correction factor for the timebase of the counter.

Dark counts are detection events in the absence of incident light. The dark count rate, CR_{dark}, is determined by closing the shutter and averaging the count rate.

The output pulses from the SPAD are counted using a counter (IDQ ID900, Sn: 1813050T010) that is locked to an external 10-MHz reference from MSL Time Standards. To verify the accuracy of the counter, an arbitrary waveform generator (Keysight 33622A, Sn: MY59001743) locked to a 10-MHz reference generates pulses at a known frequency (1 kHz, 100 kHz or 1 MHz) which have a similar pulse width (10 ns) and pulse height (2.2 V, 50-Ω load) as the output pulses from the SPAD. The counter measured the expected number of counts per second for each known input frequency. Therefore, $F_{counter} = 1$ and may be ignored. The corrected count rate is simply,

$$CR = CR_{light} - CR_{dark} \tag{11}$$

3.5.2 Spatial Non-Uniformity

The spatial non-uniformity of the SPAD is the largest component of uncertainty. Upon performing a spatial scan of each SPAD from PTB, what appeared to be interference fringes (with a contrast of up to 19 %) was observed. This fringe pattern is similar to the pattern observed by Gerrits *et al.* (see Figure 9 in Ref [7]) when a continuous-wave (CW) laser was used as the source.

Attempts were made to remove the fringes, but unfortunately none of the attempts were successful. In particular, the following changes were made to the apparatus and a spatial scan was acquired

- use a CW laser or a laser-driven light source with a monochromator,
- use a 12-position filter wheel (Thorlabs, FW212CNEB) with absorptive neutral-density filters or a continuously-variable, reflective filter wheel (Sigma Koki, OSMS-60YAM + VND-100U),
- neutral-density filters with and without anti-reflective coatings for 850-nm light,
- neutral-density filters with different optical densities,
- use a 10x objective (Thorlabs, RMS10X) or an aspheric, f=50-mm lens (Thorlabs, AL2550-B) to focus the light onto the SPAD,
- tilt the SPAD relative to the aspheric lens in a clockwise and an anti-clockwise manner,
- move the neutral-density filters to different places in the beam path.

While some of the above changes to the apparatus did change the contrast between the peaks and valleys in the apparent fringes (by a few percent), the fringes always remained.

To understand the spatial non-uniformity effects, the SPAD is positioned at 15 different XYZ coordinates relative to the focal spot of the beam to (i) show the effect of keeping the diameter of the beam where it hits the SPAD at a fixed value and moving the SPAD relative to the beam focus (i.e., vary the XY coordinates and keep Z fixed), and (ii) changing the diameter of the beam that hits the SPAD and keeping the beam centroid at a fixed value (i.e., vary the Z coordinate and keep XY fixed).

A beam-profiler camera (Dataray, S-WCD-LCM-C-1310) is mounted to the XYZ stages, in place of the SPAD, and is used to measure the centroid and the diameter ($1/e^2$) of the focused beam. Figure 3a shows the beam diameter at the focal spot and Figure 3b shows the average (average of the major and minor beam profiles) beam diameter measured by the camera as the distance between the 10x objective and the camera is changed.

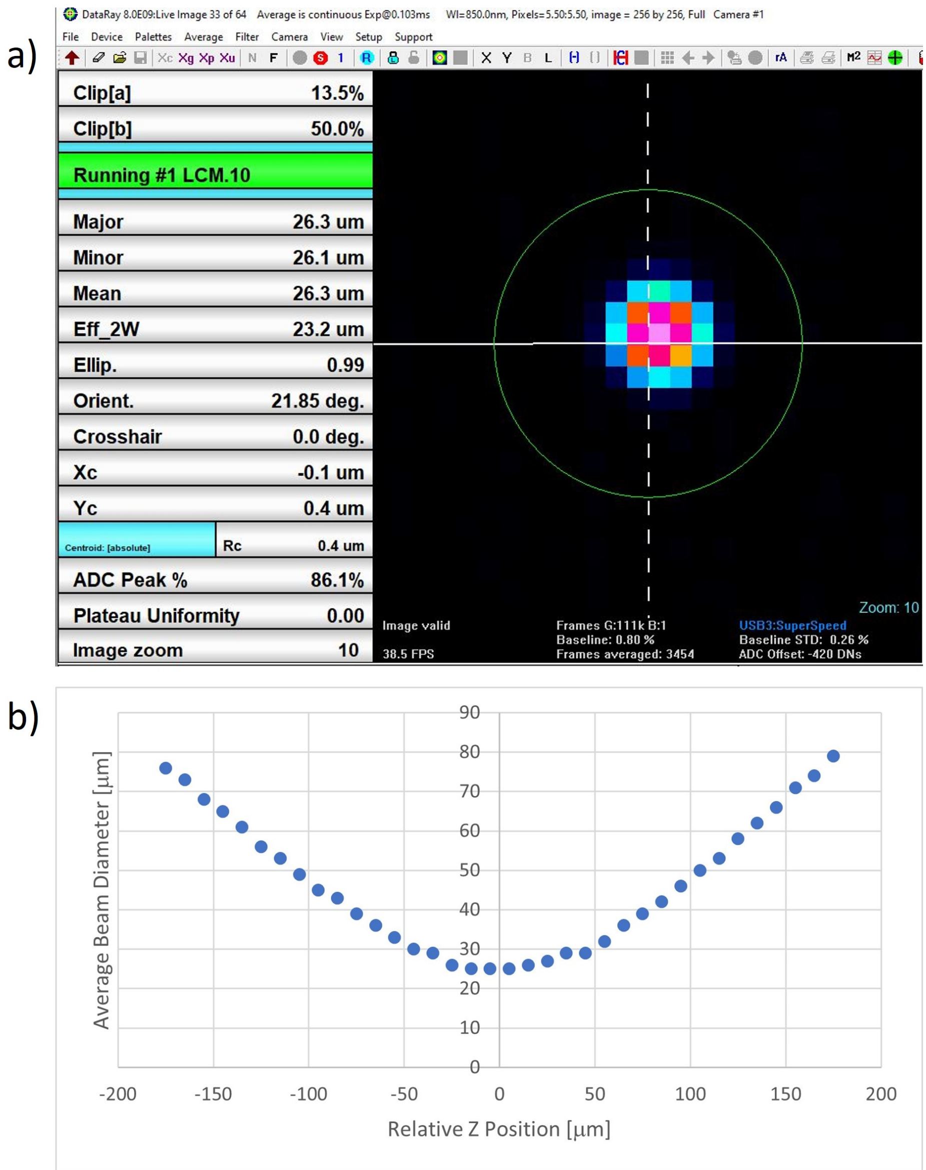

Figure 3: *a) Beam diameter at the focal spot for the 10x objective acquired with the Dataray software. b) Average beam diameter ($1/e^2$, acquired with the Dataray software) for the 10x objective as a function of the relative Z position from the focal plane (Z=0).*

To measure the detection efficiency at different beam diameters, the distance between the SPAD and the focusing lens is changed. The detection efficiency is measured at diameters of $\approx$ 25 μm, 45 μm, 60 μm and 75 μm with the centre of the beam aligned with the centre of the SPAD. For a Gaussian beam diameter of 75 μm, and a SPAD with an active diameter of 180 μm, the beam capture is 99.9990% (see Equation 2 in Ref [8]). From Figure 3b, it is shown, for example, that for a beam diameter of 45 μm the SPAD may be positioned at ΔZ=-80 μm (SPAD is closer to the focusing objective) or ΔZ=+80 μm (SPAD is further away from the focusing objective) relative to the focal spot (Z=0). Detection-efficiency data are acquired with ΔZ < 0 and ΔZ > 0 to achieve approximately the same beam diameter. When changing the Z position of the SPAD, the centroid of the beam changes by up to $\pm$6 μm in both X and/or Y relative to the centre of the SPAD. Also, the beam is not perfectly circular, but is elliptical with a minor/major aspect ratio ranging from approximately 0.8 to 1 and the aspect ratio is not symmetric about Z=0. Therefore, the beam diameters specified above are rough estimates to within $\pm 10\ \mu$m.

The detection efficiency is also measured at a constant beam diameter of $\approx 25\ \mu$m, but with the beam hitting different areas of the SPAD. The following (ΔX, ΔY) positions, in μm, of the SPAD relative to the focal spot of the beam are used: (-21, 0), (21, 0), (0, -21), (0, 21), (-15, 15), (15, 15), (15, -15), (-15, -15).

To prepare for the pilot comparison, MSL purchased a Si-SPAD (Excelitas SPM-AQRH-14, Sn. 33223). Figure 4 shows a comparison between the spatial non-uniformity of MSL's detector against the two PTB detectors. A different fringe pattern can be seen in all three detectors.

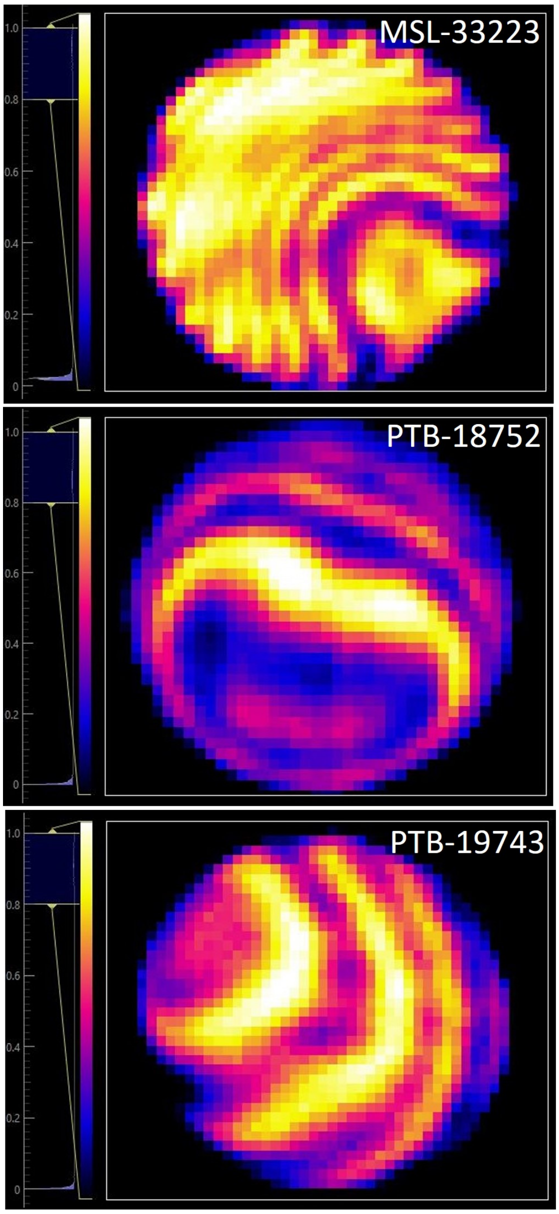

Figure 4: *Comparison of a spatial scan of MSL's Si-SPAD detector and the two PTB detectors. The contrast in each figure is the same, where blue represents 80%, magenta 90%, yellow 95% and white 100% of the normalised signal. The beam diameter is $\approx 25\ \mu$m.*

4 Results

Detection-efficiency data are acquired using 15 different XYZ positions of the SPAD relative to the beam focus (see Section 3.5.2) and each position is repeated at least 10 times. Before each repeat, the list of XYZ positions is shuffled. Data are also acquired using two different optical systems (see Section 2).

4.1 Software

The analysis to calculate the detection efficiency, defined in Equation 2, is performed using the GUM Tree Calculator [9]. This software package encapsulates information about measured quantities and automatically propagates uncertainties. Non-linear fitting software [10] fits the detection efficiency versus the count rate to Equation 3 to determine the detection efficiency at a count rate of approximately 1 count per second. A weighted fit is applied which includes weights for both the count rate and the detection efficiency. The source code for the acquisition software is available on GitHub [11].

4.2 Si-SPAD (Sn: 18752)

This section shows the results for the Perkin-Elmer SPCM-AQR-16 (Sn. 18752) for the two different optical systems (see Section 2) that were used to acquire data.

4.2.1 DFB Laser and Aspheric lens

The temperature and relative humidity of the laboratory are logged while the detection-efficiency data is acquired (which takes about 2.5 days). Since the SPAD is within an enclosure, the temperature within the enclosure is also logged. The temperature and humidity probes are calibrated by the Temperature and Humidity teams at MSL. The average temperature and relative humidity outside of the enclosure are 21.65$\pm$0.07 °C and 43$\pm$3 %rh, respectively, and the average temperature within the enclosure is 22.84$\pm$0.05 °C, where the uncertainties are the standard deviation. The temperature inside the enclosure is higher than outside the enclosure due to the heat generated by the translation stages and the SPAD.

A spatial scan of the SPAD with the beam diameter of approximately 25 μm is shown in Figure 5. The Z position of the SPAD is moved by 1060 μm relative to the aspheric lens to make the beam diameter approximately 75 μm and the corresponding spatial scan is shown in Figure 6. Spatial scans at a beam diameter of approximately 45 μm and 60 μm are also acquired but are not shown. For smaller beam diameters the non-uniformity fringes are more visible and the difference in count rate between a peak and a valley is approximately 19 %.

Table 2 lists the contributions to the detection efficiency calculation (see Equation 2) for one of the 150 measurement runs with the SPAD offset from the focal spot of the beam by -795 μm in Z. Figure 7 shows the transmission coefficient for each neutral-density filter, the optical power measured by the standard photodiode (not normalized against the monitor photodiode), and the detection efficiency versus count rate for the data in Table 2. An uncertainty budget for a particular row in Table 2 is shown in Table 3.

Figure 8 shows a plot of the ideal detection efficiency, η_0, for the 150 data runs at different XYZ positions of the SPAD relative to the focal spot of the beam. Data acquired where the count rate of the SPAD has a steep gradient (e.g., (ΔX,ΔY,ΔZ) = (15, -15, 0) μm from the beam focus) has large variability in the dataset, which is most likely due to the repeatability of setting the translation stages to the same location between each repeat. Table 4 is a sorted list of the average detection efficiency at the different XYZ positions. The average value and the standard deviation of the values in Table 4 is

$$\eta_0^{Laser+Lens,18752} = 0.520(21) \quad (12)$$

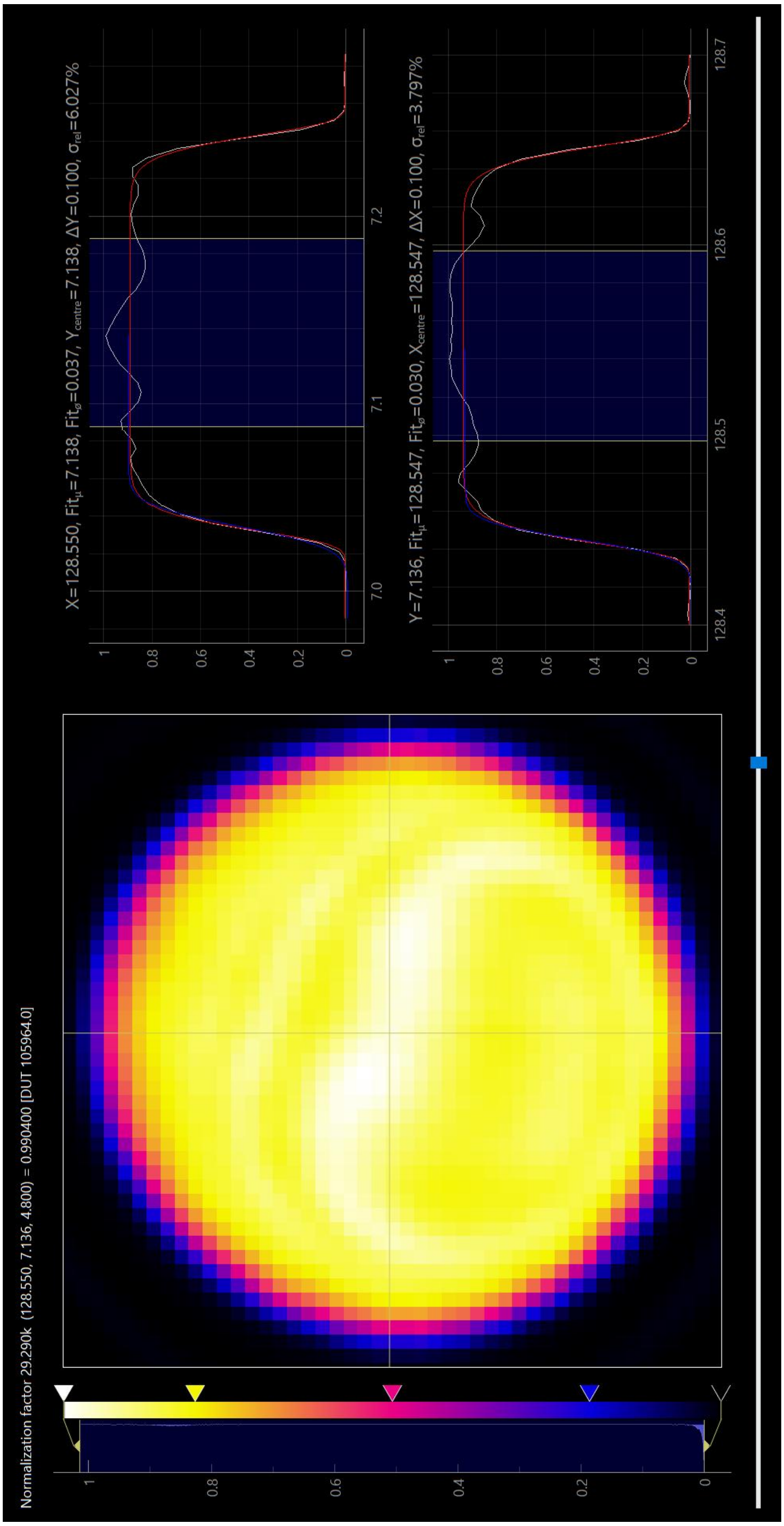

Figure 5: *Spatial scan of SPAD (Sn. 18752) for a beam diameter of $\approx$ 25 μm. The DFB laser is used as the source and the aspheric lens focuses the light. The line plots correspond to the X and Y profiles (crosshair in image). The white curve is the profile data, red curve is a fit to a Super Gaussian distribution (Eq. 18) and the blue curve is a fit to a Gaussian Cumulative distribution (Eq. 19). The shaded blue region in each plot is 100-μm wide and shows that the relative non-uniformity is 3.80 % in X and 6.03 % in Y. Each pixel in the image corresponds to a 5 μm step in X and Y.*

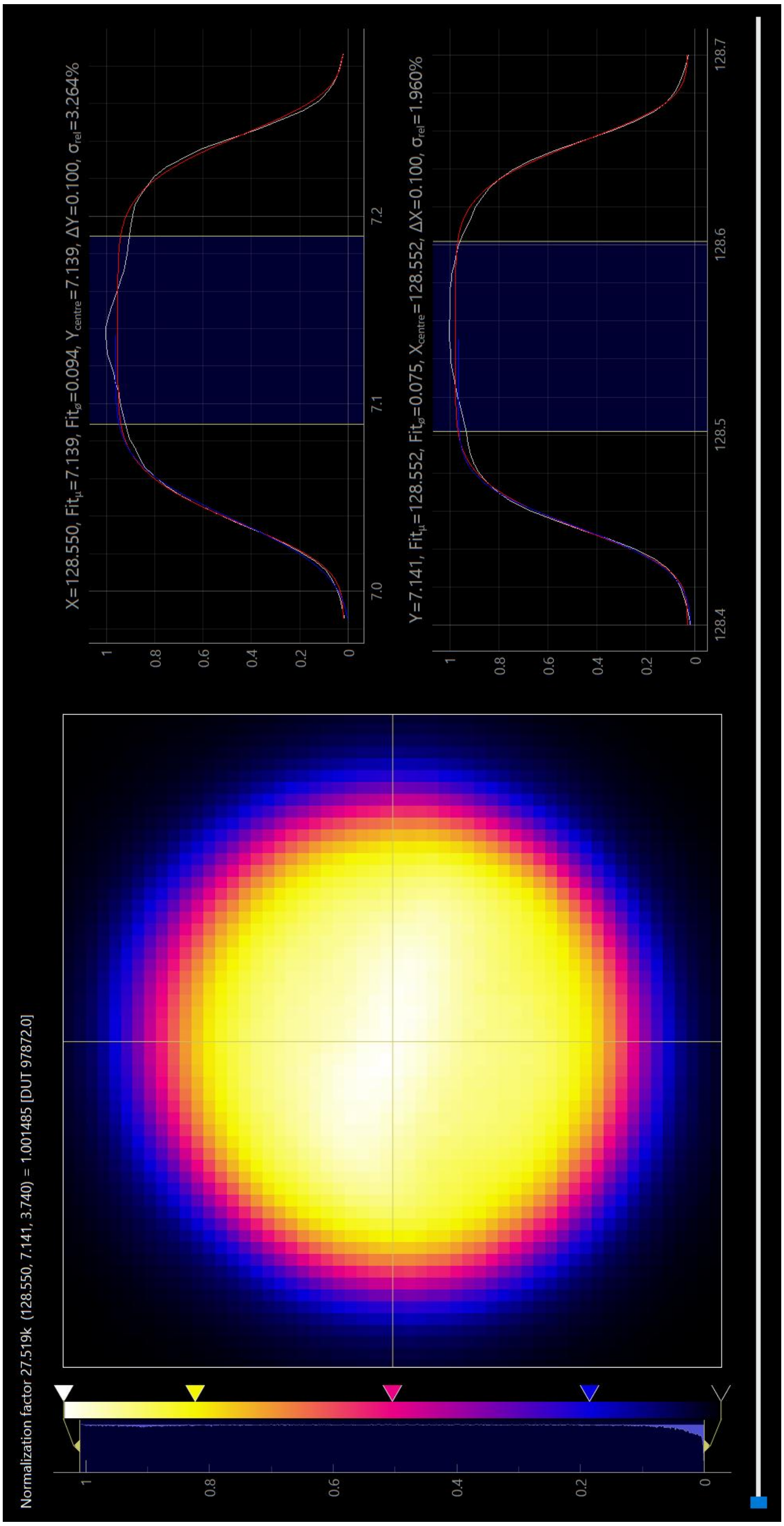

Figure 6: *Spatial scan of SPAD (Sn. 18752) for a beam diameter of $\approx$ 75 μm. The DFB laser is used as the source and the aspheric lens focuses the light. The line plots correspond to the X and Y profiles (crosshair in image). The white curve is the profile data, red curve is a fit to a Super Gaussian distribution (Eq. 18) and the blue curve is a fit to a Gaussian Cumulative distribution (Eq. 19). The shaded blue region in each plot is 100-μm wide and shows that the relative non-uniformity is 1.96 % in X and 3.26 % in Y. Each pixel in the image corresponds to a 5 μm step in X and Y.*

CR, Counts/s	V_{SPAD}^{Mon}, V	Φ_{STD}, nW	V_{STD}^{Mon}, V	T	η
749170(780)	3.6001(21)	20.650(28)	3.6544(40)	1.6775(68)$\times 10^{-5}$	0.5129(17)
587830(400)	3.5736(14)	20.954(18)	3.70691(67)	1.3177(31)$\times 10^{-5}$	0.5160(13)
444300(1100)	3.6108(52)	20.707(19)	3.6633(15)	9.821(22)$\times 10^{-6}$	0.5179(18)
345400(170)	3.63746(59)	20.189(25)	3.5724(33)	7.544(33)$\times 10^{-6}$	0.5204(18)
332610(530)	3.5722(32)	20.430(18)	3.6145(10)	7.425(18)$\times 10^{-6}$	0.5183(15)
266050(360)	3.6247(21)	20.407(17)	3.61153(57)	5.821(13)$\times 10^{-6}$	0.5214(14)
218930(170)	3.63621(95)	20.646(18)	3.6535(10)	4.771(11)$\times 10^{-6}$	0.5218(12)
101150(130)	3.61878(93)	20.183(17)	3.57192(44)	2.2064(54)$\times 10^{-6}$	0.5238(15)
57915(73)	3.66755(51)	20.349(18)	3.6008(12)	1.2466(38)$\times 10^{-6}$	0.5237(17)
35089(53)	3.5911(28)	20.720(17)	3.66605(27)	7.6873(86)$\times 10^{-7}$	0.5254(11)
7202(23)	3.6093(52)	20.518(18)	3.63108(89)	1.5700(28)$\times 10^{-7}$	0.5255(21)
842.8(8.4)	3.6057(38)	20.204(20)	3.5757(19)	1.8353(47)$\times 10^{-8}$	0.5266(54)

Table 2: Measured quantities that are used to calculate the detection efficiency, as defined in Equation 2, when the source is a DFB laser and an aspheric lens focuses the beam onto the SPAD (Sn. 18752). The SPAD is positioned (ΔX,ΔY,ΔZ) = (0, 0, -795) μm from the beam focus (beam diameter $\approx 60\ \mu$m). Additional quantities not included in the table but are needed to evaluate Equation 2 are the constants $h = 6.626\,070\,15 \times 10^{-34}\ Js$ and $c = 299\,792\,458\ m/s$ (see Section 3.1), and the vacuum wavelength $\lambda = 850.22906(97)\ nm$ (see Section 3.2.1). Values in parentheses are standard uncertainties (k=1). The corresponding plot of η versus CR is shown in Figure 7d.

Measurand	Unit	Measured Value	Uncertainty	Uncertainty (%)
Speed of Light (c)	m/s	2.99792458$\times 10^{8}$		
Plank Constant (h)	J s	6.62607015$\times 10^{-34}$		
Vacuum Wavelength (λ)	m	850.22906$\times 10^{-9}$	9.7$\times 10^{-13}$	0.00
CR / V_{SPAD}^{Mon}	Counts/(s V)	27951	36	0.13
Φ_{STD} / V_{STD}^{Mon}	W/V	5.6506$\times 10^{-9}$	4.7$\times 10^{-12}$	0.08
Transmission Coefficient (T)	1	2.2064$\times 10^{-6}$	5.4$\times 10^{-9}$	0.25
Detection efficiency (η)	1	0.5238	0.0015	
Combined uncertainty (k=1)				0.29

Table 3: Uncertainty budget of the measured detection efficiency defined in Equation 2 that corresponds to the row in Table 2 with a count rate of 101150(130) Counts/s. This budget does not include spatial, non-uniformity effects which are the dominate uncertainty component of $\approx$ 7 %.

η_0	(ΔX,ΔY,ΔZ), μm	Approx. Beam Diameter, μm
0.48140(290)	(0, 21, 0)	25
0.49080(260)	(-15, 15, 0)	25
0.50290(800)	(15, -15, 0)	25
0.50450(360)	(0, -21, 0)	25
0.50928(70)	(0, 0, 1060)	75
0.51410(420)	(15, 15, 0)	25
0.51807(98)	(0, 0, 795)	60
0.51828(50)	(0, 0, -1060)	75
0.52527(96)	(0, 0, -795)	60
0.52690(100)	(0, 0, 530)	45
0.53330(120)	(0, 0, -530)	45
0.53340(380)	(-21, 0, 0)	25
0.54176(97)	(0, 0, 0)	25
0.55040(140)	(21, 0, 0)	25
0.55620(140)	(-15, -15, 0)	25

Table 4: Average ideal detection efficiency (individual measurement runs are shown in Figure 8) for the different XYZ positions of the SPAD (Sn. 18752) relative to the beam focus. The DFB laser is used as the source and the aspheric lens focuses the light. The detection-efficiency values are sorted from smallest to largest. The detection-efficiency values in parentheses are standard uncertainties (k=1).

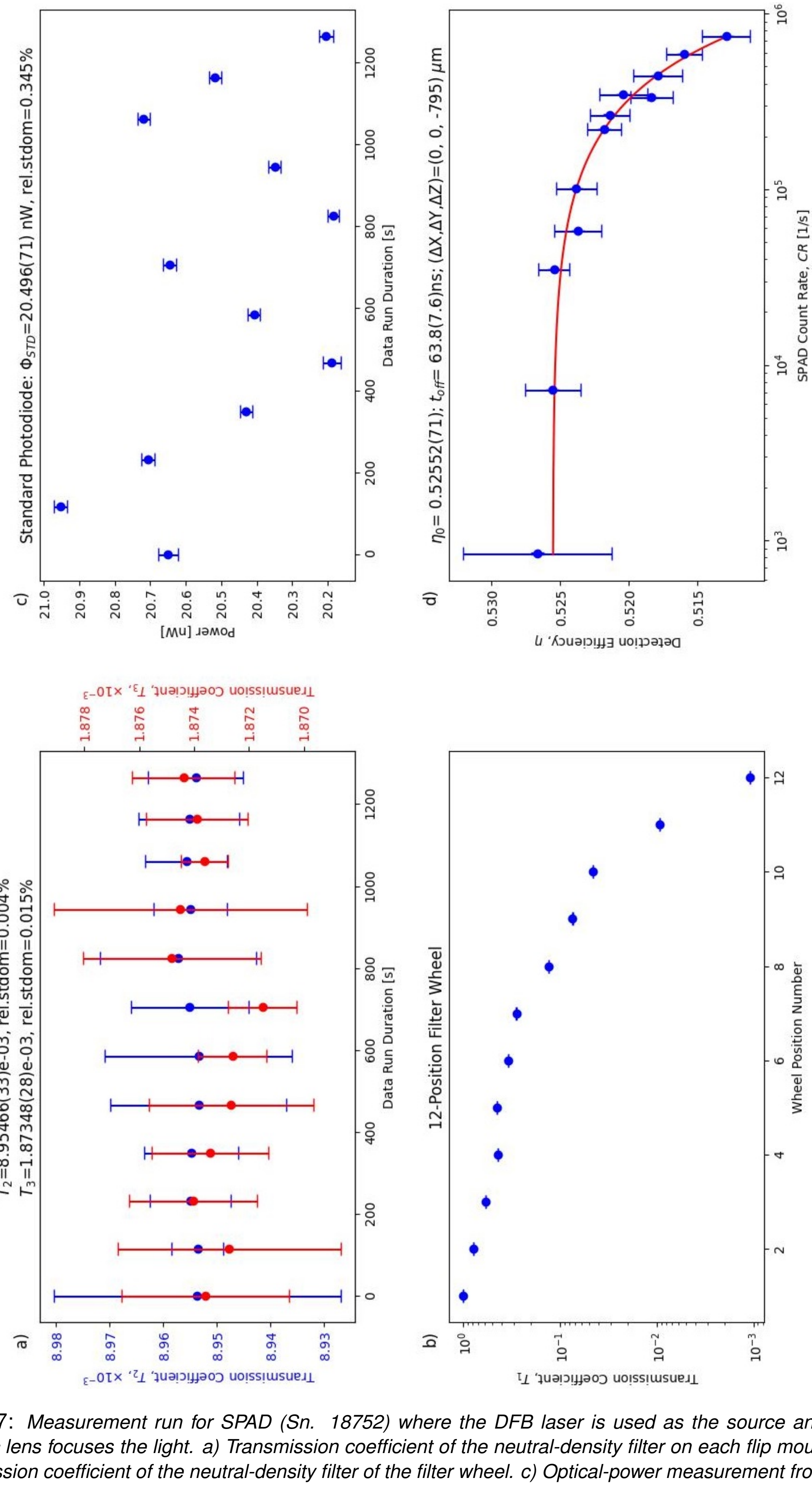

Figure 7: *Measurement run for SPAD (Sn. 18752) where the DFB laser is used as the source and the aspheric lens focuses the light. a) Transmission coefficient of the neutral-density filter on each flip mount. b) Transmission coefficient of the neutral-density filter of the filter wheel. c) Optical-power measurement from the standard photodiode (not normalized against the monitor photodiode). d) Detection-efficiency data and fit (using Equation 3) when the SPAD is positioned (ΔX,ΔY,ΔZ) = (0, 0, -795) μm from the beam focus (beam diameter ≈ 60 μm). The term "rel.stdom" in a sub-figure title is shorthand for "relative standard deviation of the mean".*

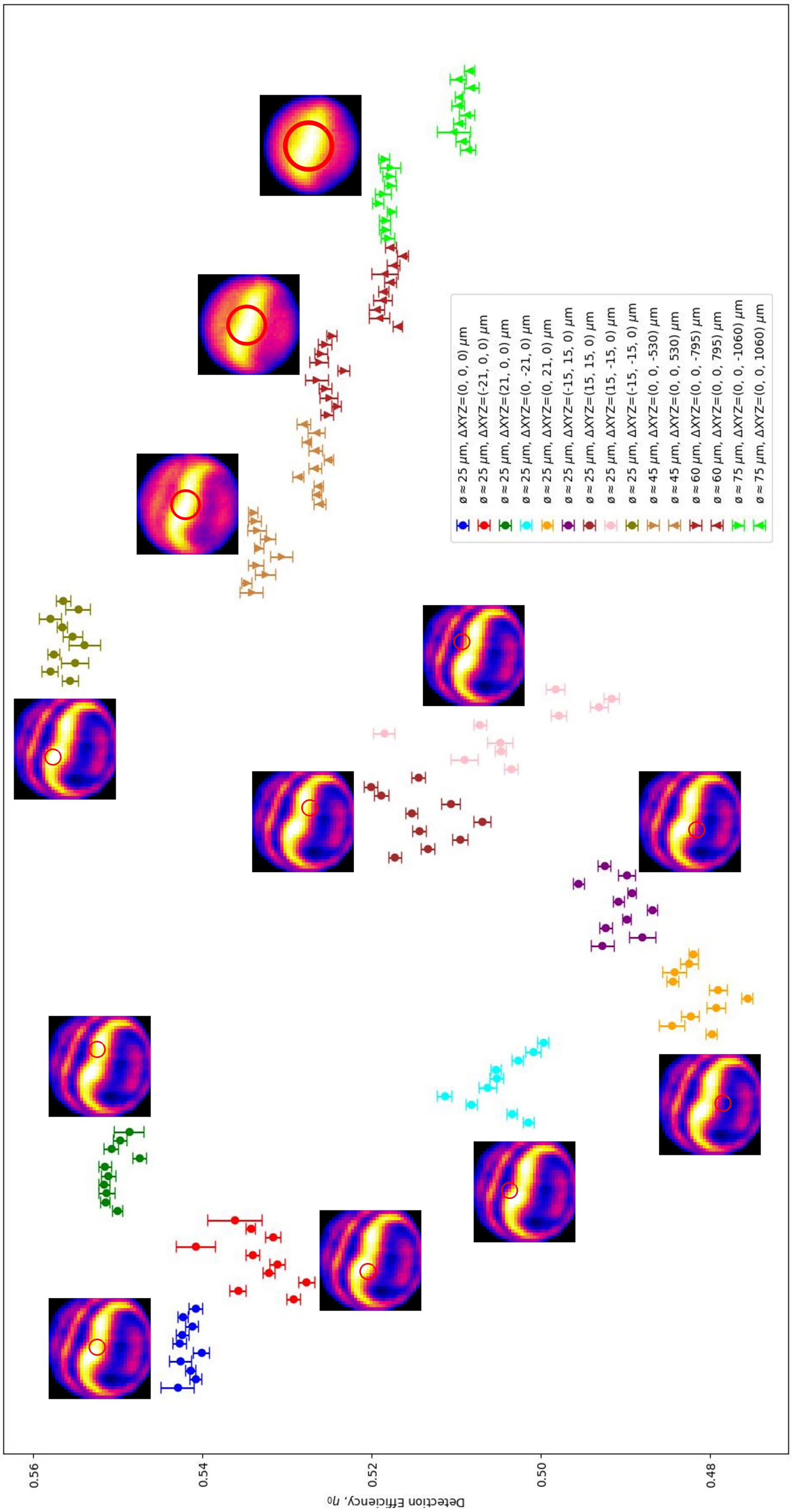

Figure 8: *Ideal detection efficiency, η_0, for the 15 XYZ positions of the SPAD (Sn. 18752) relative to the beam focus. The DFB laser is used as the source and the aspheric lens focuses the light. Next to each dataset is an image of the spatial scan with an enhanced contrast. The red circle in the image corresponds to the approximate beam diameter, $1/e^2$, and approximately where the beam hits the SPAD.*

4.2.2 LDLS and 10x Objective

The temperature and relative humidity of the laboratory are logged while the detection-efficiency data is acquired (which takes about 2.5 days). Since the SPAD is within an enclosure, the temperature within the enclosure is also logged. The temperature and humidity probes are calibrated by the Temperature and Humidity teams at MSL. The average temperature and relative humidity outside of the enclosure are 21.55$\pm$0.05 $^\circ$C and 50$\pm$7 %rh, respectively, and the average temperature within the enclosure is 22.67$\pm$0.05 $^\circ$C, where the uncertainties are the standard deviation. The temperature inside the enclosure is higher than outside the enclosure due to the heat generated by the translation stages and the SPAD.

A spatial scan of the SPAD with the beam diameter of approximately 25 μm is shown in Figure 9. The Z position of the SPAD is moved by 160 μm (see Figure 3b) to make the beam diameter approximately 75 μm and the corresponding spatial scan is shown in Figure 10. Spatial scans at a beam diameter of approximately 45 μm and 60 μm are also acquired but are not shown. For smaller beam diameters the non-uniformity fringes are more visible and the difference in count rate between a peak and a valley is approximately 13 %.

Table 5 lists the contributions to the detection efficiency calculation (see Equation 2) for one of the 159 measurement runs with the SPAD offset from the focal spot of the beam by -15 μm in both X and Y. Figure 11 shows the transmission coefficient for each neutral-density filter, the optical power measured by the standard photodiode (not normalized against the monitor photodiode), and the detection efficiency versus count rate for the data in Table 5. An uncertainty budget for a particular row in Table 5 is shown in Table 6.

Equation 3 is valid for a source of photons that follow a Poissonian distribution. This distribution is used as the model when the LDLS and monochromator combination is used as the light source. The Poissonian photon-statistics model still represents the data appropriately, as can be seen in Figure 11d.

Figure 12 shows a plot of the ideal detection efficiency, η_0, for the 159 data runs at different XYZ positions of the SPAD relative to the focal spot of the beam. Table 7 is a sorted list of the average detection efficiency at the different XYZ positions. The average value and the standard deviation of the values in Table 7 is

$$\eta_0^{LDLS+Objective,18752} = 0.486(18) \quad (13)$$

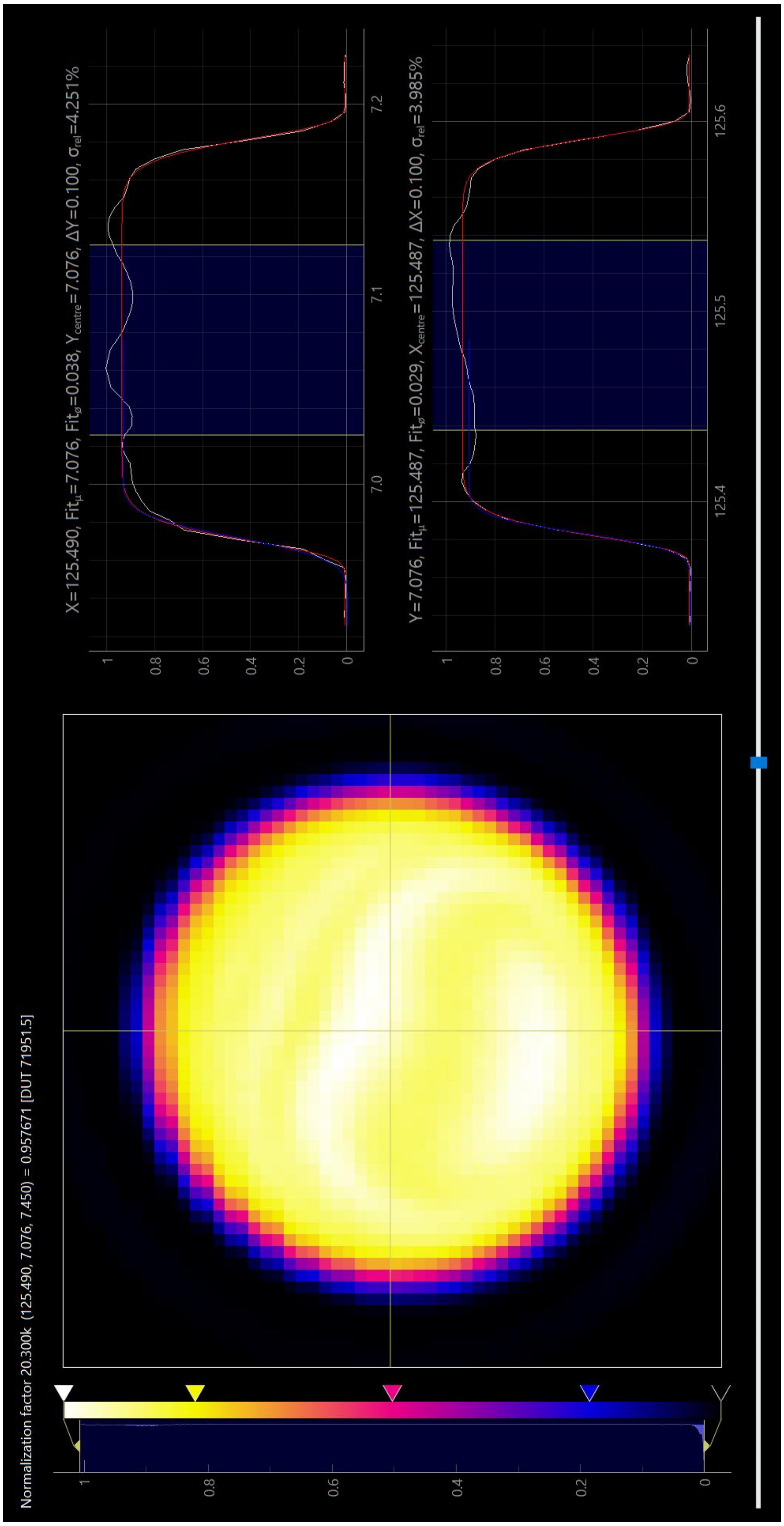

Figure 9: *Spatial scan of SPAD (Sn. 18752) for a beam diameter of $\approx$ 25 μm. The LDLS and monochromator is used as the source and the 10x objective focuses the light. The line plots correspond to the X and Y profiles (crosshair in image). The white curve is the profile data, red curve is a fit to a Super Gaussian distribution (Eq. 18) and the blue curve is a fit to a Gaussian Cumulative distribution (Eq. 19). The shaded blue region in each plot is 100-μm wide and shows that the relative non-uniformity is 3.99 % in X and 4.25 % in Y. Each pixel in the image corresponds to a 5 μm step in X and Y.*

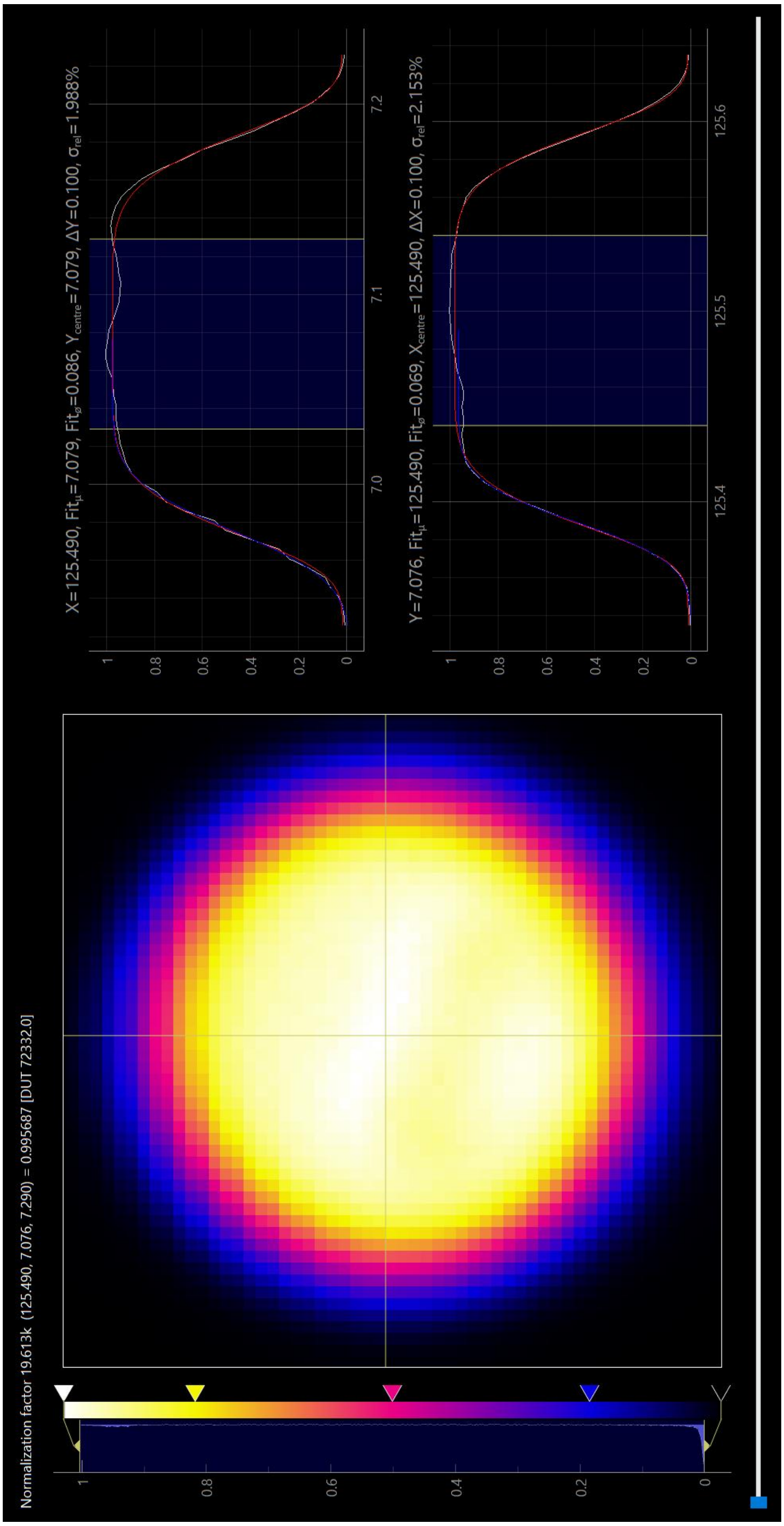

Figure 10: *Spatial scan of SPAD (Sn. 18752) for a beam diameter of $\approx$ 75 μm. The LDLS and monochromator is used as the source and the 10x objective focuses the light. The line plots correspond to the X and Y profiles (crosshair in image). The white curve is the profile data, red curve is a fit to a Super Gaussian distribution (Eq. 18) and the blue curve is a fit to a Gaussian Cumulative distribution (Eq. 19). The shaded blue region in each plot is 100-μm wide and shows that the relative non-uniformity is 2.15 % in X and 1.99 % in Y. Each pixel in the image corresponds to a 5 μm step in X and Y.*

CR, Counts/s	V_{SPAD}^{Mon}, V	Φ_{STD}, nW	V_{STD}^{Mon}, V	T	η
548640(180)	3.683581(64)	15.508(13)	3.68843(12)	1.6827(14)$\times 10^{-5}$	0.49185(60)
433870(130)	3.69169(12)	15.499(13)	3.68646(28)	1.32178(91)$\times 10^{-5}$	0.49411(54)
321830(150)	3.682531(79)	15.505(13)	3.687655(32)	9.8046(48)$\times 10^{-6}$	0.49528(53)
248210(110)	3.689655(79)	15.490(13)	3.684268(56)	7.5190(45)$\times 10^{-6}$	0.49718(55)
244250(170)	3.68704(22)	15.498(13)	3.68591(12)	7.4194(61)$\times 10^{-6}$	0.49614(68)
196430(130)	3.68718(19)	15.515(13)	3.69013(10)	5.9617(27)$\times 10^{-6}$	0.49656(56)
161798(88)	3.694388(62)	15.514(13)	3.689725(24)	4.8869(32)$\times 10^{-6}$	0.49799(59)
73235(71)	3.68374(15)	15.514(13)	3.689919(77)	2.2165(14)$\times 10^{-6}$	0.49844(70)
41329(60)	3.68925(21)	15.510(13)	3.689009(92)	1.24570(86)$\times 10^{-6}$	0.49973(90)
25638(39)	3.690391(39)	15.519(13)	3.69112(14)	7.7267(37)$\times 10^{-7}$	0.49964(89)
5210(18)	3.68667(21)	15.501(13)	3.686979(77)	1.57188(59)$\times 10^{-7}$	0.4996(18)
612.0(6.4)	3.687685(84)	15.498(13)	3.68611(17)	1.8364(19)$\times 10^{-8}$	0.5022(53)

Table 5: Measured quantities that are used to calculate the detection efficiency, as defined in Equation 2, when the light source is the LDLS and a 10x objective focuses the beam onto the SPAD (Sn. 18752). The SPAD is positioned (ΔX,ΔY,ΔZ) = (-15, -15, 0) μm from the beam focus (beam diameter $\approx$ 25 μm). Additional quantities not included in the table but are needed to evaluate Equation 2 are the constants $h = 6.626\,070\,15 \times 10^{-34}\ Js$ and $c = 299\,792\,458\ m/s$ (see Section 3.1), and the vacuum wavelength $\lambda = 850.231(62)\ nm$ (see Section 3.2.1). Values in parentheses are standard uncertainties (k=1). The corresponding plot of η versus CR is shown in Figure 11d.

Measurand	Unit	Measured Value	Uncertainty	Uncertainty (%)
Speed of Light (c)	m/s	2.99792458$\times 10^{8}$		
Plank Constant (h)	J s	6.62607015$\times 10^{-34}$		
Vacuum Wavelength (λ)	m	850.231$\times 10^{-9}$	6.2$\times 10^{-11}$	0.01
CR / V_{SPAD}^{Mon}	Counts/(s V)	19881	19	0.10
Φ_{STD} / V_{STD}^{Mon}	W/V	4.2043$\times 10^{-9}$	3.5$\times 10^{-12}$	0.08
Transmission Coefficient (T)	1	2.2165$\times 10^{-6}$	1.4$\times 10^{-9}$	0.06
Detection efficiency (η)	1	0.49844	0.00070	
Combined uncertainty (k=1)				0.14

Table 6: Uncertainty budget of the measured detection efficiency defined in Equation 2 that corresponds to the row in Table 5 with a count rate of 73235(71) Counts/s. This budget does not include spatial, non-uniformity effects which are the dominate uncertainty component of $\approx$ 7 %.

η_0	(ΔX,ΔY,ΔZ), μm	Approx. Beam Diameter, μm
0.45304(22)	(-15, 15, 0)	25
0.45470(36)	(0, 21, 0)	25
0.46143(64)	(15, 15, 0)	25
0.46637(35)	(-21, 0, 0)	25
0.48890(76)	(0, 0, 0)	25
0.49000(54)	(0, 0, 160)	75
0.49062(51)	(0, 0, -80)	45
0.49115(72)	(0, 0, 80)	45
0.49187(44)	(0, 0, 120)	60
0.49241(56)	(0, 0, -120)	60
0.49250(50)	(0, 0, -160)	75
0.49841(65)	(21, 0, 0)	25
0.49957(75)	(-15, -15, 0)	25
0.50783(76)	(15, -15, 0)	25
0.50915(41)	(0, -21, 0)	25

Table 7: Average ideal detection efficiency (individual measurement runs are shown in Figure 12) for the different XYZ positions of the SPAD (Sn. 18752) relative to the beam focus. The LDLS and monochromator is used as the source and the 10x objective focuses the light. The detection-efficiency values are sorted from smallest to largest. The detection-efficiency values in parentheses are standard uncertainties (k=1).

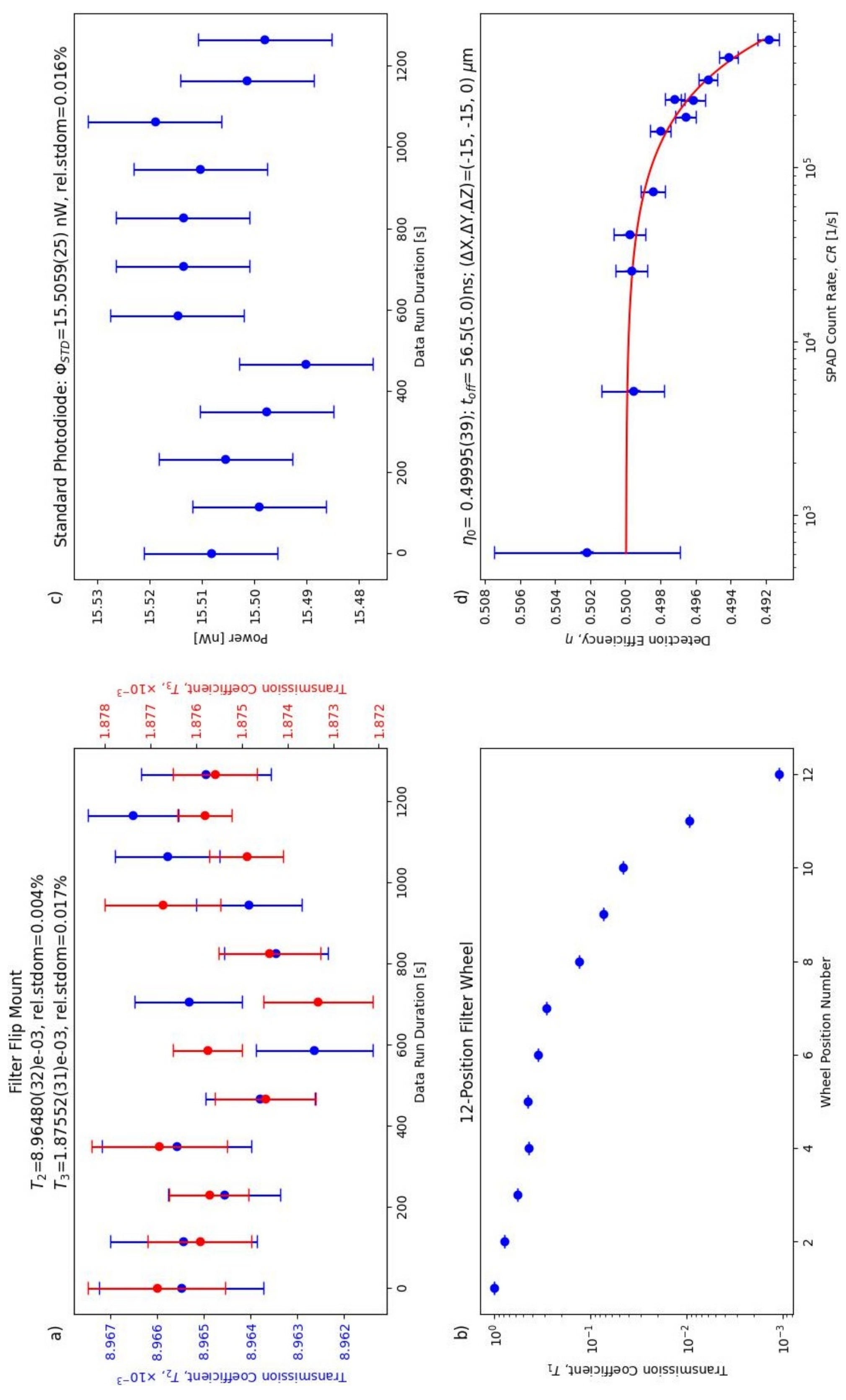

Figure 11: *Measurement run for SPAD (Sn. 18752) where the LDLS and monochromator is used as the source and the 10x objective focuses the light. a) Transmission coefficient of the neutral-density filter on each flip mount. b) Transmission coefficient of the neutral-density filter of the filter wheel. c) Optical-power measurement from the standard photodiode (not normalized against the monitor photodiode). d) Detection-efficiency data and fit (using Equation 3) when the SPAD is positioned (ΔX,ΔY,ΔZ) = (-15, -15, 0) μm from the beam focus (beam diameter $\approx$ 25 μm). The term "rel.stdom" in a sub-figure title is shorthand for "relative standard deviation of the mean".*

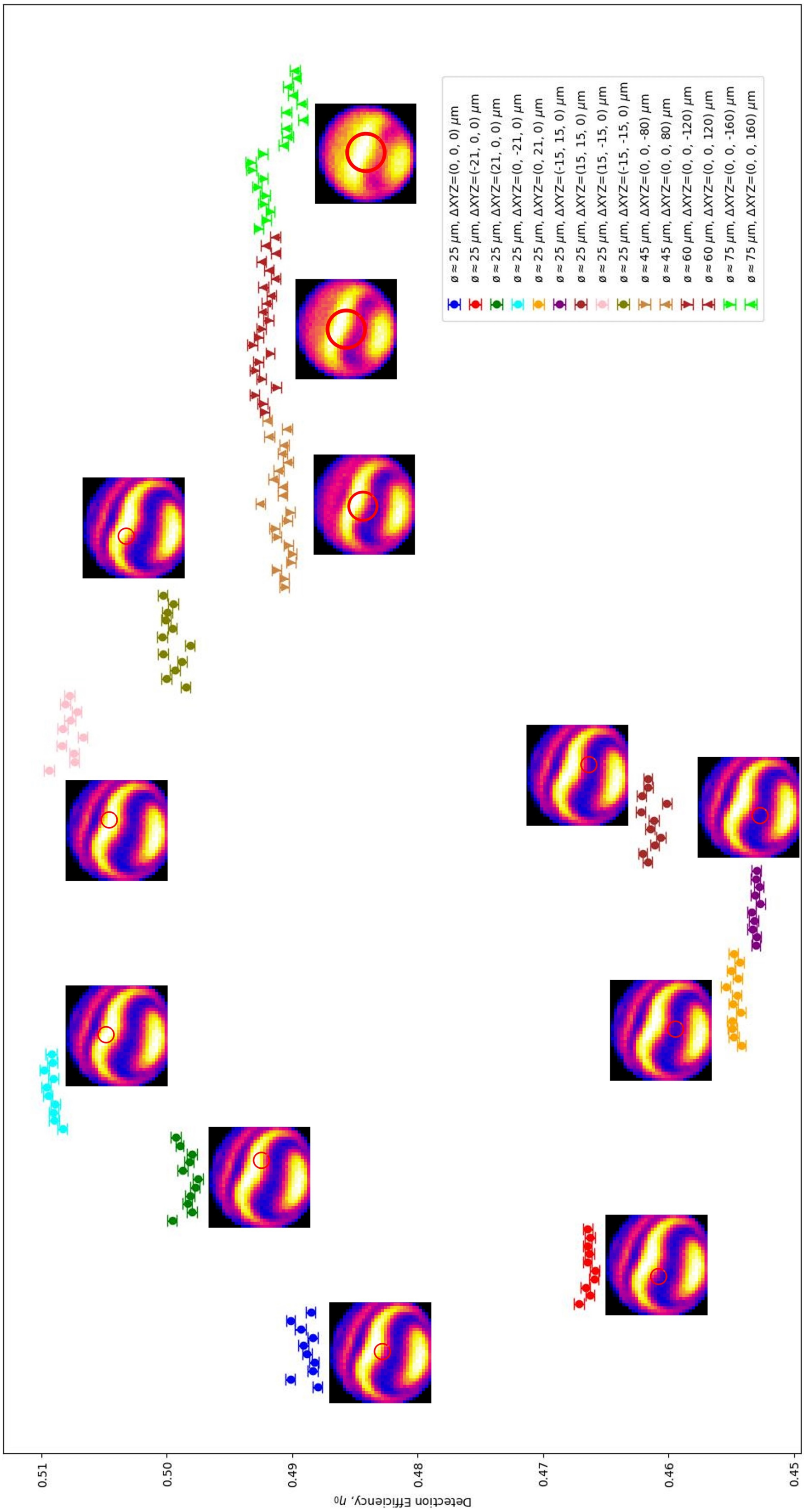

Figure 12: *Ideal detection efficiency, η_0, for the 15 XYZ positions of the SPAD (Sn. 18752) relative to the beam focus. The LDLS and monochromator is used as the source and the 10x objective focuses the light. Next to each dataset is an image of the spatial scan with an enhanced contrast. The red circle in the image corresponds to the approximate beam diameter, $1/e^2$, and approximately where the beam hits the SPAD.*

4.3 Si-SPAD (Sn: 19743)

This section shows the results for the Perkin-Elmer SPCM-AQR-16 (Sn. 19743) for the two different optical systems (see Section 2) that were used to acquire data.

4.3.1 DFB Laser and Aspheric lens

The temperature and relative humidity of the laboratory are logged while the detection-efficiency data is acquired (which takes about 2.5 days). Since the SPAD is within an enclosure, the temperature within the enclosure is also logged. The temperature and humidity probes are calibrated by the Temperature and Humidity teams at MSL. The average temperature and relative humidity outside of the enclosure are 21.72±0.04 °C and 56±5 %rh, respectively, and the average temperature within the enclosure is 22.92±0.05 °C, where the uncertainties are the standard deviation. The temperature inside the enclosure is higher than outside the enclosure due to the heat generated by the translation stages and the SPAD.

A spatial scan of the SPAD with the beam diameter of approximately 25 μm is shown in Figure 13. The Z position of the SPAD is moved by 1060 μm relative to the aspheric lens to make the beam diameter approximately 75 μm and the corresponding spatial scan is shown in Figure 14. Spatial scans at a beam diameter of approximately 45 μm and 60 μm are also acquired but are not shown. For smaller beam diameters the non-uniformity fringes are more visible and the difference in count rate between a peak and a valley is approximately 15 %.

Table 8 lists the contributions to the detection efficiency calculation (see Equation 2) for one of the 150 measurement runs with the SPAD offset from the focal spot of the beam by -1060 μm in Z. Figure 15 shows the transmission coefficient for each neutral-density filter, the optical power measured by the standard photodiode (not normalized against the monitor photodiode), and the detection efficiency versus count rate for the data in Table 8. An uncertainty budget for a particular row in Table 8 is shown in Table 9.

Figure 16 shows a plot of the ideal detection efficiency, η_0, for the 150 data runs at different XYZ positions of the SPAD relative to the focal spot of the beam. Table 10 is a sorted list of the average detection efficiency at the different XYZ positions. The average value and the standard deviation of the values in Table 10 is

$$\eta_0^{Laser+Lens,19743} = 0.536(15) \tag{14}$$

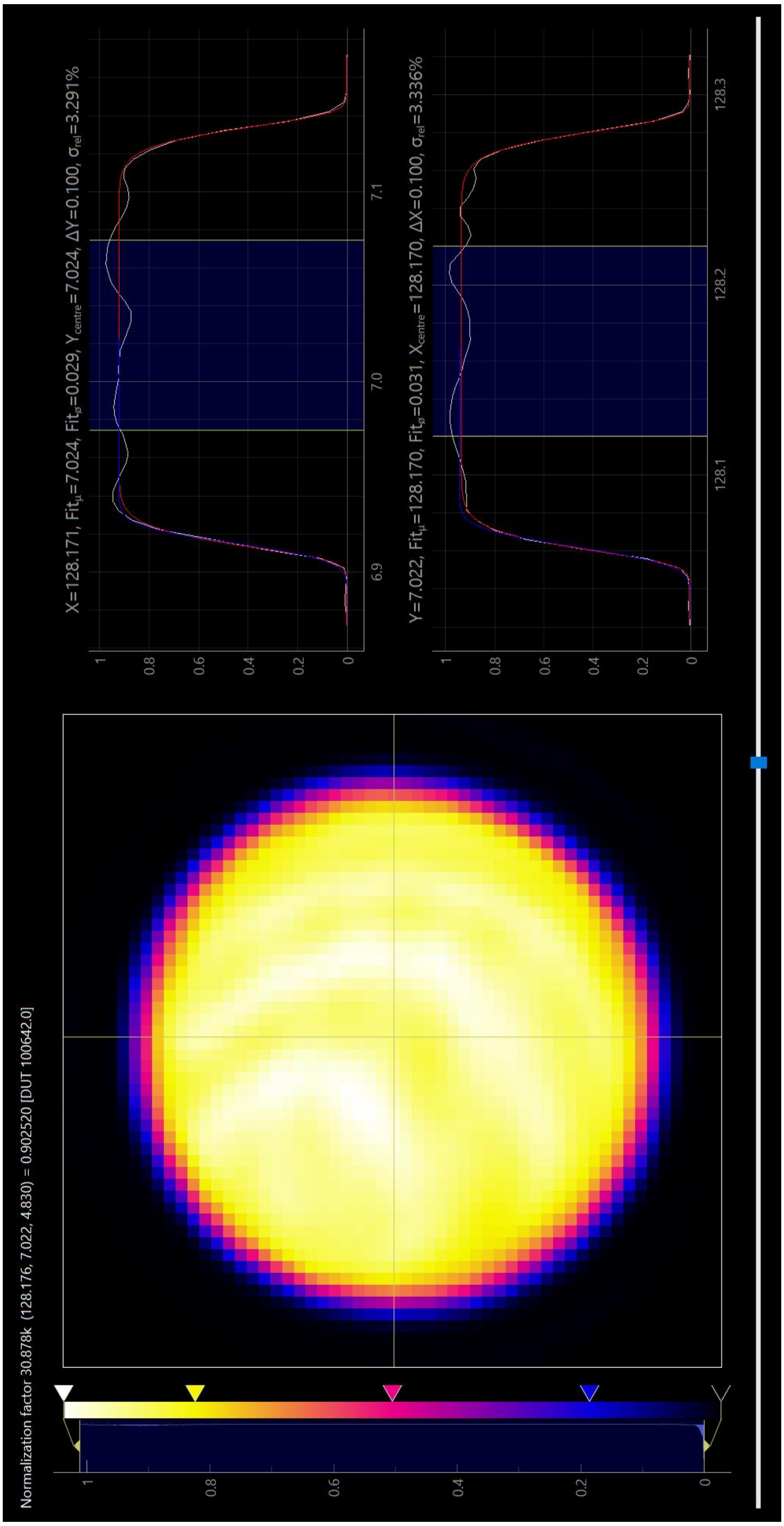

Figure 13: *Spatial scan of SPAD (Sn. 19743) for a beam diameter of* $\approx$ *25* μ*m. The DFB laser is used as the source and the aspheric lens focuses the light. The line plots correspond to the X and Y profiles (crosshair in image). The white curve is the profile data, red curve is a fit to a Super Gaussian distribution (Eq. 18) and the blue curve is a fit to a Gaussian Cumulative distribution (Eq. 19). The shaded blue region in each plot is 100-*μ*m wide and shows that the relative non-uniformity is 3.34 % in X and 3.29 % in Y. Each pixel in the image corresponds to a 5* μ*m step in X and Y.*

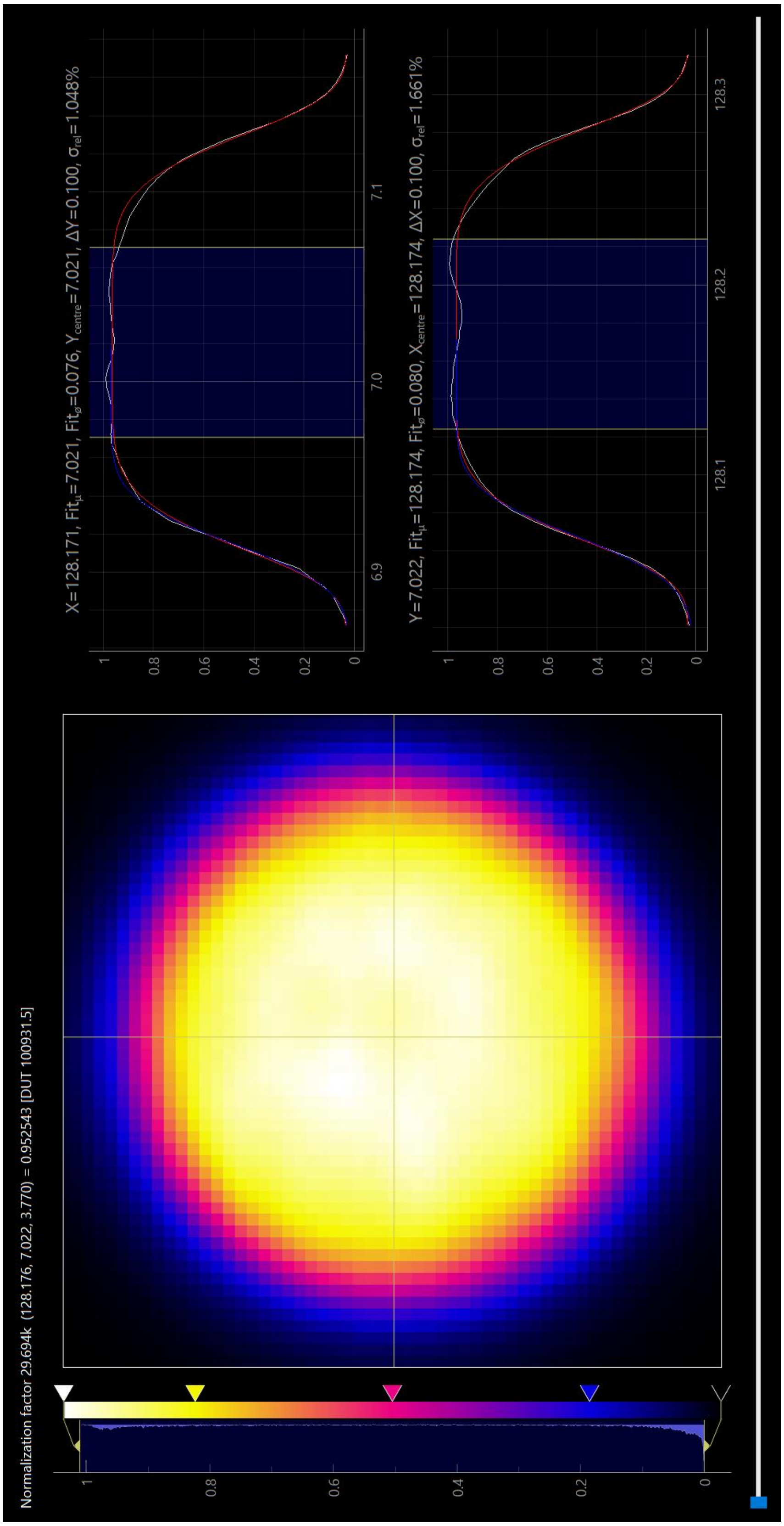

Figure 14: *Spatial scan of SPAD (Sn. 19743) for a beam diameter of $\approx$ 75 μm. The DFB laser is used as the source and the aspheric lens focuses the light. The line plots correspond to the X and Y profiles (crosshair in image). The white curve is the profile data, red curve is a fit to a Super Gaussian distribution (Eq. 18) and the blue curve is a fit to a Gaussian Cumulative distribution (Eq. 19). The shaded blue region in each plot is 100-μm wide and shows that the relative non-uniformity is 1.66 % in X and 1.05 % in Y. Each pixel in the image corresponds to a 5 μm step in X and Y.*

CR, Counts/s	V_{SPAD}^{Mon}, V	Φ_{STD}, nW	V_{STD}^{Mon}, V	T	η
721500(3000)	3.428(12)	19.274(17)	3.4137(11)	1.676(10)$\times10^{-5}$	0.5196(42)
579020(400)	3.4906(11)	19.219(20)	3.4041(23)	1.3154(41)$\times10^{-5}$	0.5218(13)
420950(340)	3.3859(17)	19.45(10)	3.446(17)	9.80(21)$\times10^{-6}$	0.5251(76)
333480(320)	3.4756(18)	19.413(19)	3.4384(17)	7.543(28)$\times10^{-6}$	0.5264(19)
324970(260)	3.4227(12)	19.297(17)	3.4179(11)	7.423(12)$\times10^{-6}$	0.52932(92)
249590(240)	3.3587(12)	19.844(21)	3.5152(22)	5.819(23)$\times10^{-6}$	0.5285(19)
213340(140)	3.4948(11)	18.931(16)	3.35321(46)	4.773(27)$\times10^{-6}$	0.5293(31)
98500(130)	3.4806(32)	19.792(18)	3.5057(14)	2.2037(44)$\times10^{-6}$	0.5315(13)
55450(120)	3.4658(40)	19.427(33)	3.4410(52)	1.245(10)$\times10^{-6}$	0.5317(39)
33867(56)	3.4215(20)	19.562(18)	3.4648(15)	7.671(17)$\times10^{-7}$	0.5340(14)
6965(24)	3.45119(77)	19.366(18)	3.4299(13)	1.5657(34)$\times10^{-7}$	0.5333(21)
814.8(7.7)	3.44472(88)	19.527(18)	3.4589(13)	1.8326(78)$\times10^{-8}$	0.5341(55)

Table 8: Measured quantities that are used to calculate the detection efficiency, as defined in Equation 2, when the source is a DFB laser and an aspheric lens focuses the beam onto the SPAD (Sn. 18752). The SPAD is positioned (ΔX,ΔY,ΔZ) = (0, 0, -1060) μm from the beam focus (beam diameter $\approx 75\ \mu$m). Additional quantities not included in the table but are needed to evaluate Equation 2 are the constants $h = 6.626\,070\,15 \times 10^{-34}\ Js$ and $c = 299\,792\,458\ m/s$ (see Section 3.1), and the vacuum wavelength $\lambda = 850.22906(97)\ nm$ (see Section 3.2.1). Values in parentheses are standard uncertainties (k=1). The corresponding plot of η versus CR is shown in Figure 15d.

Measurand	Unit	Measured Value	Uncertainty	Uncertainty (%)
Speed of Light (c)	m/s	2.99792458$\times10^{8}$		
Plank Constant (h)	J s	6.62607015$\times10^{-34}$		
Vacuum Wavelength (λ)	m	850.22906$\times10^{-9}$	9.7$\times10^{-13}$	0.00
CR / V_{SPAD}^{Mon}	Counts/(s V)	28301	45	0.16
Φ_{STD} / V_{STD}^{Mon}	W/V	5.6457$\times10^{-9}$	5.7$\times10^{-12}$	0.10
Transmission Coefficient (T)	1	2.2037$\times10^{-6}$	4.4$\times10^{-9}$	0.20
Detection efficiency (η)	1	0.5315	0.0013	
Combined uncertainty (k=1)				0.24

Table 9: Uncertainty budget of the measured detection efficiency defined in Equation 2 that corresponds to the row in Table 8 with a count rate of 98500(130) Counts/s. This budget does not include spatial, non-uniformity effects which are the dominate uncertainty component of $\approx$ 4 %.

η_0	(ΔX,ΔY,ΔZ), μm	Approx. Beam Diameter, μm
0.51301(94)	(0, 0, 0)	25
0.52030(150)	(0, 0, 530)	45
0.52370(140)	(0, 0, -530)	45
0.52557(80)	(15, -15, 0)	25
0.52795(70)	(0, 0, -795)	60
0.52960(200)	(-15, 15, 0)	25
0.53320(180)	(0, 0, -1060)	75
0.53330(150)	(0, 0, 795)	60
0.53820(220)	(21, 0, 0)	25
0.53920(180)	(0, 0, 1060)	75
0.53940(170)	(-21, 0, 0)	25
0.54030(230)	(0, -21, 0)	25
0.55200(270)	(0, 21, 0)	25
0.55270(370)	(15, 15, 0)	25
0.57520(170)	(-15, -15, 0)	25

Table 10: Average ideal detection efficiency (individual measurement runs are shown in Figure 16) for the different XYZ positions of the SPAD (Sn. 19743) relative to the beam focus. The DFB laser is used as the source and the aspheric lens focuses the light. The detection-efficiency values are sorted from smallest to largest. The detection-efficiency values in parentheses are standard uncertainties (k=1).

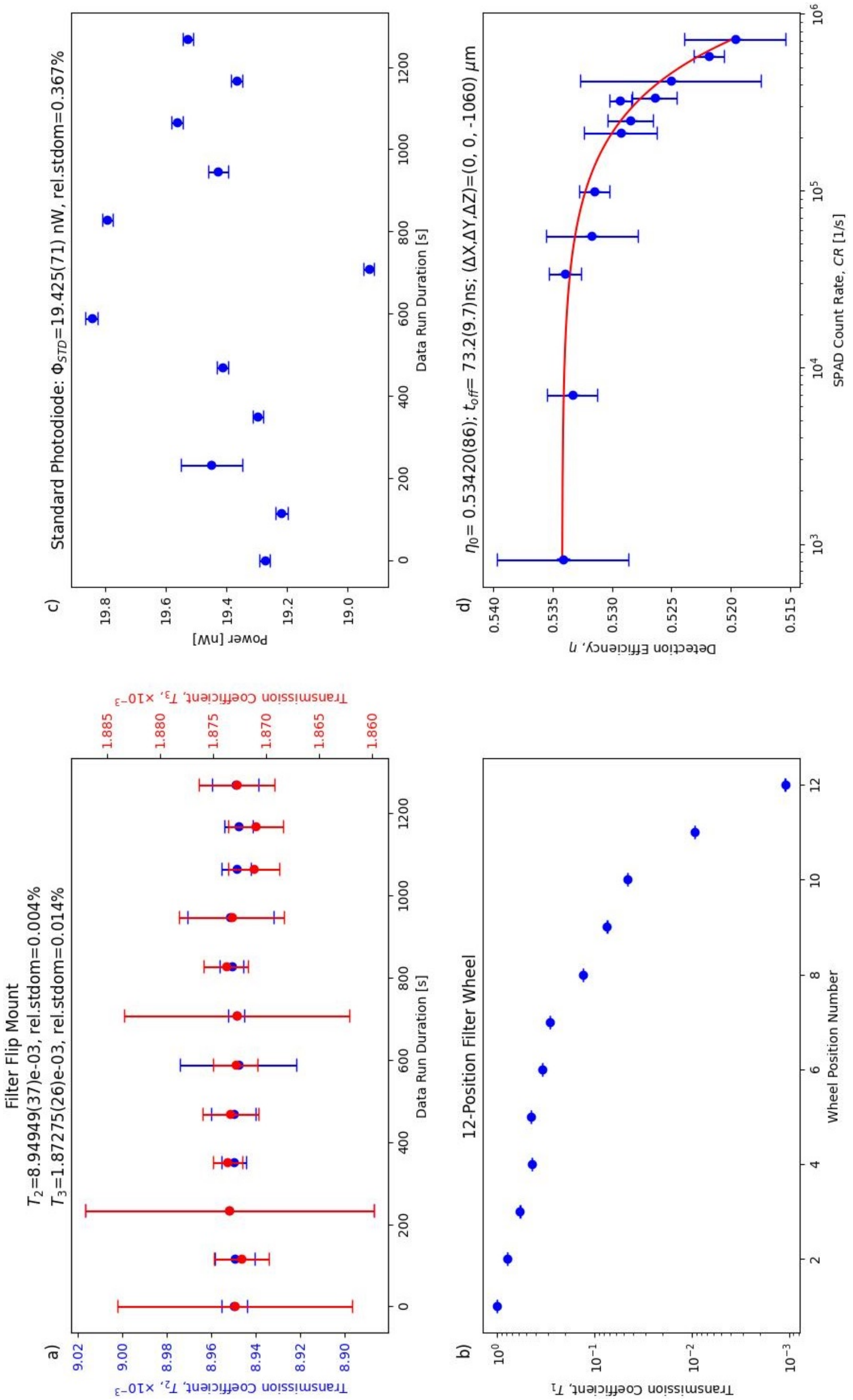

Figure 15: *Measurement run for SPAD (Sn. 19743) where the DFB laser is used as the source and the aspheric lens focuses the light. a) Transmission coefficient of the neutral-density filter on each flip mount. b) Transmission coefficient of the neutral-density filter of the filter wheel. c) Optical-power measurement from the standard photodiode (not normalized against the monitor photodiode). d) Detection-efficiency data and fit (using Equation 3) when the SPAD is positioned (ΔX,ΔY,ΔZ) = (0, 0, -1060) μm from the beam focus (beam diameter ≈ 75 μm). The term "rel.stdom" in a sub-figure title is shorthand for "relative standard deviation of the mean".*

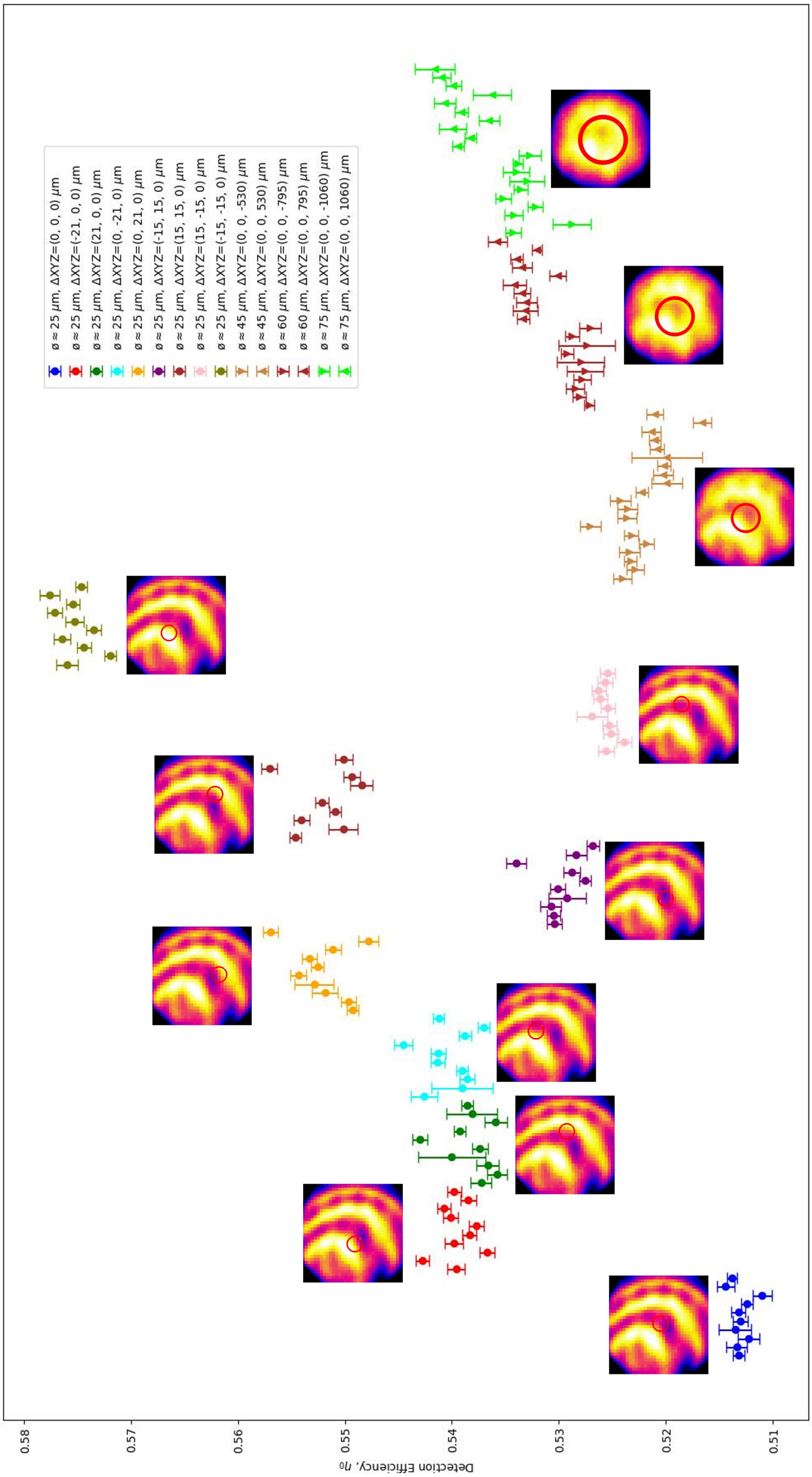

Figure 16: *Ideal detection efficiency, η_0, for the 15 XYZ positions of the SPAD (Sn. 19743) relative to the beam focus. The DFB laser is used as the source and the aspheric lens focuses the light. Next to each dataset is an image of the spatial scan with an enhanced contrast. The red circle in the image corresponds to the approximate beam diameter, $1/e^2$, and approximately where the beam hits the SPAD.*

4.3.2 LDLS and 10x Objective

The temperature and relative humidity of the laboratory are logged while the detection-efficiency data is acquired (which takes about 2.5 days). Since the SPAD is within an enclosure, the temperature within the enclosure is also logged. The temperature and humidity probes are calibrated by the Temperature and Humidity teams at MSL. The average temperature and relative humidity outside of the enclosure are 21.51±0.03 °C and 49±4 %rh, respectively, and the average temperature within the enclosure is 22.64±0.03 °C, where the uncertainties are the standard deviation. The temperature inside the enclosure is higher than outside the enclosure due to the heat generated by the translation stages and the SPAD.

A spatial scan of the SPAD with the beam diameter of approximately 25 μm is shown in Figure 17. The Z position of the SPAD is moved by 160 μm (see Figure 3b) to make the beam diameter approximately 75 μm and the corresponding spatial scan is shown in Figure 18. Spatial scans at a beam diameter of approximately 45 μm and 60 μm are also acquired but are not shown. For smaller beam diameters the non-uniformity fringes are more visible and the difference in count rate between a peak and a valley is approximately 8 %.

Table 11 lists the contributions to the detection efficiency calculation (see Equation 2) for one of the 150 measurement runs with the SPAD aligned to the focal spot of the beam. Figure 19 shows the transmission coefficient for each neutral-density filter, the optical power measured by the standard photodiode (not normalized against the monitor photodiode), and the detection efficiency versus count rate for the data in Table 11. An uncertainty budget for a particular row in Table 11 is shown in Table 12.

Equation 3 is valid for a source of photons that follow a Poissonian distribution. This distribution is used as the model when the LDLS and monochromator combination is used as the light source. The Poissonian photon-statistics model still represents the data appropriately, as can be seen in Figure 19d.

Figure 20 shows a plot of the ideal detection efficiency, η_0, for the 150 data runs at different XYZ positions of the SPAD relative to the focal spot of the beam. Table 13 is a sorted list of the average detection efficiency at the different XYZ positions. The average value and the standard deviation of the values in Table 13 is

$$\eta_0^{LDLS+Objective,19743} = 0.525(11) \tag{15}$$

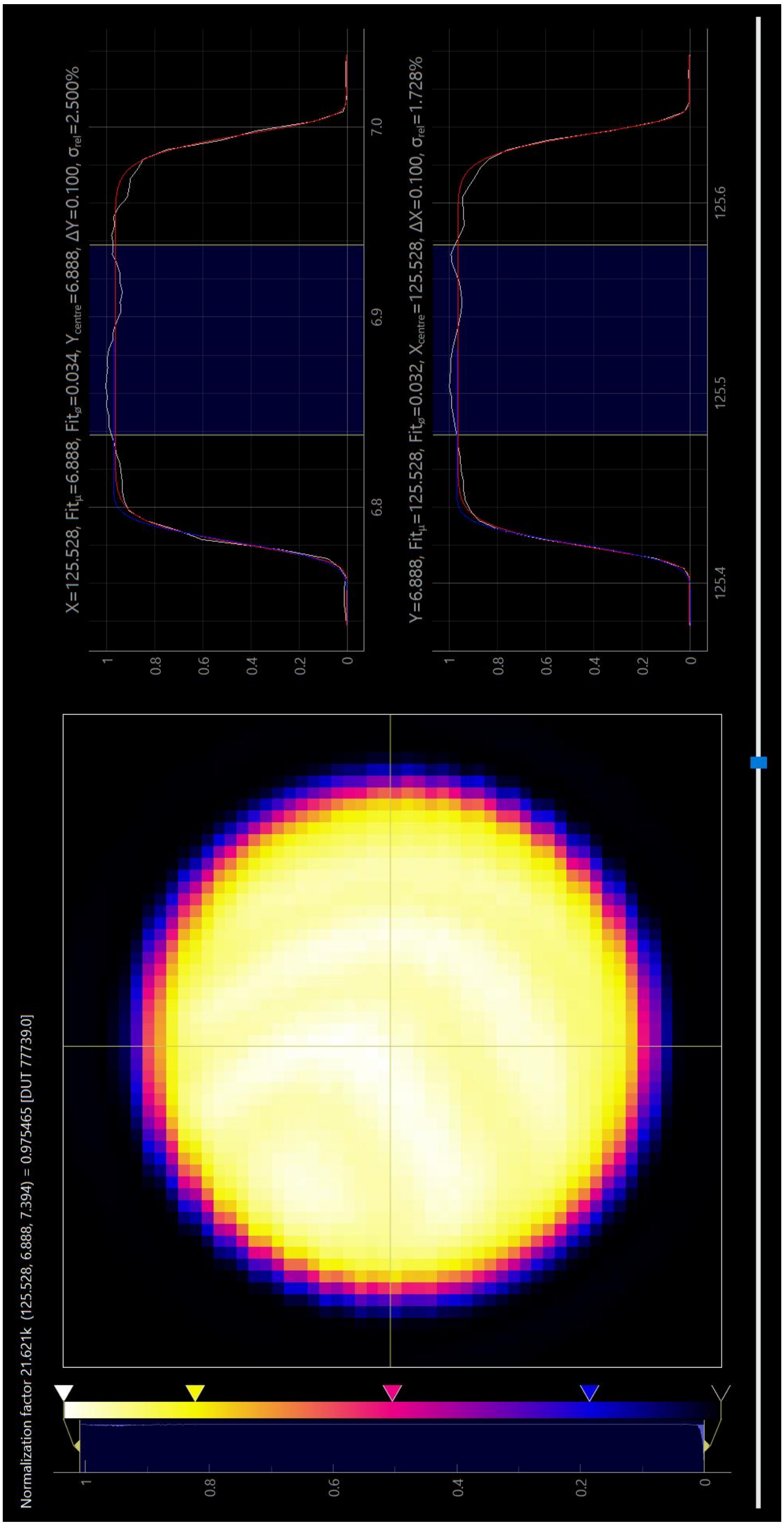

Figure 17: *Spatial scan of SPAD (Sn. 19743) for a beam diameter of $\approx$ 25 μm. The LDLS and monochromator is used as the source and the 10x objective focuses the light. The line plots correspond to the X and Y profiles (crosshair in image). The white curve is the profile data, red curve is a fit to a Super Gaussian distribution (Eq. 18) and the blue curve is a fit to a Gaussian Cumulative distribution (Eq. 19). The shaded blue region in each plot is 100-μm wide and shows that the relative non-uniformity is 1.73 % in X and 2.50 % in Y. Each pixel in the image corresponds to a 5 μm step in X and Y.*

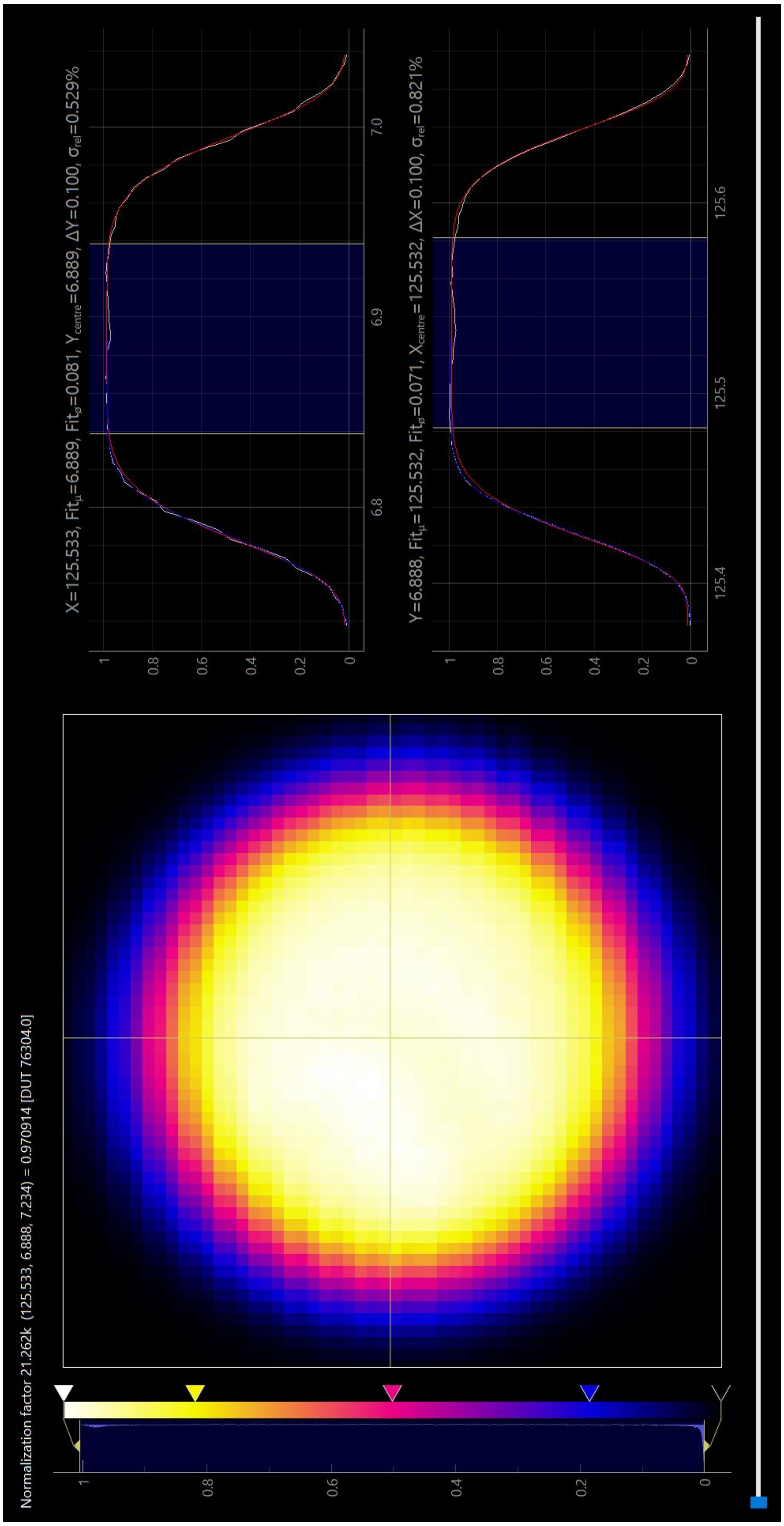

Figure 18: *Spatial scan of SPAD (Sn. 19743) for a beam diameter of $\approx$ 75 μm. The LDLS and monochromator is used as the source and the 10x objective focuses the light. The line plots correspond to the X and Y profiles (crosshair in image). The white curve is the profile data, red curve is a fit to a Super Gaussian distribution (Eq. 18) and the blue curve is a fit to a Gaussian Cumulative distribution (Eq. 19). The shaded blue region in each plot is 100-μm wide and shows that the relative non-uniformity is 0.82 % in X and 0.53 % in Y. Each pixel in the image corresponds to a 5 μm step in X and Y.*

CR, Counts/s	V^{Mon}_{SPAD}, V	Φ_{STD}, nW	V^{Mon}_{STD}, V	T	η
562240(150)	3.687409(36)	15.491(13)	3.687439(40)	1.6813(13)$\times10^{-5}$	0.50434(59)
444270(170)	3.689356(62)	15.495(13)	3.688363(19)	1.3219(10)$\times10^{-5}$	0.50660(60)
330070(180)	3.687232(53)	15.482(13)	3.685495(27)	9.7852(66)$\times10^{-6}$	0.50879(61)
254520(150)	3.69083(13)	15.492(13)	3.687554(57)	7.5186(52)$\times10^{-6}$	0.51009(63)
250763(91)	3.687493(22)	15.496(13)	3.688570(51)	7.4079(45)$\times10^{-6}$	0.51053(55)
202180(170)	3.690557(25)	15.509(13)	3.691863(87)	5.9569(39)$\times10^{-6}$	0.51147(69)
165920(94)	3.68639(10)	15.496(13)	3.688674(61)	4.8885(28)$\times10^{-6}$	0.51205(59)
75528(90)	3.687565(54)	15.496(13)	3.688679(69)	2.2193(14)$\times10^{-6}$	0.51326(81)
42403(82)	3.687594(40)	15.487(13)	3.686486(46)	1.24358(86)$\times10^{-6}$	0.5143(11)
26312(41)	3.684478(86)	15.489(13)	3.686805(19)	7.7231(49)$\times10^{-7}$	0.51424(97)
5355(16)	3.68531(12)	15.482(13)	3.685623(32)	1.57009(84)$\times10^{-7}$	0.5147(17)
627.8(6.4)	3.685860(98)	15.480(13)	3.684918(63)	1.8343(19)$\times10^{-8}$	0.5164(53)

Table 11: Measured quantities that are used to calculate the detection efficiency, as defined in Equation 2, when the light source is the LDLS and a 10x objective focuses the beam onto the SPAD (Sn. 19743). The SPAD is positioned at the beam focus (beam diameter ≈ 25 μm, (ΔX,ΔY,ΔZ) = (21, 0, 0) μm). Additional quantities not included in the table but are needed to evaluate Equation 2 are the constants $h = 6.626\,070\,15 \times 10^{-34}\ Js$ and $c = 299\,792\,458\ m/s$ (see Section 3.1), and the vacuum wavelength $\lambda = 850.231(62)\ nm$ (see Section 3.2.1). Values in parentheses are standard uncertainties (k=1). The corresponding plot of η versus CR is shown in Figure 19d.

Measurand	Unit	Measured Value	Uncertainty	Uncertainty (%)
Speed of Light (c)	m/s	2.99792458$\times10^{8}$		
Plank Constant (h)	J s	6.62607015$\times10^{-34}$		
Vacuum Wavelength (λ)	m	850.231$\times10^{-9}$	6.2$\times10^{-11}$	0.01
CR / V^{Mon}_{SPAD}	Counts/(s V)	20482	24	0.12
Φ_{STD} / V^{Mon}_{STD}	W/V	4.2009$\times10^{-9}$	3.4$\times10^{-12}$	0.08
Transmission Coefficient (T)	1	2.2193$\times10^{-6}$	1.4$\times10^{-9}$	0.06
Detection efficiency (η)	1	0.51326	0.00081	
Combined uncertainty (k=1)				0.16

Table 12: Uncertainty budget of the measured detection efficiency defined in Equation 2 that corresponds to the row in Table 11 with a count rate of 75528(90) Counts/s. This budget does not include spatial, non-uniformity effects which are the dominate uncertainty component of $\approx$ 4 %.

η_0	(ΔX,ΔY,ΔZ), μm	Approx. Beam Diameter, μm
0.50983(44)	(0, 21, 0)	25
0.51355(43)	(15, 15, 0)	25
0.51440(44)	(21, 0, 0)	25
0.51685(49)	(0, 0, 160)	75
0.51930(35)	(0, 0, 120)	60
0.52085(52)	(15, -15, 0)	25
0.52103(49)	(-15, 15, 0)	25
0.52204(43)	(0, 0, -160)	75
0.52344(51)	(0, 0, -120)	60
0.52356(47)	(0, 0, 80)	45
0.52606(31)	(0, 0, -80)	45
0.52957(57)	(0, 0, 0)	25
0.54201(33)	(-21, 0, 0)	25
0.54378(51)	(0, -21, 0)	25
0.54450(52)	(-15, -15, 0)	25

Table 13: Average ideal detection efficiency (individual measurement runs are shown in Figure 20) for the different XYZ positions of the SPAD (Sn. 19743) relative to the beam focus. The LDLS and monochromator is used as the source and the 10x objective focuses the light. The detection-efficiency values are sorted from smallest to largest. The detection-efficiency values in parentheses are standard uncertainties (k=1).

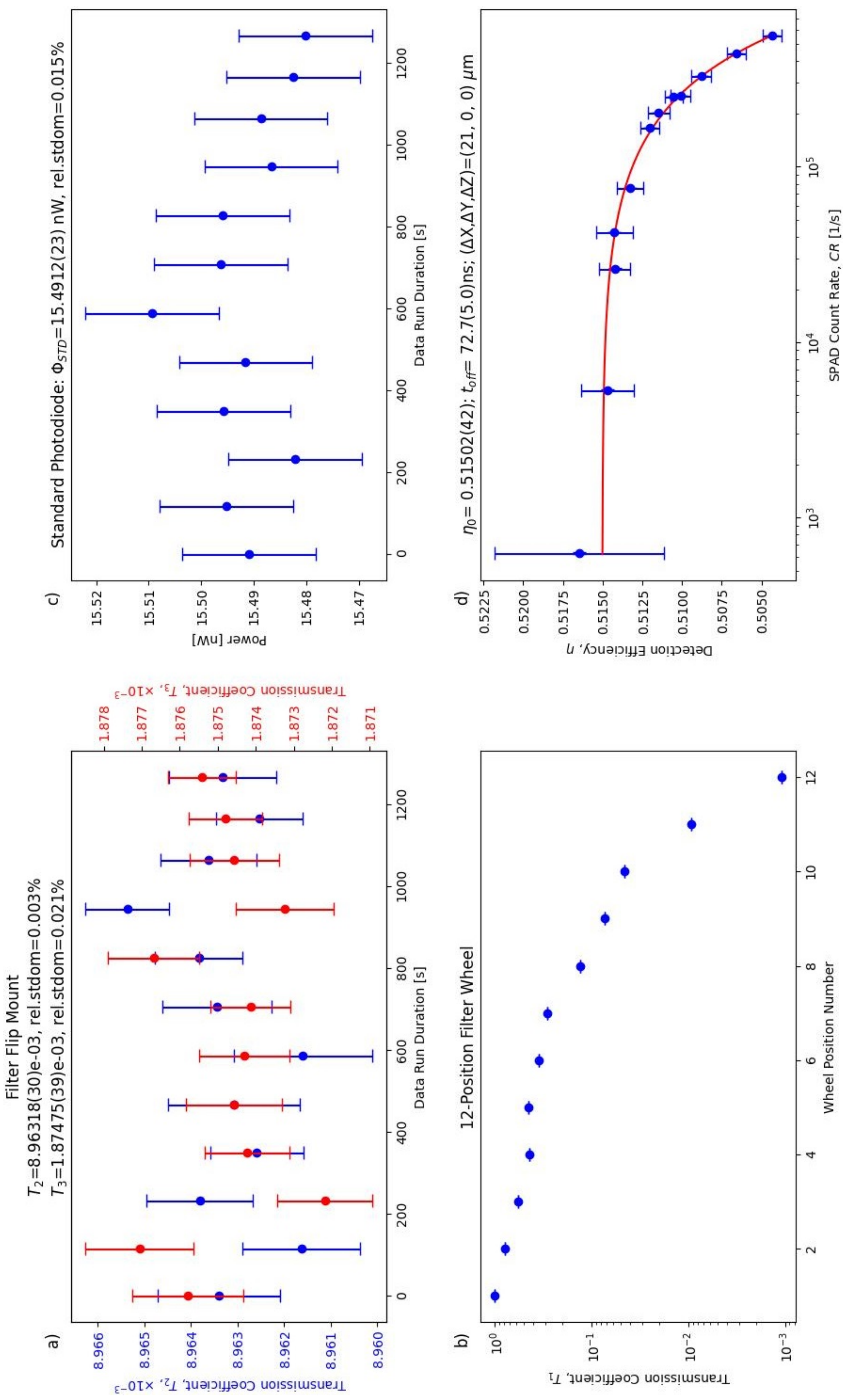

Figure 19: *Measurement run for SPAD (Sn. 19743) where the LDLS and monochromator is used as the source and the 10x objective focuses the light. a) Transmission coefficient of the neutral-density filter on each flip mount. b) Transmission coefficient of the neutral-density filter of the filter wheel. c) Optical-power measurement from the standard photodiode (not normalized against the monitor photodiode). d) Detection-efficiency data and fit (using Equation 3) when the SPAD is positioned (ΔX,ΔY,ΔZ) = (21, 0, 0) μm from the beam focus (beam diameter $\approx$ 25 μm). The term "rel.stdom" in a sub-figure title is shorthand for "relative standard deviation of the mean".*

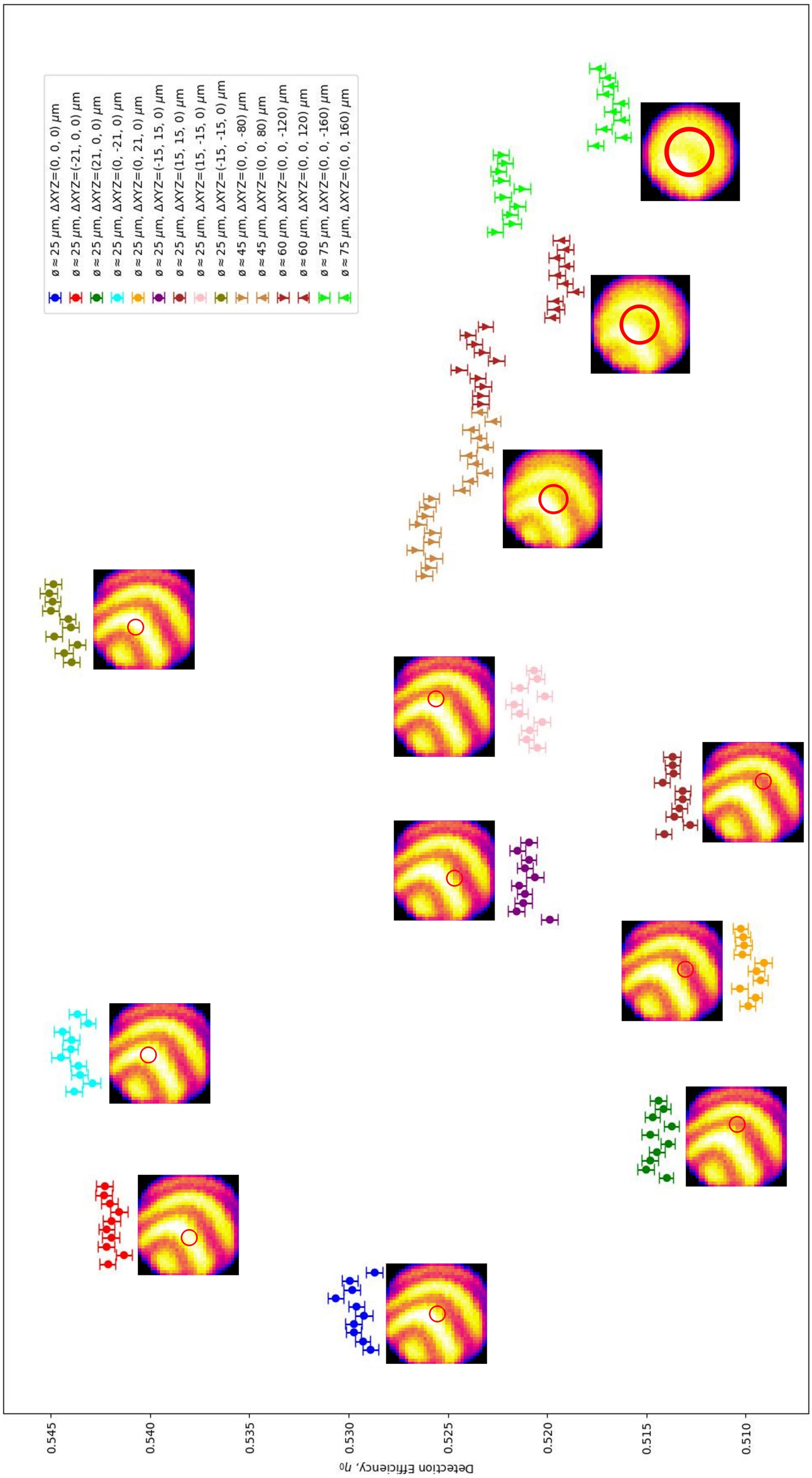

Figure 20: *Ideal detection efficiency, η_0, for the 15 XYZ positions of the SPAD (Sn. 19743) relative to the beam focus. The LDLS and monochromator is used as the source and the 10x objective focuses the light. Next to each dataset is an image of the spatial scan with an enhanced contrast. The red circle in the image corresponds to the approximate beam diameter, $1/e^2$, and approximately where the beam hits the SPAD.*

4.4 Detection Efficiency

Considering the spatial non-uniformity effects that were observed (see Section 3.5.2), the measurand that MSL has chosen to report corresponds to the detection efficiency for a beam diameter within the range of ≈ 25 μm to ≈ 75 μm (which corresponds to a beam capture of 99.9990%) striking the detector at a position within the central 75-μm diameter of the detector. This is represented pictorially in Figure 21 which shows the nine 25-μm beam diameters, one 45-μm beam diameter, one 60-μm beam diameter, and one 75-μm beam diameter that were used to measure the detection efficiency of a detector.

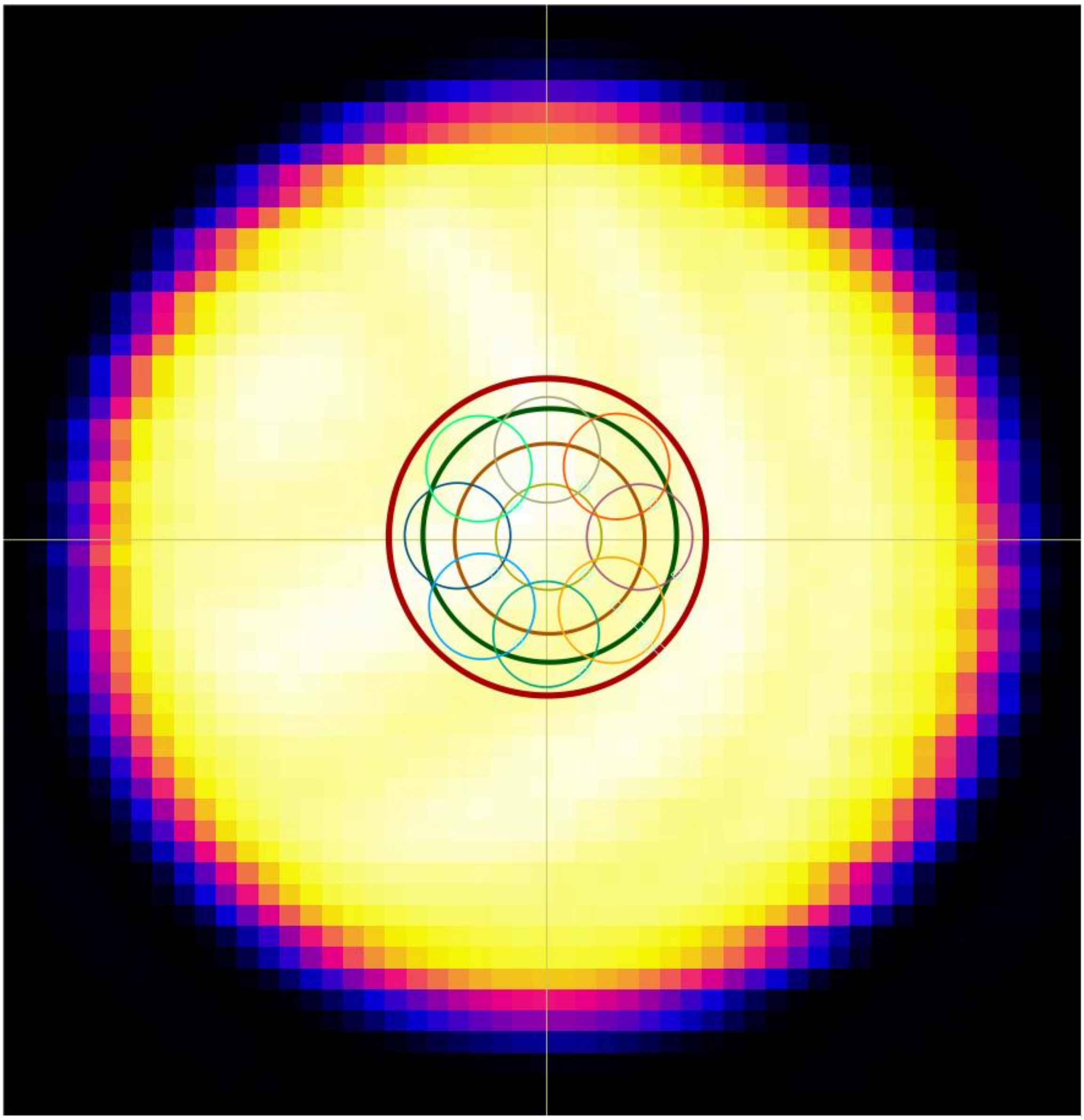

Figure 21: *Pictorial representation of the different beam diameters and beam positions that were used in this report to measure the detection efficiency.*

The detection efficiency for Perkin-Elmer SPCM-AQR-16 (Sn. 18752) is

$$\eta_0^{18752} = 0.505(37) \tag{16}$$

where the value corresponds to the midpoint between the upper limit of Equation 12 (0.520+0.021) and the lower limit of Equation 13 (0.486-0.018) with the uncertainty covering the upper and lower limits (k=1) (as shown in Figure 22).

The detection efficiency for Perkin-Elmer SPCM-AQR-16 (Sn. 19743) is

$$\eta_0^{19743} = 0.533(19) \tag{17}$$

where the value corresponds to the midpoint between the upper limit of Equation 14 (0.536+0.015) and the lower limit of Equation 15 (0.525-0.011) with the uncertainty covering the upper and lower limits (k=1) (as shown in Figure 22).

Figure 22 shows the final results for the two detectors.

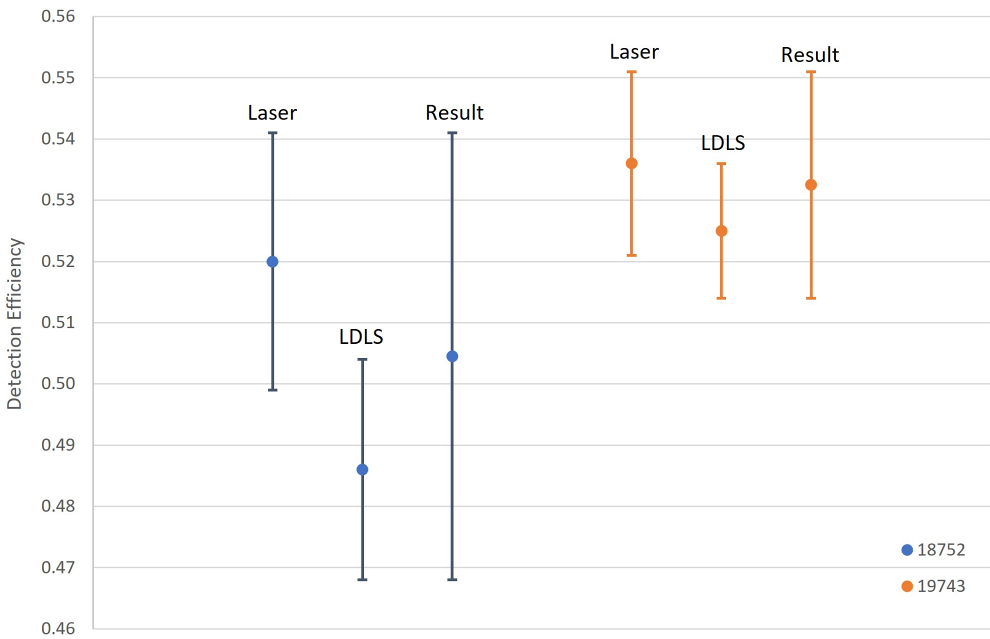

Figure 22: *Final results for the two detectors (Sn. 18752 and Sn. 19743) showing the individual results for the two optical systems (see Section 2) with the reported result.*

A Measurement Procedures

This appendix describes the procedures that were followed to align a SPAD to the beam focus and to acquire detection-efficiency data.

A.1 SPAD Alignment

The following steps were performed to align a SPAD to the beam focus. It is important that the +5 V power supply is not connected to the SPAD until the light conditions are at an appropriate level so as to not damage the SPAD.

1. Mount the SPAD to the adaptor plate that was manufactured at MSL.

2. Remove the neutral-density filters from the beam path so that the beam can be seen by eye (with the aid of a near-infrared viewer if necessary).

3. Attach the adaptor plate to the Y translation stage and manually adjust the position of the X, Y and Z stages so that the active area of the SPAD is approximately at the beam focus.

4. Insert the neutral-density filters into the beam path.

5. Connect the signal out and the power supply ports of the SPAD to the feedthrough connectors inside the light-tight enclosure and seal the enclosure (*note: the +5 V power supply must not be attached to the feedthrough connector on the external side of the enclosure*).

6. Connect the +5 V power supply to the feedthrough connector to provide power to the SPAD.

7. Run the spatial-scan software. Manually adjust the position of the X and Y stages using a step size of approximately 50 μm to maximize the count rate. Manually adjust the position of the Z stage using a step size of approximately 200 μm to maximize the count rate.

8. The optimal X position is found by keeping the Y and Z positions fixed and scanning X over a 500 μm width (centred on the value found in step 7) in steps of approximately 20 μm. Assuming that the 1D scan shows the edges of the SPAD, the data is fit to a super-Gaussian distribution,

$$a_1 \exp(-(\frac{x - a_2}{a_3\sqrt{2}})^{2a_4}) + a_5 \tag{18}$$

to determine the center, a_2. If the edges of the SPAD are not visible in the scan, the starting position of the scan must be adjusted (possibly as well as the scan width and step size). The scan procedure is repeated for Y, where X and Z are fixed. The 1D scans for X and Y are repeated until the center determined by the fit remains the same (to within a few micrometers).

9. To determine the optimal Z position, 1D scans in X and Y are performed separately and data are fit

to a Gaussian cumulative distribution function

$$a_1 \left[1 + \mathrm{erf}\left(\frac{x - a_2}{a_3\sqrt{2}}\right)\right] + a_4 \tag{19}$$

to determine an effective beam diameter, $4a_3$ (*note: although the fit may not provide an accurate value for the beam diameter, the fit may be used to determine where the beam diameter is a minimum*). The X (or Y) translation stage is positioned so that the SPAD intersects with the beam near the edge of the SPAD's active area. The Y (or X) translation stage is fixed at the optimal position determined in step 8. A 200-μm-wide scan is performed with a step size of 10 μm and data are fit to Equation 19 to determine the effective beam diameter at a particular Z position. A plot of the effective beam diameter versus Z position allows for determining the Z position where the beam diameter is a minimum.

10. 2D scans were performed at 7 different Z positions (3 positions on either side of the optimal Z position found in step 9). The scan in X and Y are each 300-μm wide and have a step size of 5 μm. The step size in Z depends on whether the 10x objective or the aspheric lens focuses the light.

A.2 Detection-Efficiency Acquisition

The following steps were performed to acquire the detection-efficiency data for a SPAD.

1. Close the shutter.

2. Move the Y and Z translation stages so that the SPAD is at the desired YZ position. The Y and Z stages remain at this value throughout the run.

3. Configure the Time Controller to use an external clock and use a 1 second count interval. The software acquires 12 samples to calculate the average count rate.

4. Configure the digital multimeter of the monitor photodiode and of the standard photodiode to be: 10 V range, 10 samples, 10 power line cycles (50 Hz), enable auto zero.

5. Move the X translation stage so that the standard photodiode is in the beam path, move the filter wheel to position 1 (the position with no neutral-density filter), move flip mount 1 and flip mount 2 to be out of the beam path.

6. Close shutter, wait 2 seconds, acquire monitor and standard photodiode signals simultaneously (*measures the dark signal of the traceable measurement*).

7. Open shutter, wait 2 seconds, acquire monitor and standard photodiode signals simultaneously (*measures the signal of the traceable measurement*).

8. Move flip mount 1 to be in beam path, change the DCV range of the digital multimeter of the standard photodiode to be 100 mV, wait 8 seconds.

9. Close shutter, wait 2 seconds, acquire monitor and standard photodiode signals simultaneously (*measures the dark signal of the neutral-density filter in flip mount 1*).

10. Open shutter, wait 2 seconds, acquire monitor and standard photodiode signals simultaneously (*measures the signal of the neutral-density filter in flip mount 1*).

11. Move flip mount 2 to be in the beam path, move flip mount 1 to be out of the beam path.

12. Close shutter, wait 2 seconds, acquire monitor and standard photodiode signals simultaneously (*measures the dark signal of the neutral-density filter in flip mount 2*).

13. Open shutter, wait 2 seconds, acquire monitor and standard photodiode signals simultaneously (*measures the signal of the neutral-density filter in flip mount 2*).

14. Move the filter wheel to the desired position, change the DCV range of the digital multimeter of the standard photodiode to be either 100 mV, 1 V or 10 V depending on the OD value of the filter in the filter wheel that is in the beam path, move flip mount 2 to be out of the beam path, wait 8 seconds.

15. Close shutter, wait 2 seconds, acquire monitor and standard photodiode signals simultaneously (*measures the dark signal of the neutral-density filter in the filter wheel*).

16. Open shutter, wait 2 seconds, acquire monitor and standard photodiode signals simultaneously (*measures the signal of the neutral-density filter in the filter wheel*).

17. Change the digital multimeter of the monitor photodiode to acquire 30 samples, move flip mount 1 in the beam path, move flip mount 2 in the beam path, move the X translation stage so that the SPAD is in the beam path.

18. Close shutter, wait 2 seconds, acquire monitor and SPAD signals simultaneously (*measures the dark signal of the SPAD*).

19. Open shutter, wait 2 seconds, acquire monitor and SPAD signals simultaneously (*measures the signal of the SPAD*).

20. If there are more positions remaining in the filter wheel go back to step 4, otherwise close the shutter and the measurement run is complete.

B References

[1] Marco López, Helmuth Hofer and Stefan Kück, *Detection efficiency calibration of single-photon silicon avalanche photodiodes traceable using double attenuator technique*, Journal of Modern Optics 62:20, 1732-1738 (2015); DOI: 10.1080/09500340.2015.1021724

[2] BIPM: The International System of Units (SI); online

[3] BIPM: Recommended values of standard frequencies; online

[4] BIPM: Recommended values of standard frequencies (2007): I_2 ($\lambda \approx$ 532 nm) [Table 16]; online

[5] BIPM: Recommended values of standard frequencies (2003): I_2 ($\lambda \approx$ 633 nm); online

[6] NIST: Refractive Index of Air Calculator; online

[7] Thomas Gerrits et al, *Calibration of free-space and fiber-coupled single-photon detectors*, Metrologia 57 015002 (2020); DOI: 10.1088/1681-7575/ab4533

[8] In-Ho Bae et al, *Detection efficiency measurement of single photon avalanche photodiodes by using a focused monochromatic beam tunable from 250 nm to 1000 nm*, Metrologia 56 035003 (2019); DOI: 10.1088/1681-7575/ab1d6c

[9] B D Hall and J S Borbely, MSLNZ/GTC: v1.4.1 (2023) Zenodo, GitHub

[10] Peter Saunders, Metrologia 40 93 (2003); DOI 10.1088/0026-1394/40/2/315; Python package is available at GitHub

[11] github.com/MSLNZ/pr-single-photons

Informal Release of results for 'Pilot study on the detection efficiency of single-photon detectors - Si-SPAD'

Daiji Fukuda and Tetsuya Tsuruta

Jan. 31 ,2025
CCPR WG-SP TG11 Pilot study
Calibration date: Feb-Jun 2024

Table 1 Calibration results for η_{DUT} at the counting rate of 1 cps.

SPAD		Wavelength	Temperature	Detection efficiency	Expanded uncertainty
name	SN	λ_c, (nm)	(°C)	η_{DUT}, (-)	(%), ($k = 2$)
SPAD1	18752	851.01	24.0	0.4647	1.43 %
SPAD2	19743	851.01	24.1	0.5795	1.42 %

National Institute of Advanced Industrial Science and Technology
National Metrology Institute of Japan

1 Detection efficiency calibration system

1.1 Calibration method

The two device under tests (DUT), which are the single photon avalanche detectors, were calibrated by the detection efficiency calibration system developed at AIST. Figure 1 shows the experimental setup for the calibration system. This system can prepare well defined input photon flux of n_{in} in the photon level from below 1 kcps to over 1 Mcps. The laser source is a continuous wave DFB laser, which has a single mode laser oscillation at the wavelength of 851.01 nm. At first, the laser output goes to free space at the collimator, and pass thorough an optical isolator to prevent its power instability. The polarization mode is adjusted by a polarization controller, which is consisted from two quarter plates and a half wave plate, and is always monitored by a polarimeter. Then, the laser light is guided to an optical fiber again and divided to three optical paths by two fiber beam splitters (FBS). At the first blanch, the laser power is always monitored by a power meter, which is defined as P_{mon}. The typical value of P_{mon} is ~ 3 mW. The second blanch is used to monitor the wavelength of the laser by a spectrum analyzer. At the third blanch, the laser power goes to the free space again and pass through an spacial filter, and finally goes into a trap detector that determines the absolute laser power at this end point. Now, we can determine the power ratio of the end point to the monitor power as

$$R_{\text{in/mon}} = P_{\text{trap}}/P_{\text{mon}}, \tag{1}$$

where P_{trap} is monitoring power at the end point measured by the trap detecter. The value of $R_{\text{in/out}}$ is assumed to be constant so that we can deduce the input photon flux of n_{in} at the end point only from P_{mon}, which is monitored during the detection efficiency calibration. Finally, the detection efficiency η_{DUT} is determined for a counting rate C_{rate}, which is defined as a photon count in unit time when the input photon flux n_{in} is induced to the DUT. The η_{DUT} is described as

$$\eta_{\text{DUT}} = \frac{C_{\text{rate}}}{P_{\text{mon}}} \times \frac{hc}{\lambda_{\text{center}}} \times \frac{1}{R_{\text{in/mon}}}, \tag{2}$$

where h and c is Planck's constant and speed of light, respectively, and λ_{center} is the center wavelength of the DFB laser. In our setup, $n_{\text{in}} = \lambda_{\text{center}} P_{\text{mon}} R_{\text{in/mon}}/hc$ can be set to the arbitral value in the range from below 1 kcps to over 1 MHz with the use of a free space optical attenuator, which is located after polarimeter in the optical beam axis in Figure 1. The optical attenuator is composed of a pin-hole to collimate the beam, which can be moved on the X-axis stage to control the optical attenuation A_{att}. It is worthy to note that the value of A_{att} itself is not affected to the uncertainty of η_{DUT}.

In our setup, typical values of parameters to generate the input photon rate of 1 kcps are $R_{\mathrm{in/mon}} = 7.75 \times 10^{-6}$, P_{mon} =30 pW and A_{att} =81 dB, for example.

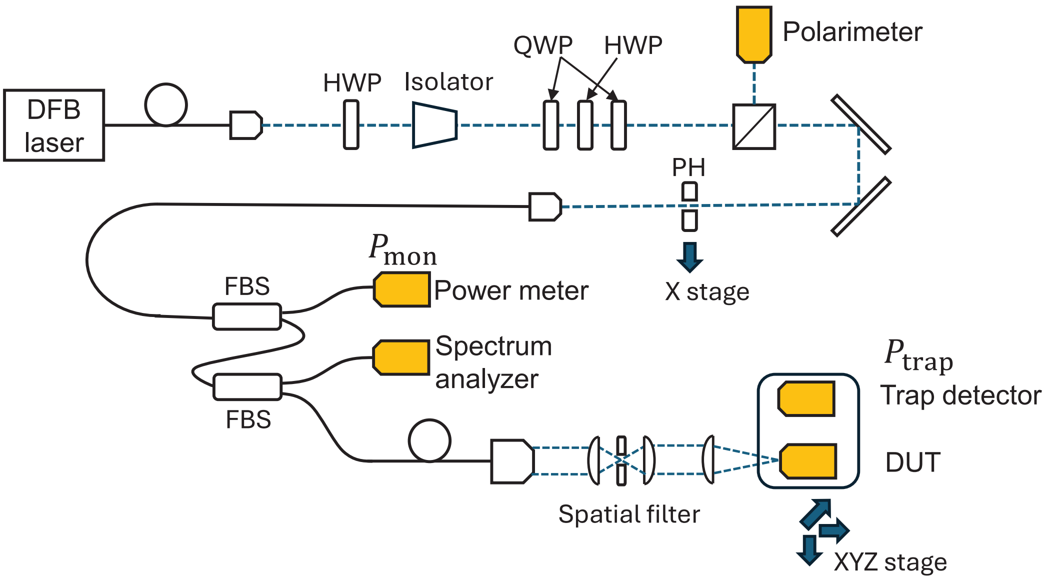

Figure 1 Experimental setup for detection efficiency calibration system. DFB:Distributed Feedback, HWP: Half Wave Plate, QWP: Quarter Wave Plate, FBS: Fiber Beam Splitter, DUT: Device Under Test.

1.2 Calibration chain

Figure 2 shows the calibration chain of our detection efficiency calibration system at NMIJ. The primary standard for the laser power at NMIJ is a laser calorimeter based on an electrical substitution method. The responsivity of the trap detector, which is consist of three-element Si photo detector, is calibrated at the power level of 50 µW at the wavelength of 851 nm. The responsivity of the trap detector is extended to the power level of 20 nW with our linearity calibration system. The ratio in Eqn. (1) is determined absolutely using the trap detector. In our detection efficiency calibration system, the absolute photon flux at the level of 1 kcps is generated, which is assured with the responsivity of the trap and the linearity of the monitor power meter.

2 DUT calibration

Two DUTs in this comparison are Silicon-avalanche single photon detectors, whose detection mechanism is based on the absorption of the single photon in a depletion layer, a creation of an electron-hole pair, and its avalanche amplification of charges in high electrical voltage. Because of this mechanism, we need to take care of dark counts and after-pulses in

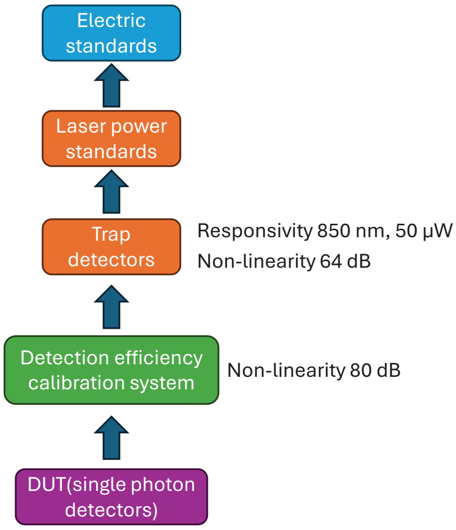

Figure 2 NMIJ calibration chain. The primary standard for laser power is a calorimeter based on an electrical-substitution method. The trap detector is calibrated by the primary standard at the power level of $50\,\mu\mathrm{W}$ and the wavelength of $850\,\mathrm{nm}$. The linearity measurements are performed to both the trap detector and the power meter.

the determination of the detection efficiency. After the clarification of these performances, we performed the calibration of η_{DUT}.

2.1 Dark count

The dark count rate was measured by placing the DUT on the XYZ stage in our experimental setup. The position of the beam was adjusted to the entrance of the DUT, but the beam shutter was OFF. The measurement time is $3600\,\mathrm{sec}$. The count of the DUT was recorded by SR400, Stanford Research Instruments. These results are summarized in Table 2. In the real case, the dark count rate measurement had been performed at each time of the data set as we shown later in section 2.5.

Table 2 Typical results of dark count of SPADs.

SPAD name	Measurement time N/sec	Dark count rate $\bar{C}_{\mathrm{dark}}$/cps
SPAD1	3600	25.11(8)
SPAD2	3600	22.13(8)

2.2 After-pulse

We characterized of an afterpulsing effect for both SPADS. In this evaluation, we measured photon arrival time distributions of single photon events subsequently after an initial single photon detection event. Our input photon state is obeyed to Poisson distribution, thus the observed photon arrival time should be independent to the photon arrival time. In this experiment, we used a time analyzer with a time resolution of 40 ps to record each photon arrival time event and construct the distribution. we set the subsequent recording time to 2.5 µs. Figure 3 (a) shows an example of observed distribution for SPAD1 at the counting rate of 30 kcps. We extracted a homogenous Poisson distribution region in the time range from 1 µs to 2.5 µs, as like a solid line in Figure 3 (a) , which is used to determine the after-pulsing probability. We repeated the measurements at several different counting rates for each DUTs, which are summarized in Figure 3 (b). To extract the after-pulsing probabilities P_{AP} for both DUTs, we fitted these data with a linear function with the first order as

$$P_{\mathrm{AP}} = ap_0 + ap \times \overline{C}_{\mathrm{rate}}, \tag{3}$$

,where ap_0 and ap is the coefficient of the linear function, and $\overline{C}_{\mathrm{rate}}$ is the counting rate of the DUT. These fitting results are summarized at Table 3.

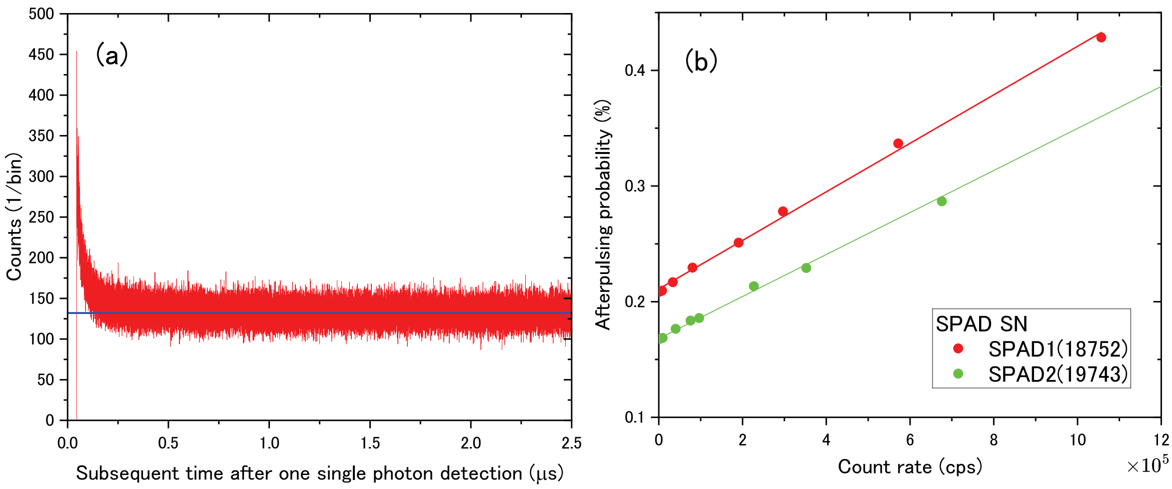

Figure 3 (a) Photon arrival time distribution for SPAD1 at the counting rate of 34 kcps. (b) After-pulsing probability as a function of counting rate for both DUTs. The solid lines are linear fits.

Table 3 After-pulsing evaluation results for both DUTs.

SPAD	ap_0 ($\times 10^{-2}$)	ap($\times 10^{-9}$)
SPAD1	0.211(18)	2.09(4)
SPAD2	0.168(12)	1.82(2)

2.3 Spacial uniformity

The spacial uniformity was measured for both DUTs by scanning the device at the fixed input photon rate of 100 kcps. The two dimensional scanning area is $280\,\mu\text{m}$ square with $10\,\mu\text{m}$ steps. The scanning profiles are shown in Figure 4. To understand the results easily, the intensity profile is normalized by the value at the center of the DUTs. We found that the response of both DUTs are strongly depending on the laser incident position. This might be due to interference of the lights reflected at the surface of the silicon and glass, because we use a continuous wave laser source. Our setup allows us to find the center of the SPAD with the repeatability better than $3\,\mu\text{m}$, so that we estimate the uncertainty in the detector response alignment to be $0.7\,\%$.

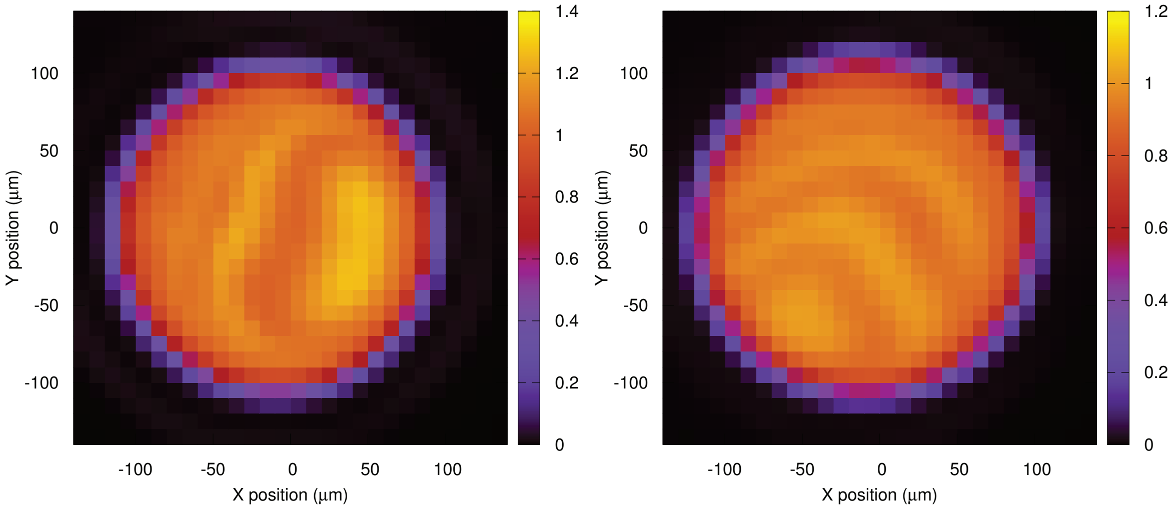

Figure 4 Intensity profile of SPAD, scannig a laser at 100 kcps. The scan step is 10 μm for SPAD1 (a) and SPAD2 (b). The intensity, which is shown in a color-bar, is normalized by the counts at the center of the DUTs.

2.4 Beam quality

Here, we denote the beam quality of the input beam in our calibration setup, which is closely related to the spacial uniformity of the DUTs. The beam qualities are evaluated based on an M^2 measurement, in which the beam 2D profile is scanning along with the propagation axis. Dots in Figure 5 show the measured radius results depending on the propagation position. These data is fitted with the following equation.

$$W(z) = w_0 \sqrt{1 + \left(\frac{M^2 \lambda (z - z_0)}{\pi w_0^2} \right)^2} \tag{4}$$

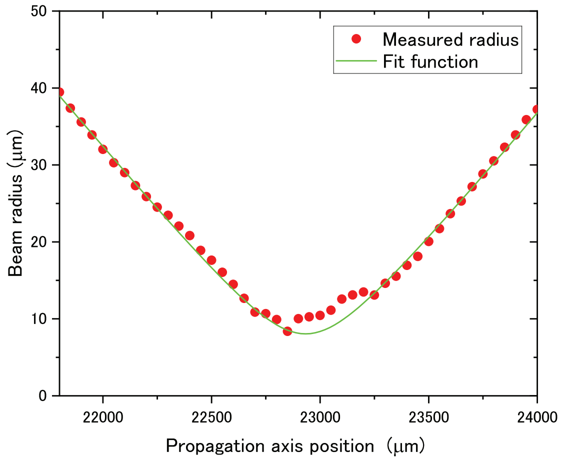

Figure 5 M^2 **measument resuls for the input beam in our experimental setup. Red points are measured radius and the solid line is the fitting curve.**

Table 4 Beam quality measurement results

Parameter	expression	value	unit
Beam radius	w_0	9.41(25)	μm
Focus point	z_0	22 933 (5)	μm
Factor	M^2	1.073(12)	-

The solid line in Figure 5 is the fitting results. From these results, we obtained the beam radius x_0 at the focusing position z_0 and M^2. These parameters are summarized in Table 4. Thus the beam diamber ($1/e^2$ of peak diameter) at the focus plane is estimated to be 20 μm in our setup.

2.5 Detection efficiency

The detection efficiency η_{DUT} was measured for both DUTs in the incident photon flux range n_{in} from 1 kcps to 1 MHz. We measured five sets of the data, then we extracted the value at the counting rate of 1 cps by interpolating the sets of data. At each incident photon rate, we accumulated counts upto at least 10^6 to minimize the statistical error. As was described already at section 2.1, we performed dark counts measurement at each measurement set. Observed photon events were counted by a single photon counter at fixed certain time, and the counting rate $\overline{C}$ is determined, which includes the effects of the dark count and after-pulsing. In the detection efficiency determination, we removed these effects using the following formula.

$$C_{\mathrm{rate}} = \overline{C} - \overline{C}_{\mathrm{dark}} - \overline{C}_{\mathrm{ap}}, \tag{5}$$

where $\overline{C}_{\mathrm{ap}}$ is the counting rate due to the after-pulsing, which can be described using the parameters in Table 3 as $\overline{C}_{\mathrm{ap}} = (ap_0 + ap \cdot \overline{C}) \cdot \overline{C}$. Then, Eqn. (5) can be re-written as

$$C_{\mathrm{rate}} = (1 - ap_0) \cdot \overline{C} - \overline{C}_{\mathrm{dark}} - ap \cdot \overline{C}^2, \tag{6}$$

The detection efficiency results depending on the counting rate C_{rate} for both DUTs are shown in Figure 6. In each DUT, five data sets were measured in the experiments. In order to deduce the detection efficiency η_{DUT} at the counting rate of 1 cps, we extrapolated the dataset with a linear function. Table 5 shows the summary of the extrapolated detection efficiency at 1 cps for both SPADs. The final detection efficiencies reported in Table 1 are obtained by averaging the results of five datasets.

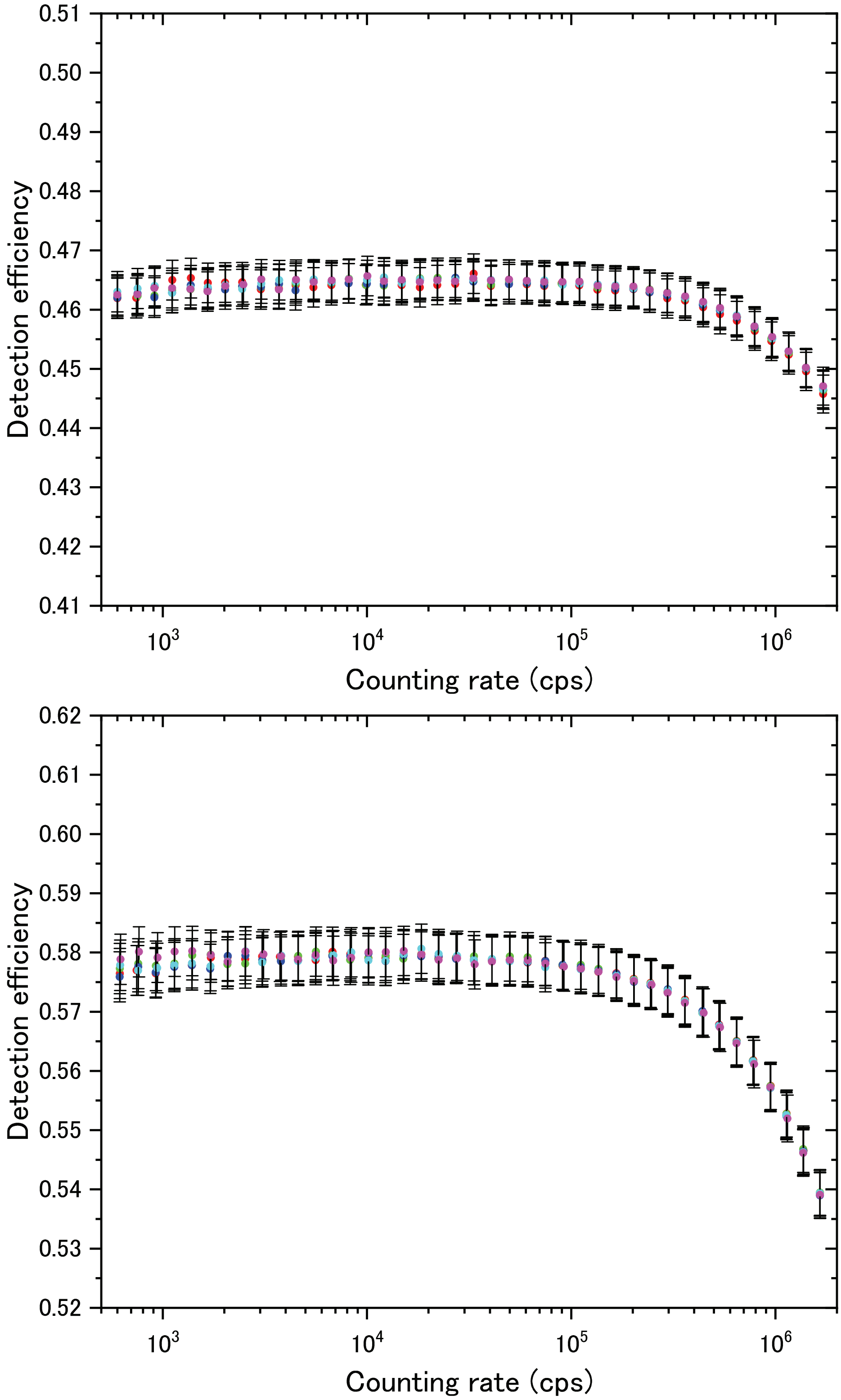

Figure 6 Intensity profile of SPAD, scanning a laser at 100 kcps. The scan step is 10 μm for SPAD1 (a) and SPAD2 (b). The intensity, which is shown in a color-bar, is normalized by the counts at the center of the DUTs.

Table 5 Summary of the detection efficiency measurements. η_{DUT} **is the interpolated detection efficiency at the counting rate of 1 cps. The values in the brackets are the fitting errors. The standard uncertainty** $(k = 1)$ **is the averaged standard uncertainties for 43 measurement points in each dataset.**

SPAD	dataset	wavelength λ, nm	Temperature T, °C	Humidity %	Pressure hPa	Detection efficiency η_{DUT}	standard uncertainty $k = 1$, $\times 10^{-3}$
SPAD1	1	851.01	24.0	41.0	1012.6	0.46453(15)	3.320
	2	851.01	24.0	41.0	1011.6	0.46460(17)	3.321
	3	851.01	24.0	41.0	1010.2	0.46451(17)	3.324
	4	851.01	24.0	41.0	1008.8	0.46491(15)	3.323
	5	851.01	24.0	41.0	1007.4	0.46486(17)	4.323
SPAD2	1	851.01	24.1	42.0	999.3	0.57981(10)	4.124
	2	851.01	24.1	42.9	995.5	0.57940(18)	4.123
	3	851.01	24.1	43.0	995.2	0.57929(20)	4.122
	4	851.01	24.1	43.0	995.2	0.57954(16)	4.124
	5	851.01	24.1	43.9	997.2	0.57941(19)	4.123

2.6 Uncertainty estimation

We estimated the measurement uncertainty of the detection efficiency using the following equation.

$$\left\{\frac{u(\eta_{\mathrm{DUT}})}{\eta_{\mathrm{DUT}}}\right\}^2 = \left\{\frac{u(C_{\mathrm{rate}})}{C_{\mathrm{rate}}}\right\}^2 + \left\{\frac{u(P_{\mathrm{mon}})}{P_{\mathrm{mon}}}\right\}^2 + \left\{\frac{u(R_{\mathrm{out/mon}})}{R_{\mathrm{out/mon}}}\right\}^2 + \left\{\frac{u(\eta_{\mathrm{DUT}}^{\mathrm{align}})}{\eta_{\mathrm{DUT}}^{\mathrm{align}}}\right\}^2, \tag{7}$$

where $\eta_{\mathrm{DUT}}^{\mathrm{align}}$ is the uncertainty component related to the beam alignment of the DUT, which is already discussed in subsection 2.3. The first term in the right hand in Eqn. (7) can be written as

$$u^2(C_{\mathrm{rate}}) = (1 - ap_0 - 2 \cdot ap \cdot \overline{C})u^2(\overline{C}) + u^2(\overline{C}_{\mathrm{dark}}), \tag{8}$$

where $u(\overline{C}) = \sqrt{C/N}$ and u$(\overline{C}_{\mathrm{dark}}) = \sqrt{C_{\mathrm{dark}}/N_{\mathrm{dark}}}$ is dominated by the statistical error. The second term in the right hand in Eqn. (7) can be written as

$$\left\{\frac{u(P_{\mathrm{mon}})}{P_{\mathrm{mon}}}\right\}^2 = \left\{\frac{u(\overline{P}_{\mathrm{mon}})}{\overline{P}_{\mathrm{mon}}}\right\}^2 + \left\{\frac{u(F_{\mathrm{mon,nl}})}{F_{\mathrm{mon,nl}}}\right\}^2, \tag{9}$$

where $u(\overline{P}_{\mathrm{mon}})$ is the standard deviation of the monitor power measurement with the monitor and $u(F_{\mathrm{mon,nl}})$ is the uncertainty of a non-linearity measurement of the monitor power meter. The third term in the right hand in Eqn. (7) can be written as

$$\begin{aligned}\left\{\frac{u(R_{\mathrm{out/mon}})}{R_{\mathrm{out/mon}}}\right\}^2 = \left\{\frac{u(\overline{P}_{\mathrm{trap}})}{\overline{P}_{\mathrm{trap}}}\right\}^2 + \left\{\frac{u(F_{\mathrm{trap}}^{\mathrm{nl}})}{F_{\mathrm{trap}}^{\mathrm{nl}}}\right\}^2 + \left\{\frac{u(F_{\mathrm{trap}}^{\mathrm{IV}})}{F_{\mathrm{trap}}^{\mathrm{IV}}}\right\}^2 + \left\{\frac{u(R_{\mathrm{trap}})}{R_{\mathrm{trap}}}\right\}^2 \\ + \left\{\frac{u(\overline{P}_{\mathrm{mon}}^{R_{\mathrm{out/mon}}})}{\overline{P}_{\mathrm{mon}}^{R_{\mathrm{out/mon}}}}\right\}^2 + \left\{\frac{u(R_{\mathrm{out/mon}}^{\mathrm{stab}})}{R_{\mathrm{out/mon}}^{\mathrm{stab}}}\right\}^2,\end{aligned} \tag{10}$$

where $u(\overline{P}_{\mathrm{trap}})$ is the standard deviation of the trap power measurement in the determination of $R_{\mathrm{in/out}}$, $u(F_{\mathrm{trap}}^{\mathrm{nl}})$ is the uncertainty of nonlinearity of the trap detector, $u(F_{\mathrm{trap}}^{\mathrm{IV}})$ is the uncertainty of the calibration factor of the current-voltage amplifier, $u(R_{\mathrm{trap}})$ is the uncertainty of the responsibility of the trap detector, $u(\overline{P}_{\mathrm{mon}}^{R_{\mathrm{out/mon}}})$ is the uncertainty of the nonlinearity of the monitor power meter when we applied optical attenuation, and $u(R_{\mathrm{out/mon}}^{\mathrm{stab}})$ is the uncertainty of the stability for $R_{\mathrm{out/mon}}$, respectively.

The standard uncertainty ($k = 1$) is calculated at every measurement points (there are 43 different counting rate points in one dataset.). In this experiment, the dominant uncertainty factor is the spacial uniformity of the DUT ($u(\eta_{\mathrm{DUT}})$) so that the standard uncertainty is less dependent on the counting rate. The average uncertainties of 43 measurement points in each dataset are also shown in Table 5. We considered the average standard uncertainty for all dataset puls the fitting error to estimate the standard uncertainty of η_{DUT} at 1 cps.

Table 6 Summary of standard uncertainties $(k = 1)$.

Component	Value	unit
$u(\overline{P}_{\mathrm{mon}})/\overline{P}_{\mathrm{mon}}$	0.02	%
$u(F^{\mathrm{nl}}_{\mathrm{mon}})/F^{\mathrm{nl}}_{\mathrm{mon}}$	0.01	%
$u(\overline{P}_{\mathrm{trap}})/\overline{P}_{\mathrm{trap}}$	0.02	%
$u(F^{\mathrm{nl}}_{\mathrm{trap}})/F^{\mathrm{nl}}_{\mathrm{trap}}$	0.01	%
$u(F^{\mathrm{IV}}_{\mathrm{trap}})/F^{\mathrm{IV}}_{\mathrm{trap}}$	0.01	%
$u(R_{\mathrm{trap}})/R_{\mathrm{trap}}$	0.15	%
$u(\overline{P}^{R_{\mathrm{out/mon}}}_{\mathrm{mon}})/\overline{P}^{R_{\mathrm{out/mon}}}_{\mathrm{mon}}$	0.02	%
$u(R^{\mathrm{stab}}_{\mathrm{out/mon}})/R^{\mathrm{stab}}_{\mathrm{out/mon}}$	0.01	%

Report on a Pilot Study of the Detection Efficiency of a Silicon Single-Photon Avalanche Diode (Si-SPAD)

Jeongwan Jin, Shivam Chanana, and Ka-Ming Liu

National Research Council (NRC) Canada

CONTENTS

1. Introduction
2. Traceability Chain
3. Spectral Responsibility of NRC Transfer Standards Detector
4. Experimental Setup
5. Experimental Parameters of the Light Source
6. Measurement of SPAD No. 19743
    a. Spatial Uniformity
    b. Detection Efficiencies and Uncertainties
7. Measurement of SPAD No. 18752
    a. Spatial Uniformity
    b. Detection Efficiencies and Uncertainties
8. Acknowledgements
9. References

NRC Contact: Jeongwan Jin (Jeongwan.Jin@nrc-cnrc.gc.ca)

Angela Gamouras (Angela.Gamouras@nrc-cnrc.gc.ca)

1. INTRODUCTION

The National Research Council (NRC) Canada has recently developed a detection efficiency measurement system for free-space single-photon detectors [1]. This system utilizes the detector substitution calibration method in combination with a double-attenuation technique [2]. In this approach, the single-photon detector under test is directly compared to a SI-traceable transfer standards detector (TSD) calibrated against the NRC primary cryogenic radiometer in the microwatt power range (refer to Section 2 and 3).

The input optical power is attenuated to a level detectable by single-photon detectors—approximately 100 fW—using two neutral density filters. Using this system, we calibrated the detection efficiency of the two single-photon avalanche photodiodes (SPADs), *Perkin-Elmer-SPCM-AQR-16 SN19743 and SN18752*.

The calibration setup is detailed in Section 4. A continuous-wave laser centered at 850.63 nm was used for the calibration process. Various incident photon flux levels were prepared using a variable optical attenuator at the input of the calibration system. Laser power stability was measured using a beam splitter and monitor photodiode. Faulty detections and dark counts were measured after blocking the input optical signal with a shutter, and these values were subtracted from the recorded data. A polarizer was used to ensure horizontal input light polarization, and a beam was focused to a 17-µm-diameter spot on the SPAD detector chip (refer to Section 5).

The detection efficiency, η_{det}, of the SPADs was calculated using the following equation:

$$\eta_{det} = \frac{\left(\frac{hc}{\lambda}\right)\times N_{det}}{E_0\times\prod_{n=1}^{2} T_i} = \frac{hc}{\lambda}\times s\times\frac{A_1A_2}{A_0}\times\frac{Q_0Q_3}{Q_1Q_2},$$

where E_0 is the total light intensity, and $T_{i\,(i=1,2)}$ are the transmission coefficients of the neutral density filters. h, c, and λ represent the Planck's constant, the speed of light, and the laser wavelength, respectively, while s denotes the spectral response of the TSD. $A_{i(i=0,1,2)}$ and $Q_{i(i=0,1,2)} = \frac{V_i}{V_{i,\ MON}}$ correspond to amplification coefficients and normalized voltages, respectively, relative to the monitor photodiode voltage $V_{i(i=1,2,3),\ MON)}$ of the TSD. The subscripts 0, 1, and 2 represent the absence of filters, the presence of Filter 1, and the presence of Filter 2 in the optical path, respectively. Additionally, $Q_3 = \frac{N_{SPAD}}{V_{SPAD,\ MON}}$ represents the normalized photon detections (refer to Section 6 and 7).

Uncertainty in the detection efficiency was evaluated using standard error propagation. The same amplification $A\ (A_0 = A_1 = A_2)$ was applied for determining all three Q values measured with the TSD.

$$\frac{\Delta\eta_{det}}{\eta_{det}} = \sqrt{\left(\frac{\Delta\lambda}{\lambda}\right)^2 + \left(\frac{\Delta s}{s}\right)^2 + \left(\frac{\Delta A}{A}\right)^2 + \sum_{i=0}^{3}\left(\frac{\Delta Q_i}{Q_i}\right)^2}$$

2. TRACEABILITY CHAIN

The NRC calibration traceability chain establishes traceability to the International System of Units (SI) through a hierarchy of measurement standards. A transfer standard detector (TSD), calibrated against the NRC primary cryogenic radiometer, is SI-traceable and was used to calibrate the detection efficiencies of the two SPADs [1, 3, 4, 5].

3. SPECTRAL RESPONSIVITY OF NRC TRANSFER STANDARDS DETECTOR (TSD)

The table below outlines the spectral responsivity and its associated uncertainty budget of the TSD [1].

Parameter	**Value (A/W)**
Spectral Responsivity at 850 nm	0.453
Spectral Responsivity Uncertainty	0.000598

4. EXPERIMENTAL SETUP

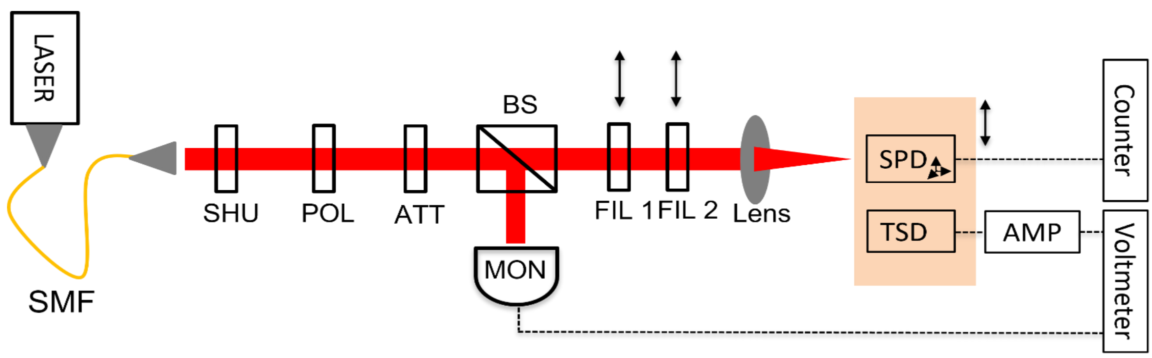

Diagram of NRC free-space Single-Photon Detector (SPD) detection efficiency measurement setup [1]. Two neutral density filters (FILs) attenuate the input flux to the femtowatt level. SMF: Single mode fiber; SHU: Shutter; POL: Polarizer; ATT: Attenuator; BS: Beam splitter; MON: Monitor photodiode; AMP: transimpedance amplifier.

5. EXPERIMENTAL PARAMETERS OF THE LIGHT SOURCE

Parameter	Specification
Light source	Continuous wave laser
Wavelength	850.63 nm
Polarization	Linear (Horizontal Polarization)
Bandwidth	126 pm
Beam diameter at SPAD	17 μm

6. Measurement of SPAD No. 19743

Spatial uniformity and measured detection efficiencies of the SPAD No. 19743

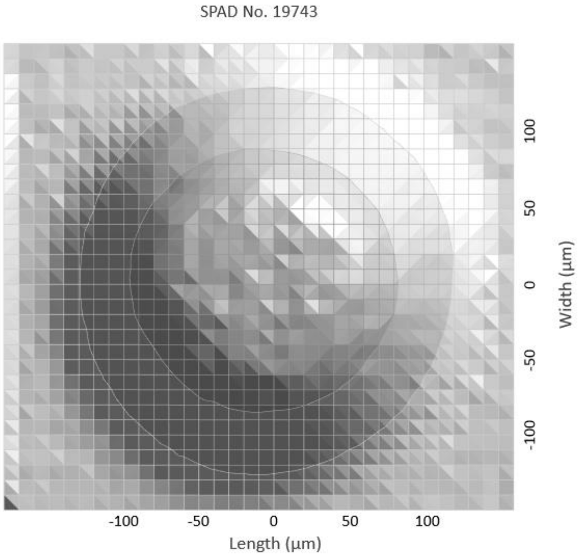

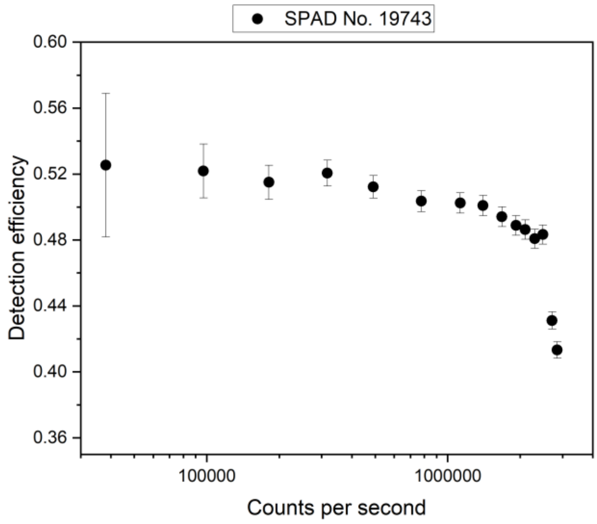

Measured detection efficiencies and uncertainties of the SPAD No. 19743

Detection efficiency = 0.538 ± 0.011

SPAD No. 19743

Temperature: 22.79 °C		Humidity: 32.09 %rh
Counts per second	**Detection efficiency**	**Uncertainty**
38125	0.52542	0.04352
96910	0.52184	0.01638
181190	0.51499	0.01030
316717	0.52055	0.00781
491139	0.51223	0.00687
776822	0.50354	0.00634
1127467	0.50246	0.00617
1400995	0.50092	0.00611
1678993	0.49412	0.00600
1921468	0.48884	0.00592
2096507	0.48629	0.00588
2296547	0.48075	0.00581
2481889	0.48330	0.00583
2711958	0.43120	0.00520
2845949	0.41332	0.00498

7. Measurement of SPAD No. 18752

Spatial uniformity and measured detection efficiencies of the SPAD No. 18752

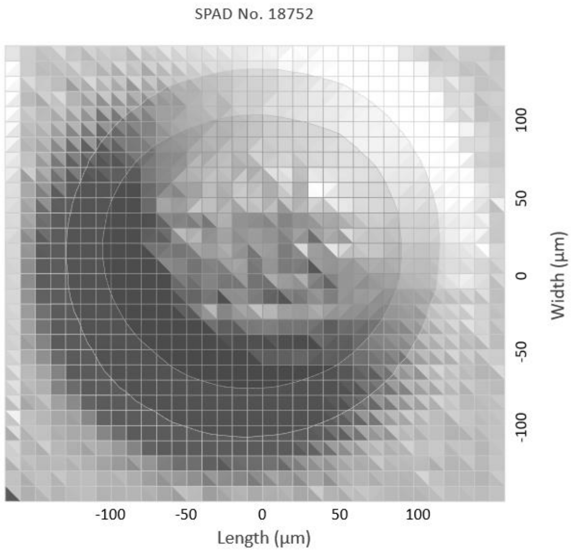

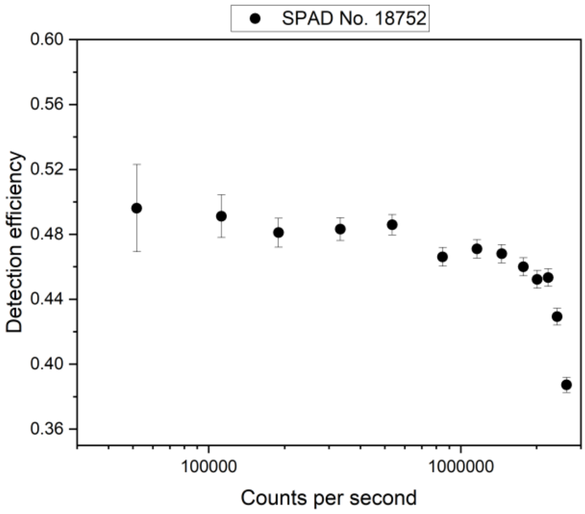

Measured detection efficiencies and uncertainties of the SPAD No. 18752

Detection efficiency = 0.503 ± 0.010

SPAD No. 18752

Temperature: 22.85 °C		Humidity: 32.48 %rh
Counts per second	**Detection efficiency**	**Uncertainty**
51784	0.49614	0.02685
112215	0.49120	0.01322
189212	0.48104	0.00888
332755	0.48319	0.00702
534376	0.48589	0.00633
846830	0.46612	0.00580
1159854	0.47107	0.00577
1454400	0.46800	0.00569
1771483	0.45995	0.00557
2011088	0.45228	0.00547
2221737	0.45334	0.00547
2410987	0.42930	0.00518
2629316	0.38723	0.00467

8. ACKNOWLEDGEMENTS

The authors would like to acknowledge Angela Gamouras for facilitating initial discussions that led to NRC's participation in this pilot study.

9. REFERENCES

[1] Jeongwan Jin, Thomas Gerrits and A. Gamouras, Calibration and comparison of detection efficiency for free-space single-photon avalanche diodes at 850 nm, *Applied Optics*, **61** 5244 (2022).

[2] M. López, H. Hofer, and S. Kück, Detection efficiency calibration of single-photon silicon avalanche photodiodes traceable using double attenuator, *J. Mod. Opt.* **62** S21 (2015).

[3] A. Gamouras, A. D. W. Todd, É. Côté, and N. L. Rowell, "The development of the advanced cryogenic radiometer facility at NRC," *J. Phys. Conf. Ser.* **972**, 012014 (2018).

[4] L. P. Boivin and K. Gibb, "Monochromator-based cryogenic radiometry at the NRC," *Metrologia* **32**, 565 (1995).

[5] L. P. Boivin, "Measurements using two types of transfer radiometer developed for a monochromator-based cryogenic radiometer facility," *Metrologia* **35**, 363 (1998).